THÈSE DE DOCTORAT

NNT : 2023UPAST131

Développement d'une méthodologie de caractérisation d'un système de refroidissement liquide pour machines électriques

Development of an Experimental Methodology for Characterising Liquid Cooling Systems for Electric Motors

Thèse de doctorat de l'université Paris-Saclay et de l'université Duisburg-Essen

École doctorale n°579
Sciences Mécaniques et Energétiques, Matériaux et Géosciences (SMEMaG)
Sciences de l'ingénierie et des systèmes, CentraleSupélec, doctorat en énergétique

Thèse préparée dans les unités de recherche de l'
IFP Energies Nouvelles (Rueil-Malmaison) et de l'
Institut für Energie- und Material-Prozesse EMPI (Université Duisburg-Essen)

Sous la co-direction de
Dr HdR **Gilles BRUNEAUX** et Professeur **Sebastian KAISER**

Thèse présentée et soutenue à l'Université Duisburg-Essen (Allemagne), le 4 octobre 2023, par

Ivano CORNACCHIA

Composition du Jury

Membres du jury avec voix délibérative

Burak ATAKAN Professeur, Université Duisburg-Essen	Président
Wilko ROHLFS Professeur, Université de Twente	Rapporteur & Examinateur
Matthieu FENOT Dr et HdR, Université de Poitiers	Rapporteur & Examinateur
Sebastian KAISER Professeur, Université Duisburg-Essen	Examinateur
Guillaume PILLA Dr et HdR, ONERA	Examinateur

Development of an Experimental Methodology for Characterising Liquid Cooling Systems for Electric Motors

Von der Fakultät für Ingenieurwissenschaften, Abteilung Maschinenbau und Verfahrenstechnik der

Universität Duisburg-Essen

zur Erlangung des akademischen Grades eines

Doktors der Ingenieurwissenschaften

Dr.-Ing.

genehmigte Dissertation von

Ivano CORNACCHIA

aus Rom (Italien)

Gutachter :	Univ.-Prof. Dr. Sebastian KAISER
	Univ.-Prof. Dr. Wilko ROHLFS
	Dr. Matthieu FENOT

Tag der mündlichen Prüfung: 4.10.2023

ÉCOLE DOCTORALE
Sciences mécaniques et énergétiques, matériaux et géosciences (SMEMAG)

Titre : Développement d'une méthodologie de caractérisation d'un système de refroidissement liquide pour machines électriques.

Mots clés : fluides à haut nombre de Prandtl, têtes de bobine, jet impactant, échange chaleur par convection.

Résumé : Le véhicule électrique est une technologie prometteuse pour réduire les émissions de particules et de gaz à effet de serre dans les zones urbaines. Le secteur de la recherche et du développement de l'industrie automobile met au point des moteurs électriques avancés pour répondre aux normes actuelles en matière de traction. Les moteurs doivent avoir une densité de puissance et de couple élevée et un encombrement réduit, d'où la nécessité d'une conception et de matériaux électromécaniques avancés. L'aspect thermique du moteur n'est pas d'une importance secondaire, car les pertes de puissance intrinsèques entraînent une augmentation de la température du moteur, ce qui provoque une perte de performances, voire une défaillance électromécanique. Les têtes des bobines du stator sont un composant critique car l'isolation électrique se dégrade lorsqu'elle est exposée à des températures élevées.

Le refroidissement direct par injection d'huile diélectrique est une solution efficace pour réduire la température des têtes des bobines et étendre la plage de fonctionnement du moteur. La modélisation des injections est difficile en raison des interactions thermiques et mécaniques complexes entre le liquide, l'air et le solide. La complexité est encore accrue par les géométries complexes des enroulements d'extrémité et par les propriétés thermiques particulières des huiles, qui sont connues comme étant des fluides à haut nombre de Prandtl. Des recherches expérimentales supplémentaires sont nécessaires pour étayer l'analyse numérique en fournissant des estimations des paramètres fondamentaux du transfert de chaleur.

L'impact d'un jet à surface libre est pris en compte. La littérature expérimentale connue propose des études fondamentales qui évaluent le coefficient de convection et les corrélations entre les nombres adimensionnels de Nusselt, Reynolds et Prandtl. La littérature n'est pas abondante, n'est pas représentative de la gamme thermique des têtes des bobines, n'utilise pas les types de fluides de la mobilité électrique et utilise des formes de cibles solides qui permettent de simplifier les hypothèses sur le transfert de chaleur. La présente recherche vise à étendre cette littérature en comblant ces lacunes.

Un appareil expérimental est construit pour reproduire une injection d'huile simplifiée sur une plaque plate chauffée, dans la plage de température des enroulements terminaux. Une méthode est développée pour évaluer les coefficients de convection locaux, les nombres de Nusselt locaux et les corrélations de Nusselt, en s'appuyant sur des mesures et des simulations. Divers diagnostics sont utilisés pour caractériser la plaque solide et l'injection de liquide (avant et après l'impaction), y compris une technique optique basée sur la fluorescence induite par laser.

Les principaux résultats de cette recherche sont organisés en cinq chapitres. Le premier explique le cadre industriel, l'état de l'art en matière d'impaction de jet et les objectifs de la recherche. Le deuxième chapitre présente les détails techniques des méthodes, des matériaux, des formulations et des hypothèses. Dans la troisième partie, l'injection et la plaque sont caractérisées, en mesurant les températures de la plaque à l'aide de thermocouples intégrés et en simulant le flux de chaleur. Dans le quatrième, le liquide est caractérisé après l'impaction, en mesurant l'épaisseur et la température à l'aide de diverses techniques.

Ce projet de recherche contribue à mieux définir les défis industriels, scientifiques et techniques liés au refroidissement des têtes des bobines par impaction de jet et avec des fluides à fort coefficient de Prandtl. Des autres contributions sont apportées par le développement de nouvelles méthodes de diagnostic et d'estimations représentatives de l'échange thermique par convection.

Title: Development of an Experimental Methodology for Characterising Liquid Cooling Systems for Electric Motors
Key words: High-Prandtl Fluids, End-Windings, Jet Impingement, Convective Heat Transfer.

Summary: The electric vehicle is a promising technology to reduce particulate matter and greenhouse gas emission in urban areas. The R&D sector of the automotive industry is developing advanced electric motors to meet today's standards for traction. Motors with high power density, high torque density and reduced bulk are required, thus the need for advanced electro-mechanical design and materials. The thermal management of the motor is not of secondary importance, because intrinsic power losses lead to the rise of the motor temperature, causing a loss of performances and even electro-mechanical failure. The stator end-windings are a critical component because the electrical insulation degrades when exposed to high temperature.

Direct cooling with dielectric lubricant oil injections is an effective solution for mitigating the temperature of the end-windings and extend the operating range of the motor. Modelling the injections is difficult because of the complex thermal and mechanical interactions between the liquid, the air and the solid. More complexity is added by the end-windings intricated geometries and by the peculiar thermal properties of the oils, which are known as high-Prandtl fluids. More experimental research is needed to support the numerical analysis by providing estimates of the fundamental parameters of the heat transfer.

Free-surface jet impingement is considered. The known experimental literature proposes fundamental studies, which evaluate the convective coefficient and the correlations between the dimensionless numbers Nusselt, Reynolds and Prandtl. The literature is not abundant, not representative of the thermal range of the end-windings, not using fluid types of electric mobility and uses solid target shapes which allow simplifying assumptions on the heat transfer. The present research aims to extend this literature by fulfilling these knowledge gaps.

An experimental apparatus is built to replicate a simplified oil injection over a flat heated plate, within the temperature range of the end-windings. A method is developed to evaluate local convective coefficients, local Nusselt numbers and Nusselt correlations, relying on measurements and simulations. Various diagnostics are employed to characterise the solid plate and the liquid injection (before and after impingement), including an optical technique based on laser induced fluorescence.

The main findings of this research are organised in five chapters. In the first, the industrial framework, the state of art on jet impingement and the objectives of the research are explained. In the second, the technical details of the methods, materials, formulations, and assumptions, are given. In the third, the injection and the plate are characterised, by taking measurements of the plate temperatures with embedded thermocouples and by simulating the heat flux. In the fourth, the liquid is characterised after impingement, by taking measurements of thickness and temperature with diverse techniques, including thermocouples, contact needles, and imaging methods. In the fifth, the results from the previous chapters are combined to determine the convective coefficient, the Nusselt number and the Nusselt correlations, which are compared to the most similar literature. Lastly, the manuscript ends by reporting the conclusions and the perspectives for future work.

This research project contributes to better define the industrial, scientific and technical challenges related to the cooling of the end-windings with jet impingement and high-Prandtl fluids. Additional contributions are given by the development of new diagnostic methods and representative estimates of convective heat transfer.

Title: Entwicklung einer Methode zur Charakterisierung eines Flüssigkeitskühlsystems für elektrische Maschinen.

Schlüsselwörter: Flüssigkeiten mit hoher Prandtl-Zahl, Spulenköpfe, Impaktstrahl, Wärmeaustausch durch Konvektion.

Zusammenfassung: Das Elektrofahrzeug ist eine vielversprechende Technologie zur Verringerung der Feinstaub- und Treibhausgasemissionen in städtischen Gebieten. Der F&E-Bereich der Automobilindustrie entwickelt fortschrittliche Elektromotoren, um die heutigen Standards für die Traktion zu erfüllen. Erforderlich sind Motoren mit hoher Leistungs- und Drehmomentdichte und geringem Platzbedarf, was fortschrittliche elektromechanische Konstruktionen und Werkstoffe erforderlich macht. Das Wärmemanagement des Motors ist nicht von untergeordneter Bedeutung, da intrinsische Leistungsverluste zu einem Anstieg der Motortemperatur führen, was einen Leistungsverlust und sogar einen elektromechanischen Ausfall zur Folge hat. Die Statorendwicklungen sind eine kritische Komponente, da die elektrische Isolierung bei hohen Temperaturen abnimmt.

Die direkte Kühlung mit dielektrischen Schmieröleinspritzungen ist eine wirksame Lösung, um die Temperatur der Endwicklungen zu senken und den Betriebsbereich des Motors zu erweitern. Die Modellierung der Einspritzungen ist aufgrund der komplexen thermischen und mechanischen Wechselwirkungen zwischen der Flüssigkeit, der Luft und dem Festkörper schwierig. Die Komplexität wird durch die komplizierten Geometrien der Endwicklungen und die besonderen thermischen Eigenschaften der Öle, die als Hoch-Prandtl-Flüssigkeiten bekannt sind, noch erhöht. Weitere experimentelle Untersuchungen sind erforderlich, um die numerische Analyse durch Schätzungen der grundlegenden Parameter der Wärmeübertragung zu unterstützen.

Es wird das Auftreffen eines Freistrahls auf der Oberfläche betrachtet. In der bekannten experimentellen Literatur werden grundlegende Studien vorgeschlagen, die den Konvektionskoeffizienten und die Korrelationen zwischen den dimensionslosen Zahlen Nusselt, Reynolds und Prandtl bewerten. Die Literatur ist nicht reichhaltig, nicht repräsentativ für den thermischen Bereich der Endwinde, verwendet keine Fluidtypen mit elektrischer Mobilität und verwendet feste Zielformen, die vereinfachende Annahmen zum Wärmeübergang erlauben. Die vorliegende Forschungsarbeit zielt darauf ab, diese Literatur zu erweitern, indem diese Wissenslücken geschlossen werden.

Es wird eine Versuchsvorrichtung gebaut, um eine vereinfachte Öleinspritzung über eine flache beheizte Platte im Temperaturbereich der Endwindungen nachzubilden. Es wird eine Methode entwickelt, um lokale Konvektionskoeffizienten, lokale Nusselt-Zahlen und Nusselt-Korrelationen auf der Grundlage von Messungen und Simulationen zu ermitteln. Zur Charakterisierung der festen Platte und der Flüssigkeitsinjektion (vor und nach dem Aufprall) werden verschiedene Diagnosemethoden eingesetzt, darunter eine optische Technik auf der Grundlage der laserinduzierten Fluoreszenz.

Die wichtigsten Ergebnisse dieser Forschung sind in fünf Kapiteln zusammengefasst. Im ersten Kapitel werden die industriellen Rahmenbedingungen, der Stand der Technik beim Aufprall von Düsen und die Ziele der Forschung erläutert. Im zweiten Kapitel werden die technischen Details der Methoden, Materialien, Formulierungen und Annahmen beschrieben. Im dritten Teil werden die Einspritzung und die Platte charakterisiert, indem die Temperatur der Platte mit eingebetteten Thermoelementen gemessen und der Wärmefluss simuliert wird. Im vierten Teil wird die Flüssigkeit nach dem Aufprall charakterisiert, indem die Dicke und die Temperatur mit verschiedenen Techniken gemessen werden, darunter Thermoelemente, Kontaktnadeln und bildgebende Verfahren. Im fünften Kapitel werden die Ergebnisse aus den vorangegangenen Kapiteln kombiniert, um den Konvektionskoeffizienten, die Nusselt-Zahl und die Nusselt-Korrelationen zu bestimmen, die mit der am meisten vergleichbaren Literatur verglichen werden. Schließlich schließt das Manuskript mit den Schlussfolgerungen und den Perspektiven für zukünftige Arbeiten.

Dieses Forschungsprojekt trägt dazu bei, die industriellen, wissenschaftlichen und technischen Herausforderungen im Zusammenhang mit der Kühlung von Endwindungen mit Jet Impingement und Hoch-Prandtl-Flüssigkeiten besser zu definieren. Weitere Beiträge werden durch die Entwicklung neuer Diagnosemethoden und repräsentativer Schätzungen des konvektiven Wärmeübergangs geleistet.

“Ignoranti quem portum petat nullus suus ventus est.”

The wind is never favourable to the sailor who doesn’t know where he’s going.

L. A. Seneca, Ep. ad Luc.71

Acknowledgments

During these years, I had the chance to meet and collaborate with many people, who helped me and contributed in their own way to this PhD. I would like to spend few words herby to thank them all.

I start by thanking the members of the committee of the PhD dissertation, who committed themselves to review and examine my work.

I express my deepest gratitude to my supervisors Dr. Baptiste CHAREYRON, Dr. Guillaume PILLA, Dr. Gilles BRUNEAUX and Prof. Sebastian KAISER, who guided me daily with patience and wisdom, supported me with encouraging words, and trained me through their knowledge and expertise.

In the IFPEN, I had the possibility to work in a stimulating environment for technology and innovation. I am grateful to the researchers Dr. Adèle PEAUBEAU, Dr. Guillaume VINAY, and Dr. Luis-Marie MALBEC, for their significant contribution to my work. I am deeply in debt with the members of the Laboratory DIOP for their technical support and for getting me out of everyday struggle: Jérôme CHEREL, Vincent RICORDEAU, Clément BRAMOULLE, and Francis LENGLET.

I would like to express my deepest gratitude to the IFPEN scientists and technicians who have helped me and advised me in their own specific way: Dr. Christian ANGELBERGER, Dr. Julien KASHDAN, Eng. Pierre VIOT, Dr. Gianluca ZITO, Dr. Ralph SINDJUI, Dr. Michele BARDI, Eng. Breno ALVEZ MENDES, Dr. Adrien GILSON, Fabien COLLIN, Vincent MOREL, Philippe GRIMAUD, Jean Luc HUBERT, Vincenzo DI PIAZZA, Denis GROSJEAN and Christophe DUFRESNES

In the Universität Duisburg-Essen, I was warmly welcomed and supported by brilliant scientists and expert technicians, who trained me and helped me pursuing my research. Thanks to Dr. Niklas JÜNGST, Dr-to-be Jonas KÜLMANN, Dr-to-be Kai BANKE, Natascha SCLÖSSER, Jörg ALBRECHT, Dr. Markus PRENTING, and Dr. Ahmad SAYLAM.

I am grateful to Prof. Andreas KEMPF (Universität Duisburg-Essen), Prof. Mathieu FENOT (Université de Poitiers), Prof. Luc VERVISCH (INSA), Prof. Christine ROUSSELLE (Université d'Orléans), and Dr. Julien LABAUNE (ONERA), for validating the intermediate milestones of my PhD and for their valuable advises.

Thanks to my companions, who have shared with me the harsh life of a PhD student: Dr. Erwan RONDEAUX, Dr. Mouad DOUADI, Dr. Claudia CANTARELLI, Dr-to-be Daniel CARLOS DA SILVA, Dr-to-be Jeremy CREUX, Dr. Fangyi WANG, Dr-to-be Esra BAUER, and Dr-to-be Judith LAICHTER and Dr-to-be Quan VAN HOANG.

My eternal gratitude goes to my MOTHER, my FATHER, and my BROTHER. There are simply no words to describe how much you gave me.

Thank to my duckling love Dr. Carolina CHIEFFO, for supporting me, encouraging me, and providing me relief in the most difficult times.

Résumé Substantiel en Français

- **Contexte**

La demande pour les véhicules électriques est de plus en plus importante dans le monde du fait de leur impact positif sur la réduction de la pollution dans les centres urbains. L'industrie automobile met donc au point de nouveaux groupes motopropulseurs électriques, en particulier le moteur électrique, l'électronique de puissance et le système de stockage. En ce qui concerne le système de propulsion, les moteurs électriques évoluent vers une plus grande densité de puissance et de couple élevée et un faible encombrement, afin de répondre aux exigences du marché automobile. Des efforts sont déployés pour optimiser la conception électromagnétique des moteurs et intégrer des matériaux plus performants. La gestion thermique devient également fondamentale dans le processus de conception, car le refroidissement traditionnel est insuffisant pour préserver les performances du moteur et son intégrité.

Quel que soit la zone de fonctionnement, le moteur chauffe en raison des pertes intrinsèques aux matériaux composant le moteur. L'exposition à une température excessive est dangereuse pour certains composants car ils peuvent perdre leurs propriétés de manière temporaire ou permanente. Les composants les plus sensibles sont les aimants permanents situé au rotor et les têtes des bobines au stator. Notamment, l'isolation des bobinages qui fixe la limite maximale de température (conventionnellement 150-180 °C). En effet, à haute température ses propriétés se dégradent et des points chauds sont susceptibles d'apparaître, pouvant entrainer une défaillance électrique.

Les systèmes de refroidissement sont de plus en plus intégrés à l'architecture du moteur et leur action sont ciblées sur les composants critiques. L'utilisation d'huile est d'intérêt, grâce aux propriétés diélectriques, et donc à la possibilité d'un contact direct avec les composants électriquement actifs. Des essais expérimentaux sur des moteurs réels prouvent que le refroidissement des têtes des bobines par injection d'huile réduit l'augmentation de la température et prolonge la durée d'utilisation des moteurs sous des fortes contraintes.

La prédiction du transfert de chaleur sur les têtes des bobines par injection d'huile pose des problèmes de modélisation, car une injection d'huile est une interaction complexe de type multi-échelle et multi-physique. En outre, la géométrie et les propriétés des têtes des bobines, ainsi que les propriétés rhéologiques et thermiques particulière des huiles, ajoutent de la complexité à la simulation. Plus précisément, les huiles sont considérées comme des fluides à haut nombre de Prandtl, dont la couche limite thermique est beaucoup plus petite que la couche limite dynamique, ce qui rend les simulations par éléments finis coûteuses pour les domaines à grande échelle en raison de la nécessité d'un maillage très fin. Par conséquent, les études expérimentales sont importantes pour aider et valider l'analyse numérique.

Il existe de nombreuses techniques d'injection et de nombreux types de fluides, mais cette thèse concentre sur le transfert de chaleur par convection d'un jet impactant à surface libre avec de l'huile lubrifiante pour la mobilité électrique. Dans ce cadre, la littérature propose des méthodes expérimentales pour évaluer le coefficient de convection local, le nombre de Nusselt et les corrélations entre les nombres de Nusselt, Reynolds et Prandtl, pour diverses géométries d'injection, types de buses, types de fluides et régimes d'écoulement. Les recherches déjà présentes dans la littérature sont généralement des expériences fondamentales, dont les cibles typiques sont des plaques minces ou des cylindres allongés, car elles permettent de simplifier les hypothèses sur le transfert de chaleur et facilitent le diagnostic.

- **Objectifs de la recherche et structure du manuscrit**

L'analyse bibliographique sur l'impact des jets avec des fluides à haut nombre de Prandtl révèle que la littérature est limitée, qu'elle n'est pas assez représentative de la gamme de température des moteurs ni des fluides utilisés dans la mobilité électrique. En outre, les géométries des cibles du jet ne sont pas représentatives non plus, et les expériences reposent souvent sur des hypothèses simplificatrices lors de l'évaluation des paramètres clés du transfert de chaleur. Cette recherche vise à l'élargissement de la littérature scientifique en comblant ces lacunes de connaissances et en évitant des fortes hypothèses simplificatrices lors de l'évaluation du transfert de chaleur.

Dans cette étude, l'injection d'huile sur les têtes des bobines est reproduite par un jet impactant sur une plaque plane générique et chauffée. Une méthode expérimentale est développée pour évaluer le coefficient de convection local, le nombre de Nusselt local et les corrélations de Nusselt. Cette méthode caractérise l'injection, la plaque et le liquide après l'impact.

Divers diagnostics et approches sont utilisés : la température de la plaque est mesurée par des thermocouples, le flux de chaleur à l'interface solide-liquide est évalué à l'aide d'une simulation, la température et l'épaisseur de l'huile après impact sont mesurées avec de sondes et de méthodes optiques, et les principaux paramètres de l'injection et du chauffage sont mesurés avec de capteurs spécifiques. Les principaux résultats de cette recherche sont organisés en cinq chapitres.

Le chapitre 1 est une revue bibliographique. Les moteurs électriques pour les applications automobiles sont décrits, expliquant la nécessité de refroidir les têtes des bobines, les avantages de l'huile et des systèmes de refroidissement les plus avancés. Ensuite, l'état de l'art sur les jets impactant avec des fluides à haut nombre de Prandtl est réalisé, avec un accent particulier sur les méthodes expérimentales et les paramètres clés du transfert de chaleur. Enfin, un aperçu des techniques de mesure des température et épaisseur disponibles dans la littérature sert à choisir les méthodes de diagnostics pertinents à utiliser et à explorer dans cette recherche.

Le chapitre 2 présente les détails techniques des méthodes et des matériaux utilisés. Une vue d'ensemble est donnée sur les formulations du transfert de chaleur, les éléments du banc de test, les systèmes de diagnostic et les protocoles. La plaque est une plaque d'aluminium plate, qui est refroidie par le dessus via l'injection d'huile et chauffée par le bas via une résistance électrique. Les paramètres d'injection sont mesurés et contrôlés à l'aide de capteurs intégrés dans le circuit d'huile. Des thermocouples implantés dans la plaque mesurent la température interne et celle de l'interface solide-liquide. Le flux de chaleur est évalué à l'aide d'un modèle de plaque basé sur la méthode à éléments finis. Des mesures ponctuelles et globales de la température et de l'épaisseur du liquide sont effectuées à l'aide de sondes, de capteurs optiques et par traitement d'images (par exemple, la fluorescence induite par laser et avec 2 colorants et 2 canaux de détection).

Le chapitre 3 est consacré à la caractérisation de la plaque et des injections. Les mesures de température de la plaque et les calculs du flux de chaleur sont présentés et analysés. Les paramètres d'injection et de chauffage sont également caractérisés. Ce chapitre comprend l'établissement du protocole expérimental, l'analyse des incertitudes, la validation des simulations et une étude paramétrique pour différentes combinaisons d'injection et de chauffage. Les résultats permettent d'avancer des considérations sur l'efficacité du refroidissement et sur l'homogénéité de la température.

Le chapitre 4 porte sur la caractérisation du liquide après l'impact. La température et l'épaisseur sont mesurées à l'aide de différentes techniques. L'accent est mis sur le développement et sur les phases de validation de la méthode d'imagerie basée sur la

fluorescence induite par laser. Les résultats pour différentes combinaisons d'injection et de chauffage sont présentés et analysés, des comparaisons sont faites entre les différentes techniques et l'incertitude des mesures est évaluée avec des expériences dédiées.

Le chapitre 5 est consacré à la caractérisation du transfert de chaleur par convection. Les résultats des chapitres 3 et 4 sont combinés pour estimer le coefficient de convection local et le nombre de Nusselt local. Les corrélations de Nusselt sont déterminées pour le point d'impact et le long de la direction radiale. Le chapitre comprend une analyse d'incertitude et une comparaison avec la littérature connue.

- **Conclusions**

La méthode expérimentale permet de mesurer finement la température de plaque dans une gamme représentative des zones de fonctionnement des têtes des bobines. La robustesse de la méthode, l'incertitude des mesures et la validité des hypothèses sont déterminées par des analyses spécifiques. En ce qui concerne la diminution de la température, une étude paramétrique des paramètres d'injection et de chauffage montre que l'augmentation du diamètre de la buse, l'augmentation de la pression d'injection et la diminution de la température d'injection réduisent la température de surface. Une observation intéressante est que toute variation des paramètres d'injection déplace le profil de température de surface vers une plage de température plus élevée ou plus basse sans modifier le gradient de température, alors que la variation de la puissance de chauffage modifie les gradients de température le long de la direction radiale du jet. Au contraire, le flux de chaleur obtenu à partir des simulations présente une faible variabilité globale, sauf au point d'impact.

Les mesures de la température et de l'épaisseur du liquide après l'impact sont effectuées à l'aide de différentes techniques, dont l'incertitude est quantifiée. Pour les mesures ponctuelles, les thermocouples et l'aiguille de contact font preuve de robustesse et fiabilité, même si certains problèmes de précision et de perturbation de l'écoulement subsistent. La méthode d'imagerie pour les mesures à champ large (basée sur la fluorescence induite par laser) est développée avec succès et appliquée au jet impactant. L'évaluation de la température est affectée par une imprécision persistent, bien que la plage globale soit plausible et en accord avec les mesures des thermocouples. Toutefois, l'évaluation de l'épaisseur est relativement précise et correspond aux mesures réalisées à l'aide de l'aiguille. Des améliorations sont possibles et les principaux points critiques de la méthode ont été identifiés.

D'après la caractérisation des injections, de la plaque et du liquide, la méthode permet en effet d'atteindre les objectifs fixés au début de cette thèse. Des estimations du coefficient de convection local, du nombre de Nusselt local et des corrélations de Nusselt (au point d'impact et le long de la direction radiale du jet) sont données pour une gamme relativement large de nombres de Reynolds et de Prandtl. Un bon accord est trouvé avec la littérature la plus similaire, confirmant que la présente étude contribue à étendre les connaissances sur les jets impactantes avec des fluides à haut nombre de Prandtl, dans une gamme thermique représentative (c.-à-d. liée au refroidissement des têtes de bobines) et pour des cibles d'épaisseur génériques (donc sans la nécessité de fortes hypothèses simplificatrices).

Table of Contents

1 INTRODUCTION AND STATE OF ART

- **Chapter introduction**

In this introductory chapter, the present research is put into perspective, starting from a more general industrial context, and arriving to the scientific questions about liquid injections and diagnostic systems. The chapter has three parts.

The first part illustrates the challenges for a competitive electric mobility and the problems related to the cooling of the electric motors, especially the end-windings. Direct oil injections are proven effective, but their modelling is complicated and needs to be supported by experimental data. The injection configuration considered in this research is the impinging jet.

The second part is an insight of the physics of jet impingement heat transfer. On one side are the lubricant oils, that is, high-Prandtl fluids with particular rheological and thermal characteristics. On the other are solid targets, whose temperature distribution is influenced by their shape and material. Convective heat transfer is quantified at the interface between the two.

In the third part, a review of the pertinent experimental approaches and diagnostic techniques is presented for studying jet impingement heat transfer. Focus is given on laser induced fluorescence for temperature and thickness measurements.

1.1 Thermal management of electric motors

1.1.1 Electric motors for mobility and traction

- **Diffusion of electric mobility**

The electric vehicle (EV) is an interesting solution for reducing localised pollution related to mobility. The EV is effective for improving the air quality in urbanised or densely populated areas. The penetration of the EV is diverse and heterogeneous (from light electric kick scooter to heavy lorries), mostly driven by government policies. Asia is the leading continent in terms of micromobility (e.g., electric kick scooters), public transport electrification and lorries (*IEA*, 2020). In Europe and North America, electrification is generally restrained to corporate fleets, public transport and other services related to distribution and delivery (*IRENA*, 2019). Electric vehicles sales have grown over the past decade, reaching 16.5 million vehicles on the road worldwide, 47 % of which are in China (*IEA*, 2022). As Figure 1.1 illustrates, the world sales trend is growing exponentially and not only in western countries: China is the first market, followed by the USA and the European countries. These three regions are the major stakeholders, covering the 90 % of the global market (*IEA*, 2022).

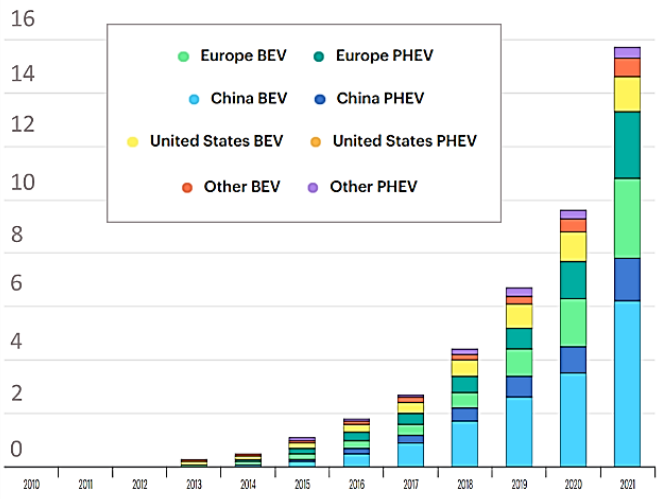

Figure 1.1 – Sales trends in millions of USD of the world EV market from 2010 to 2021 (*IEA*, 2022).

- **Transformation of the automotive industry**

The automobile industry is undergoing radical conversion to readapt research and production toward electric mobility. An electric propulsion system is significantly different from that of a vehicle based on internal combustion engine (ICE), essentially for two main reasons: the components of the powertrain and the requirements for traction. The components of an electric vehicle are intrinsically different from the standard ICE vehicle. As showed in Figure 1.2, various types of vehicles exist, representing various levels of powertrain hybridisation and combining various energy sources (i.e., petrol derivatives, hydrogen, and chemical storage). In any case, three elements are always fundamental in any EV: the electric motor, the power electronics, and the battery pack. These three also represent the main axes of research of the automotive industry.

Concerning traction, the ICE is technologically more advanced to better fulfils the requirements for today's mobility. The typical power and torque curves for road traction are given in Figure 1.3. Two operative regimes are distinguished accordingly to speed. For the initial acceleration phase, high torque is necessary to start vehicle motion and to overcome gradeability, thus constant torque and increasing power are required at low speed. Within cruise regime, lower torque is needed, in favour of increasing speed at constant power. Consequently, for moderate and high speed, constant power and decreasing torque are necessary.

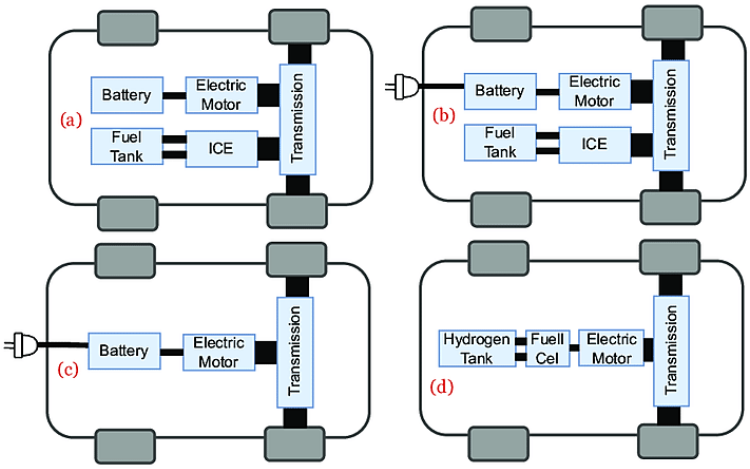

Figure 1.2 – Types of electric vehicles (*Saldarriaga-Zuluaga et al.*, 2022).

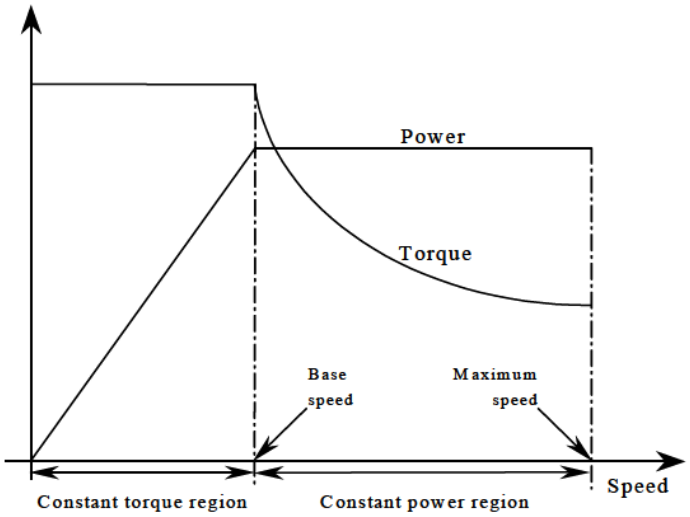

Figure 1.3 – Typical power and torque curves demanded for traction (*Tabbache et al.*, 2013).

Electric motors are traditionally employed for slow variant or steady state applications, either in the industrial sector (e.g., ventilation, treadmills, pumping, etc.) and in heavy duty traction (e.g., trains). New technical challenges appear for electric mobility, since electric motors are demanded rapidly variant load conditions. Comprehensive reviews on electric vehicles and motors summarise the essential criteria for competitive mobility (*Gieras* and *Bianchi*, 2004; *Yildirim et al.*, 2014). Among them, the most important are high torque density, high power density and small bulk.

The choice of an electric motors is a compromise between efficiency, manufacture simplicity and cost. In vehicles, no specific motor type is dominating the market uncontested. The most common motors are the permanent magnets synchronous motor (PMSM) and the induction motor (IM). The reluctance motor (RM) is not used yet on vehicles but is gaining popularity. Their working principle are explained in the following.

- **Electric motors principles and technologies for mobility**

The motor has two fundamental components: the stator and the rotor, both made of ferromagnetic material (especially iron). The stator is a mechanically fixed but electrically active element that generates a rotating magnetic field, as illustrated in Figure 1.4 without the rotor. The rotor interacts with the stator magnetic field and generates mechanical torque. Figure 1.5 illustrates the three basic stator-rotor configurations for producing torque. The stator in the figure is powered by a 3-phase sinusoidal current (but other configurations exist). Depending on the rotor features, torque is generated in three ways:

i. If the rotor has short-circuited windings, the temporal variation of the stator induction flux generates a difference of electric potential in the rotor windings (according to Lentz's law $E = -d\Phi/dt$). Consequently, electric current flows in the rotor windings and a counter-magnetic field originates. The interaction between the stator field and the rotor field produces mechanical torque. This type of machine is called induction motor (IM) and it rotates at a different speed than that of the stator magnetic field, to perpetuate the induction.

ii. If the rotor is cylindrical, homogeneous, and provided with its own permanent magnetic field (i.e., with permanent magnets or wound rotor), the rotor adjusts its position to

follow the rotating stator field. The type of machine is called synchronous motor (SM), as the rotor rotates at the same speed as the stator magnetic field.

iii. If the rotor is not as above (i.e., anisotropic and non-homogeneous), the magnetic field lines of the stator would close through different reluctance paths through the rotor. The reluctance represents the resistance to magnetic flux and reluctance is greater in air than in iron. It follows that that the rotor adjusts its position to allow the path with the minimal reluctance. The resulting torque is therefore named “reluctance torque” and is the same that makes a compass needle align to the Earth magnetic field.

In Figure 1.6 Figure 1.7, Figure 1.8, examples are given of these three types of electric motors. An example of commercial electric vehicle with an IM is the Tesla S P100D, released in 2019 with two motors. Vehicles with PMSM are the Toyota Prius (2016) and the BMWi3 (2018).

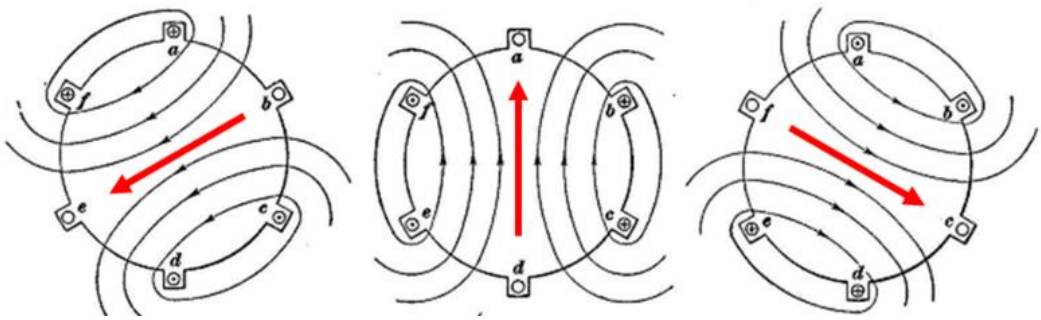

Figure 1.4 – Field lines and direction of the rotating magnetic field generated by the stator, for three consecutive time steps (*Lawrence*, 1920).

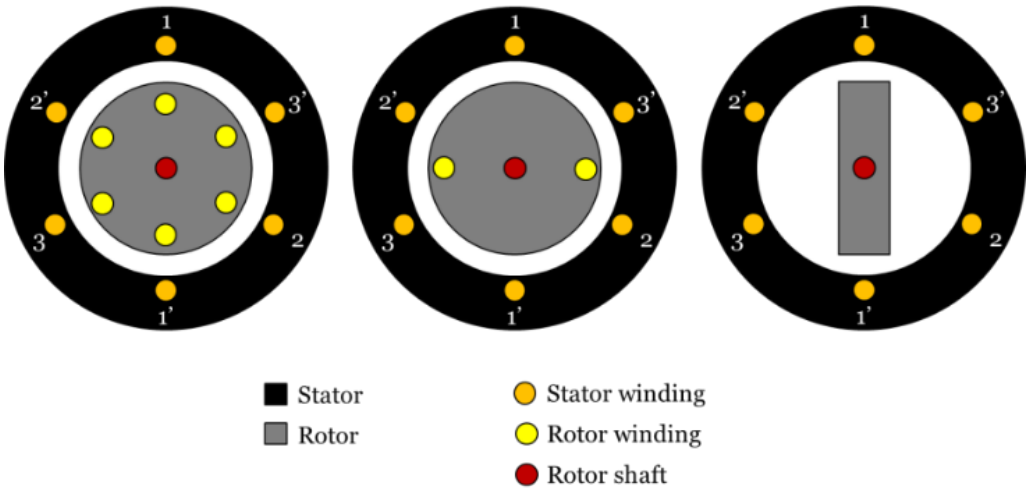

Figure 1.5 – Most essential stator/rotor configurations of a 3-phase electric motor. (Left) Perfectly symmetric rotor with short-circuited windings. (Centre) Perfectly symmetric rotor with DC powered windings. (Right) Non-symmetric and passive rotor.

Figure 1.6 – Example of an induction motor with a squirrel cage rotor (*Wikipedia* 2023a).

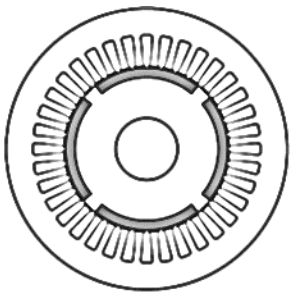

Figure 1.7 – Schematic view of a PMSM (*Todorov* and *Stoev*, 2015).

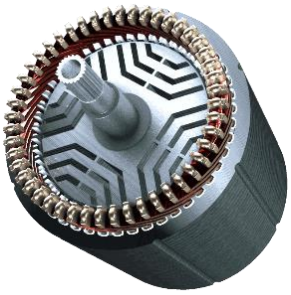

Figure 1.8 – Example of a reluctance motor (*Oswos* 2023).

In Figure 1.9, more focus is given to the recurring sub-components of the motor and their main purpose. In the stator, the electric current runs through electrically insulated copper wires, located into dedicated slots. The bundles of wires form closed loops (windings), that are bent backwards at the edges of the machine. A distinction is made between slot-windings and end-windings if the wires are inside or outside the slots of the ferromagnetic material (Figure 1.10). The whole structure is held in a housing which protects internal components, allows safe access to electrical terminals and provides structural support. The rotor has a shaft, which is mounted over bearings and is flanged to the transmission system.

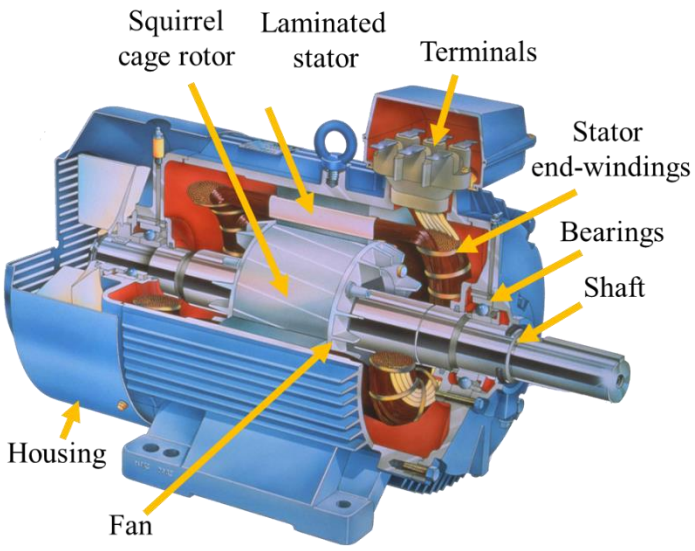

Figure 1.9 – Sectioned view of an induction motor (*Electricalaxis* 2023).

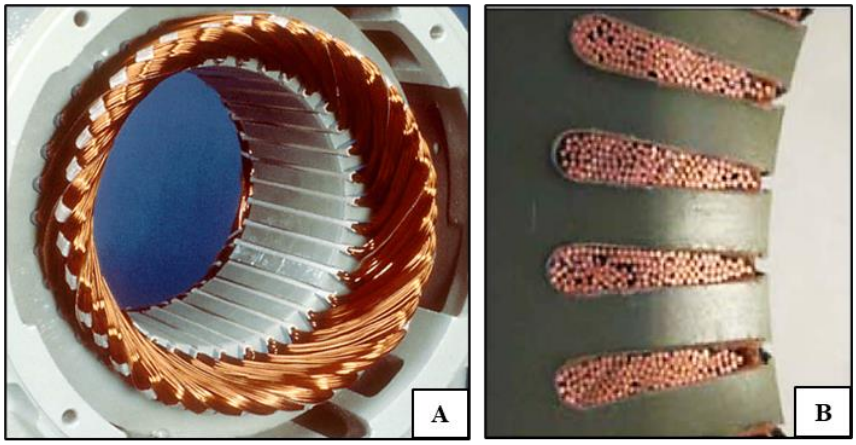

Figure 1.10 – Stator copper windings. (A) End-windings (*Gavrilenko*, 2020). (B) Slot-windings (*Kato et al.*, 2013).

During any operation of the electric motor, all these functional components play an active role and are subject to stress from electrical or mechanical phenomena. As in every machine, a part of the energy delivered to run the motor is not converted into useful work but is lost in the form of thermal energy. This causes the temperature of the motor to rise and adds further stress. As investigated in the next section, this thermal stress can affect the performance and lifetime of the motor.

1.1.2 Losses and thermal limits of electric motors

- **Nature of the losses**

Electric motors have very high efficiency (typically > 85 %), but energy losses are always present and cause the temperature of the motor to rise. Three phenomena generate losses:

i. When an electric current flows in the copper windings of the stator (and the rotor, if present), heat power is generated according to Joule's law as RI^2 (where R is the electric resistance and I the current intensity). Electric resistance increases at high temperature.

ii. Magnetic losses are caused by magnetic hysteresis and eddy currents, which occur in the ferromagnetic material of the rotor and the stator. These losses are typically evaluated as $k\, f^a\, B^b$ (where f is the electric frequency, B the magnetic induction field, whilst k, a and b are characteristic coefficients). Magnetic losses are also load-independent and always present when the machine is run.

iii. Mechanical losses are caused by mechanical friction in shaft bearings, in brushes (if present in electrically active rotors), in the gap between stator and rotor (caused by viscous drag of air). Various formulations exist to calculate mechanical losses. They increase with the speed and the size of the machine.

The loss distribution varies with the regime of the motor and comprehensive examples are found in dedicated literature (*Benhaddadi et al.*, 2011; *Yang et al.*, 2017). A qualitative distribution of losses is given in Figure 1.11 which highlights that the largest contribution is given by the Joule's effect in the copper windings.

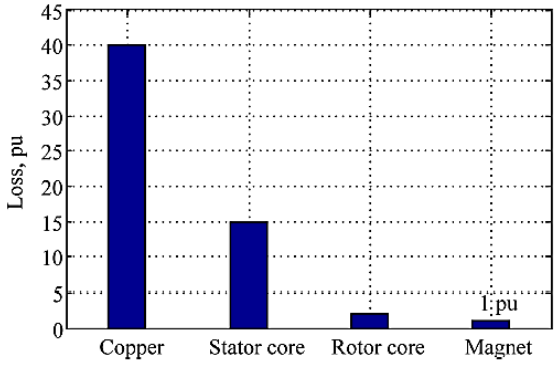

Figure 1.11 – Rated losses in an IPM electric motor (*Yang et al.*, 2017).

- **Effects of prolonged exposure to high temperature**

The most relevant drawback is that electromagnetic losses convert into heat, causing temperature to rise (*Gundabattini et al.*, 2020). As Figure 1.12 illustrates, the windings and magnets temperature could increase significantly, especially when high torque or high power are required. Excessive temperature affects the electromagnetic behaviour (e.g., alteration of magnetic properties, increase of electric resistance, etc.) and lifespan (e.g., degradation of components, occurrence of electrical failures, etc.). An example of torque reduction due to excessive temperature increase is given in Figure 1.13.

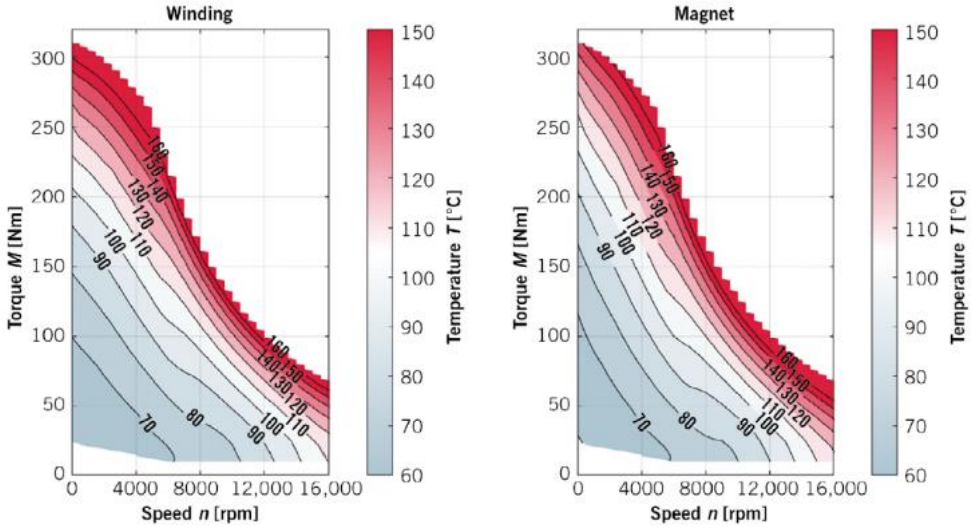

Figure 1.12 – Average temperature of the stator windings and rotor magnets for various operating points in the torque-speed map (*Schröder et al.*, 2022).

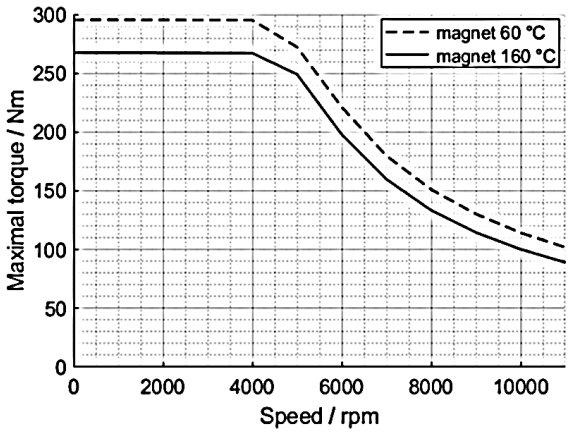

Figure 1.13 – Decrease of motor torque caused by excessive temperature increase (*Herold et al.*, 2020).

- **Temperature limits**

Two electrically active components are severely affected by excessive temperature: the permanent magnets (PM) and the electric insulation of the windings. These components also set the maximal operation range of the motor. More specifically:

i. Typical permanent magnets for rotors are made of Samarium-Cobalt (Sm-Co), Neodymium-Iron-Boron (Nd-Fe-B) and ferrites (*Trout*, 2001). Ferromagnetic materials suffer of demagnetisation (i.e., loss of coercivity) at excessive temperatures. Demagnetisation permanent when the Curie temperature is passed. As showed by Table 1.1 and Figure 1.14, Nd-Fe-B alloys are generally preferred for their larger coercivity also at high temperature. Even though high-temperature resistant magnets are available in the market, 150-180 °C is recognised as the conventional limit for today's standard.

ii. There are several types of insulation in electric motors (as Figure 1.15), which contribute to define the final aspects of the end-windings, as in Figure 1.16. For prolonged exposure to high temperature, the insulation material deteriorates, and this could lead to electrical failure. This is more pronounced in the "hotspots", that is, localised small regions of the motor where the temperature is considerably high because of design or manufacturing imperfections. The thermal limit of the insulation material depends on the composition and the exposure time. Insulation thermal resistance is classified by maximum hotspot temperature allowed in extreme conditions (i.e., 40 °C ambient air and 10 °C overheat margin), according to several standardisations (*IEC*, 2019; *NEMA*, 2016). Table 1.2 shows the different classes defined by NEMA. For electric motors, the maximum hotspot temperature is conventionally fixed to 180 °C.

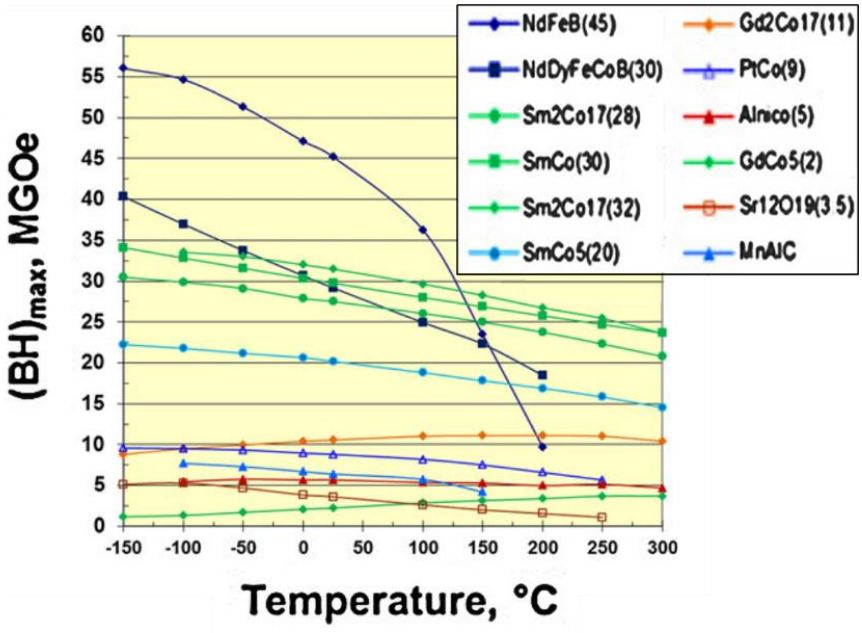

Figure 1.14 – Coercivity loss at high temperature for various magnets types (*Kramer et al.*, 2012).

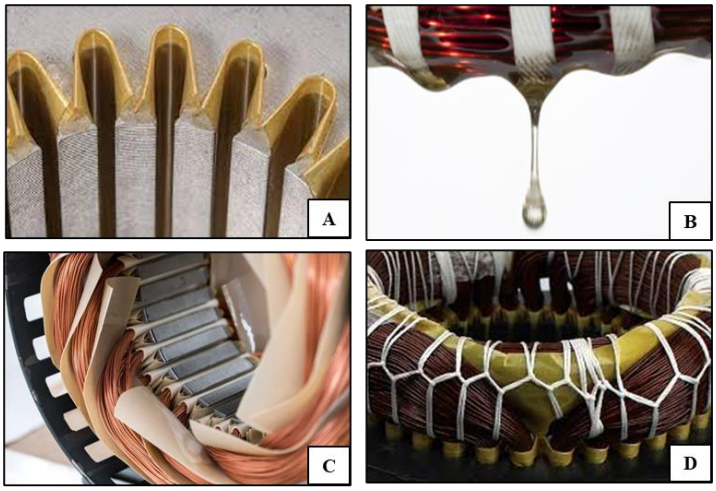

Figure 1.15 – Insulation and supports in electric motors. (A) Slot liner (*Elantas* 2023a). (B) Impregnating material (*Elantas* 2023a). (C) Phase insulation sheets (A*zomaterials* 2023). (D) Bands for structural resistance (*Elantas* 2023b).

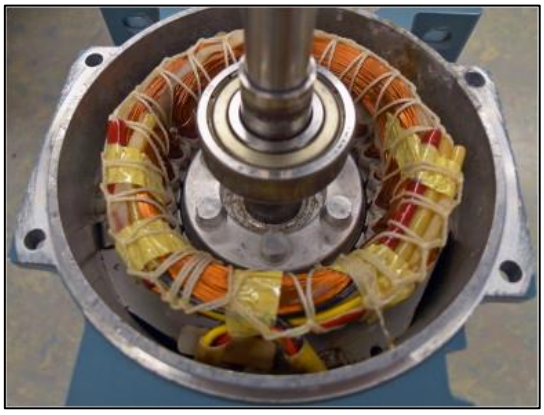

Figure 1.16 – Final aspect of the end-windings with all the insulation layers (*Hultman* and *Leijon*, 2013).

Table 1.1 – Characteristic temperatures for industrial permanent magnets (PM).

PM TYPE	MAX OPERATING TEMPERATURE [°C]	SOURCE
Nd-Fe-B	100 – 180	(*Trout*, 2001)
Sm-Co	160 – 170	(*Bochenkov* and *Lutz*, 2004)
$SmCo_5$	250	(*Coey*, 2002)
Sm_2Co_{17}	350	(*Coey*, 2002)
PM TYPE	**CURIE TEMPERATURE [°C]**	**SOURCE**
Nd-Fe-B	583 – 673	(*Wikipedia*, 2019b)
Sm-Co	993 – 1073	(*Wikipedia*, 2019b)

Table 1.2 – Electric insulation classes according to NEMA classification.

CLASS	MAX WINDING TEMPERATURE * [°C]	ALLOWABLE TEMPERATURE AT FULL LOAD [°C]	MAX AMBIENT TEMPERATURE RISE [°C]	MAX HOTSPOT TEMPERATURE RISE ** [°C]
A	105	60	+40	+5
B	130	80	+40	+10
F	155	105	+40	+10
H	180	120	+40	+15

* Example for class F:

Max temperature = Allowable temperature + max ambient temperature + max hotspot temperature = 105 °C + 40 °C +10 °C = 155 °C

** The max hotspot temperature is the temperature at the centre of the winding, at which lifespan is halved

- **Improved design for mitigating temperature rise**

In terms of machine design, various strategies are adopted to reduce losses and reduce temperature rise. The first strategy is to reduce losses with advanced materials and improved machine architecture. An example is given by the introduction of the PM in the rotor, which eliminates Joule's effect in the rotor. Moreover, manufacturer of PM and electric insulations (especially epoxies), are developing components with improved electro-mechanical performances and endurance at high temperature. The second strategy is the modification of the winding geometry. In Figure 1.17, several winding types and configurations are illustrated that are all used in electric mobility (*Kato et al.*, 2013). Among them, more regular and compact configurations are gaining popularity. The hairpin configuration in particular denotes intrinsically higher efficiency than distributed windings (*Magnussen et al.*, 2004). Despite more expensive and complex manufacturing, these winding designs are being investigated also for their advantages in terms of easier accessibility to the hot surfaces of the end-windings.

Beside the effort put into the electro-mechanical design, advanced thermal design is still relevant for managing the motor temperature since losses are inevitable and waste heat must be dissipated anyway. Cooling is always necessary to assure the correct working conditions of the motor and preserve the integrity of the components.

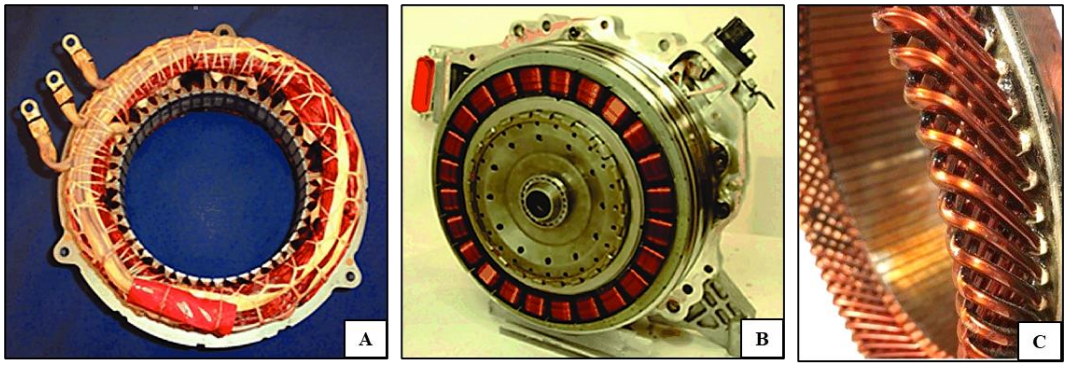

Figure 1.17 – Types of winding technologies. (A) Concentrated windings (*Sarlioglu et al.*, 2016). (B) Distributed windings (*Sarlioglu et al.*, 2016). (C) End-windings with hairpin configuration (*Rivière et al.*, 2019).

1.1.3 Base and advanced cooling techniques

Traditionally, the heat generated from the motor is transferred via conduction towards the housing. Heat is hence removed via natural convection or via forced convection. Radiative heat transfer is negligible at the relatively low temperatures reached by the motor. For electric mobility, traditional cooling methods are often insufficient.

The maximum current density J is an indicator to evaluate the appropriate cooling methods (*Yang et al.*, 2017). As reported in Table 1.3, natural air cooling is advised for current density $J < 5$ A mm, forced air convection up to $J = 10$ A/mm², and liquid cooling up to $J = 30$ A/mm². For electric vehicles, the typical current density lays within 15 A/mm² < J < 30 A/mm², therefore liquid cooling is the most suitable.

Table 1.3 – Typical values for different cooling methods (*Gai et al.*, 2019).

COOLING METHOD AND FLUID		PRESSURE [kPa]	MAGNETIC FIELD [kA/m]	CURRENT DENSITY [A/mm²]	HEAT EXCHANGE COEFFICIENT [W/m²/K]
Natural convection	**Air**	10	NA	1.5 – 5	5 – 30
Forced gas convection	**Air**	< 15	< 80	5 – 10	20 – 300
Forced liquid convection	**Indirect**	20 – 60	90 – 130	7 – 20	100 – 10000
	Direct	60 – 100	100 – 200	10 – 30	200 – 25000

The association between the current density and the cooling method is a good indicator, however further technical considerations should be considered. Most internal active components are usually the difficult to reach by a cooling system. The rotor for example is a moving component and is separated by an air gap from the stator. Another example is given by the fact that reducing the ferromagnetic material to make room for a cooling system (e.g., cooling canal) affects inevitably the electromagnetic behaviour of the motor. Lastly, the electrically active components must not be in contact with a conductive fluid.

Numerous reviews on traditional and advanced cooling systems for electric mobility are available (*Carriero et al.*, 2018; *Deisenroth* and *Ohadi*, 2019; *Gai et al.*, 2019; *Popescu et al.*, 2015; *Tuysuz et al.*, 2017; *Yang et al.*, 2017). This literature summarises that there are essentially two main approaches: housing cooling and localised cooling. The first is simpler, does not require significant design alteration but is more limited in efficacy. The second is more complex, because specific components and heat sources are addresses, but the cooling effectiveness is greater.

- **Housing cooling**

The principle of housing cooling is that waste heat flows towards the housing, where a coolant fluid extracts the heat of the motor via forced convection. The key strategy to increase housing cooling is by increasing the conductivity (choosing high-conductivity materials) or by increasing heat transfer towards the housing (modifying the geometry).

- <u>Enhanced conductivity</u>

Most of the thermal resistance is due to the air gap ($k \approx 0.02$ W/m/K), and to the imperfect sheet-to-sheet contact of the laminated core (*Cousineau et al.*, 2015). The use of high-thermal conductivity electrical steel is extensive but relatively limited in efficacy because it is already high (e.g., $k \approx 66$ W/m/K for carbon steel 1% C).

A more effective solution is given by the electric insulation. Varnish is the most common, whilst epoxy and silicon are growing of interest, due to better thermal endurance (*Kulan et al.*, 2020; *Liu et al.*, 2017). Potting is a particular type of impregnation consisting in the full coverage of the end-windings windings by solid material as in Figure 1.18. The use of different impregnation materials and potting is investigated in various dedicated studies (*Li et al.*, 2017; *Liu et al.*, 2019b; *Nategh et al.*, 2014; *Sun et al.*, 2019), which lead to the conclusion that hotspot temperature is reduced, allowing higher torque density, with moderate alteration of the machine.

High-thermal conductivity impregnating materials are interesting, but their effectiveness is limited for three reasons. First, the overall conductivity is low (i.e., $k \approx$ 3-5 W/m/K). Second the additional manufacturing complexity makes this solution less appealing. Third, the axial and radial thermal conductivity of the end-windings is considerably different (*Wereszczak et al.*, 2017).

- Liquid convection

Liquid jackets are extensively used for electric motors for mobility. The liquid jacket is an external cooling circuit where a fluid flows in forced convection as showed in Figure 1.19 . The coolant fluid is often a mixture of water and ethylene glycol or propylene (EGW and PGW). Typical mixtures are 50% - 50% but it is found that increasing glycol concentration consents better thermal exchange (*Deriszadeh et al.*, 2019). The effectiveness of the configuration depends primarily on geometrical aspects of the circuit, such as the number of turns and the shape of ducts (*Ye et al.*, 2013). Water jackets are the most effective solutions for the base cooling of the motor. Several drawbacks are present, such as the great temperature gradients between the stator outer surface, the windings and the end-windings (*Gai et al.*, 2019; *Galea et al.*, 2012). Imperfect contact between the jacket and the stator is also problematic and causes additional thermal resistance (*Kulkarni et al.*, 2012).

Figure 1.18 – Potted windings (left) vs non-potted windings (right) (D*reisilker* 2023).

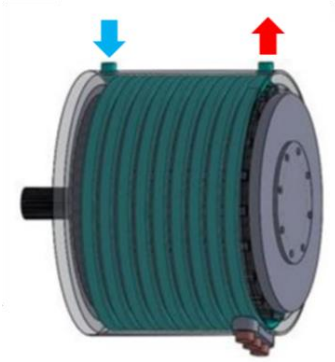

Figure 1.19 – Water jacket (*Huang et al.*, 2019).

- **Localised cooling**

Localised cooling means that the coolant addresses a specific heat source. A liquid coolant is normally used due the high convective coefficient. Phase-change cooling has higher rate of heat extraction, however it is still at an early stage of development because it is more complex to manage the evaporated phase. Localised cooling is "direct" when the coolant is in close contact with the heat source, or "indirect" when is not. Within this framework, oil is a more popular fluid than water because is dielectric, it has a relatively large heat capacity (about half that of water), and adjuvants can be added to modify specific properties to better adapt the oil to the cooling system. The use of oil is being pushed by the automotive industry because the oil is already present in the vehicle (e.g., in the gearbox) and because it has potential to replace water, thus only one multi-purpose fluid would be present in the vehicle. Numerous cooling configurations are found in the literature, with different level of integration in the motor design. Some of them are:

- Cooling canals for stator windings

A coolant (water or oil) flows in dedicated canals and removes the heat generated in the stator slot-windings. Good compatibility is possible with concentrated windings, as unused hollow space in slots can host electrically separated canals, as in Figure 1.20. The feasibility of the system is investigated in various studies (*Broomfield* and *Marvin*, 2019; *Lindh et al.*, 2019; *Schiefer* and *Doppelbauer*, 2015) but further investigation is needed to evaluate compatibility with the electric design. The advantage is the

proximity of the coolant to the heat source, but the drawback is disturbance of the magnetic field induced by the canal (*Gai et al.*, 2019).

- Integrated systems for stator and rotor

Kawamura et al. 2011 presents the design of an electric motor (for a Formula 1 vehicle), featuring a closed circuit flowing through the stator (including slot- and end-windings) and the rotor hollow shaft. A thin seal sleeve is added to separate the rotor from the stator and avoid oil spilling in the air gap (Figure 1.21). A similar approach is proposed in a patent for an IM (*Zysset*, 2001) where the stator and the hollow shaft are connected through a passive self-cooling oil circuit. Another configuration is proposed by *Lim* and *Kim* 2014, who investigate numerically the cooling action of a semi-flooded stator (Figure 1.22). A prototype with an additional oil spray is also tested, showing larger heat removal and more uniform temperature distribution. A similar approach is followed by (*Park* and *Kim*, 2019), who observe much larger heat transfer when adding spray cooling (5000-10000 W/m²/K) than with cooling canals alone (2000-9000 W/m²/K). Similar configurations with oil are found in various other studies (*Camilleri et al.*, 2016; *Guo* and *Zhang*, 2019; *Lee et al.*, 2016; *Xu et al.*, 2017), where the effective temperature mitigation allows the motor to stay longer under high-torque operating conditions.

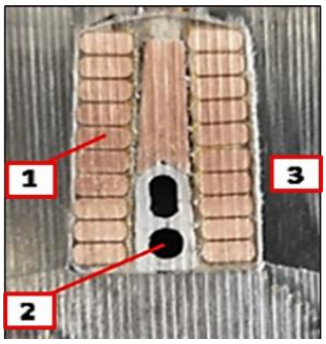

Figure 1.20 – Stator cross section with cooling canal (*Broomfield* and *Marvin*, 2019). (1) Winding. (2) Canal. (3) Tooth..

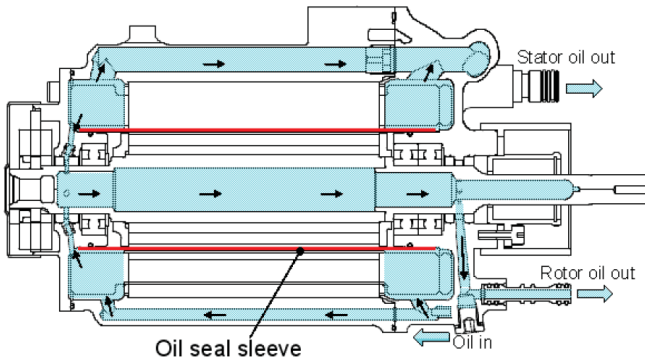

Figure 1.21 – Integrated oil cooling circuit for stator, windings and shaft (*Kawamura et al.*, 2011).

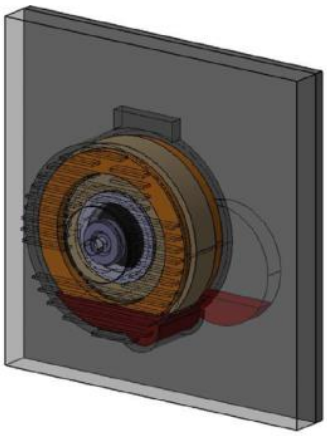

Figure 1.22 – Semi flooded stator (*Lim* and *Kim*, 2014).

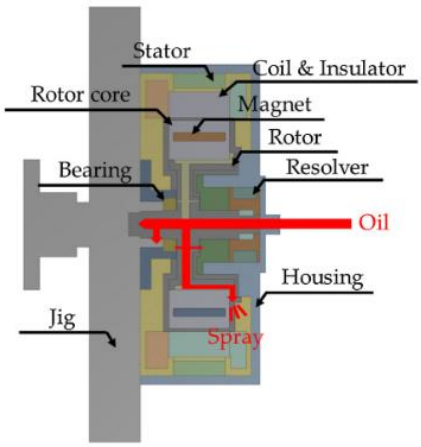

Figure 1.23 – Hollow shaft with spray cooling (*Park* and *Kim*, 2019).

- Integrated systems with centrifugal injection

The least perturbing method to introduce a cooling fluid inside a spinning rotor is through a hollow shaft because the centrifugal action is minimal along the shaft. Reaching the outer surface is more complicated because the presence of canals with flowing liquid could affect the torque of the motor. The simplest configuration is reported in a Tesla patent (*Zhou et al.*, 2009), based on a round trip inside the hollow shaft (Figure 1.24). An more complex concept is proposed in a patent by *Miyamoto et al.* 2017, where a hollow shaft is provided by two orifices injecting oil on end-windings as a result of centrifugal action (Figure 1.25). *Assaad et al.* 2018 develop a real prototype from a modified TEFC-IM. According to their assessment, this configuration has significant drawbacks: linear increase of oil flow rate leads to exponential increase of mechanical friction. Moreover, foam formation makes oil evacuation more difficult. On the other hand, the implementation of the oil cooling system doubles the useful power the motor (in the continuous range), with respect to the initial air-cooled configuration. A more intricated configuration is investigated numerically by *Wang et al.* 2022, which allows cooling of the PM of the rotor as well.

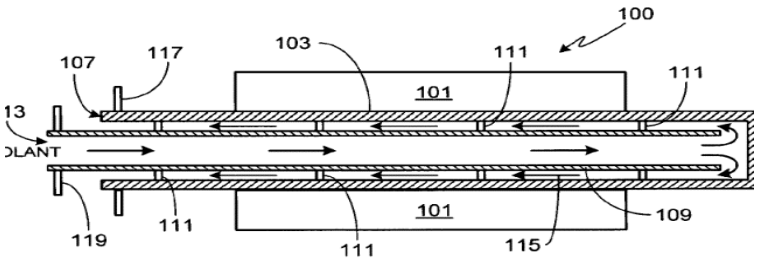

Figure 1.24 – Oil cooling through a round trip circuit in the hollow shaft (*Zhou et al.*, 2009).

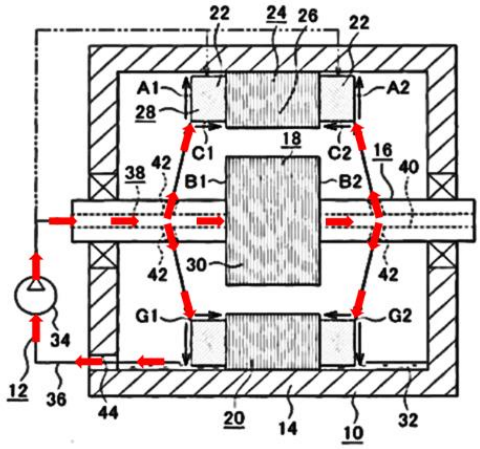

Figure 1.25 – Oil cooling with centrifugal injection (*Miyamoto et al.*, 2017).

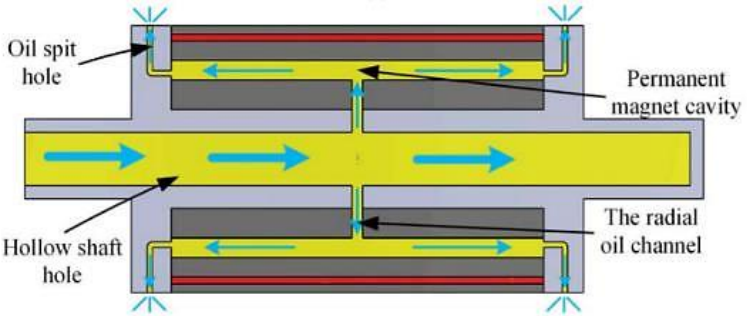

Figure 1.26 – Oil cooling through hollow shaft with centrifugal injection (*Wang et al.*, 2022).

- Injection cooling

Typically, direct injection has high rate of heat dissipation and does not require significant alteration of the motor. In the literature, most of the injection cooling targets the end-windings. Injection on the rotor is still in a testing phase, because the mechanical performances are affected and only the peripheral regions of the rotor are cooled effectively. *Davin et al.*, 2015 classified by cooling efficiency diverse injection techniques on real motor, including spray, dripping and jet impingement (Figure 1.27). The results show that dripping has the largest rate of heat removal and spray achieves similar cooling action with lesser flow rate. It is observed that the air flow generated by the rotor causes significant non-homogeneity in the oil distribution, thus in the surface temperature of the end-windings. *Liu et al.*, 2019a undertakes a similar study and tested different jet arrays (Figure 1.28). They observe that temperature mitigation improves with more uniform oil distribution and especially with flowrate, thus the importance of the jet array.
In terms of fundamental studies the literature is scarce. The most relevant publication is by *Bennion* and *Moreno* 2015, who investigated convective heat transfer with a jet impinging on a heated cylinder, whose grooved surface replicates the wires of the windings (Figure 1.29). Follow-up studies are undertaken by *Kekelia et al.* 2019 and *Feng et al.* 2021. In their studies, they used automatic transmission fluid (ATF). This choice is motivated by two reasons: the fluid is already present in the powertrain of the electric vehicle, and because automatic transmission, dual clutch transmission and continuously variable transmission are taking over manual transmission in the years to come (*Shah et al.*, 2020).

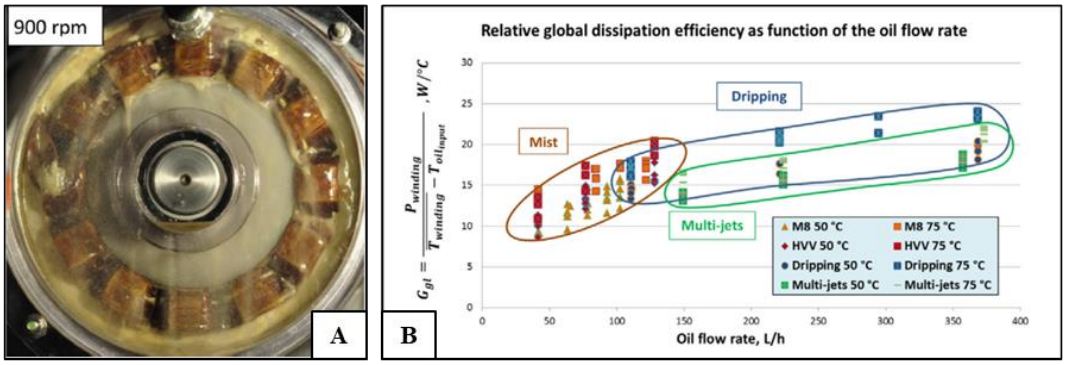

Figure 1.27 – Oil injection on end-windings (*Davin et al.*, 2015). (A) Image of the oil injection with a spinning rotor. (B) Dissipation efficiency for several injection configurations.

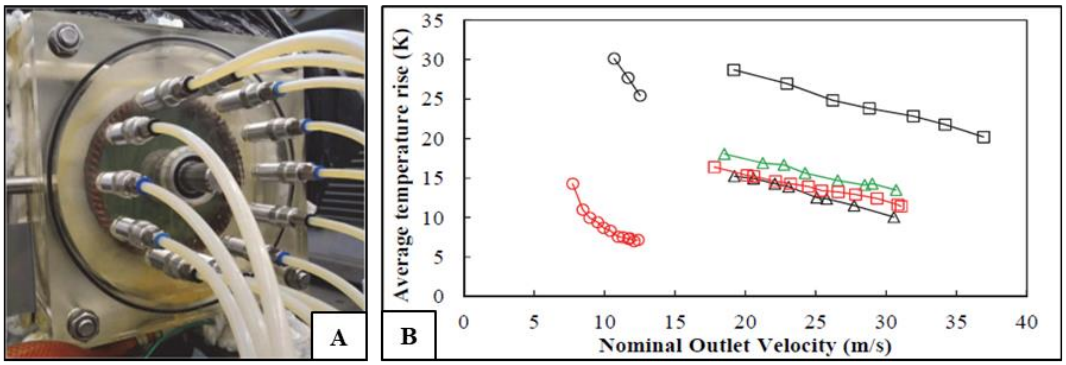

Figure 1.28 – Oil injection on end-windings (*Liu et al.*, 2019a). (A) Image of the oil injection array. (B) Average temperature rise of end-windings for increasing velocity and for different injection arrangements.

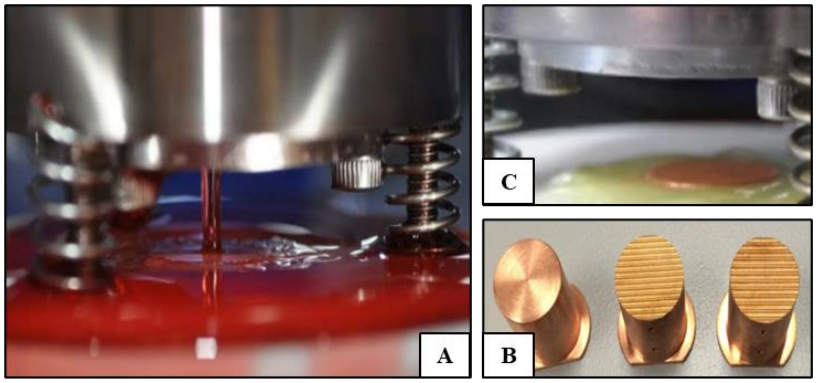

Figure 1.29 – Experimental setup for oil injection on heated cylinder (*Bennion* and *Moreno*, 2015). (A) liquid injection. (B) Test facility without injection. (C) Heated and grooved cylinders.

1.1.4 Injection cooling of the end-windings

The automotive industry aims to improve thermal management of the electric motors for mobility with advanced cooling systems. Because of the strict requirements for traction, cooling systems are becoming more specialised for individual components. Addressing the most internal components and concentrated heat sources is technically difficult. This often includes alteration of the machine design that could affect electro-mechanical functioning. More specifically, the PM of the rotor are difficult to cool, because the rotor is a moving component, is the furthest from the housing, and the presence of dedicated cooling systems is challenging because it could affect the electromechanical behaviour, thus reduce the motor power and torque. Contrarily, the stator end-windings are less problematic in terms of access or alteration of the motor architecture, however they are a much more critical component. Three reasons support this conclusion: they set the lowest temperature threshold of the motor (due to the thermal limits of the insulation), they are generally poorly cooled (only by air convection or enhanced conductivity), and their cooling it is a more generalised problem for mobility (every motor has stator windings but not necessary PM rotors).

As observed, the end-windings are a critical component for thermal management. Experiments on real motors prove that direct oil injection on the end-windings is effective in two ways. The first is that the direct contact between the coolant and the hot surface reduces the operational temperature and homogenises the temperature distribution. In such a way, the occurrence of hotspots in the insulation is drastically reduced. The second is that the motor stays longer under high-torque operating conditions. Given the benefits of direct cooling, the next step for the automotive industry is to size and optimise cooling systems for motors and vehicles.

In this framework, simulations are used, but modelling the injections is complex because of the multi-physical and multi-scale heat transfer:

i. The oil interacts thermically with the solid surface of the end-windings and also mechanically with the surrounding air.

ii. The oil distribution and flow on the end-windings surface is influenced by the injection type (e.g., jet, spray, dripping, etc.), by the injection geometry (e.g., injector orientation, surface curvature, etc.), by the air flow (induced by the spinning rotor), and by gravitational effects.

iii. The end-windings have a complicated geometry and, depending on the winding type, non-homogeneous surface, materials and thermal properties.

iv. Oil are fluids with very peculiar properties in terms of thermal properties, rheological properties, and convective heat transfer.

v. The heat transfer and the flow are significantly different between the region where the first solid-liquid interaction occurs (e.g., impingement point or droplet landing point) and the region where the flowing film is fully developed (e.g., lower region of the end-windings).

vi. In general, simulating a very large domain with high accuracy is computationally expensive, because the thermal boundary is much smaller than the dynamic one and requires a very fine mesh.

Consequently, it is difficult to predict heat transfer accurately for such complex injection configurations, thus sizing cooling systems and designing electric motors. Numerical models need validation from experiments. In light of all these considerations, more experimental and fundamental studies on oil injection cooling are needed to better understand the air-liquid-solid interactions and heat transfer. Diverse types of injection are examined in the literature (e.g., dripping, jet, spray, etc.) but in this doctoral research only impinging jet is investigated. Spray cooling would be equally interesting and would require a research project on its own, but the choice is motivated by the recent advancements in jet impingement cooling in the laboratories hosting the present research.

1.2 Jet impingement with high-Prandtl fluids

1.2.1 Overview on conjugated heat transfer with an impinging jet

In this section, the fundamentals of the jet impingement are given, with a particular focus on the thermal physics of high-Prandtl fluids. Starting by some conventional definitions, conjugate heat transfer (CHT) is the combination of heat transfer in solids and in fluids. Within solids, the mechanism for transferring heat is conduction. Within liquids, this is more complex, and the general term convection is used. In CHT, the two mechanisms are involved. A generic example of CHT is a cold liquid jet impinging on a hot solid surface, resulting in heat flowing from the solid to the liquid. Jet impingement is an injection configuration, obtained when a fluid is issued from an orifice, impacts on a solid wall, and its trajectory is deflected outwardly. The physics of an impinging jet is complex and, even though an extensive literature is available, numerous aspects are not fully understood yet.

- **Configurations**

Various configurations exist, but the coarsest difference is given by the number of phases and the geometry (Figure 1.30):

A. When a fluid is injected in the same fluid (or with similar characteristics), it is a submerged jet (e.g., air injected in air).

B. When a fluid is injected in a different fluid (with very different characteristics), it is a free-surface jet (e.g., a liquid injected in air).

C. When the fluid is injected in an enclosed environment, it is a confined jet.

The jet impingement configuration examined in this research is: free-surface (liquid injected in air), axisymmetric, circular, perpendicular to the solid wall, and in the same direction of gravity. The essential scheme of such jet is in Figure 1.31, where the characteristic elements of this configuration are shown. The most relevant elements are the impingement point (where the liquid column hits the solid and the fluid velocity), the stagnation region (where the fluid trajectory is converted from axial to radial), a low-thickness high-velocity region, the hydraulic jump (an abrupt increase of thickness), and a high-thickness and low-velocity region. Notice that this jet type has two interfaces: the solid-liquid interface (usually referred to as the solid wall) and the air-liquid interface (usually referred to as the free surface).

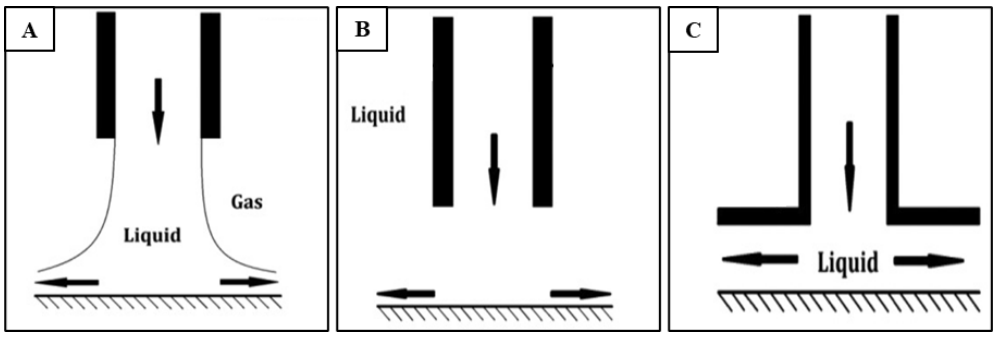

Figure 1.30 – Types of jet impingement (A) Free-surface jet. (B) Submerged jet. (C) Confined jet. *Molana* and *Banooni*, 2013.

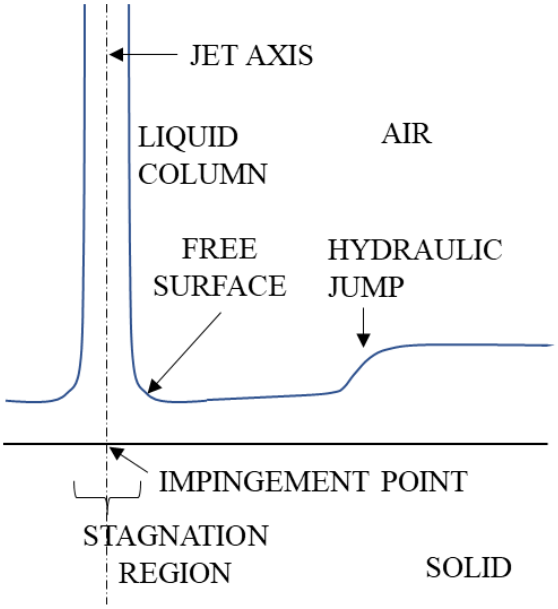

Figure 1.31 – Characteristic elements of a free-surface impinging jet.

- **Dimensionless numbers Reynolds and Prandtl**

The motion of the fluid and the thermal exchange are closely related, interdependent and influenced by many parameters. It is important to identify few but representative parameters to account for specific jet characteristics and enable comparison between studies. Dimensionless parameters, such as the Reynolds (*Re*) and the Prandtl (*Pr*) numbers are generally used for this purpose. Reynolds represents the ratio between inertial and

viscous forces, while Prandtl, the ratio between momentum and thermal diffusivity. Common practice is their evaluation at the nozzle to identify injection regime and fluid properties. Their formulations (at the nozzle) are given below.

$$Re = \frac{\rho_L U d}{\mu_L} \quad (1)$$

$$Pr = \frac{C_P \mu_L}{k_L} \quad (2)$$

U is the bulk velocity at the nozzle, d the nozzle diameter, ρ_L the density, μ_L is the dynamic viscosity of the liquid, C_P the specific heat of the liquid and k_L the thermal conductivity of the liquid.

The Reynolds number at the nozzle defines the flow regime. For $Re < 2000$ the flow is considered laminar, turbulent for $Re > 4000$, and transitional between the two. In general, increasing the Reynolds increases convective heat transfer, as shown by (*Elison* and *Webb*, 1994), for either laminar, transient and turbulent jets.

Prandtl is closely related to the fluid characteristics and may differ of several orders of magnitude from one fluid to another. The Prandtl range for oil is very large (within $50 < Pr < 10000$), due to the diverse chemical compositions of the oil (normally adjusted for very specific applications), and the large variability with temperature. Within the context of electric mobility, new lubricant fluids are being developed. The typical properties are hard to find in the literature because of the extensive variability due to the use of additives and because of confidentiality issues imposed by the manufacturer. For an idea of the properties of an ATF, only a dated study is found in *Kemp* and *Linden* 1990.

- **Boundary layers in high-Prandtl fluids**

In Figure 1.32, the sub-regions are illustrated for a generic cooling and laminar jet and a liquid such as water ($Pr \approx 6.9$ at 25 °C). The following description is based on *Liu et al.* 1991 and *Lienhard* 2006), who provide a comprehensive overview on the fluid dynamics and thermal transfer of free jets. The peak of heat transfer occurs in the region I, that is, the stagnation region. Here, the dynamic boundary layer δ_V and the thermal boundary layers δ_T are the thinnest, and they start growing along the jet-radial direction. In region II, the dynamic boundary layer increases until it has the same thickness δ as the free surface. Similarly, in region III the thermal boundary layer reaches the free surface. In regions I, II and III, the bulk velocity is less than the velocity of the free surface. Region IV marks a transition to the turbulent regime that is reached in region V, and the bulk velocity becomes greater than the one of the free-surface. Region V may relaminarize farther downstream (*Lienhard*, 2006). More comprehensive reviews on heat transfer for free-surface liquid jets, specific to every region and sub-region, are available in literature (*Eggers* and *Villermaux*, 2008; *Jambunathan et al.*, 1992; *Webb* and *Ma*, 1995).

If a fluid like an oil is considered ($Pr >> 10$), the flow and the heat transfer are much different. One peculiarity of high-Prandtl fluids is that the thermal boundary layer is much thinner than the dynamic boundary layer, as they are bound by the relation $\delta_V/\delta_T \sim Pr^{1/3}$. As Figure 1.33 illustrates, the dynamic and thermal boundary layers develop at different rates depending on the Prandtl number. The left part of the image represents fluids like oils, and the right represents fluids like gases. Concerning oils, the temperature gradient (along the wall-normal direction, between the hot solid surface and the unperturbed cold flow) is extremely steep within a very narrow layer of the fluid. When relating this thermal behaviour to jet impingement, the thermal boundary layer of an oil is similar to the trace

δ_T' in Figure 1.32. Notice that in the stagnation region, where boundary layers are the thinnest, the thermal boundary layer is extremely small for high-Prandtl fluids. Reference Prandtl values for common working fluids are in Table 1.4, along with the estimate of the ratio between dynamic and thermal boundary layers.

Considering this characteristic of high-Prandtl fluids, simulating such configuration with a CFD software would require an extreme level of mesh refinement (the closer to the solid), thus significant computational effort. This is a limiting factor for large domains and intricated geometries. As a matter of fact, few numerical studies are found in the literature on jet impingement with high-Prandtl fluids, as pointed out by *Poubeau et al.* 2022.

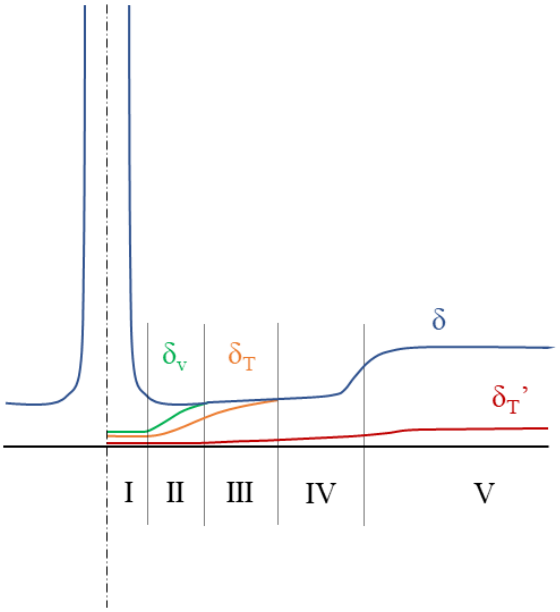

Figure 1.32 – Scheme of the sub-regions of an impinging jet and the boundary layers.

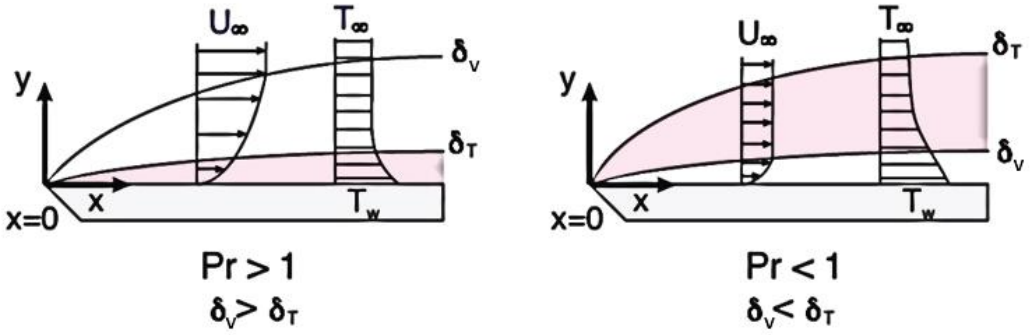

Figure 1.33 – Evolution the dynamic and thermal boundary layer for different Prandtl numbers (recoloured image from *Wikipedia* 2023c).

Table 1.4 – Typical Prandtl number for common fluids for engineering purposes.

FLUID	PRANDTL	δ_V / δ_T
Gas	0.5 – 1	0.8 – 1
Liquid water	1 – 13	1 – 2.4
Synthetic coolant FC-77	20 – 25	2.7 – 2.9
Oil	50 - 10000	3.7 – 21.5

- **Temperature distribution in the solid**

In generic studies on jet impingement, minor importance is given to the characterisation of the solid target where the jet impinges. The assumption of a thermally thin or thick object allows simplification of the heat transfer within the solid target. Such concept is better quantified by the Biot number, a dimensionless number representing the ratio between liquid convection and conductivity within the plate:

$$Bi = \frac{h\delta_S}{k_S} \qquad (3)$$

Where h is the convection coefficient of the liquid, δ_S the thickness of the solid target and k_S its thermal conductivity. When $Bi < 0.1$, the target can be considered thermally thin, while thermally thick for $Bi > 0.1$. The internal temperature distribution of thermally thin or thick targets and the way heat is transferred within the solid is influenced by the target shape, thickness and thermal properties.

A comprehensive explanation is provided by the two numerical studies by *Rahman et al.* 1999 and *Bula et al.* 2000 of conjugate heat transfer of an oil jet impinging on a disk. Figure 1.34 shows the internal temperature distribution which is found for two disks with different thickness. A common trait is that the isothermal lines have a concentric distribution around the impingement point, whereas the distribution far from impingement point is influenced by the disk thickness. For small thickness, the isothermal lines tend to have a vertical orientation, and for large thickness they have a horizontal orientation. In their studies they also observed that reducing thickness has two effects within the solid: radial heat transfer increases and the difference $T_{max} - T_{min}$ increases. Another observation is that thermal conductivity plays a role in terms of temperature uniformity of the interface. As in Figure 1.35, the difference $T_{max} - T_{min}$ at the solid-liquid interface is smaller for more conductive materials and is invariant with thickness (at least for the disk thickness twice larger than the disk diameter, that is, $b > 1$).

From the two studies, it can be foreseen that the closer to the impingement point (where T_{min} is found) the steeper the temperature gradients are expected, for solid objects with high thermal conductivity and large thickness. These considerations are retrieved in later sections of this chapter, where the experimental approaches in the literature and in this research are discussed.

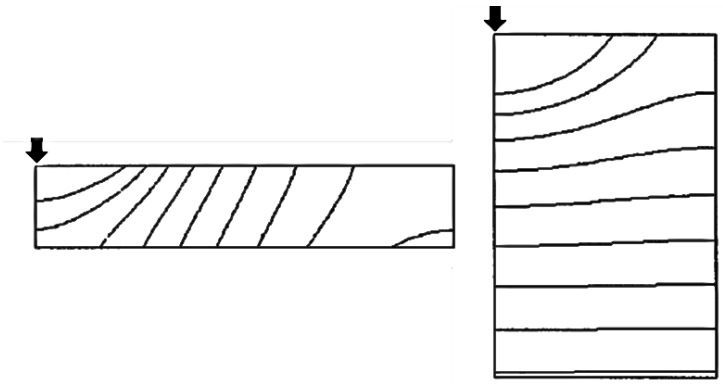

Figure 1.34 – Example of isothermal lines distribution in two disks with different thicknesses (*Rahman et al.*, 1999). The impingement point is positioned on the up-left corner. Half of the disks are depicted.

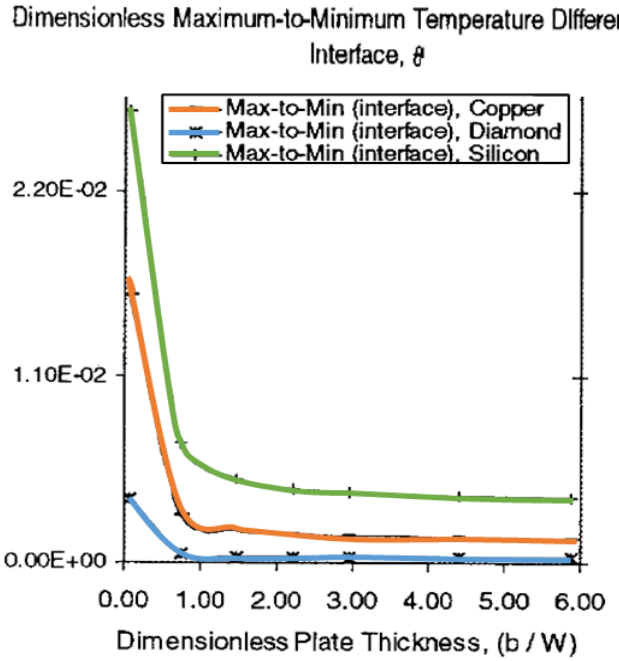

Figure 1.35 – $T_{max} - T_{min}$ at the solid-liquid interface for disks with variable thickness *b* and thermal conductivity ($k_{diamond} > k_{copper} > k_{silicon}$). Extracted and recoloured image form *Bula et al.* 2000.

1.2.2 Convective coefficient and Nusselt number

In conjugated heat transfer, the convective coefficient *h* is the parameter quantifying the heat transfer at the solid-liquid interface according to Newton's law of cooling:

$$h = \frac{q}{T_{surf} - T_{\infty}} \qquad (4)$$

Where *q* is the heat flux normal to the solid surface, T_{surf} the surface temperature (i.e., the solid-liquid interface) and T_{∞} the temperature of the undisturbed flow. This formulation is employed in many studies on convection and is a practical parameter for different types of engineering problems. An example of *h* is given in Figure 1.36 for a submerged air jet. As the image shows, the convective coefficient is typically much large at the impingement point and it decreases outwardly. In terms of result presentation, it is common practice to normalise the distance from the impingement point by the nozzle diameter (*r/d*).

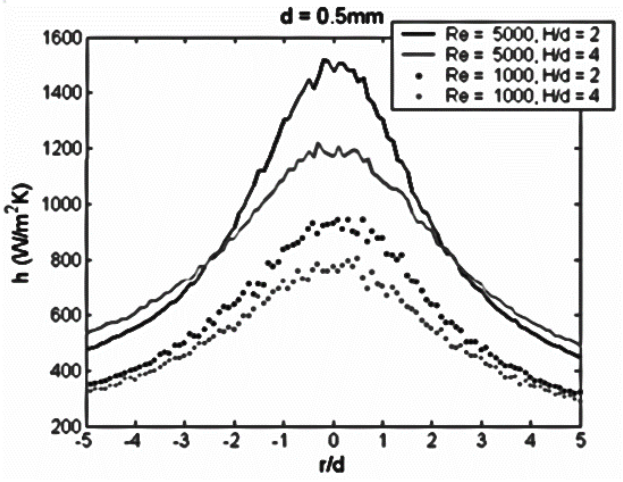

Figure 1.36 – Radial variation of the heat transfer coefficient for an air jet (*Glynn et al.*, 2005).

The convective coefficient figures in the Nusselt number, a dimensionless number representing the ratio between convective and conductive heat transfer within the liquid. In jet impingement problems, *Nu* features the nozzle diameter *d*:

$$Nu = \frac{hd}{k} \tag{5}$$

In CFD simulations the Nusselt number is important to determine (through the computation of the convective coefficient), because directly associated with the heat which is transferred within the thermal boundary layer (between the solid and the liquid). Evaluating the convective coefficient experimentally has a double purpose: characteristic heat transfer is quantified for a realistic physical setup, and valuable experimental support is provided to the numerical analysis. In the literature, many approaches exist for evaluating the coefficient and its constituent parameter. In this section, a very brief overview is given, highlighting the typical formulations used for high-Prandtl fluids.

- **Fluid temperature distribution with high-Prandtl fluids**

For generic impingement problems, T_∞ is typically evaluated at the nozzle and the fluid temperature is assumed uniform after impingement and along the jet-radial direction. Such "adiabatic fluid" assumption is relatively consistent for a reasonably large mass flow of the fluid. This is acceptable as far as viscous effects are irrelevant. High-Prandtl fluids feature very high viscosity (compared to other fluids such as water or air), especially at low temperature. In flows, the closer to the solid wall the more viscous forces take over inertial forces. Viscous friction causes the fluid to increase its local temperature with respect to the unperturbed flow. In other terms, using the nozzle temperature as T_∞ could lead to erroneous determination of the convective coefficient. The effects of viscous dissipation could become important when evaluating the heat transfer coefficient for high-Prandtl fluids (*Metzger et al.*, 1974).

For high-Prandtl fluids, better representation of the convective heat transfer in the presence of significant viscous effects is possible with the use of the adiabatic wall temperature T_{aw}, that is, the temperature at which the heat flux is zero. As in the scheme of Figure 1.37, T_{aw} is higher than T_∞ and the heat flux q is directed towards the fluid if $T_w > T_{aw}$.

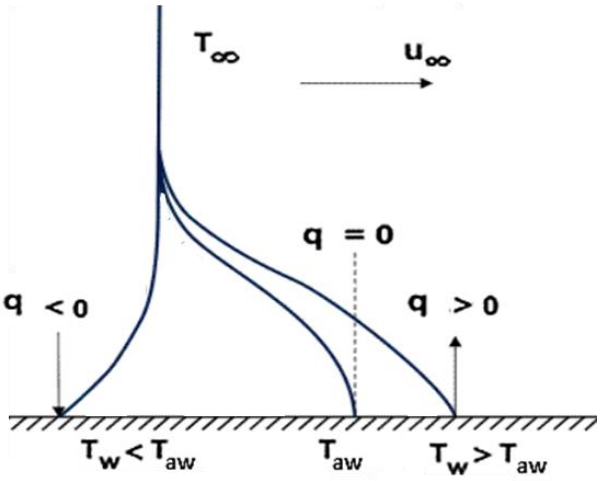

Figure 1.37 – Scheme illustrating the direction of the heat flux q, depending on the wall temperature T_w, the adiabatic wall temperature T_{aw}, and the unperturbed fluid temperature T_∞ (*Kurganov* 2011).

This approach is well-known in aerodynamics, especially for turbine film cooling and air flows close to sonic conditions, for accounting for the extra heat due to viscous dissipation. The same is valid for high-Prandtl fluids at relatively moderate flow velocity. The adiabatic wall temperature is related to the fluid flow and properties as it follows:

$$T_{aw} = T_{\infty} + r\frac{U_{\infty}^2}{2C_P} \qquad (6)$$

where U_∞ is the unperturbed flow velocity, C_P the heat capacity of the liquid and r the recovery factor. This last represents the relative increase of the temperature due to viscous dissipation, and it depends on the flow regime and the thermal properties of the liquid. Consequently, equation (4) becomes:

$$h = \frac{q}{T_{surf} - T_{aw}} \qquad (7)$$

Where T_∞ is replaced by T_{aw}. For a better visualisation of the effects of viscous dissipation, two examples are given for jet impingement with transformer oil at relatively high velocity. Figure 1.38 shows the difference (thus the error) in the estimate of the Nusselt number, when the considerable effects of viscosity are considered or not. In Figure 1.39 the local variation of the recovery factor is illustrated, showing that it is significant nearby the impingement point, typically within $1 < r/d < 3$.

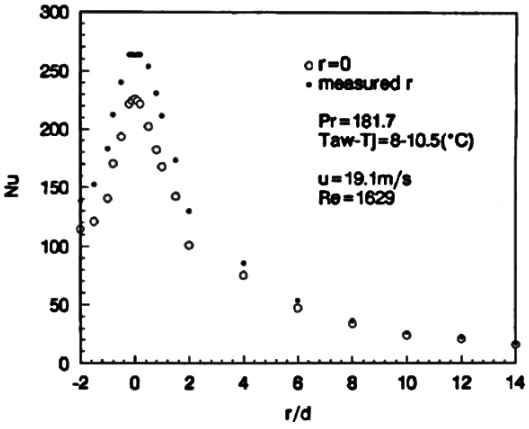

Figure 1.38 – Difference in the Nusselt number evaluation when viscous dissipation is considered (black dots) or not (white circles). Example of a laminar jet of transformer oil (*Ma et al.*, 1997a).

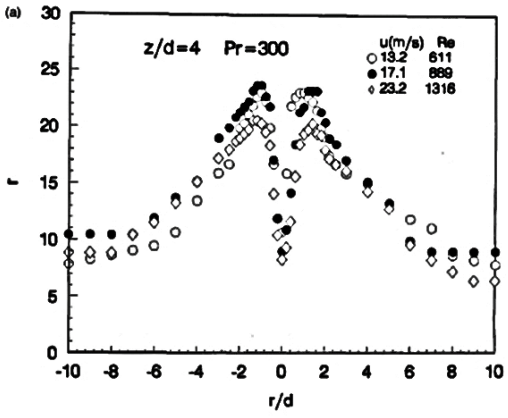

Figure 1.39 – Radial distribution of the recovery factor for a pipe-type nozzle. Example of a laminar jet of transformer oil (*Ma et al.*, 1997a).

As observed in these two figures, the use of the adiabatic wall temperature is more accurate for determining the convective coefficient, when viscous effects are relevant, for example at high injection velocity and low temperature. In the known literature on high-Prandtl fluids the adiabatic wall temperature is adopted (*Leland* and *Pais*, 1999; *Ma et al.*, 1997a; *Metzger et al.*, 1974).

- **Parametric variations of the injection**

Numerous parameters influence heat exchange, thus the Nusselt number. This includes the flow regime, the thermophysical properties, and the geometry. Many studies are available in the literature on jet impingement. Much less studies address high-Prandtl fluids. Even fewer are specific to lubricant oil for automotive transmission (*Bennion* and

Moreno, 2015). Regardless the fluid type, Figure 1.40 shows that the Nusselt number has its maximum at the impingement point ($r/d = 0$ in the figure), and at small distances from the maximum its value has already decreased significantly. Depending on the fluid type, the magnitude of the convective coefficient is different and the slope of the Nusselt number with increasing *r/d*, thus the importance of the investigated fluid.

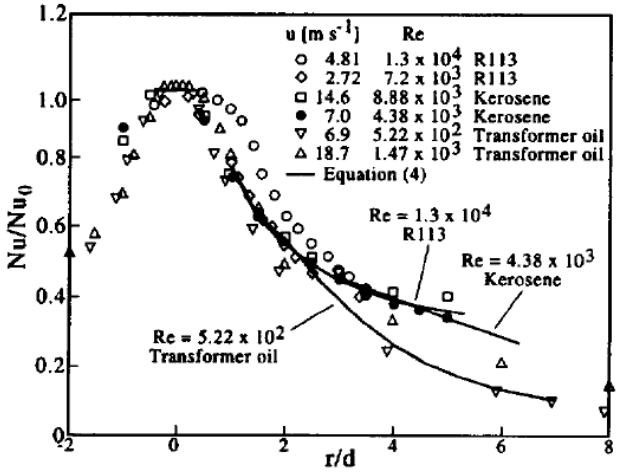

Figure 1.40 – Normalised Nusselt number for various high-Prandtl fluids (*Sun et al.*, 1998).

In terms of geometry, the literature provides many parametric studies. Some intrusting findings are mentioned in the following, as pertinent within the context of the cooling of the end-windings. For instance, the nozzle type has influence on the radial variation of the convective coefficient (*Garimella* and *Nenaydykh*, 1996; *Iciek*, 1982; *Ma et al.*, 1997a). The nozzle-to-target distance has relatively poor influence on the Nusselt number for free-surface jets with respect to submerged jets (*Elison* and *Webb*, 1994; *Ma et al.*, 1997a). For inclined jets, the peak of Nusselt number transits uphill with respect to the impingement point (*Akansu et al.*, 2008; *Ingole* and *Sundaram*, 2018; *Pawar* and *Patel*, 2020; *Stevens* and *Webb*, 1991b; *Webb* and *Ma*, 1995). Surface roughness is found to increase heat transfer in the stagnation region, due to the disruption of the boundary layer (*Gabour* and *Lienhard*, 1994).

It is hard to understand the influence of individual parameter or property. Literature shows that heat transfer values can be very specific to a given geometry, flow regime, fluid property and much more. Comparison between experiments would be difficult, as well as data exploitation for engineering applications. To overcome such hurdle, the use of correlations between dimensionless parameters is adopted, as explained in the next section.

1.2.3 Nusselt correlations

Nusselt correlation connect heat transfer with flow regime, fluid properties and geometry. The most generic correlation associates the Nusselt number with the Reynolds and Prandtl numbers:

$$Nu = C\, Re^m Pr^n \qquad (8)$$

Where the coefficients *C*, *m* and *n* are determined empirically with data fitting. The Nusselt correlations have large use in all sorts of engineering problems, because they provide a concise and dimensionless synthesis of a particular injection configuration and geometry. They are frequently used for sizing, approximations, and validation of numerical

models. Equation (8) usually is related to the impingement point, and more complex formulations are used for the jet-radial distribution. In this case, formulations are similar to the one below (*Jambunathan et al.*, 1992):

$$Nu = \frac{a\ Re^{b}}{1-(r/d)^{c}} \tag{9}$$

where further empirical parameters appear (*a*, *b* and *c*) and dependency from the distance from the impingement point (*r/d* and $a = f(r/d)$). Various tables of correlations for the impingement point are found in the literature for a large number of free-jets, as in *Molana* and *Banooni* 2013.

For liquid and axisymmetric jet impingement, the literature shows that *Nu* increases with both *Re* and *Pr*, that the coefficients *m* and *n* are comprised between 0 and 1, and that the scaling factor *C* is significantly different between studies. More specific correlations are deduced theoretically (*Liu et al.*, 1991; *Webb* and *Ma*, 1995) for every sub-region of a laminar jet with uniform heat flux, concluding that the stagnation region ($0 < r/d < 0.8$) is correlated by $Nu = 0.797\ Re^{1/2}\ Pr^{1/3}$ for liquids with $Pr > 3$. More complex formulations are found for the other regions.

Concerning the correlation at the impingement point, various experimental studies observe that $Nu \sim Re^{0.7\text{-}0.9}$ and $Nu \sim Re^{0.4\text{-}0.7}$ for turbulent and laminar injections respectively, when using diverse fluid types such as water (*Elison* and *Webb*, 1994; *Stevens* and *Webb*, 1991a), lubricant oil (*Leland* and *Pais*, 1999) and other fluids with $Pr > 1$ (*Sun et al.*, 1998). Concerning the Prandtl number, various experiments suggest the relation $Nu \sim Pr^{0.2\text{-}0.4}$ (*Lee et al.*, 1997; *Ma et al.*, 1997b; *Ma et al.*, 1997c; *Ma et al.*, 1997a). From this literature, it appears that some discrepancies between the authors are still present at correlating high-Prandtl fluids.

1.2.4 Representative convective heat transfer

The studies addressing high-Prandtl fluids are still limited in number, but relatively good agreement is found on the variation of the Nusselt number with the Reynolds and Prandtl numbers, and the most basic geometric parameters (e.g., nozzle types, nozzle-to-target distance, target, or jet inclination, vertical or horizontal orientation of the jet, etc.). Nevertheless, slight discrepancies are still present in terms of transition between different flow regimes, target geometries, and working fluids. Moreover, more investigation is needed to find more meaningful parameters for correlating datapoints, to understand the influence of the injection velocity profiles, to understand local relation between heating and fluid viscosity, to explore convective heat transfer with different target materials, and to better understand the influence of surface roughness.

From the literature survey on high-Prandtl fluids, the Nusselt number is usually not determined locally but averaged within a surface and the Nusselt correlations from the literature are hardly exploitable for real cases (e.g., sizing of injection cooling systems). Within the context of the cooling of the end-windings the studies are even scarcer. More representative estimates of the convective coefficient and Nusselt number are needed in terms of surface temperature range, injection parameters, flow regimes and fluid types.

Some of these aspects are investigated in this research. Considering the temperature limits of the electrical insulation, the surface temperature of the target should be investigated within $150\ °C < T < 180\ °C$. Considering reasonable injection parameters, similar to those found in vehicles, the temperature of the oil should be kept above ambient temperature (to reduce viscosity and assure oil fluidity), the injection pressure slightly above the atmospheric pressure (to prevent splattering and to assure oil coverage on the

solid target), and more generally the investigation should be undertaken within the laminar and transitional regimes Re < 4000 (to limit viscous dissipation within the oil). Considering the fluid type, a specific oil for electric mobility should be used (as typical high-Prandtl fluids in the literature are transformer oil, lubricants for aeronautics and fluorocarbons).

Lastly, the studies are undertaken with strong simplifying assumptions on some of the most important parameters (e.g., uniform temperature or heat flux at the solid-liquid interface). On one hand, this is necessary for understanding the influence of specific parameters on the heat flux or for technical convenience (e.g., for diagnostics and evaluation methods). On the other, the estimates of the heat transfer are given for not representative geometries or injection configurations of real case. This aspect is deepened in the following part of this chapter.

1.3 Investigation of jet impingement with high-Prandtl fluids

1.3.1 Experimental approaches and solid target shapes

It is very common in the literature on jet impingement the use of thin plates or disks and elongated cylinders (Figure 1.41), because these target shapes have significant advantages in terms of accessibility of the diagnostic systems and allow simplifying assumptions on heat transfer. Nevertheless, if a target shape is suitable for some types of evaluation, it can be a limiting factor. This is connected to the problems of being representative for real engineering problems, and to the applicability of the diagnostic beyond fundamental studies, which are discussed in this section.

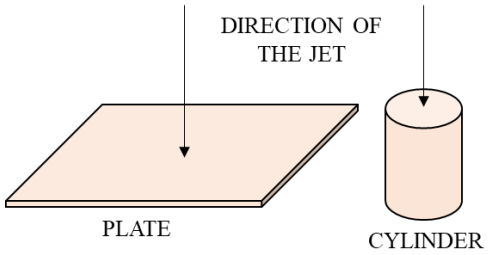

Figure 1.41 – The typical experimental geometries for investigating jet impingement are thin plates/disks (left) and an elongated cylinder (right).

- **Thin plates and disks**

In thermally thin solid targets such as plates and disks (i.e., $Bi < 0.1$), this shape forces redistribution of heat along the jet-radial direction (see section 1.3.1). Consequently, the temperature difference between the fluid-wetted and unwetted side of the target is expected to be small, while the temperature gradients along the jet-radial direction are expected to be large. This phenomenon is enhanced by materials with low thermal conductivity.

In light of these considerations, this target type is suitable for temperature measurements (along the jet-radial direction), also allowing the assumption of a uniform heat flux at the solid-liquid interface. The first is that the plate temperature variations are expected to be large in the jet-radial direction, allowing high-precision and high-resolution measurements. The second is that the temperature of the fluid-wetted surface can be approximated by that of the unwetted surface, thus the possibility to install the temperature diagnostics in a sheltered position from the injection. The third is that the heat flux at the solid-liquid interface can be assumed uniform, in reason of the thermal thinness. Evidence of the

advantages of this target shape is given by the large number of studies using this shape for jet impingement (example in Figure 1.42). This is expanded in the next section on diagnostic systems, however some examples with high-Prandtl fluids are found in the dedicated literature (*Feng et al.*, 2021; *Ma et al.*, 1997c; *Ma et al.*, 1997a; *Renon et al.*, 2021), who used electrically heated metallic thin plates, measured the temperature on the unwetted side, and evaluated the heat flux directly from the electric power delivered to the plate. As a result, it is possible to evaluate the distribution of the convective coefficient along the jet-radial direction or even 2D mapping, using various types of diagnostics.

- **Elongated cylinders**

This target shape refers to cylinders, whose height is comparable (in extent) to the diameter. An elongated cylinder can be considered a thermally thick target (see section 1.3.1) thus the temperature gradient along its symmetry axis is expected to be large. Additionally, when the jet impinges normally to the upper surface of the cylinder, the heat flux on the impingement point is also normal to the plate. These characteristics are exploited by several studies, because they are suitable to evaluate heat exchange at the impingement point (*Bennion* and *Moreno*, 2015; *Leland* and *Pais*, 1999; *Metzger et al.*, 1974). In these studies, a high-Prandtl fluid impinges on a copper cylinder, heated from below and thermally insulated on the lateral surface (example in Figure 1.43). The surface temperature and the heat flux are typically evaluated with embedded probes.

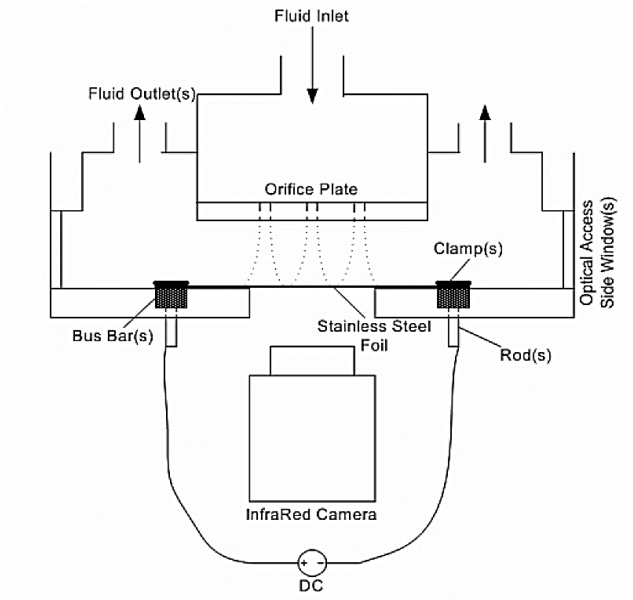

Figure 1.42 – Experimental apparatus for studying an impinging air jet with a thin plate (*Glynn et al.*, 2005).

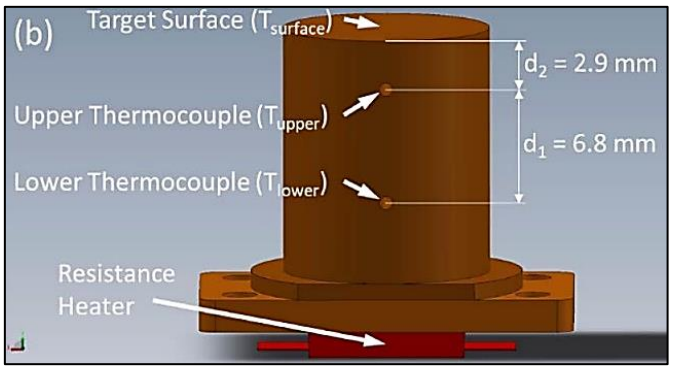

Figure 1.43 – Example of cylindrical target for studying an impinging oil jet (*Kekelia et al.*, 2019).

- **Representativity and adaptability to the industrial context**

The cited literature shows that thin plates or disks and elongated cylinders are suitable for fundamental studies on jet impingement. For industrial applications, these target shapes may not be fully representative of the temperature and heat flux distributions. Consequently, the estimates of the Nusselt number and correlations may not be exploitable. For example, in generalised engineering applications, it is not always possible to assume a uniform heat flux at the solid-liquid interface. Concerning elongated cylinders, the evaluation of heat transfer is limited to the impingement point and is surface-averaged. Concerning thin plates or disks, there are very few studies taking direct measurements of the temperature of the actual surface-liquid interface.

Beside representativity, another typical problem faced in different industrial frameworks is the adaptability of the diagnostic system. Many methods developed from fundamental studies meet with difficulty at being applied in generalised engineering cases (e.g., the unwetted surface of a target is not always accessible).

In light of these considerations and within the context of the cooling of the end-windings, it is important to develop experimental methods to characterise thermal transfer in generic thermally thick targets, and diagnostic systems which can be also applied on real electric motors.

1.3.2 Key parameters and diagnostic techniques for solids and liquids

This section is a brief overview of the diagnostic techniques proposed by the literature for measuring the key parameters identified by this research. The selected literature aims for free-surface and submerged jets, however some techniques are more developed for similar flow configurations, such as free-falling liquid films. In this overview, the target shape and the jet type have an influence on the applicability of the measurement technique (mostly optical), in terms of optical access and accuracy. Focus is given to laser induced fluorescence (LIF).

- **Key parameters**

For the oil cooling of the end-windings, it is important to characterise heat transfer through the convective coefficient and the Nusselt correlations, for generic thermally thick targets shapes, for high-Prandtl fluids (e.g., lubricants), and considering the possible constraints in diagnostic access found in industrial scenarios (e.g., limited access to diagnostics). With the aim of fulfilling the scientific knowledge gaps of jet impingement and meet the needs of the industry, it is important to evaluate:

i. Surface temperature: for generic thermally thick objects, steep temperature gradients characterise the surrounding solid of the impingement point, thus the surface temperature must be measured the closest as possible to the physical solid-liquid interface.

ii. Heat flux: must be evaluated locally, because no simplifying assumption are possible for generic thermally thick targets.

iii. Liquid temperature: with high-Prandtl fluids, the fluid temperature requires measurements at various locations, including at the nozzle (i.e., bulk flow temperature), along the jet-radial direction (i.e., mean film temperature and

temperature of the air-liquid interface) and along the plate-normal direction (i.e., between the solid-liquid and the air-liquid interfaces).

iv. Convection coefficient and Nusselt number: local estimates are needed for typical lubricant oils for electric powertrains, within the typical thermal range of the end-windings.

v. Reynolds and Prandtl numbers: the Nusselt correlations are evaluated for a representative and relatively large Reynolds and Prandtl range, thus it is important to evaluate the injection parameters (i.e., the fluid thermal and rheological properties, injection velocity, injection pressure and flow rate).

vi. Liquid thickness: jet impingement features different flow regions, whose thickness is not involved directly in the heat transfer quantification, but it provides complementary information about fluid coverage and flow regions.

- **Diagnostics for temperature in solids**

  - Probes

Thermocouples are temperature sensors based on the Seebeck effect. They are amongst the most reliable measurement instruments for temperature, such that even when optical techniques are used, calibration and benchmark temperature are always measured also with thermocouples. They are less suitable for small scale flows in reason of the flow disturbance caused by their size (typically minimum Ø = 0.1 mm). For studies on jet impingement with transformer oil, (*Ma et al.*, 1997c) take measurements of the surface temperature with a moving thermocouple, in contact with the unwetted side of the plate. In other studies on jet impingement with lubricant oils (*Bennion* and *Moreno*, 2015; *Kekelia et al.*, 2019; *Leland* and *Pais*, 1999) use target-embedded thermocouple (example in previous figure Figure 1.43). In this case at least two thermocouples are used, to measure the solid-liquid interface temperature and to evaluate the heat flux (from a temperature difference). For these studies, T and J type thermocouples are used.
Measurements of the heat flux are taken with a similar principle, that is, aligning multiple temperature sensor over a control surface. Examples for air jets are found in *Mohanty* and *Tawfek* 1993, who use a sequence of seventeen 3-wire heat flux sensor (Ø = 3 mm), embedded in fixed positions inside the target plate. A similar study is undertaken by *O'Donovan* and *Murray* 2007, using heat flux sensor foils (0.1 mm x 1.4 mm) for impinging air jets. Heat flux sensors are not suitable for small scale measurements because of their size, which pre-determines the spatial resolution of the measurements.

  - Infrared thermography

This optical technique is an imaging method based on the detection of the infrared light (i.e., $\lambda > 700$ nm) emitted by the surface of an object. From the infrared intensity, the temperature is deduced according to the blackbody radiation-law. The technique is suitable for surface temperature detection (frequently used in jet impingement as well) but typically probes are more accurate. *Glynn et al.* 2005 evaluated the convective coefficient for air and water jets, by placing an infrared camera on the unwetted side of a thin plate (see previous Figure 1.42). A similar study is undertaken by *Fenot et al.*

2005, who evaluated the Nusselt number of an impinging air jet with an estimated uncertainty of 12 %. A later study by *Haustein et al.* 2012, with water jets impinging on a transparent plate, measures the surface temperature (1.1 °C uncertainty) and evaluates the Nusselt number (uncertainty 12 %). Concerning free-falling wavy liquid films, also in *Markides et al.* 2016 the surface temperature of a thin foil is measured with an infrared camera. In all the cited studies, the infrared camera is sheltered from the flow, because positioned on the unwetted side of a thin plate.

- Thermochromic liquid crystals thermography

Thermochromic liquid crystals (TLC) can reversibly change their colour (in the visible spectrum) depending on their temperature. For surface temperature measurements, the target is usually coated with a thin layer of TLC. In general, they are used for qualitative evaluations, given the restrained temperature range and colour variation. An example of visualisations of the solid target wall temperature (with impinging air jets) is provided by *Goldstein et al.* 1986. Concerning quantitative measurements, *Lee* and *Lee* 1999 measured the temperature (uncertainty 1.5-3.6 %) and evaluated the Nusselt number (uncertainty 3.3-6.2 %), with narrow-band TLC (red at 35 °C and blue at 35.8 °C). Similarly, *Eiamsa-ard et al.* 2015 evaluates temperatures between 29-42 °C and the Nusselt number with uncertainty 3.3-4.9 % (this last showed in Figure 1.45).

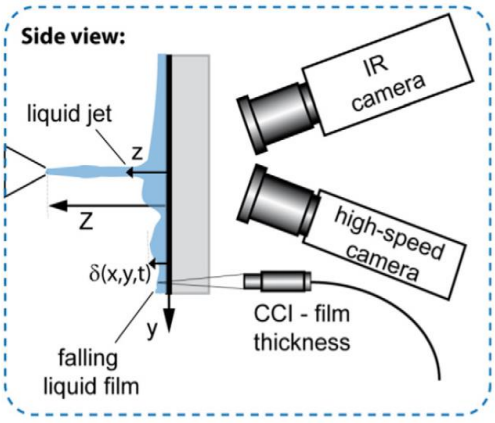

Figure 1.44 – Example of optical setup with infrared thermography (*Haustein et al.*, 2012).

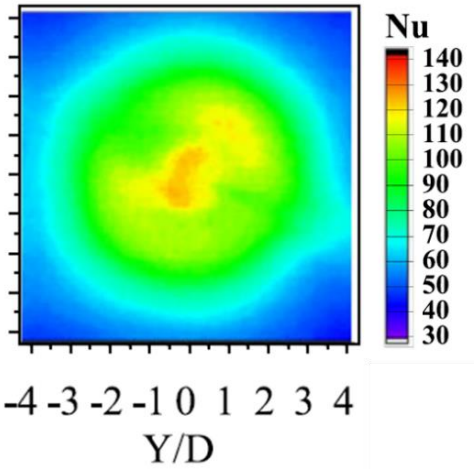

Figure 1.45 – Example of evaluation of the Nusselt number with thermochromic liquid crystals thermography (*Eiamsa-ard et al.*, 2015).

- Fluorescence and phosphorescence thermography

Fluorescence and phosphorescence are similar light-emission phenomena. A fluorescent or phosphorescent substance can emit light subsequent to an excitation at a smaller wavelength. Depending on the substance, their light emission could vary with the temperature and could be detect by a camera. They are suitable for pointwise and field measurements of the surface temperature of solid objects, in a non-intrusive way. The measurement precision and accuracy depend on many factors, but physical probes are generally better. For surface temperature measurements phosphor particles are typically mixed with a blending agent and applied as a thin coating. Extensive use is found for gas turbines and burning chambers, as reviewed by *Aldén et al.* 2011. Within the context of jet impingement, an example of pointwise measurements of the surface temperature is given by *Bizzak* and *Chyu* 1995. In the study, an air jet impinges on a quartz plate with a thin coat of thermographic phosphor. The laser induced fluoresced

technique is used, with UV laser is for excitation and a CCD camera for detection. The temperature measurement is taken from the opposite surface to the impingement one. The Nusselt number is evaluated with 11 % uncertainty.

- **Diagnostics for temperature and thickness in liquids**

  - Infrared thermography

Within the context of free-falling wavy liquid films, an example of temperature measurement is given by *Charogiannis* and *Markides* 2019. In their experimental apparatus, a water and glycerol mixture flows over a plate and an infrared camera (above the liquid) is used to measure the temperature of the air-liquid interface. An example of the measurement is in Figure 1.46. Notice that the technique is not intrusive but can only measure surface temperature and cannot distinguish the internal or mean temperature of the liquid.

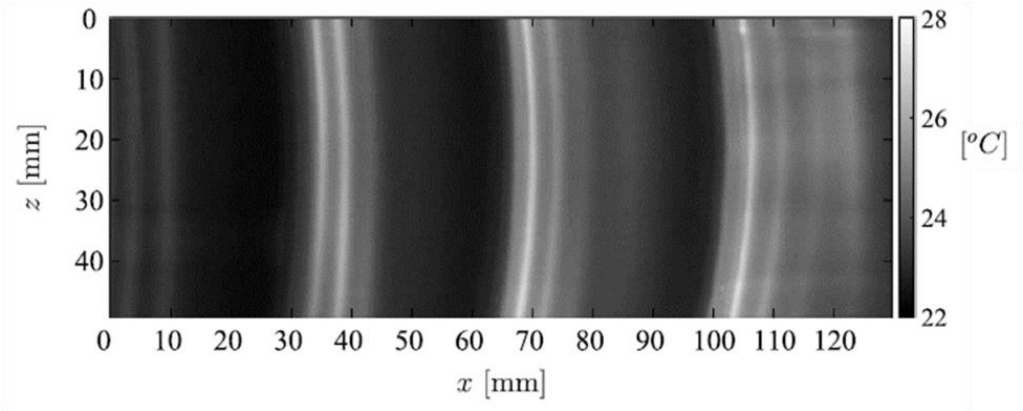

Figure 1.46 – Temperature measurement with infrared thermography of the air-liquid interface of a free-falling wavy liquid film (*Charogiannis* and *Markides*, 2019).

  - Thermochromic liquid crystals thermography

For measuring the temperature in liquids, TLC are added in the fluid and their colour change is observed with a colour camera. Examples of seeded flow are found in *Ashforth-Frost* and *Rudel* 2002, who used encapsulated TLC for flow and heat transfer visualisation in in a water jet (Figure 1.47). TLC usually suffer of restrained temperature range and colour variation.

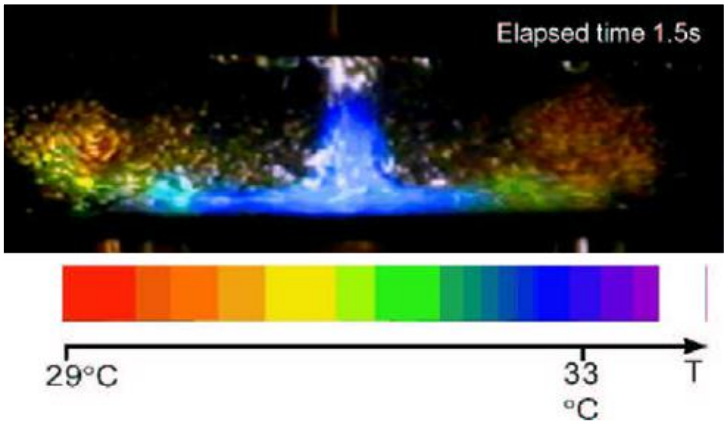

Figure 1.47 – Thermal field obtained with encapsulated thermochromic liquid crystals (*Ashforth-Frost* and *Rudel*, 2002).

- Fluorescence and phosphorescence thermography and thickness measurements

Fluorescence- and phosphorescence-based techniques are extensively used for field measurements in flows, due to the small disturbance. The usual approach is to add a "tracer" into the flow, such as dyes or particles. In the first case, a continuous measurement field is obtained, whereas in the second, discrete and local measurements are obtained, and a field must be deduced afterwards. Numerous applications for thermometry are found for generic flows and sprays. Also submerged liquid jets of water are a popular model experiment, where a hot mixture of water and tracer is released in a tank filed with cold still water, and a field measurement is taken for a crossed section of the jet (Figure 1.48). Precision, accuracy and technical constraints of these techniques are very specific to the application and the equipment.
An example of seeded-flow with phosphor particles is provided by *Fond et al.* 2012, who measured instant and time-averaged temperature for a submerged water jet (Figure 1.49). More examples are reported in dedicated reviews about phosphors (*Abram et al.*, 2018; *Aldén et al.*, 2011), where it is pointed out that popular applications concern thermometry with seeded flows in a combustion related context.
A study involving liquid droplet seeded flow and LIF technique is undertaken by *Wright* and *Seitz* 2019, where an impinging air jet with dispersed toluene droplets is investigated and temperature is measured (with 12.5 °C of uncertainty).
Concerning field measurements of temperature with LIF, comprehensive examples are available in the literature (*Bruchhausen et al.*, 2005; *Chaze et al.*, 2016; *Funatani et al.*, 2004; *Nebuchinov et al.*, 2017; *Sakakibara et al.*, 1997; *Sakakibara* and *Adrian*, 1999), where the typical temperature range is 20 °C < T < 70 °C and the uncertainty estimate is ≈ 0.5-1.5 °C.
The LIF technique with fluorescent dyes is extensively used for temperature and thickness measurements when studying free-falling wavy liquid films. The typical experiment is on an inclined plane, where a mixture of water and glycerol flows downward from an upper tank. A series of related studies (*Charogiannis et al.*, 2015; *Charogiannis et al.*, 2017; *Charogiannis* and *Markides*, 2019; *Collignon et al.*, 2021; *Markides et al.*, 2016) develop different types of diagnostic techniques including LIF, for temperature and thickness fields of the cross-section of the falling film (about 0.5 °C uncertainty on temperature), as illustrated in Figure 1.50.
Lastly, thickness measurements with fluorescent dyes and LIF are also found in tribology studies. *Myant et al.* 2010 and *Hidrovo* and *Hart* 2001 investigate static films of lubricant oil (range 0.1 µm < δ < 50 µm), obtaining a thickness map obtained with flood illumination. Figure 1.51 is a demonstration of a thickness measurement.

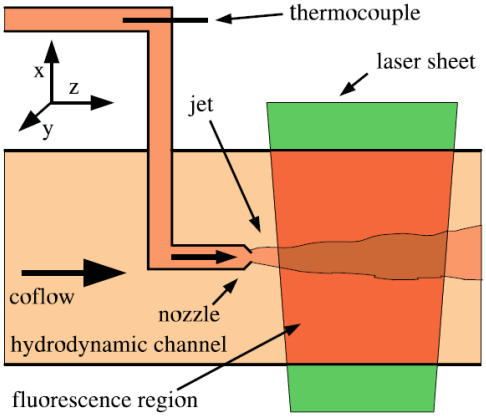

Figure 1.48 – Scheme of the typical experimental apparatus for field measurements of submerged jets (*Bruchhausen et al.*, 2005).

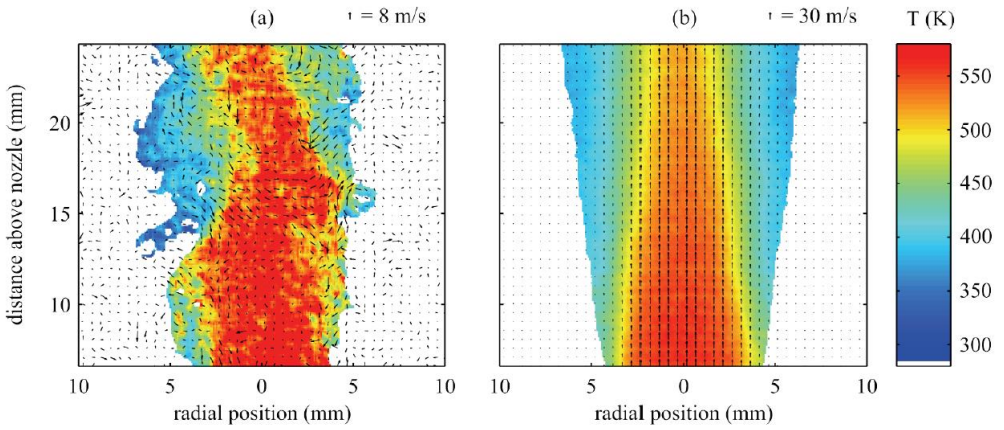

Figure 1.49 – Instantaneous (a) and time-averaged (b) temperature measurement, obtained for phosphor-seeded submerged jet (*Fond et al.*, 2012).

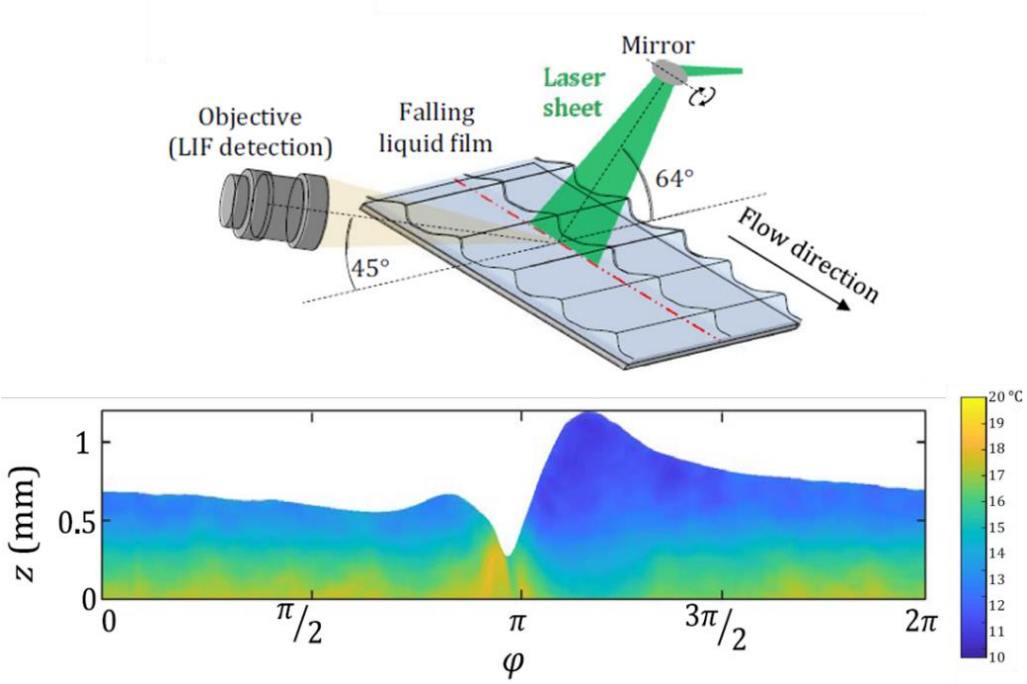

Figure 1.50 – Experimental setup (above) for measurements of temperature and thickness (below), of a crossed-section of a free-falling wavy liquid film (*Collignon et al.*, 2021).

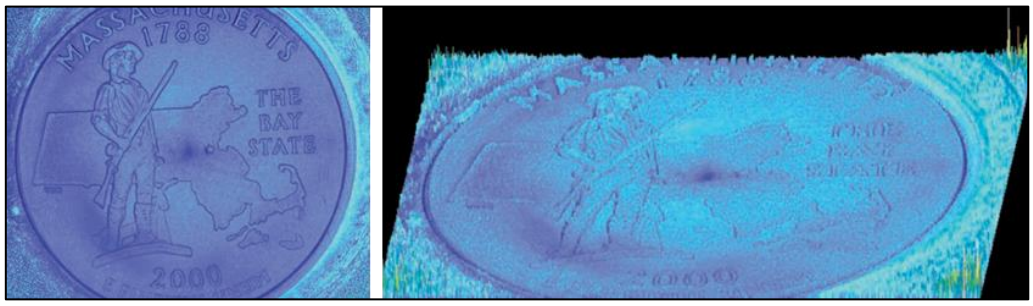

Figure 1.51 – Demonstration of thickness measurement with LIF, using a thin layer of oil over a coin (*Hidrovo* and *Hart*, 2001).

- Contact needle

Zhao and *Cerro* 1992 used a contact needle for falling flows along rough surfaces. A slight electrical voltage is applied to the needle and when it interacts with a liquid film

or a solid surface, a voltage spike confirms the contact. In their study they point out that the signal is reliable when conductive liquids are investigated, but for dielectric fluids (i.e., silicon oil), visual confirmation is necessary (i.e., a real-time video with a close-up of the needle). This technique provides overall accurate and precise measurements, but it is time consuming, intrusive, and restrained to pointwise measurements.

- Light absorption

Beer-Lambert law of absorption states that light intensity attenuates with an exponential trend when travelling through a medium. A light absorption method is compared to a conductance probe in *Mouza et al.* 2000, using a low-velocity flowing film, showing overall good agreement. Normally this technique suffers of optical access because the incident light source should be placed the closest as possible to the flow.

- Confocal chromatic imaging

The technique is based on the lens chromatic aberration. With the aid of a particular optical setup, a specimen is illuminated with white light (i.e., all the wavelengths of the visible spectrum), but only a specific wavelength can be detected, and the thickness of the specimen can be deduced such wavelength. This technique is used for a free-surface impinging jet by *Haustein et al.* 2012, for taking pointwise measurements of the liquid through a transparent plate (uncertainty estimated at 13 %). The main limitation of the technique is due to technological aspects.

- **Discussion about pertinent techniques for the present research**

From the brief review presented in this section, various observations can be made, summarized in a few points:

i. Numerous techniques exist for measuring all the key parameters highlighted at the beginning this section. The literature offers a wide range of probe and optical measurements for solids and liquids, with overall good precision. Either pointwise or field measurements are possible.

ii. Concerning those studies specific to jet impingement with high-Prandtl fluids, the temperature of the solid is measured essentially with thermocouples and infrared thermography. The liquid temperature is measured exclusively at the nozzle. The liquid film thickness is hardly investigated.

iii. The target shape and the jet type may have an indirect influence on the development of the technique, especially for the optical ones. In many cases, even advanced diagnostics are developed on identical model experiments. On one side this is an advantage in terms of variety of techniques, on the other the model experiments may not be representative of the geometric constraints in engineering problems. A practical example observed for jet impingement: optical measurements of the solid-liquid interface are normally taken from the opposite side of the impingement, which is not always accessible in real case scenarios.

The literature review suggests that thermocouples are suitable for measuring temperature of thermally thick solid targets, assuring relatively high spatial resolution and precision. For the heat flux determination, sensors may not be a reasonable choice because they may perturb the heat transfer and because their relevant size affects the spatial resolution of the measurement. It follows that a numerical approach should be considered for the heat flux. Concerning the liquid, optical methods appear suitable for field and simultaneous measurements of temperature and thickness, because one or multiple techniques can be implemented without perturbing the flow.

In this research, the potential for LIF should be explored for applications with free-jets with high-Prandtl fluids for electric mobility, because LIF allows temperature and thickness field measurements of a flowing film. This technique should be developed with a relatively compact design, also allowing optical access from the fluid-wetted side of the target, so that it can be used for future implementation on real motors.

1.3.3 LIF measurements in liquid films

- **Principles of fluorescence**

The LIF technique requires an excitation source (e.g., laser, LED, halogen source, etc), a fluorophore (e.g., molecule, atom, etc.), and a detection device (e.g., camera, photodiode, etc.). The excitation source emits light at a specific wavelength λ_{ex} to excite the fluorophore to induce fluorescence. Referring to the simplified Jablonski diagram illustrated in Figure 1.52, fluorescence occurs in three phases: (i) a fluorophore increases its energy state to a higher one by absorbing the energy of an excitation photon, (ii) part of the energy is then dissipated by the fluorophore through non-radiative mechanisms of energy transfer (i.e., vibrational relaxation and internal conversion), and lastly (iii) the fluorophore returns to its original energy state by releasing energy through photon emission and this is called fluorescence. If a mechanism known as intersystem crossing occurs during the non-radiative phase (ii), the fluorophore still emits a photon in phase (iii), but this is called phosphorescence. In any case, the emitted photon has a larger wavelength with respect to the excitation photon ($\lambda_{ex} > \lambda_{em}$), because part of the excitation energy is converted to other forms before emission. Typical time scales are 10^{-14} s for absorption, 10^{-9} s for fluorescence, and 10^{-3} s for phosphorescence. Fluorescence emission typically occurs in the UV spectrum ($250\ \text{nm} < \lambda < 380\ \text{nm}$) and in the visible spectrum ($380\ \text{nm} < \lambda < 750\ \text{nm}$). Successively, the fluorescent emission is detected by a device which converts the emitted photons into an electric signal, hence a measurement is possible.

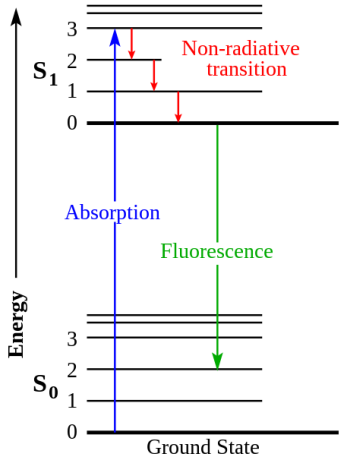

Figure 1.52 – Simplified Jablonski diagram for fluorescence photoluminescence (*Wikipedia* 2023d).

- **Ratiometric approach for temperature measurements with LIF**

Figure 1.53 is a scheme of a temperature measurement with 2-colour LIF, using one dye or a mixture of two dyes. The peculiarity of the fluorescent spectrum of the dyes is that a part is temperature sensitive, and another is temperature insensitive. The two channels detect the emission in two different wavelength ranges. The first detects the temperature sensitive part of the fluorescent emission, and the second detects the temperature insensitive part. In the figure, the two channels are arbitrarily named "*Blue*" and "*Red*" depending on whether shorter or longer wavelengths are detected. The ratio between the total intensity detected in the red channel and the blue channel is a function of the temperature. If the dependence of the channel ratio with the temperature is known (e.g., from a calibration process), an unknown temperature can be deduced from a fluorescent intensity measurement. This method based on the channel ratio is called ratiometric approach. If one detection channel is used, the technique is called 1-colour LIF.

More detailed formulations about the technique are found in the comprehensive studies of *Coppeta* and *Rogers* 1998 and *Sakakibara* and *Adrian* 1999. They explain that the intrinsic advantage of the ratiometric approach (with respect to the 1-colour 1-dye LIF) is that the channel ratio is independent from the excitation light and the target volume. The dependence on the dye concentration still remains, however it can be overcome with an appropriate selection of the detection channels (*Lavieille et al.*, 2001).

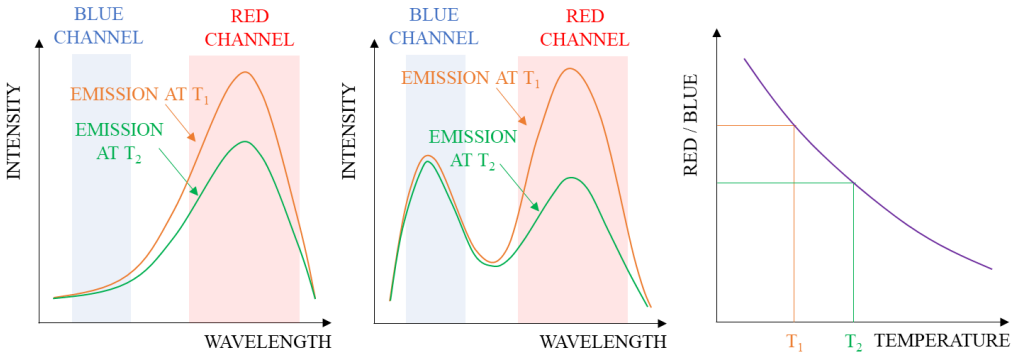

Figure 1.53 – Example of the ratiometric approach with 2-colour LIF for temperature measurements. (Left) Fluorescent emission of a dye, at two different temperatures, and the two channel bands. (Centre) Fluorescent emission of a mixture of two dyes, at two different temperatures, and the two channels. (Right) Temperature variation of the intensity ratio between the two channels.

- **Temperature and thickness measurements in liquid films**

The 2-colour 2-dye LIF technique can be used for temperature and thickness measurements of liquid films. In the context of tribology with thin films of lubricant oil, a series of publications (*Hidrovo*, 2002; *Hidrovo* and *Hart*, 2000; *Hidrovo* and *Hart*, 2001) demonstrate the importance the emission-reabsorption phenomenon and the optical thickness for these type of measurements.

The fluorescence emission of a dye dissolved in a liquid film is a function of various parameters associated with the incident excitation light (e.g., intensity and wavelength) and the properties of the dye (e.g., absorptivity and quantum yield). Concerning optical thickness, in optically thin systems the fluorescent intensity is linear with the physical thickness of the system, while it is exponential for optically thick systems. A visual example is given in Figure 1.54: the diagonal stripes indicate the optically thick band, while the optically thin band is found for smaller film thickness. For larger film thickness, the

excitation light cannot penetrate the film because is absorbed by the outer liquid, consequently the fluorescence emission becomes independent from the film thickness.

Concerning spectral conflict, there are three kinds, each leading to specific problematics in measurements, as better explained in *Coppeta* and *Rogers* 1998. The spectral conflict of interest for *Hidrovo* and *Hart* 2000 is when the emission spectrum of one dye overlaps with the absorption spectrum of the second dye (see region β in Figure 1.55), resulting in the first dye boosting the fluorescent emission of the second dye. It appears that this spectral conflict is more suitable for thickness measurements and is enhanced in optically thick systems. Conversely, when the emission-reabsorption process is low, temperature measurements are favoured (i.e., in optically thin systems and with low spectral conflict between dyes).

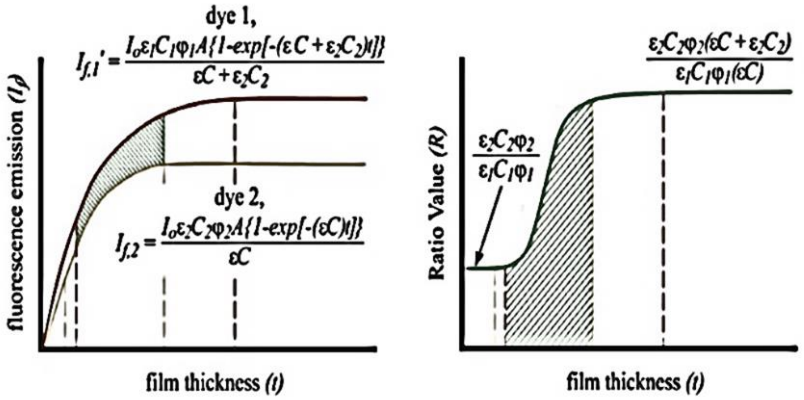

Figure 1.54 – (Left) Fluorescent emission of two individual dyes. (Right) Ratio of the two fluorescent emissions (*Hidrovo* and *Hart*, 2001).

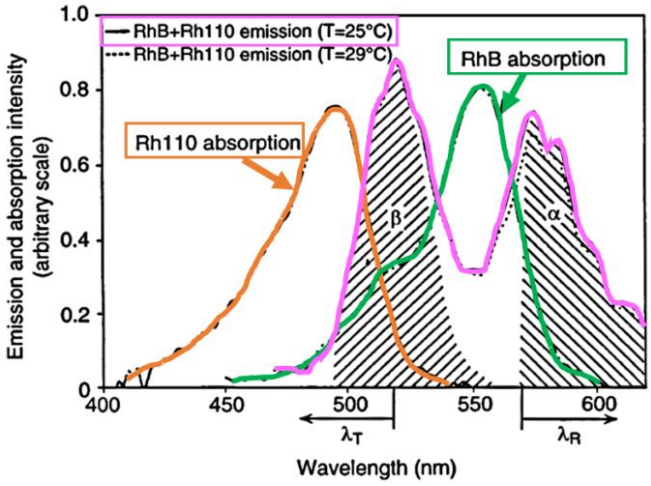

Figure 1.55 – Emission spectrum of a mixture of Rhodamine B (RhB) + Rhodamine 110 (Rh110). Extracted and recoloured from *Sakakibara* and *Adrian* 1999.

- **2-colour 2-dye LIF and detection with RGB camera**

In the literature there are examples of temperature measurements with 2-colour 1-dye LIF for submerged water jets (*Funatani et al.*, 2004; *Sakakibara* and *Adrian*, 1999) and 2-colour 2-dye (*Kim H. J.* and *Kihm K. D.*, 2001; *Sakakibara* and *Adrian*, 1999). A common trait in their optical benches is the use of a beam splitter and two different black and white cameras, each with its own filter (see Figure 1.56). This technical solution is an advantage for separating the temperature sensitive from the temperature insensitive band of the fluorescent spectrum.

Potentially, the same result is obtained with a single RGB camera, because each of the three RGB channel is equivalent to a black and with camera plus a filter. The advantages are multiple: the optical bench is more compact, less optical components are required, more simultaneous measurements can be taken, and there is no need to align cameras. The disadvantage is that it is more technically constraining for dye-filter-camera matching and sensitivity.

In the literature, studies using RGB cameras are less common, and they present various and specific technical challenges. A common one is the wavelength compatibility between the dye emission and the camera spectral response (i.e., the sensitivity to specific wavelengths). As in Figure 1.57, the RGB channels have a peak of sensitivity and overlap, therefore they cannot be considered a perfect filter. Moreover, it is not possible to use a specific filter for each camera channel.

Examples of simultaneous measurement of temperature and scalar concentration in submerged water jets with RGB cameras are found in *Ren et al.* 2020, who provided a demonstration using 2-colour 2-dye LIF , and in *Lavieille et al.* 2004, who developed a method based on three channels, thus 3-colour 1-dye LIF.

As a matter of fact, the literature lacks simultaneous measurements of temperature and thickness of a free-surface oil jet with 2-colour 2-dye LIF and detection with a RGB camera. This imaging method needs to be explored because of two advantages for a potential application on real end-windings: compactness of the optical bench and simultaneous characterisation of temperature and thickness.

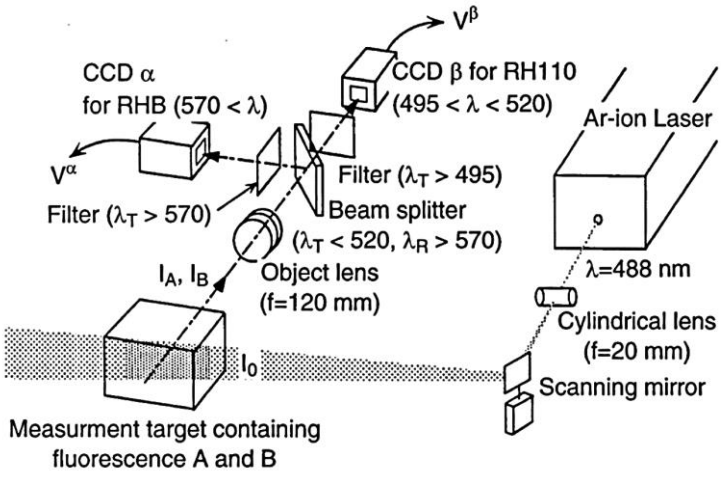

Figure 1.56 – Typical experimental apparatus for 2-colour LIF (*Sakakibara* and *Adrian*, 1999).

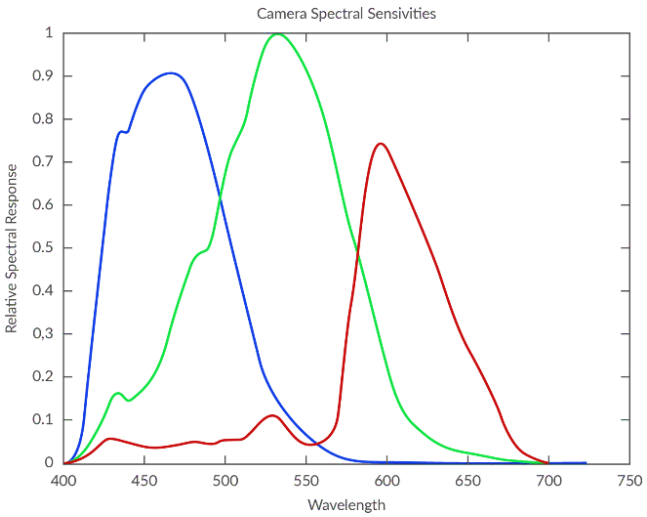

Figure 1.57 – Example of spectral response of a RGB camera.

1.4 Chapter conclusions and thesis outline

- **Industrial driver**

Hybrid and full electric vehicles are now a non-negligible part of the road automotive market, and their sales are growing. The R&D sectors of the automotive industry are undergoing radical conversion along three main axes: electric motor, power electronic and storage. The present research belongs to the first axis.

The electric motor is a century-old technology but only in recent times it is being consistently implemented for propelling road vehicles. The strict requirements for traction lead to the development of motors with high power density, high torque density and reduced bulk. This is challenging for the electro-mechanical design of the motor as well as for the thermal design. When the motor is running, due to intrinsic power losses of the electromagnetically active components, the temperature of the motor increases. Prolonged exposure to excessive temperature causes performance reduction and risk of failure. The stator end-windings are a very critical element because of the high risk of hotspot formation in the electric insulation, because of the relatively low thermal resistance and overall bad cooling. Better cooling systems are hence a necessity for the correct operation of the motor.

Innovative cooling systems are becoming more component-targeted and integrated in the motor architecture. Specific to the end-windings, dielectric oil injection is of interest because of the evidence of high heat dissipation rate, mitigation of the surface temperature and overall extension of the motor performance range. The modelling of the injection is complex in reason of the multi-physical interactions, resulting in difficulty with designing the cooling systems. Additionally, experimental characterisations are undertaken on real motors and are difficult to generalise.

The main difficulties are encountered with: (i) the thermo-mechanical air-liquid-solid interactions over the complicated geometry of the end-windings, (ii) the poor thermal characterisation of the end-windings, (iii) the thermal physics of high-Prandtl fluids such as oils, (iv) the lack of characteristic values of heat transfer, (v) the need to develop methods and diagnostic techniques which are applicable in an industrial context.

- **State of art**

There are numerous injection techniques, and in the present research the free-surface axisymmetric jet impingement is investigated. The bibliographic review presented in this chapter points out that the restrained number of studies addressing heat transfer with high-Prandtl fluids. This implies lack of estimates of the local convective coefficient, within a representative thermal range, fluid type and injection flow, likely to be found in electric powertrains.

The literature on high-Prandtl focuses on the Nusselt correlations of the impingement point. The overall trend in the correlation between the dimensionless numbers Nusselt, Reynolds and Prandtl, is known. Despite that, more investigation is needed because of the discrepancies between authors, and to propose additional parameters for improved and effective correlations. In general, it is important to extend the correlations to more fluid types and flow regimes pertinent to electric powertrains.

The typical experimental characterisation in the literature is often limited to a fundamental characterisation with model experiments. On one side, this is important for direct comparison, however the methods are hardly reusable on real case studies. Recurrent solid target types are thin plates/disks and elongated cylinders, because they consent advantageous technical solutions for developing diagnostic systems and because they allow

simplification of heat transfer. More specifically, thin plates/disks allow to assume the temperature of the unwetted side as the one of the actual solid-liquid interface, and to consider a uniform heat flux. In elongated cylinders, evaluations and measurements are usually restrained to the impingement point, along the main cylinder axis. Consequently, for generic jet impingement with thermally thick targets and high-Prandtl fluids, difficulty is met when characterising the steep temperature gradients (in both in the fluid and the liquid) within the narrow region around the impingement point. Moreover, no simplification is possible for evaluating the heat transfer with generic thermally thick targets.

Various diagnostic techniques are examined in this chapter to address such problems. Concerning temperature diagnostic in solid, it is hard to measure the actual solid-liquid interface from the wetted side because of the presence of the liquid. In the review, few optical methods are found for the wetted side, whereas thermocouples are considered reliable and precise probes but are embedded or positioned on the unwetted side. Concerning heat flux, the dimension of the probe could be a limiting factor for the spatial resolution of the measurement. Concerning the fluid, optical diagnostics are undoubtedly preferred, in reason of the non-intrusive nature of the measurements. In this research, laser induced fluorescence LIF is considered because of its versatility.

The literature on LIF is extensive for simultaneous measurements of different variables, but the literature specific to temperature and thickness measurements of free-jet impingement with high-Prandtl fluids is scarce. Similar configurations are found, that is, temperature measurement for submerged water jets, temperature and thickness measurements for water-glycerol free-falling liquid films, temperature and thickness measurements for lubricant oil tribology.

Many of the diagnostic techniques in the literature are difficult to apply to real case studies. Model experiments offer simplification of the geometry and optical access, whereas they hardly consider the constraints in industrial applications. Consequently, the 2-colour 2-dyes LIF with RGB camera detection is an interesting topic of investigation, for the sake of compactness and versatility of the diagnostic system.

- **Scope of the present research**

This research deeper investigates free-surface jet impingement cooling with high-Prandtl fluids, for generic thermally thick targets, with injections of lubricant oil for electric mobility, within the maximum thermal range of the electric insulation of the end-windings (approximately 150-180 °C).

This research also aims to develop diagnostic systems with a compact design and possibly with access from the oil-wetted surface of the target. The deliverable objectives of this research are: (i) an experimental apparatus, (ii) an experimental method, (iii) and a database.

The experimental apparatus (i) needs to replicate an oil injection on a heated solid surface, to reproduce the thermal range of interest, to finely regulate and monitor the parameters of the injection and heating, and to provide different types of diagnostic systems for the liquid and the solid.

The experimental method (ii) aims to provide a fundamental characterisation of the convective heat transfer. The method is developed to evaluate all the key parameters of the solid and the liquid listed in section 1.4.1, via pointwise and wide field measurements, with diagnostic system which can be potentially used on real motors.

The database (iii) includes the local distribution of the convective coefficient and the Nusselt correlations for variable Reynolds and Prandtl range. Such database is and will be

used for implementing numerical models, sizing cooling systems and other engineering purposes.

- **Thesis outline**

The manuscript is organised in five chapters. Beside chapter 1, providing the context and the state of art, the other four chapters describe the experimental apparatus and the most important findings. A brief overview of the contents is reported below:

[2] Methods and materials

An experimental apparatus is built to replicate a cooling oil injection on a heated plate. The apparatus is made of an oil circuit, an instrumented plate and an electric heater. The geometric complexity of the end-windings is not replicated. Instead, a heater is used to mimic the heat produced by the windings, and a mineral oil base (i.e., a lubricant without additives) is used as working fluid. The plate is a thick aluminium slab with embedded thermocouples, positioned the close as possible to the solid-liquid interface. The heat flux is evaluated from a finite element model (FEM) simulation, using experimental temperatures as boundary conditions. For the temperature and thickness of the liquid jet (after impingement), various probe and optical diagnostic methods are implemented, including LIF. Concerning this last, the technique used is 2-colour 2-dye LIF with RGB camera detection and flood illumination from above the plate.

[3] Thermal characterisation of the plate

This chapter describes the temperature measurements of the solid target and the heat flux evaluation. The injection and heating parameters are also characterised. This chapter includes the establishment of the experimental protocol, the analysis of the uncertainties, the validation of the simulations, and a parametric study for different injection/heating.

[4] Characterisation of the liquid

This chapter describes the temperature and thickness measurements of the liquid after impingement on the plate. Pointwise measurements are taken with probes and optical methods. Wide field measurements are taken with LIF imaging. More specifically, the different phases of development of the LIF-based optical method are described, including the spectroscopic analysis for dye selection, the imaging method, the uncertainty analysis, and measurements for various injection and heating parameters.

[5] Convective heat transfer of an impinging jet

This chapter collects the measurements of the previous two chapters to evaluate the convective coefficient and to deduce Nusselt correlations, for various injection and heating. An analysis of the uncertainty is also included.

2 METHODS AND MATERIALS

- **Chapter introduction**

In this chapter, the experimental methods and materials used in this research are described. The first section is an overview of the formulations and the experimental apparatus for studying conjugated heat transfer between a cooling oil injection and a heated flat plate. The second and third describes the methods, diagnostics, protocols and data processing for characterising the solid plate and the oil jet, respectively.

2.1 Experimental apparatus for conjugated heat transfer

2.1.1 Formulations

- **Convection coefficient and assumptions**

A steady state oil injection on a plate is considered as in Figure 2.1. The local convective heat transfer coefficient is evaluated with Newton's law, combining parameters issued from experiments and simulations (see section 1.3.2). The formulation used in this research is:

$$h = \frac{q}{T_{surf} - T_{oil}} \qquad (10)$$

where T_{surf} is the surface temperature (referring to the solid-liquid interface), T_{oil} is the oil temperature, and q is the plate-normal heat flux at the solid-liquid interface. The temperatures T_{surf} is measured by plate-embedded thermocouples, whose sensitive elements are placed as close as possible to the solid-liquid interface. The oil temperature T_{oil} is measured before the injection and after impingement, employing various measurement techniques. When referring to the injection $T_{oil} = T_{inj}$. The heat flux q at the solid-liquid interface is determined numerically, using a finite element method (FEM) to simulate conductive heat transfer within the plate.

Equation (10) requires the following assumptions: (i) the effects of viscous dissipation are considered negligible, and (ii) phase-change or radiative heat transfer are negligible. As introduced in chapter 1 (see section 1.3.2), the adiabatic wall temperature T_{aw} could be used (instead of T_{oil}) to account of the effects of viscosity. For this reason, assumption (i) is verified (a posteriori) to determine the error made by adopting one temperature instead of another for the evaluation of the convective coefficient. The difference $T_{aw} - T_{oil}$ is calculated using the experimental T_{oil} and deducing the adiabatic wall temperature indirectly (as $T_{aw} = 0.5rU^2/C_p$). Given the range of injection velocity and oil heat capacity, with typical recovery factors taken from the literature (i.e., $5 < r < 25$ from *Ma et al.*, 1997a), it is evaluated that $T_{aw} - T_{inj} < 0.3$ °C for the vast majority of the experiments ($T_{aw} - T_{inj} = 0.8$ °C is the maximum ever calculated). These estimates are similar to the uncertainty of the temperature measurement in this research (presented later in this manuscript). Assumption (ii) is justified by the fact that experiments are carried out below the smoke point of the oil, and that the net radiative power released by the heated plate to the laboratory does not exceed 1 W (assuming the plate and the laboratory as blackbodies with unit emissivity). In comparison, the typical electric power for heating the plate is three orders of magnitude greater (as shown in the results).

The oil temperature evolves simultaneously along the plate-normal direction (z axis) and the jet-radial direction (x axis). Further assumptions are therefore needed for the oil temperature, depending on the approach. Two possible approaches are examined in this research. The first is the "adiabatic fluid" approach: the oil temperature T_{oil} is measured at the nozzle (by a circuit-embedded thermocouple) and is assumed uniform everywhere within the liquid. This is reasonable and common practice for generic problems of conjugated heat transfer, with a sufficiently large flowrate. The second is the "non-adiabatic fluid": T_{oil} is measured after impingement on the plate (with optical and non-optical techniques) and the local value is used, assuming that this last corresponds to the unperturbed fluid temperature T_∞.

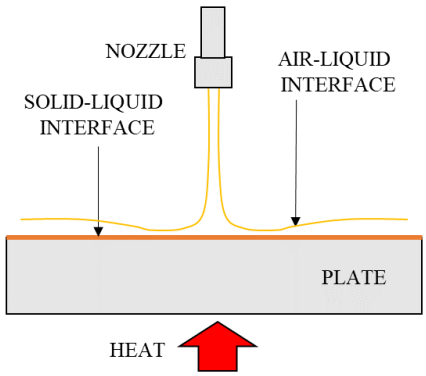

Figure 2.1 – 2D scheme of the injection.

- **Dimensionless numbers**

Once the convective coefficient h is determined, the Nusselt number is calculated as:

$$Nu = \frac{hd}{k} \tag{11}$$

Where d is the nozzle diameter and k the thermal conductivity of the oil. The dimensionless numbers Reynolds and Prandtl of the injection are evaluated at the nozzle with the following formulations:

$$Re = \frac{\rho U d}{\mu} \tag{12}$$

$$Pr = \frac{\mu C_P}{k} \tag{13}$$

Where ρ is the oil density, μ is the oil dynamic viscosity, C_P is the oil heat capacity, and U the bulk velocity. The fluid properties are deduced exclusively from the measurement of T_{inj} at the nozzle. The bulk velocity is determined from the flowrate and the nozzle diameter.

2.1.2 Overview of the experimental apparatus

- **Main components and functionalities**

Figure 2.2 is a schematic illustration of the oil injection over the heated plate, where the characteristic elements of the impinging jet are reported, as well as the nozzle, the plate and the heater. As shown in Figure 2.3, the nozzle injects over the centre the plate, which

is also considered as the centre of the *x*-*y*-*z* coordinate system. Since the jet is axisymmetric, in this manuscript the *x* axis also refers to the jet-radial radial direction, and the *y* axis is not considered.

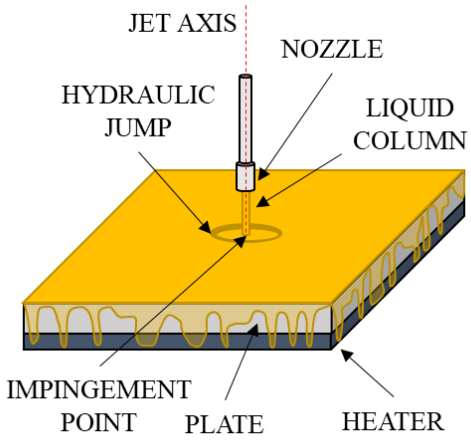

Figure 2.2– Essential scheme of the impinging jet on the plate.

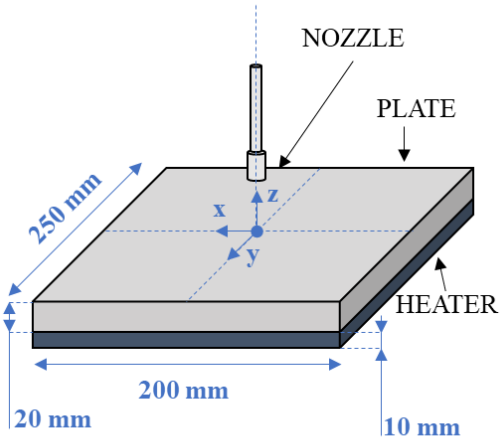

Figure 2.3 – Plate, heater and nozzle. The coordinate system is centred on the geometric centre of the upper surface of the plate.

Figure 2.4, shows the whole experimental apparatus where the three fundamental elements are highlighted: the oil circuit (in blue), the plate (in black) and the electric heater (in red). The oil circuit allows fine manual regulation of the injection pressure and temperature via several valves (i.e., V1 and V2) and a thermal bath for the injection temperature (in green). Several sensors installed before the nozzle measure and monitor the injection pressure, temperature and flowrate.

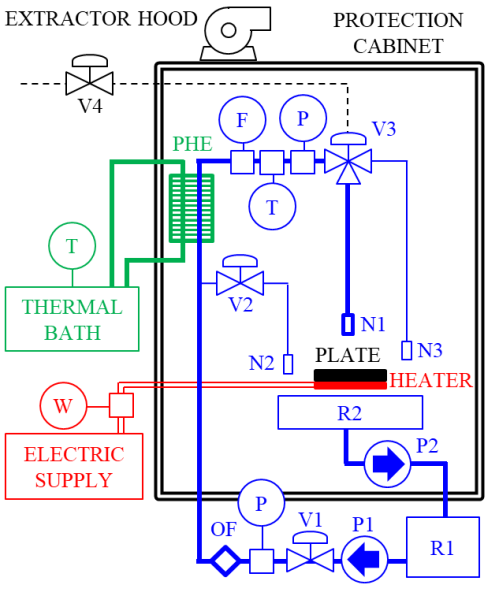

Figure 2.4 – Experimental bench with impinging jet over plate. (V1 and V2) regulation valves, (V3) three-way valve for redirecting the injection, (V4) on-off valve for activating V3 with compressed air, (N1) main nozzle, (N2) secondary nozzle for regulation, (N3) nozzle for redirected injection, (P1 and P2) pumps, (R1 and R2) reservoirs, (OF) oil filter, (PHE) plate heat exchanger, (T) temperature sensor, (P) pressure sensor, (F) flowmeter, (W) wattmeter.

Figure 2.5 – Upper surface of the heater. The electrical resistance is installed inside the carved canal.

The fluid is a generic mineral oil base (whose formulation is specific for electric mobility) without additives, whose rheological and thermal properties depend exclusively on temperature. The properties are known but cannot be reported in this manuscript for confidentiality issues. The nozzle is mounted onto a movable stage, which enables fine repositioning of the nozzle in any *x*-*y*-*z* direction (precision 1 µm). The nozzles are custom made (see annexe to chapter 2), have a round orifice and have two diameters d = 1-2 mm.

The plate is a slab (25 cm x 20 cm x 2 cm) made of aluminium alloy AU4G-2017A and positioned over an electric heater. The heater is a steel slab (25 cm x 20 cm x 1 cm), whose upper surface is shape (Figure 2.5) such that a resistive coil can be inserted. The electric power P_e injected in the coil has a power regulator, and a wattmeter. The maximum output is 1.7 kW.

- **Technical limits**

For all the experiments presented in this research, the nozzle-to-plate distance is fixed to z/d = 10. This ratio is chosen empirically, to prevent interaction between the hydraulic jump and the nozzle. When the nozzle is close to the plate, the liquid may touch the nozzle. This usually happens when the hydraulic jump is formed close to the impingement point, at low injection temperature or pressure.

A steady-state condition is achieved when the injection temperature, injection pressure and plate temperature are constant. This is technically possible with $T_{inj} > 60$ °C and $P_e > 0.8$ kW. The injection pressure P_{inj} is regulated to have the widest range, without splattering or flow instabilities.

The maximum heating power is fixed to $P_e = 1.5$ kW (not to compromise the integrity of the electric coil), the maximum $T_{inj} = 90$ °C (to limit localised smoke formation, especially on the hot corners of the plate), and the maximum $P_{inj} = 30$ kPa (defined by the resistance of oil filter in the circuit).

Concerning the jet symmetry, the higher the injection temperature, pressure and heating power, the more the jet is unstable (pulsating), the more the hydraulic jump is not round, and the more frequently splattering occurs. This occurs at high injection temperature/pressure. In this research, those conditions are avoided, even though few of them are investigated anyway.

- **Data acquisition**

All the signals from sensors and controllers are conveyed to a programmable unit. In this way, the bench operator can record data and operate and regulate automatic devices. The user interface for monitoring and data storage programmed in a software named MORPHEE. The recording frequency is set to 1 Hz, and at the end of the measurement an Excel table is issued with the measured values of every sensor per second.

The diagnostic system of the oil circuit and heater includes the following sensors: a pressure gage (PR-33 X Ei, *Keller GmbH*), a flowmeter (Oval gear OM-006 *Flomec*), a circuit-embedded thermocouple (T type, insulated hot junction, shielded, Ø = 1 mm, *Italcoppie Sensori S.r.l.*), and a wattmeter (CPL35, *Loreme SAS*).

- **Stabilisation and measurements**

The bench operator can change the nozzle, regulate the injection temperature through the regulation of the temperature of the oil bath, open/close the circuit valves for adjusting the injection pressure and set the controller for a constant value of the electric power for

heating the plate. For a given experiment, there is a stabilisation phase and a measurement phase. The stabilisation phase starts with the oil being injected over the plate, for a given heating power and nozzle position. It ends when the desired oil temperature (at the nozzle) and oil pressure are steady state. The measurement phase can hence begin. The plate and the injection are characterised simultaneously, but in parallel with respect to the liquid (after impingement). Various diagnostic techniques are used, as explained in the rest of this chapter.

2.1.3 Method flowchart

One of the objectives of this research is obtaining the correlation between the three dimensionless numbers Reynolds, Prandtl and Nusselt (see section 1.2.3). The parameters needed to determine each of them (see equation (11), (12) and (13)) are evaluated by coupling different approaches (i.e., experiments and simulations) and exploiting data from non-optical and optical techniques. Figure 2.6 summarise the phases carried out in this research (including the main parameters issued from each of them) to determine such correlations.

The starting point is setting the injection and heating conditions. The following parameters are regulated: nozzle d, injection pressure P_{inj}, injection temperature T_{inj} and heating power P_e. The injection temperature T_{inj} at the nozzle and the velocity U (deduced from the flowrate $\dot{V}$) are necessary to evaluate the dimensionless numbers Re and Pr in equations (12) and (13).

Subsequently, the plate and the oil are characterised in parallel. The surface temperature T_{surf} and the heat flux q are obtained from the plate characterisation (presented and discussed in chapter 3). The injection and heating parameters are measured while characterising the plate, so that the Reynolds and Prandtl number can be evaluated at the nozzle (therefore they are presented in chapter 3 as well). The local oil temperature (after impingement) T_{oil} is obtained from the liquid characterisation (presented and discussed in chapter 4).

After the two characterisations, the convective coefficient h is calculated with equation (10), and the Nusselt number with equation (11). The Nusselt correlations with the Reynolds and Prandtl number are hence determined. These results are in chapter 5.

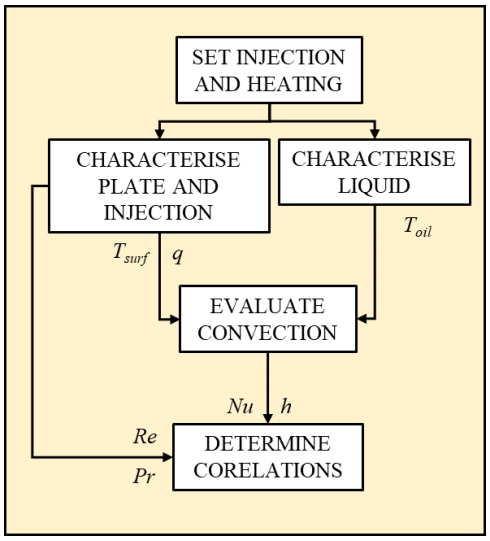

Figure 2.6 – Method flowchart for characterising heat transfer between an impinging jet and a heated plate. The key parameters determined from each phase are highlighted. The injection and heating parameters are determined while characterising the plate.

2.2 Thermal characterisation of the plate

2.2.1 Diagnostic system for temperature measurements

- **Positioning and components**

The temperature diagnostic system is made of several elements: seven thermocouples (T type, insulated hot junction, shielded, Ø = 1 mm, *Italcoppie Sensori S.r.l.*), a gateway module (QuantumX CX27C, *Hottinger Baldwin Messtechnik GmbH*) and an amplifier (MX1609KB-R, *Hottinger Baldwin Messtechnik GmbH*). The diagnostic system is calibrated to 0.1 °C with a calibration furnace.

Embedded thermocouples are used for measuring the plate temperature. Figure 2.7 shows a scheme of the placement of the thermocouples: five surface thermocouples (TC3, TC4, TC5, TC6 and TC7) are used to measure T_{surf} while two internal thermocouples (TC1 and TC2) a with are used to measure the internal temperature of the plate T_{int} at different depth from the upper surface. The tip of the surface thermocouples is positioned as close as possible to the upper surface of the plate, in order to take accurate measurements at the solid-liquid interface. Note that the tip of the thermocouple TC3 corresponds to the geometric centre of the upper surface of the plate.

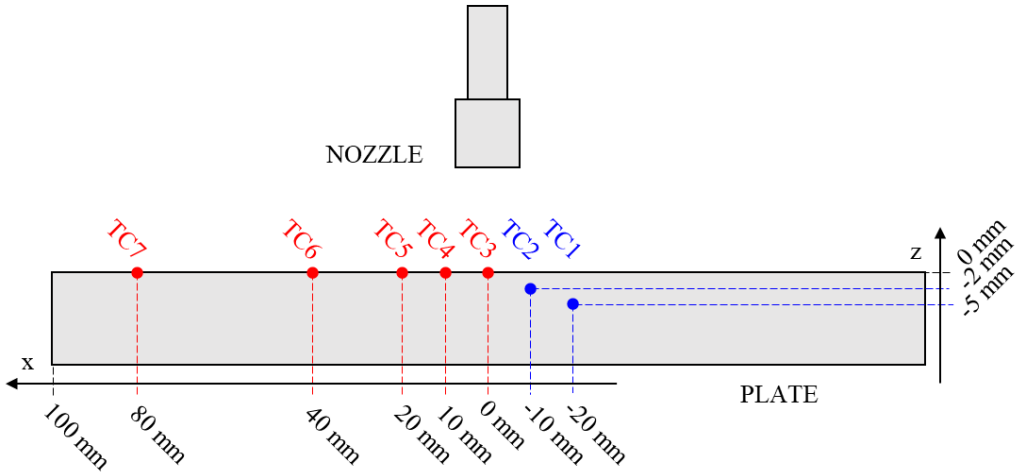

Figure 2.7 – Position of the plate-embedded thermocouples.

- **Protocol for thermocouple embedding**

The plate thermocouples are inserted from the bottom through dedicated canals. The tip of the thermocouples is round and the hollow space between the thermocouple and the plate is filled with solidifying aluminium paste (Figure 2.8). The protocol includes several phases, shown in Figure 2.9: (A) the thermocouple is inserted from below the plate until the tip comes out from above, (B) using a smooth object, the thermocouple tip is pushed back in the hole, (C) aluminium paste is applied to fill the hollow space, (D after hardening, the excess paste is taken off with sandpaper.

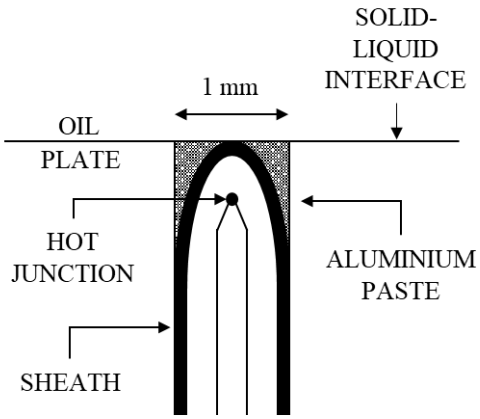

Figure 2.8 – Scheme of the tip of a surface thermocouple embedded in the plate.

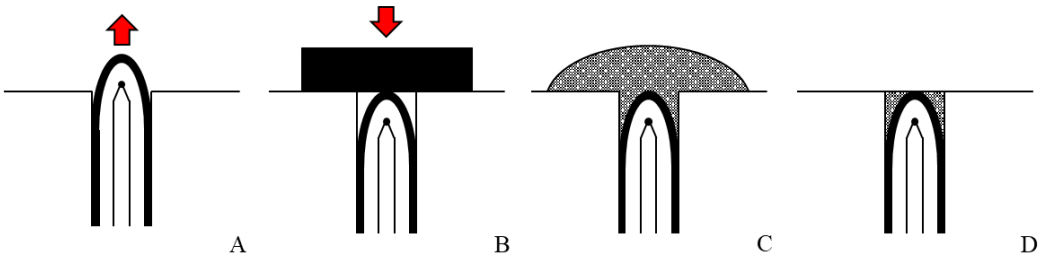

Figure 2.9 – Protocol for positioning a surface thermocouple in the plate. (A) Insert the thermocouple from the below the plate and push until the tip comes out. (B) Use a flat object to push the tip back. (C) Apply the aluminium paste and let dry until solid. (D) Remove the excess aluminium paste.

2.2.2 Numerical model for heat flux evaluation

The plate is represented by a 3D FEM model, with the aim to reproduce the internal temperature distribution of the plate. Then, the heat flux can be evaluated at the solid-liquid interface. The software used for creating the model and solving the heat transfer problem is CONVERGE CFD (Version 3.0, *Convergent Science Inc.*). Within the plate, only conductive heat transfer is considered, a natural air convection boundary is set on the sides, and convective heat transfer is considered with the liquid jet.

- **Assumptions**

The assumptions of the model are: (i) all the measured electric power is converted into heat and transferred entirely to the plate, (ii) the heat flux from the upper surface of the heater to the bottom surface of the plate is homogeneous and perfectly normal to the contact surface between the heater and the plate, (iii) the plate properties are constant and uniform. Assumption (i) is reasonable for various reasons. First, the electrical resistance of the resistive coil is much higher than that of the wires connecting the coil from the electric supply, thus losses along the connections are negligible. Moreover, the heat transfer due to the oil injection is expected to be much larger than the heat transfer due to natural convection and the heat transfer along thermal bridges (e.g., mechanical supports). Assumption (ii) may be inaccurate close to the plate-heater interface, but not close to the liquid-plate, thanks to the large thickness of the plate and the high conductivity of aluminium. For assumption (iii), the plate properties are assumed homogeneous, including the where the thermocouples are located.

- **Mesh, inputs and outputs**

The model plate has the same dimensions of the physical plate. A regular hexahedral mesh is used and nested cylindrical boxes for mesh refinement are applied, whose cell size Δx_n becomes smaller the closer to the centre of the upper surface, as in Figure 2.10.

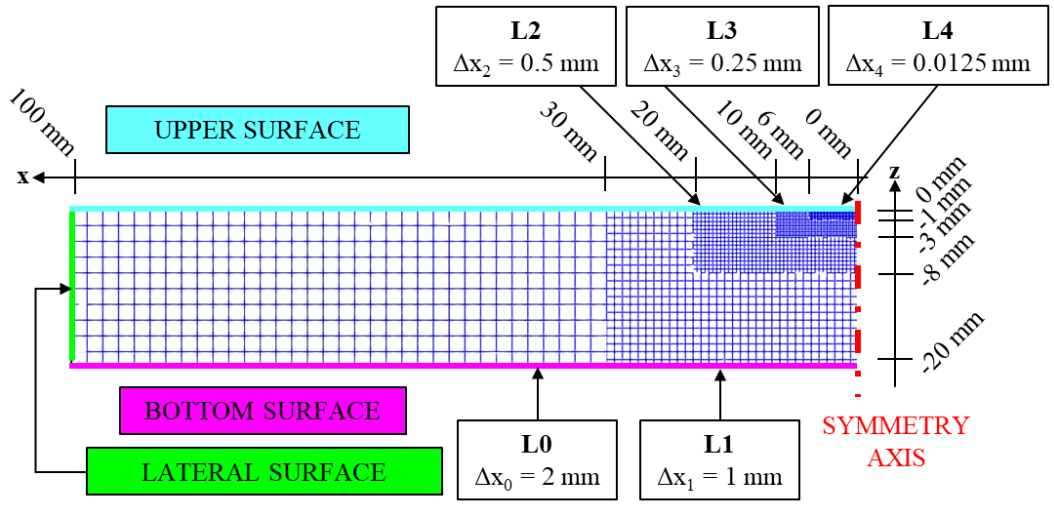

Figure 2.10 – Half-section of plate in the FEM model. The upper, bottom and lateral surface are the boundaries. Δx_n is the cell size. L0 is the base mesh while L1 to L4 are the refinement boxes. L5 is not illustrated (Δx_n = 0.0625 mm, x = 1 mm, z = 0.6 mm).

The boundary conditions are taken from the experiments and then set at the upper surface, the bottom surface, and the lateral surface. On the lateral surface, a natural air convection condition is set, by assuming the convective coefficient of air at the laboratory temperature. On the bottom surface, a uniform heat flux q_{in} is set, given by the ratio of the electric power (P_e) and the surface (S = 25 cm x 20 cm), as in:

$$q_{in} = \frac{P_e}{S} \qquad (14)$$

On the upper surface, the experimental T_{surf} is set in the form of a temperature map $T(x,y)$. This requires three steps to adjust measurements from thermocouples to the mesh: (i) sorting of the experimental data, (ii) conversion into a temperature map, (iii) map adaptation to mesh. More technical details and explanations of the limits of the process are reported in annexe to chapter 2.

The output of the FEM model is the internal temperature distribution of the plate. The internal plate temperature calculated by the simulations is compared by the internal temperature from the experiments, by extracting the temperature of the cell at the same z of the thermocouples. After validation, the heat flux at the solid-liquid interface is computed for every cell of the boundary surface:

$$q = 2\frac{k_{plate}}{\Delta x}(T_{cc} - T_b) \qquad (15)$$

Where Δx_n is the cell size, T_{cc} the temperature at the cell-centre and T_b the boundary temperature (Figure 2.11). At the end of the simulation, ParaView (Version 5.9.1, open-

source program developed by *Sandia National Laboratories*, *Kitware Inc.* and *Los Alamos National Laboratory*) is used to extract the cell data of temperature and heat flux.

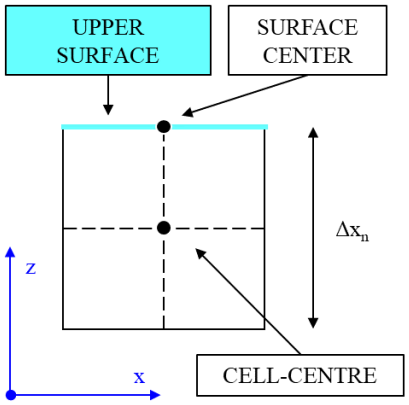

Figure 2.11 – Detail of a cell sharing its upper surface with the model boundary surface.

2.2.3 Experimental protocol for measuring temperature and processing data

The nozzle is moved along the *x-y-z* axis while injecting oil, so that the jet position is varied, and the plate temperature (T_{surf} and T_{int}) can be measured at different locations. In such way the plate temperature along the *x* axis (for the same *y* coordinate) is measured. This is equivalent to moving the thermocouple within the plate with a fixed nozzle position.

Two experimental protocols, "A" and "B" are used. The common thread of the protocols is that there is a stabilisation phase and a measurement phase. In the stabilisation phase, the nozzle is positioned over a specific *x-y* and the injection and heating are regulated, until steady state is achieved (i.e., until the injection and heating parameters and the plate temperature are steady). Then, the measurement phase begins. In this case the nozzle is repositioned from its original position along the *x* axis. The repositioning is done manually (with micrometre precision) and at regular time intervals. The essential difference between the two is the initial nozzle position (as in Figure 2.12), hence the number of thermocouples used to measure the impingement point. For both, the assumption is that nozzle repositioning does not perturb the flow.

At the end of the measuring phase, the datafile issued from MORPHEE reports the temperature for every recording instant. The temperature is processed via MATLAB and is time-averaged for the time needed for every nozzle repositioning.

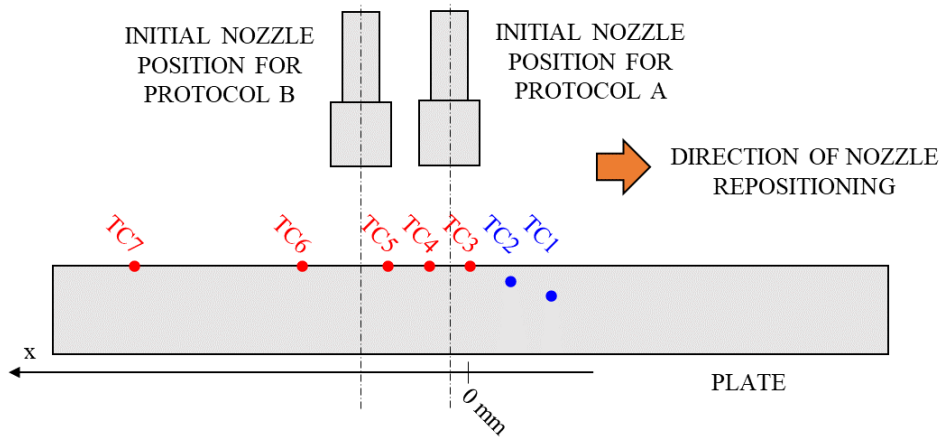

Figure 2.12 – Initial position of the nozzle for protocol A and B. The arrow indicates the direction of the repositioning in a measurement.

2.2.4 Experimental plan

During an initial phase with a more rudimental bench, the fundaments of the method are developed. The technical possibilities of the bench are explored, different approaches for evaluating heat transfer are tested, additional components are implemented, and more precise diagnostic systems are installed. The outcomes of this early phase of the study are not reported in this manuscript but can be found in *Cornacchia et al.* 2021.

In a later phase, experiments are performed to establish the measurement protocol, to evaluate the robustness of the method, and to evaluate the uncertainty of the results. Also, an extensive parametric study is undertaken varying the injection and heating parameters to evaluate the heat transfer coefficient and the Nusselt correlations. The results are reported in chapter 3 and 5.

The list of the experiments (in Table 2.1) is the combination of two nozzle diameters (d = 1-2 mm), three oil temperatures (T_{inj} = 60-75-90 °C), three injection pressures (P_{inj} = 13-17-20 kPa) and three heating power (P_e = 0.9-1.2-1.5 kW). The nozzle-to-plate distance is kept at z/d = 10 to prevent any interaction between the liquid and the nozzle.

Table 2.1 – List of the experiments performed for the evaluation of the convective coefficient.

INJECTION			HEATING
d	P_{inj}	T_{inj}	P_e
[mm]	[kPa]	[°C]	[kW]
1	20	60	0.9-1.2-1.5
		75	0.9-1.2-1.5
		90	0.9-1.2-1.5
1	17	60	0.9-1.2-1.5
		75	0.9-1.2-1.5
		90	0.9-1.2-1.5
2	13	60	0.9-1.2-1.5
		75	0.9-1.2-1.5
		90	0.9-1.2-1.5
2	17	60	0.9-1.2-1.5
		75	0.9-1.2-1.5
		90	0.9-1.2-1.5

2.3 Characterisation of the liquid

2.3.1 Pointwise measurements

- **Thickness measurements**

An optical sensor is used to measure the thickness of the liquid film (ILD1420 CL1, *Micro-Epsilon Messtechnik GmbH & Co. KG*). The working principle is based on triangulation: a laser beam hits the target surface, the diffused part of the reflected light is detected by a CMOS sensor, the detected light signal is transformed into an electrical signal, and the instrument provides an output in millimetres. The sensor is installed over the bench with the impinging jet as in Figure 2.13. The orientation and distance (with respect to the plate) are determined by the detection range of the sensor and the shading of the injector. The sensor is adjusted so that the laser beam points towards the tip of the thermocouple TC3. The manufacturer warns that laser beam should hit the target surface perpendicularly for the best measurement accuracy. Because of the presence of the nozzle the sensor must be tilted. Once the sensor position is fixed, the signal is calibrated using

solid objects with known thickness. The film thickness is measured at different distances from the jet axis (after the hydraulic jump) by moving the nozzle along the *x* axis. Five experiments are performed with this method (no repetition), as in Table 2.2.

The contact needle is the other technique used for measuring thickness, for both static films and impinging jets. A sewing needle is mounted on a movable stage allowing translation in the *z* direction with micrometre precision. The needle is lowered from above, and when a visible perturbation is induced on the air-liquid interface (Figure 2.14), the measurement is taken. The measuring protocol has four steps: (i) for setting zero thickness, the tip of the needle is first put in contact with the plate, then the needle is fastened to its mechanical support, (ii) the needle is lifted away from the liquid, (iii) the needle is lowered until a visible perturbation is induced, hence thickness is read on the micrometric screw, (iv) for the impinging jet only, a thickness profile is measured by repositioning the nozzle along the *x* axis. Various experiments are performed with this method (three repetitions for each), whose injection and heating conditions are reported in Table 2.2.With the current setup it is not possible to measure thickness when the temperature at the nozzle is T_{inj} = 90 °C and the diameter is d = 2 mm. Because of pressure fluctuations, the air-liquid interface fluctuates (in time along *z*), thus the measurements cannot be accurate.

In chapter 4, these the measurements of thickness are compared to the wide-field measurements obtained with the LIF imaging method.

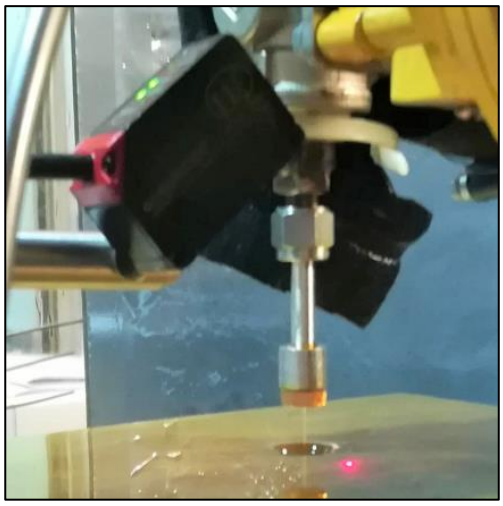

Figure 2.13 – Triangulation laser for thickness measurements of the impinging jet.

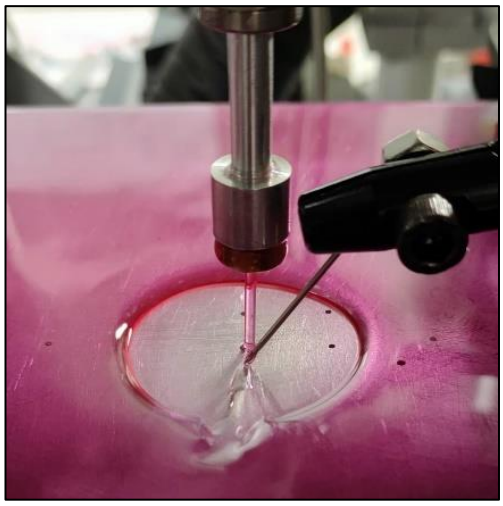

Figure 2.14 – Contact needle for thickness measurements.

Table 2.2 – Injection and heating parameters investigated for temperature measurement of the impinging jet.

TECHNIQUE	INJECTION			HEATING
	d	P_{inj}	T_{inj}	P_e
	[mm]	[kPa]	[°C]	[kW]
OPTICAL SENSOR	1	20	60	0.9
			75	0.5-0.9-1.2
			90	0.9
CONTACT NEEDLE	2	17	60	0.9-1.2-1.5
			75	1.2
	2	13	75	1.2

- **Temperature measurements**

The temperature of the film is measured along the *z* direction with a descending thermocouple and along the *x* direction using a different thermocouple.

In the first case, the thermocouple (T type, insulated hot junction, shielded, Ø = 1 mm, *Italcoppie Sensori S.r.l.*), is on a moving stage and can be moved in the *z* direction (Figure 2.15). The tip of the thermocouple is at 90 ° with respect to the direction of the flow. The protocol is similar to the one of the contact needle: (i) the tip-to-plate distance is set to zero by putting the tip of the thermocouple in contact with the plate and then it is fastened to its mechanical support, (ii) the thermocouple is lifted away from the liquid, (iii) the thermocouple is lowered progressively until the thermocouple touches the plate, and temperature is measured. Only one injection and heating conditions is performed (Table 2.3) and the experiment is repeated three times. The thermocouple is positioned over the plate-embedded thermocouple TC5, so that a measurement of the solid-liquid interface is also taken with the plate-embedded thermocouple.

In the second approach, another thermocouple (T type, welded and exposed junction 363-0266, Ø = 1 mm, *RS Group plc*), is positioned within the liquid film at four distances from the jet axis x = 10-20-40-80 mm. These positions correspond to the ones of the plate-embedded thermocouples TC4, TC5, TC6 and TC7, respectively. The tip of the thermocouple (shown in Figure 2.16). Placing the thermocouple within the liquid film without perturbing the flow is not an easy task: before the hydraulic jump, the film thickness is less than the tip of the thermocouple, while after the hydraulic jump, the film thickness is only 3-4 times larger. Two injection and heating conditions are investigated (Table 2.3), and the experiments are repeated five times.

In chapter 4, these pointwise measurements of thickness are compared to the wide-field measurements (optical method based on LIF and imaging) and to the injection temperature (measured with the circuit embedded thermocouple).

Figure 2.15 –Thermocouple for measuring the temperature of the liquid film along the plate-normal direction.

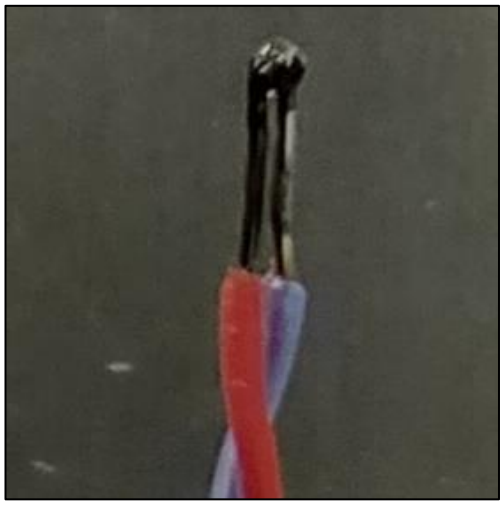

Figure 2.16 – Tip (Ø ≈ 0.9 mm) of the thermocouple used for measuring the temperature of the liquid film along the jet-radial direction.

Table 2.3 – Injection and heating parameters investigated for temperature measurement of the impinging jet.

MEASUREMENT DIRECTION	INJECTION			HEATING
	d	P_{inj}	T_{inj}	P_e
	[mm]	[kPa]	[°C]	[kW]
Along *z*	1	2	75	0.9
Along *x*	2	17	60-75	1.2

2.3.2 Field measurements with LIF

- **Overview on 2-colour 2-dye LIF with RGB camera**

In this study the technique 2-colour 2-dye laser induced fluorescence mentioned in 1.3.3 is developed for field measurements using a RGB camera. Such camera has three arrays of pixels (or "channels") for detecting light with specific wavelengths bands. As the name suggests, the channels are more sensitive to either red, green, or blue light. The advantage of using a RGB camera for 2-colour 2-dye LIF is that each channel acts as a bandpass filter and three identical images are taken at different light frequencies (or "colours").

For temperature measurements with the ratiometric approach, the RGB camera and the two fluorescent dyes are selected to fulfil the following criteria: (i) one camera channel must detect the temperature-sensitive wavelengths of the fluorescent emission of one dye, while the other channel must detect the temperature-insensitive wavelengths of the fluorescent emission of the other dye, and (ii) since the camera channels are not perfect filters, the wavelength of the fluorescent emission peak of the dyes should be as close as possible to the wavelength of the peak of sensitivity of the corresponding camera channel. For thickness measurement, since the fluorescence intensity is used directly to deduce thickness, the only criterium is that one of the dyes should be as temperature-insensitive as possible. The selection of the optimal dye and camera combination is developed in this research (in chapter 4), using two optical benches for characterising static films and impinging jets.

- **Fluorescent dyes**

Three fluorescent dyes are examined: Lumilux 345 (Lumilux Yellow CD 345, *Honeywell Speciality Chemical Seelze GmbH*), Pyrromethene 597 (CAS RN 137829-79-9, *Merck KGaA*) and Pyrromethene 650 (CAS RN 157410-23-6, *Tokyo Chemical Industry*). In this manuscript, their names are abbreviated with "LUM345", "PYR597" and "PYR650", respectively. All dyes emit in the visible spectrum.

The dyes are dissolved into the same oil used for the impinging jet. Three solutions are prepared for each dye (with concentration C = 1 mmol/L) that are diluted for obtaining smaller concentration and dye mixtures. The dyes do not dissolve directly into the oil used in this research, therefore the solvent dichloromethane (CAS RN 75-09-2, *Merck KGaA*) is used. The protocol for dissolving the dye has three steps: (i) the dye is dissolved into the dichloromethane, (ii) the oil is added to the solution with dye and dichloromethane, (iii) the solution with the three compounds is heated gently, until the dichloromethane evaporates completely. For small quantities (< 500 mL), a heated plate with a magnetic stirrer is sufficient. For larger quantities (> 500 mL), a rotatory evaporator is needed.

- **Optical bench 1**

Bench 1 is built to measure the fluorescence intensity of static films, to develop the basis of the imaging method, and to evaluate the uncertainty of the optical method. The excitation source is a blue laser (λ = 450 nm) and there are two types of optical paths. The first type is illustrated in Figure 2.17 and is made of a mechanical aperture and a negative lens. In this way, a round illumination disk is generated over the liquid film (estimated irradiance $\approx$ 100 W/m²). In the second type of optical path the mechanical aperture and the negative lens are replaced by a beam homogeniser, as in Figure 2.18. The optical components are listed in Table 2.4

The fluorescent sample is poured in either a containing plate or a step plate. The containing plate is a smooth plate, with borders to keep the liquid in place. The step plate has 10 steps, whose depth ranges between 0.2 mm and 3.8 mm. Both plates are made of aluminium and are screwed over an electric heater, whose temperature is controlled via an automatic regulator and an embedded thermocouple underneath. The upper surface of the static film can be free or contained within a thin glass slide for microscopy. In Figure 2.19 an example is given of a free-surface film within the containing plate, and in Figure 2.20 an example is given for a glass-confined film within the step plate.

The temperature of the liquid is measured by another thermocouple (T type, welded and exposed junction 363-0266, Ø = 1 mm, *RS Group plc*), with a nominal precision of 0.5 °C. The thermocouple is simply inserted within the liquid film and the temperature is displayed on a digital thermometer.

The detection system is perpendicular to the oil film and consists of a long-pass filter, a camera lens and an RGB camera. The long-pass filter has a cut-off wavelength of λ = 475 nm. In the first part of the research, a colour filter is used. This filter is eventually replaced by a high optical density dichroic filter. Two combinations of lens and camera are used. The first is a 25 mm lens and the RGB camera a2A1920-160ucPRO (*Basler AG*). The second has a 35 mm lens and a the RGB camera acA1920-50gc (*Basler AG*). Bench 1 also features a fibre spectrometer placed next to the camera.

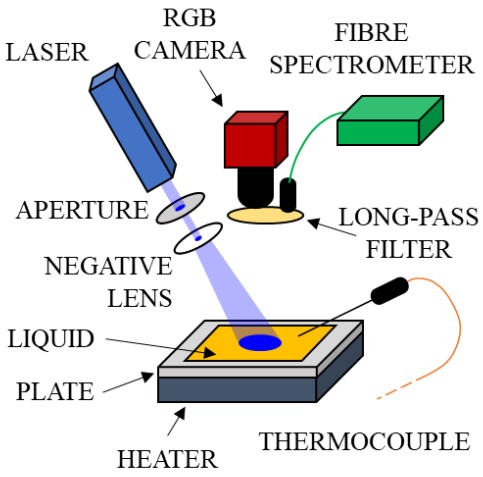

Figure 2.17 – Bench 1 for characterising a static film. Optical path with mechanical aperture and negative lens.

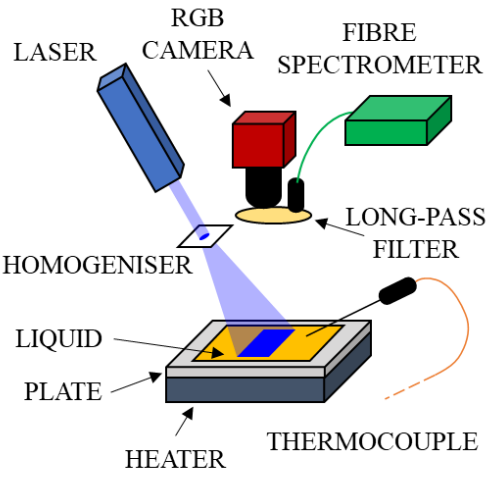

Figure 2.18 – Bench 1 for characterising a static film. Optical path with beam homogeniser.

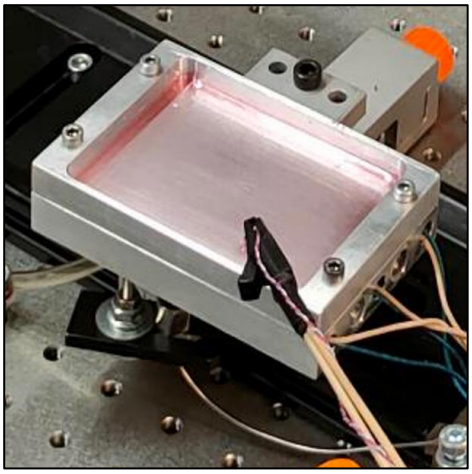

Figure 2.19 – Plate for free-surface liquid film characterisation for bench 1.

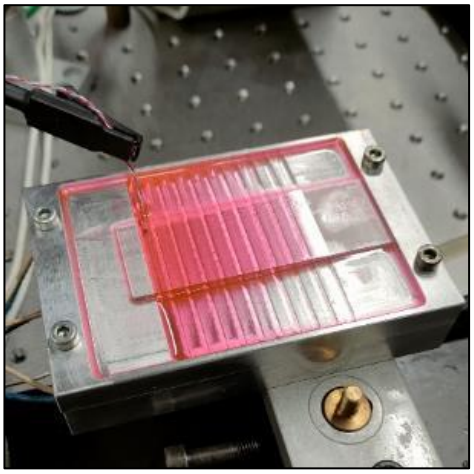

Figure 2.20 – Step plate with glass-confined liquid film for bench 1.

- **Optical bench 2**

Bench 2 is used for evaluating temperature and thickness of either a static film or an impinging jet. In the first case, a metallic frame is fixed over the plate to keep the liquid in place, as illustrated in Figure 2.21. For the impinging jet, the frame is removed, as in Figure 2.22. Concerning the static films, free-surface and glass-contained films can be characterised simultaneously, as in Figure 2.23. The thickness of the free-surface film is measured with the contact needle. The thickness of the glass-contained film is determined by the thickness of the pair of gauges block (placed between the plate and the glass slide for microscope). Eight pairs of gauges blocks are available with thickness δ = 0.1-0.19-0.51-0.71-1.04-1.55-2.94-4.1 mm. For measuring the film temperature, the plate-embedded thermocouples (TC3, TC4, TC5, TC6 and TC7) are used. The optical components are listed in Table 2.4

The camera lenses, aperture, orientation and distance from the plate are adjusted to provide the largest field of view, trying to minimise image distortion and assure that the liquid film is within the depth of field. Additionally, knowing that the nozzle-to-plate distance is fixed to z/d = 10, only the injections with the nozzle d = 2 mm are considered, as the absolute nozzle-to-plate distance is larger. The camera is not perfectly perpendicular to the plate, but it is slightly tilted (≈ 15 °). This implies that Scheimpflug condition does not apply on the entire field of view, however the final images have acceptable defocusing and perspective distortion.

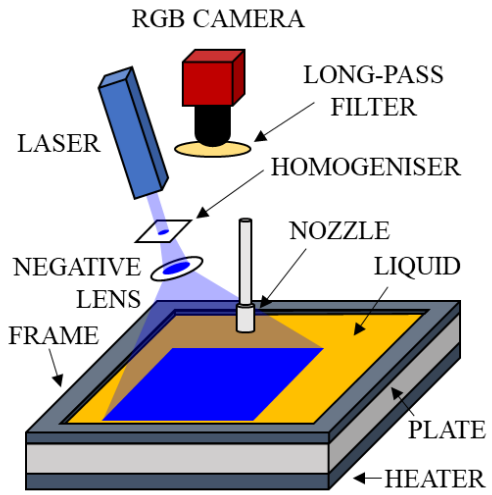

Figure 2.21 – Bench 2 for characterising a static film and for in situ calibration.

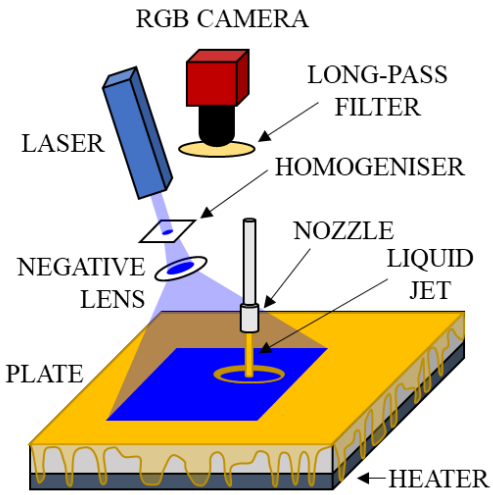

Figure 2.22 – Bench 2 for characterising an impinging jet.

Table 2.4 – Detailed list of the optical components for characterising liquid films.

COMPONENT	BENCH 1		BENCH 2
EXCITATION SOURCE	Blue laser 455 nm (3354, *Laserland Co.ltd.*)		
EXCITATION PATH	Round concave lens (Focal length -100 mm, Ø = 25.4 mm, LC1120-A, *Thorlabs Inc.*) + Mechanical aperture	Beam homogeniser (18-00244, *SUSS MicroOptics SA*)	Round concave lens (Focal length -100 mm, Ø = 25.4 mm, LC1120-A, *Thorlabs Inc.*) + Beam homogeniser (18-00244, *SUSS MicroOptics SA*)
LONG-PASSFILTER	Colour filter cut-off 475 nm (GG455, Ø = 50 mm, δ = 3 mm, *Schott AG*)		Dichroic filter cut-off 475 nm (High optical density 84-743, Ø = 2.5 mm, d = 3 mm, *Edmund Optics Inc.*)
	Dichroic filter cut-off 475 nm (High optical density 84-743, Ø = 2.5 mm, δ = 3 mm, *Edmund Optics Inc.*)		
CAMERA + LENSES	RGB camera (a2A1920-160ucPRO, *Basler AG*) + Focal length 25 mm (C125-2522-5M-P, *Basler AG*)		RGB camera (acA1920-50gc, *Basler AG*) + Focal length 50 mm (AF Nikkor, *Nikon Inc.*)
	RGB camera (acA1920-50gc, *Basler AG*) + Focal length 35 mm (LM25HC, *Kowa Optimed*)		
SPECTROMETER	Spectrometer (Flame, *Ocean Optics Inc.*)		None

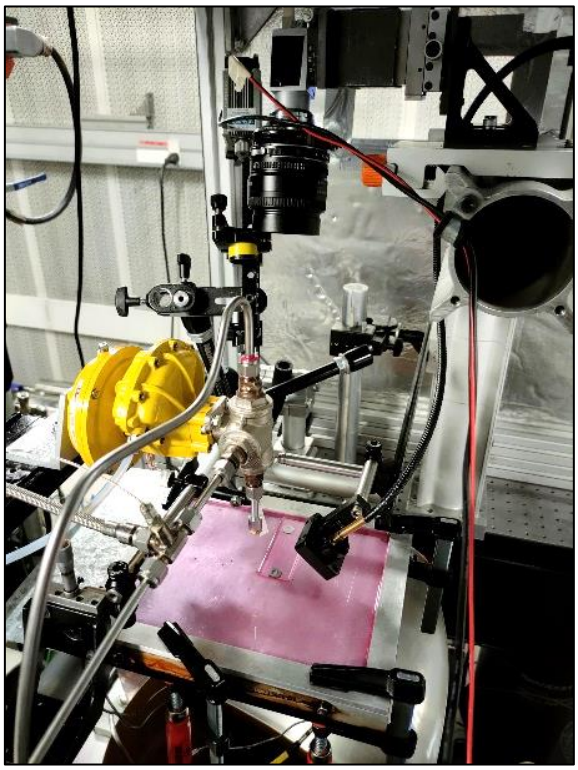

Figure 2.23 – Bench 2 for simultaneous characterisation of a free-surface and glass-confined static films.

- **Experimental protocols**

For characterising either a static liquid films, the liquid is poured over the plate, heated to the desired temperature, and then the fluorescence intensity is measured (with the spectrometer or the RGB camera). Similarly, with the impinging jet, measurements are taken when the injection and the plate temperature are steady state.

When preparing the free-surface films with bench 1, a volume of 5 mL of liquid sample is used, corresponding to a film thickness of about δ = 0.8-0.9 mm. For bench 2, the liquid is added until the desired thickness is measured by the contact needle. When preparing glass-confined films, no specific volume of liquid is used, regardless the bench.

2.3.3 Image processing with LIF

- **Camera settings and image format**

The software Pylon Viewer (Version 6.3.0, *Basler AG*) is used for controlling the camera settings. The exposure time t_{exp} is set with the aim of not saturating any of the camera channels. In the camera settings, the digitisation depth is set to 16 bits, and the pixel format is set to Bayer RG12 (to preserve the original pixel data and avoid colour reconstructing after demosaicing process).

In a single measurement, with exposure time t_{exp}, N images are saved in the Tiff format. Subsequently they are processed with MATLAB. A single image I is equivalent to a matrix with size (X_1, X_2, X_3), where X_1 and X_2 are the image size (width x hight), and X_3 identifies the camera channel. Each element of the matrix corresponds to an intensity level expressed in arbitrary units called "counts".

- **Basic image processing**

The first image treatment is background subtraction, removing the non-useful fluorescence intensity from the surrounding environment. Image averaging follows for reducing time-intensity fluctuations associated with photon noise. For each channel, every raw image I is processed as below:

$$Red = [\langle I \rangle - I_{BG}]_{Red\ channel} \quad (16)$$

$$Green = [\langle I \rangle - I_{BG}]_{Green\ channel} \quad (17)$$

$$Blue = [\langle I \rangle - I_{BG}]_{Blue\ channel} \quad (18)$$

Where the notation $\langle\,\rangle$ identifies the average of N successive raw images I, while I_{BG} is the average of N raw images $I_{background}$ of the background, as below:

$$I_{BG} = \langle I_{background} \rangle \quad (19)$$

Several backgrounds were tested, such as the bare surface of the plate, a film with pure oil or the dark images. When referring to the dark images, equation (19) becomes:

$$I_{DARK} = \langle I_{dark} \rangle \quad (20)$$

The background images are usually taken with the laboratory light switched off and the laser light on. The dark images I_{dark} are taken with both the laboratory and excitation light switched off. If the images I of the field and the background $I_{background}$ are taken with different exposure times, I_{BG} is multiplied by a factor t_{exp}/t_{exp_BG}.

- **Flat-field correction**

It is common practice in LIF measurements to correct the different intensity between contiguous pixels caused, for example, by the uneven intensity of the excitation light. This be achieved by dividing the image by a flat-field. For each channel, I_{FF} is the intensity of the flat-field calculated as:

$$I_{FF} = \langle I_{flat-field} \rangle - I_{BG} \tag{21}$$

After flat-field correction, equations (16), (17) and (18) become:

$$Red_{FF} = \left[\frac{\langle I \rangle - I_{BG}}{I_{FF}}\right]_{Red\ channel} \tag{22}$$

$$Green_{FF} = \left[\frac{\langle I \rangle - I_{BG}}{I_{FF}}\right]_{Green\ channel} \tag{23}$$

$$Blue_{FF} = \left[\frac{\langle I \rangle - I_{BG}}{I_{FF}}\right]_{Blue\ channel} \tag{24}$$

In a preliminary phase of this research, three flat-field were tested: a fluorescent panel, a post-it and a free-surface static film (Figure 2.24). Only the last is used, because the detection of the fluorescent intensity is best in all the three channels of the RGB camera.

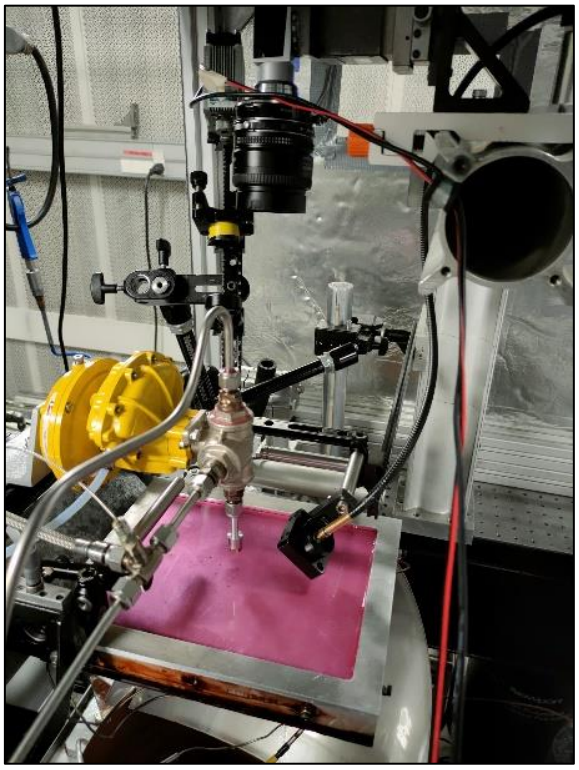

Figure 2.24 – Free-surface static film used for flat-field correction in bench 2**.**

2.3.4 Field measurements of thickness and temperature with LIF

- **Calibration and measurements**

The variation of the fluorescence intensity of the dye mixture depends on the variation of the temperature and the thickness of the oil film. In the calibration phase, measurements of the flat-field corrected channel ratio $Red_{FF}/Blue_{FF}$ and channel $Blue_{FF}$ are taken for films with known temperature T and thickness δ. For films with unknown T and δ, an algorithm is necessary to distinguish fluorescence variations attributed to temperature and to thickness by solving a 2-equation 2-variable system. In this research, the dyes are selected so that $Blue_{FF}$ depends mostly on thickness, while Red_{FF} depends on both temperature and thickness.

- **Iterative and interpolative algorithms**

Two different and independent numerical algorithms. The iterative algorithm relies on an iteration loop between the two equations below:

$$Blue_{FF} = a_1 + a_2 T + a_3 \delta + a_4 T\delta + a_5 T^2 + a_6 \delta^2 \qquad (25)$$

$$Red_{FF}/Blue_{FF} = b_1 + b_2 T + b_3 \delta + b_4 T\delta + b_5 T^2 + b_6 \delta^2 \qquad (26)$$

The equations are polynomial functions, where T and δ are the unknowns, the coefficients a and b are known (from calibration), and $Blue_{FF}$ and $Red_{FF}/Blue_{FF}$ are also known from the field measurements. The detailed scheme of the iterative algorithm is reported in annexe to chapter 2.

The interpolative algorithm is based on the MATLAB function *f = scatteredInterpolant*, and it needs two equations to determine T and δ are (individually, without the need to loop between equations):

$$T = f_1(\, Blue_{FF} \;,\; Red_{FF}/Blue_{FF}\,) \qquad (27)$$

$$\delta = f_2(\, Blue_{FF} \;,\; Red_{FF}/Blue_{FF}\,) \qquad (28)$$

The interpolative functions f_1 and f_2 calculate the values of T and δ by interpolating a grid of known values, from a common calibration dataset. The scheme of the interpolative algorithm is in annexe to chapter 2.

The calibration dataset is built with bench 2, using glass-confined static films. The film temperature is varied between 30 °C < T < 120 °C and thickness between 0.1 mm < δ < 4.1 mm. A more detailed scheme is provided in annexe to chapter 2.

2.3.5 Experimental plan

As for the thermal characterisation of the plate, this research requires numerous phases of development, which are presented in chapter 4. Concerning the wide-filed measurements with the LIF technique and the imaging method, several experiments are performed with the impinging jet. Temperature and thickness are evaluated for the injection and heating conditions reported in Table 2.5.

Table 2.5 – List of the injection and heating conditions investigated for the evaluation of the convective coefficient.

INJECTION			HEATING
d	P_{inj}	T_{inj}	P_e
[mm]	[kPa]	[°C]	[kW]
2	13	90	0.9
2	17	60 75	0.9-1.2-1.5 1.2

2.4 Chapter conclusions

This chapter describes the methods and the experimental apparatus for characterising heat transfer between a liquid injection and a solid object. The aim is not to characterise a specific end-windings geometry or oil type, but to develop an experimental method and apparatus for multi-purpose characterisation of conjugated heat transfer.

The method is developed to quantify the convective heat transfer (at the solid-liquid interface), through the convective coefficient and the correlation between the dimensionless numbers Nusselt-Reynolds-Prandtl. The method requires four phases: (i) measurement of the injection parameters and the plate temperatures, (ii) evaluation of the heat flux with a finite element model simulation, (iii) measurements of the temperature and thickness of the liquid film, and (iv) determination of the convective coefficient and correlations.

The experimental apparatus is composed of a heating system, (that replicates the heat generated in the windings), a flow system (for conditioning the oil before the injection), and moveable nozzle (to consent local measurements). Fine regulation of the injection and the heating parameters is possible, so that numerous operating points can be tested. The diagnostic system consents measurements of the fundamental parameters of the injection (temperature, pressure and flowrate), the heating power, the temperatures of the plate, the temperature of the liquid (after impingement), and the thickness of the liquid (after impingement).

The characterisation of the plate and the liquid are undertaken in parallel, and the results are presented separately in chapter 3 and 4 respectively. For both characterisations, the various phases of development are presented in the rest of the manuscript. This includes some preliminary evaluations, the protocol establishment, and the uncertainty analysis. The evaluation of the convective coefficient, Nusselt number and Nusselt correlations are presented in chapter 5.

3 CHARACTERISATION OF THE INJECTION AND THE PLATE

- **Chapter introduction**

This chapter presents the results related to the characterisation of the injection and the establishment the experimental method. The chapter is divided in three parts.

The first part is dedicated to the injection and heating parameters. The measurements are taken simultaneously with the measurements of the plate temperature, and the dimensionless parameters of the injection are evaluated.

The second part illustrates the measurements of the plate temperature, taken with plate-embedded thermocouples. First, several experiments are performed to evaluate the overall data consistency of the temperature, to evaluate the limits of protocol validity, and to familiarise with typical temperature values and variations. Successively, further experiments are needed to establish the protocol and to evaluate the overall uncertainty of the measurements. Finally, a parametric study on injection and heating condition is undertaken to investigate the mitigation effects.

The third part describes the two outcomes of the simulations, that is, the internal temperature distribution of the plate and the heat flux at the solid-liquid interface. The simulated internal temperature distribution is compared with experimental data for validating the model. An uncertainty analysis follows, to understand how the input parameters affect the estimates of the heat flux. Lastly, the heat flux is computed for the same parametric variation on the injection and heating parameters.

3.1 Injection and heating

3.1.1 Characterisation of the injection and heating parameters

- **Injection and heating**

As mentioned in section 2.1.2, the regulation of the injection parameters is manual. During the experiments, T_{inj} is regulated allowing maximum ± 0.2 °C tolerance from the targeted temperature, while maximum ± 1 kPa is allowed for P_{inj}. When applying the measuring protocol (for a specific experiment), typical standard deviation for T_{inj} is 0.1-0.2 °C, < 0.1 kPa for P_{inj}, < 0.3 % for P_e and < 0.5 % for the volume flowrate $\dot{V}$. Similar standard deviation is observed when repeating the same experiment.

The injection and heating parameters for all the experiments are reported in Table 3.1 and Table 3.2. This also include the measurement of the volume flowrate $\dot{V}$, the evaluation of the dimensionless numbers *Re* and *Pr*, the calculation of the input heat flux q_{in} and the bulk velocity *U*. Notice that largest oil density variation in the investigated T_{inj} range is not greater than 2 %, thus the volume flowrate is considered (for practical convenience) instead of the mass flowrate (despite more meaningful in fundamental terms),

In the investigated range, increasing one among T_{inj}, P_{inj} and *d* (without modifying the other two), increases the flowrate $\dot{V}$ (and the velocity). If T_{inj} increases by + 1 °C, the volume flowrate increases by approximately + 0.3-0.6 %. If P_{inj} increases of 1 kPa, the flowrate increases of + 7.1-7.5 %. If *d* doubles, the flowrate increases by + 75.2 %. As a matter of fact, *d* has the most relevant influence on flowrate on the current experimental

bench, for the given parametric variations. Concerning the heat flux q_{in}, proportionality is showed with the heating power P_e and the range covered is 17 kW/m² < q_{in} < 31 kW/m².

The results show low standard deviation while performing and when repeating the experiments, for a relatively wide range of steady injections and heating. This confirms that the experimental apparatus allows precise measurements and fine regulation of the injection and heating parameters, which are likely to be found in electric powertrains.

Table 3.1 – Injection parameters. The nozzle diameter, oil temperature and oil pressure are regulated, monitored and measured. The volume flowrate is measured. The Reynolds and Prandtl are evaluated after measurements. The values in the table are the average of three repetitions of the same experiment.

INJECTION						
d	P_{inj}	T_{inj}	$\dot{V}$	U	Re	Pr
[mm]	[kPa]	[°C]	[L/min]	[m/s]	[/]	[/]
1	20	60	0.49	10.4	520	240
		75	0.53	11.2	950	160
		90	0.55	11.7	1400	120
1	17	60	0.39	8.2	410	240
		75	0.41	8.9	670	160
		90	0.45	9.3	1120	120
2	17	60	1.61	8.4	550	240
		75	1.67	8.9	940	160
		90	1.67	8.8	1460	120
2	13	60	0.94	5.0	950	240
		75	1.06	5.5	1500	160
		90	1.16	6.1	2110	120

Table 3.2 – Heating power. The heating power is regulated, monitored and measured (max P_e = 1710 W). The input heat flux is evaluated after measurements. The values in the table are issued from three repetitions of the same experiment.

HEATING		
P_e	P_e	q_{in}
[% of max P_e]	[W]	[kW/m²]
50	855	17.1
70	1197	23.8
90	1539	30.8

- **Reynolds and Prandtl numbers**

Given the precise characterisation of the injection parameters, the dimensionless numbers are calculated according to the formulations in section 2.1.1. As in Table 3.1, any combination of d, P_{inj}, and T_{inj} leading to the augmentation of $\dot{V}$, also increases Re. Any increase of T_{inj} by + 1 °C increases Re of + 4-6 %, increasing P_{inj} by 1 kPa produces and increase of + 8-18 %, while doubling the diameter leads to an increase of + 88 %. Consequently, for the given parametric study, the Re is more sensitive to the modification of the nozzle diameter or the injection pressure, rather than to any variations of the oil properties induced by the injection temperature.

The Prandtl number depends exclusively on temperature, and any increase of T_{inj} implies the decrease of Pr, mostly because high-Prandtl fluids have large temperature variable viscosity (– 55 % decrease in viscosity from T_{inj} = 60 °C to T_{inj} = 90 °C).

The estimate of the uncertainty is < 5 % for Reynolds and < 1 % for Prandtl, during and when repeating the experiment. Coherently with the fine regulation and precise measurement of the injection parameters, also the dimensionless numbers of the injection

can be characterised. In conclusion, the Reynolds number covers the laminar and transitional regime, approximately between $520 < Re < 2100$, and the overall variation of the Prandtl number Is $120 < Pr < 240$.

3.2 Measurements of the plate temperature

3.2.1 Preliminary characterisations and method establishment

The details about the assumptions, the protocols, and the specifications of the diagnostic system, are reported in section 2.2. The investigation is undertaken for the reference experiment $d = 1$ mm, $T_{inj} = 75$ °C, $P_{inj} = 20$ kPa and $P_e = 1.2$ kW. Notice that TC3 is considered as the reference thermocouple, meaning that the nozzle position is adjusted in such a way, that the minimum temperature is always detected when the nozzle is injecting over TC3. Consequently, TC3 defines the position of the jet axis as well (more details in the uncertainty analysis).

- **Radial distribution of the plate temperature**

The raw output of the measurement is the recording of the temperature with 1 Hz frequency (see example in annexe to chapter 3). The datapoints are hence averaged by the time of the nozzle repositioning (see influence of time in annexe to chapter 3). In such a way, the temperature can be plotted as a function of the distance from the jet axis, as in Figure 3.1 and Figure 3.2. The two figures show the jet-radial variation of the plate temperature, close and far from the impingement point. Notice that for every trace of the plot, the data points on the left are measured earlier than those on the right. The datapoints are the average of three consecutive repetitions of the experiments. The error bars are not shown, but the standard deviation of the temperature is smaller than 0.1 °C for a single nozzle repositioning in a single experiment, while it is about 0.2-0.3 °C for each x/d when repeating the experiments.

In Figure 3.1, the surface temperature has a minimum at the impingement point, while the temperature increases at greater x/d. The overall trend is therefore coherent with the expectations and with the known literature (*Rahman et al.*, 1999). Fine temperature gradients are measured (with respect to the thermocouple calibration of 0.1 °C), approximately between $0.1\ °C/mm < \Delta T/\Delta x < 1\ °C/mm$. Considering the traces TC3, TC4 and TC5, the difference between the temperature measured by different thermocouples at the same x/d is relatively small (< 0.3 °C), approximately in the range $x/d > +10$ and $x/d < -10$. This occurrence shows coherence and consistency, as the different thermocouples measure the same thermal region. Such temperature difference becomes much larger the closer to the impingement point $x/d = 0$, where the largest difference is $T_{TC3} - T_{TC5} = 1.9$ °C. In this case, less consistency is shown, but this aspect is better investigated lately in the evaluation of the uncertainty. Concerning the thermocouples TC1, TC2 and TC3, the deeper the sensor, the higher the temperature, in the range $-10 < x/d < 0$, as expected from the literature. Outside of this range, the temperature difference between the traces is too small, comparable with the thermocouple precision.

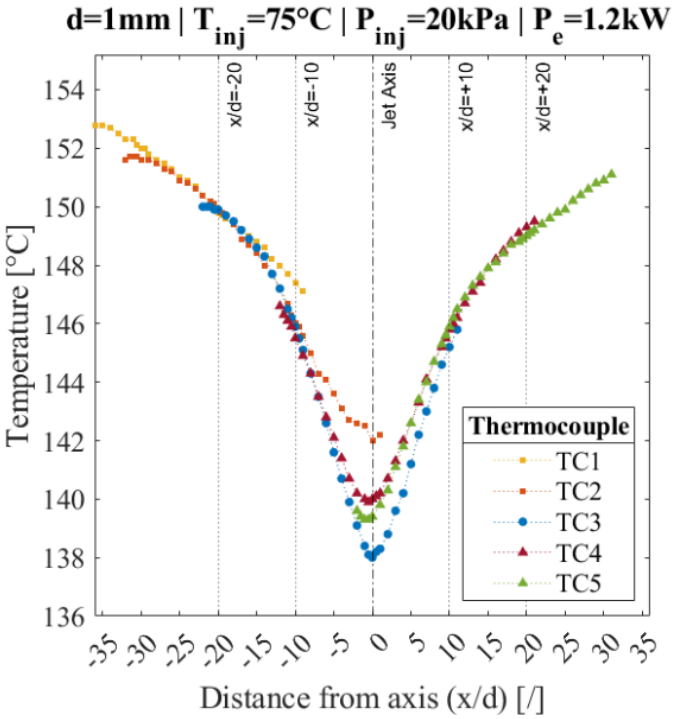

Figure 3.1 – Surface and internal temperature of the plate for the reference conditions. Protocol B is applied. TC1 and TC2 refer to the internal thermocouples. TC3, TC4 and TC5 refer to the surface thermocouples.

In Figure 3.2, the measurements by TC6 and TC7, far from the impingement point are added to the ones of Figure 3.1. Some discrepancy is observed for $x/d > 20$, because the temperature difference between the temperature measured at the same x/d by different thermocouples is larger than 1 °C. Additionally, the traces of TC6 and TC7 do not appear to reconnect around $x/d = 60$, and the temperature rises abruptly. Such occurrence is attributed to flow perturbation due to an excessive nozzle repositioning from the initial position at the beginning of the measurement. Empirical observations witness that the flow slows down at the plate edges, the farther the nozzle is repositioned from its initial position. Consequently, there is a reduction of heat transfer towards the liquid causing the plate temperature to rise.

In conclusion, the results are consistent for any x/d but the flow (thus the thermal equilibrium) is perturbed the farther the nozzle is repositioned from its initial position (the peripheral thermocouples are more affected). It follows that the method is robust in the region $-10 < x/d < +10$, which corresponds to the region of interest for studying jet impingement, because it is where largest temperature variations occur and where the impingement point is located.

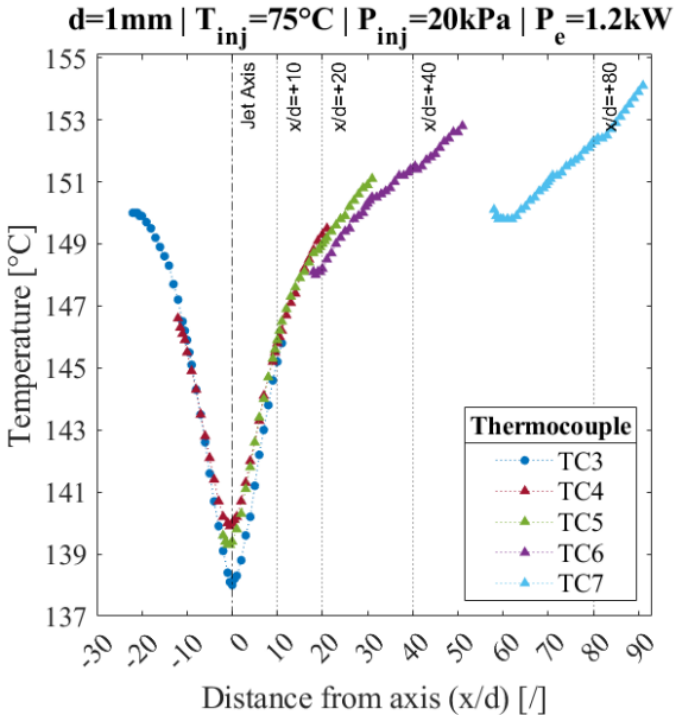

Figure 3.2 – Surface temperature of the plate for the reference experiment. Protocol B is applied. Only the measurements by the surface thermocouples are showed.

- **Compare protocols**

Protocol A and B are applied for the same reference experiment: d = 1 mm, T_{inj} = 75 °C, P_{inj} = 20 kPa and P_e = 1.5 kW. The experiments are performed once for each protocol. The two protocols yield overall resembling traces. Close to the jet axis, in range $-10 < x/d < +10$, the temperature difference on the same x/d obtained by different protocols is typically $|T_A - T_B| = 0.3$ °C (for both TC2 and TC3). Far from the impingement, in the range $x/d > +10$, this difference is 0.7 °C, 0.3 °C and 0.8 °C, for TC5, TC7 and TC6, respectively. The results illustrate that relatively small difference characterises the traces obtained with the two protocols. For both, the results exhibit consistency in the range $-10 < x/d < +10$, as well as good reproducibility of the experiment. The same discrepancies far from the impingement point (discussed in Figure 3.2 with the peripheral thermocouples TC6 and TC7) appear with protocol A as well.

Both protocols fulfil their primary purpose of measuring the plate temperature distributions, and both exhibit the same limits of validity. Nevertheless, protocol B is to prefer to protocol A, in reason of the larger reliability and exploitability of the results for different types of analysis. This conclusion is supported by the fact that multiple measurements of the same injection region with different thermocouples are useful to better monitor the experiment and to better quantify uncertainty. Thanks to protocol B, it is observed that using multiple thermocouples for measuring the same x/d, the difference is greater the closer to the impingement point. The temperature at the impingement point seems, in fact, to be affected by relevant uncertainty, because significant difference is observed depending on the thermocouple used. This finding is important and examined in the next section about the uncertainty of the temperature measurements.

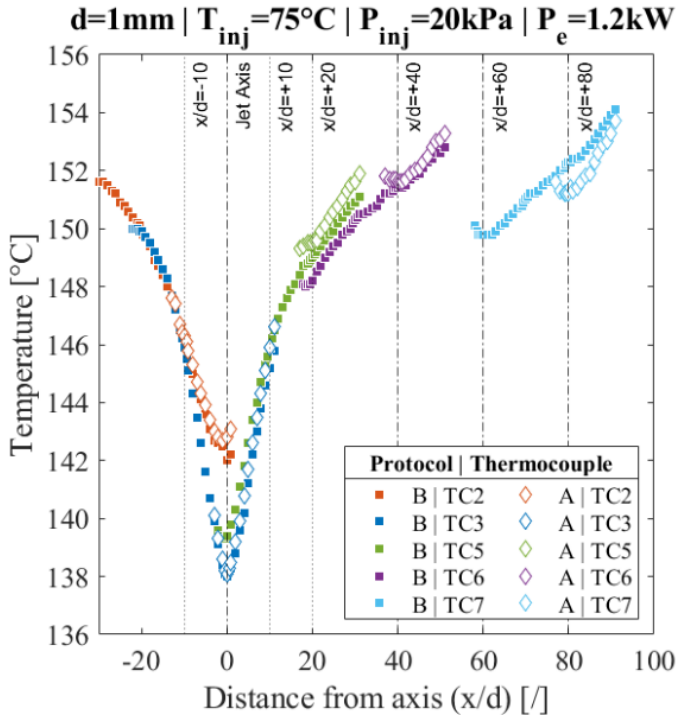

Figure 3.3 – Surface and internal temperature of the plate for the reference experiment. Protocol A and B are compared. TC2 refers to the internal thermocouple. TC3, TC5, TC6 and TC7 refer to the surface thermocouples.

- **Spatial resolution**

The spatial resolution of the measurements is investigated by diminishing the length of the nozzle replacement when the jet is approaching a thermocouple. In this experiment the shortest repositioning is $x = 0.2$ mm and protocol B is used. The results in Figure 3.4 show that finer temperature differences are measured along the x direction with a shorter repositioning length. The smallest detectable variation is 0.1 °C between two repositioning, which corresponds to the calibration of the diagnostic system.

Figure 3.4 highlights another important aspect of the measurement, that is, the fact the three thermocouples measure slightly different temperatures the closer to the impingement point. The trace TC3 has a minimum in $x = 0 \pm 0.2$ mm, because the initial nozzle position is adjusted on purpose to measure the absolute minimum temperature on $x = 0$ mm. For TC4 and TC5, the minimum temperature is measured at $x/d = 0.5 \pm 0.05$ and $x/d = 0.8 \pm 0.2$, respectively. It follows that the minimum temperature is not measured on the same x/d by the three thermocouples.

From this figure, two observations are made. The first is that even though the thermocouple diameter (i.e., Ø = 1 mm) is larger than the repositioning length, the protocol allows measurements with a finer resolution along x (about 0.2 mm). The second is that the three thermocouples measure different temperatures in the same region where they are expected to measure the same temperature. This aspect requires deeper investigation, which is presented in the uncertainty analysis. Nevertheless, the thermocouple TC3 is arbitrarily kept as the reference thermocouple for practical convenience.

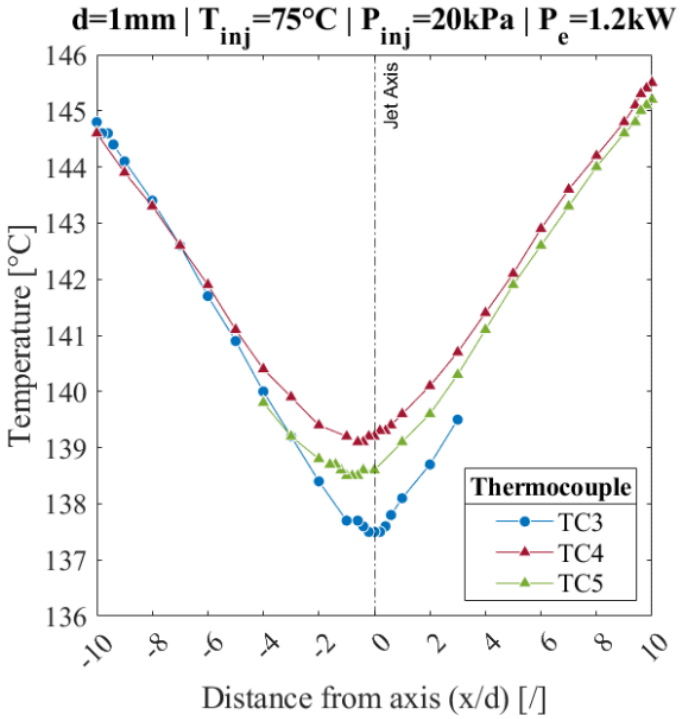

Figure 3.4 – Surface temperature of the plate for the reference experiment. Protocol B is applied with a shorter nozzle repositioning. TC3, TC4 and TC5 refer to the surface thermocouples.

3.2.2 Uncertainty analysis of temperature measurements

Uncertainty is quantified using the measurements presented in the previous section 3.2.1 for the reference experiment (i.e., d = 1 mm, T_{inj} = 75 °C, P_{inj} = 20 kPa and P_e = 1.2 kW). The analysis splits into the evaluation of precision and accuracy. The fist aims to quantify the statistical error when the nozzle is repositioned from a *x/d* to another and when the same experiment is repeated. The second aims to evaluate how far the temperature measurement is form the exact solid-liquid interface and impingement point, in terms of systematic error. Notice that the thermocouples are calibrated to 0.1 °C, meaning that this is the minimum uncertainty.

- **Precision**

The uncertainty related to the measurement precision is quantified through the experiment repeatability. More specifically, via the standard deviation of the temperature for each *x/d* measured by the same thermocouple. For the experiment showed in Figure 3.1 and Figure 3.2, two standard deviations are calculated. For a single experiment and *x/d*, the time-averaging of the temperature standard deviation is < 0.1 °C. For three repetitions of the same experiment, the standard deviation of a single *x/d* is 0.2-0.3 °C for the thermocouples TC1, TC2, TC3 and TC4, whereas it is 0.3-0.7°C for the thermocouples TC5, TC6 and TC7. In this case the standard deviations says that the measurement is more precise the closer to the impingement point.

The standard deviation of the experiment comparing the protocols in Figure 3.3 is not available. Although, the difference between measurements on the same *x/d* with different protocols is generally $|T_A - T_B|$ = 0.3 °C for TC1, TC2, TC3 and TC4, whereas it is $|T_A - T_B|$ = 0.3-0.8 °C for the thermocouples TC5, TC6 and TC7. It follows that the difference in temperature, when using a protocol or another, is similar to the precision of a single *x/d*.

In conclusion, 0.3 °C is representative of the statistical error associated with experiment repetition. More specifically, it represents the precision of a measurement performed by a single thermocouple on a single x/d, within the range of interest $-10 < x/d < +10$.

- **Accuracy**

The uncertainty related to the measurement accuracy can be quantified via the difference between the temperature measured by different thermocouples on the same x/d. The first aspect to verify is the alignment between the nozzle axis and the reference thermocouple. For the evaluation, the previously discussed Figure 3.4 is needed. As explained, the initial nozzle position (before applying the measuring protocol) is adjusted so that the absolute minimum temperature is found by TC3 at $x/d = 0$. The figure highlights that this choice is not optimal for the thermocouples TC4 and TC5, which measure different temperatures even though they are expected to measure the same ones. This occurrence suggests that there may be a slight misalignment along the y coordinate, probably due to some imperfections in the geometry of the experimental apparatus.

A verification test is performed by repeating the experiment of Figure 3.4 with a voluntary misalignment along y. The results are results are plotted in Figure 3.5. The arbitrary position $[x_0, y_0]$ along the coordinate system of the translation stage (where the nozzle is fixed) is chosen as the potential position of the actual jet axis, where the minimum temperatures is expected. Notice that $[x_0, y_0]$ is nearby the tip of TC3, but the minimum temperature is not measured exactly on it. The measurement is taken with the usual protocol B, by repositioning the nozzle along the x axis, however the y coordinate is also varied by adding or removing 1 mm to y_0.

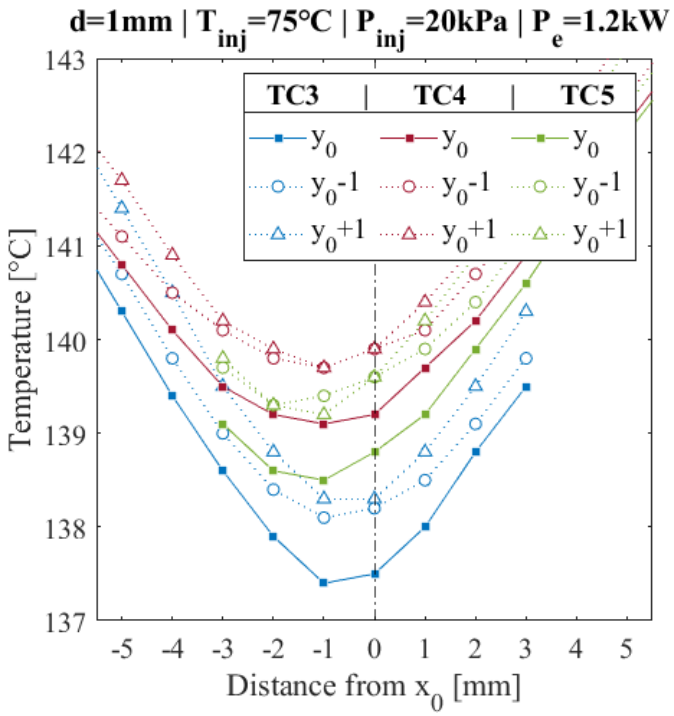

Figure 3.5 – Surface temperature of the plate for the reference experiment. Parametric study on the nozzle adjustment coordinates with respect to an arbitrary axis origin (x_0, y_0). Protocol B is applied. TC3, TC4 and TC5 refer to the surface thermocouples.

Figure 3.5 shows that the traces with $y_0 \pm 1$ are always above the one with y_0, regardless the thermocouple. This result means that the coordinate y_0 is an accurate estimate of the actual impingement point for every thermocouple. Concerning TC3, x_0 needs a slight correction (about 0.5 mm) so that the minimum temperature is measured exactly at $x/d = 0$. In other words, Figure 3.5 shows that inaccurate alignment along y leads to measure the temperature inaccurately by approximately ± 1 °C/mm. It is important to underline that this misalignment can be quantified and corrected.

Figure 3.5 also shows that each thermocouple detects the minimum temperature at different x coordinates: $-1\text{ mm} < x < 0\text{ mm}$ for TC3, $x = -1\text{ mm}$ for TC4, and $-2\text{ mm} < x < -1\text{ mm}$ for TC5. Something analogous is observed for the previous Figure 3.4. This occurrence means that despite the alignment along y can be corrected, a misalignment persists between the thermocouples TC3, TC4 and TC5, evaluated to about 0.8 mm. The origin of this error is attributed to imperfect alignment along y between the translation stage and the plate but also between the thermocouple canals themselves.

The uncertainty related to the measurement accuracy is completed by considering the positioning of the thermocouple along the z direction. Figure 3.4 shows that the minimum temperature depends essentially on the thermocouple used. In this experiment, the largest difference between measurements by different thermocouples is 1.9 °C. Two potential sources of error are hence considered. The first is attributed to manufacturing imperfections in the position of the junction between different thermocouples, while the second is probably related to inevitable inaccuracy in the embedding protocol. The first cannot be evaluated in this research. Considering the second, the inaccuracy related to the incorrect positioning along z of the hot junction with respect to the exact solid-liquid interface could be estimated. Considering that the plate temperature gradient along the jet axis is approximately $\Delta T/\Delta z \approx 2.0$ °C (calculated from Figure 3.1), and assuming a considerably large incorrect positioning of 0.1 mm from the exact solid-liquid interface, the measurement error should be approximately $\Delta T \approx 0.2$ °C. Such estimate alone is insufficient to justify the 1.9 °C of difference between the thermocouple measurements at the impingement point observed in Figure 3.1, Figure 3.4 and Figure 3.5.

Given the impracticality of repeating the experiments by re-embedding the thermocouples and changing their position, in this research TC3 is selected arbitrarily as the reference thermocouple for measuring the surface temperature. For pursuing the research, the error associated with the alignment in the z direction is assumed as 1 °C (max 2 °C) for every x/d.

- **Total uncertainty**

From this analysis, the uncertainty on the temperature measurement taken by TC3 is evaluated as the contribution of the following: 0.1 °C for the thermocouple calibration, 0.3 °C for the statistical error and 1 °C (max 2 °C) for positioning along z. Most of the uncertainty seems to be related with the positioning of the sensor. Notice that the uncertainty associated with the misalignment along y is not considered for TC3 because it can be corrected. The total uncertainty is hence 1.4 °C (max 2.4 °C).

This estimate can affect the convective coefficient in two ways. In a direct way, since the surface temperature is in the formulation of the convective coefficient. In an indirect way, as the uncertainty could propagate through the heat flux. These aspects are examined with specific uncertainty analysis of the heat flux and of the convective coefficient.

3.2.3 Cooling effectiveness and surface temperature mitigation

A parametric study is presented in this section to evaluate the cooling efficacy and uniformity. The injection and heating parameters are varied as in Table 3.1 and Table 3.2 and the surface temperature measured with TC3 is shown.

- **Same diameter, variable heating power, injection temperature and injection pressure**

In Figure 3.6, the heating power P_e is varied while keeping the same injection parameters. Increasing the heating power coherently shifts the surface temperature to a higher range. Approximately the rate of increase is + 4.5 °C increase of T_{surf} every + 100 W increase of P_e.

In Figure 3.7 the injection temperature T_{inj} is varied, while keeping the same injection pressure P_{inj} and heating power P_e. For these injections, *Re* and *Pr* vary significantly and simultaneously but with opposite trends. The flowrate $\dot{V}$ increases, reasonably in reason of the relevant decrease of viscosity at higher temperature. The overall T_{surf} profile shifts to higher temperature for increasing T_{inj}. The proportion is approximately + 1 °C increase of T_{surf} per + 3 °C increase of T_{inj}.

In Figure 3.8 the injection pressure P_{inj} is varied, while keeping the same injection temperature T_{inj} and heating power P_e. Increasing P_{inj} leads to the increase of the flowrate $\dot{V}$, thus the *Re*. Pr is the same, as the injection temperature is the same. The overall T_{surf} profile shifts to lower temperature in the proportion – 4 °C decrease of T_{surf} every + 1 kPa increase of P_{inj}.

To summarise the observations from these three figures, the surface temperature T_{surf} is lowered by either the decrease of T_{inj} or the increase of P_{inj}. The flowrate $\dot{V}$ alone cannot be considered as an indicator for cooling, because in both Figure 3.7 and Figure 3.8 it increases (at different rates), but in the first case T_{surf} increases and in the second T_{surf} decreases.

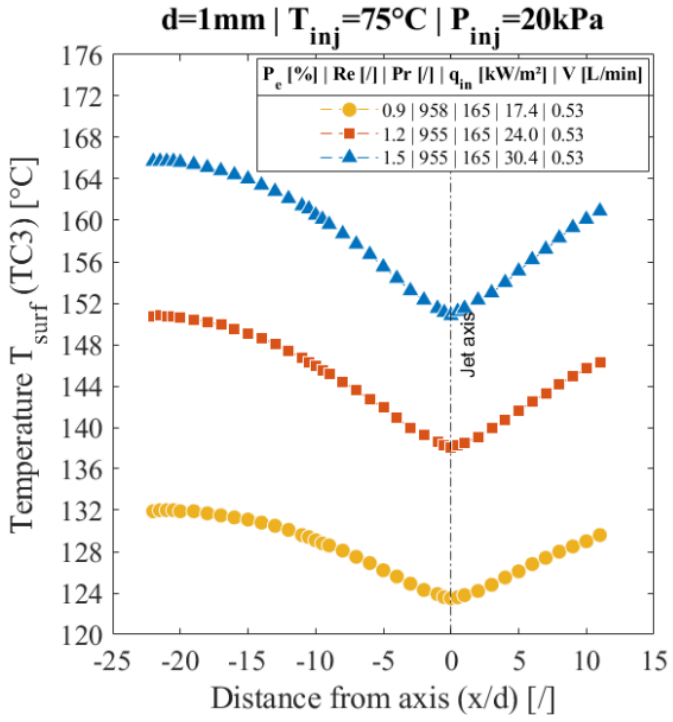

Figure 3.6 – Surface temperature for a different heating power (same nozzle diameter, injection temperature and injection pressure).

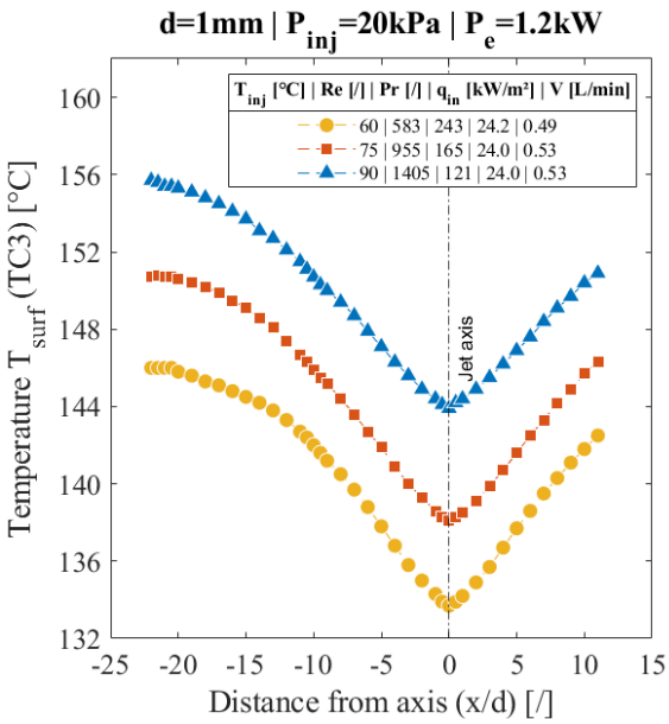

Figure 3.7 – Surface temperature for different injection temperature (same nozzle diameter, injection pressure and heating power).

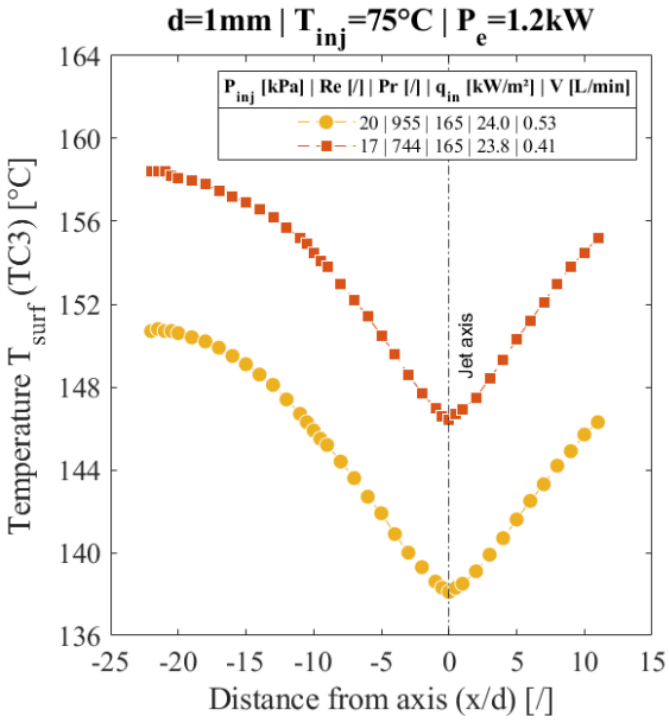

Figure 3.8 – Surface temperature of the plate for different injection pressure (same nozzle diameter, injection temperature and heating power).

- **Same temperature and heating power, variable diameter and pressure**

The three figures Figure 3.9, Figure 3.10 and Figure 3.11 represent the lowest, intermediate and highest temperature range detected in this parametric study. The surface temperature varies extensively within the study, as the lowest temperature range is about 90 °C < T_{surf} < 100 °C in Figure 3.9, and the highest is about 175 °C < T_{surf} < 185 °C in Figure 3.11. The representative temperature range of the end-windings is therefore fully achieved.

In all the three Figure 3.9, Figure 3.10 and Figure 3.11, it is observed that doubling the size of the nozzle diameter (while keeping the same T_{inj}, P_{inj} and P_e) is followed by a relevant increase of the flowrate $\dot{V}$ (about 4 times larger) and a conspicuous decrease of the surface temperature (approximately – 35 °C). In terms of temperature mitigation, the increase of the diameter appears very effective. Another observation is that, for a given heating power P_e and injection temperature T_{inj}, any combination of the injection parameters d and P_{inj}, resulting in the increase of the flowrate $\dot{V}$, lowers the surface temperature profile.

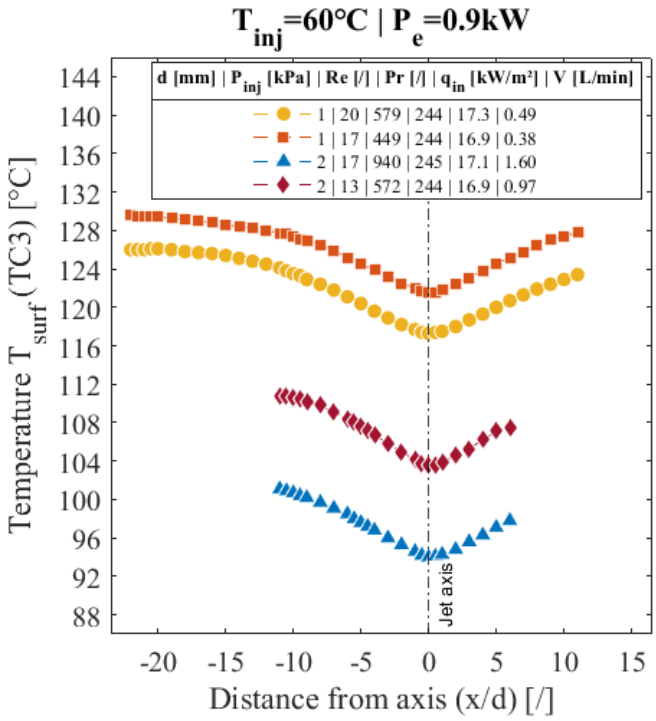

Figure 3.9 – Lowest temperature range.

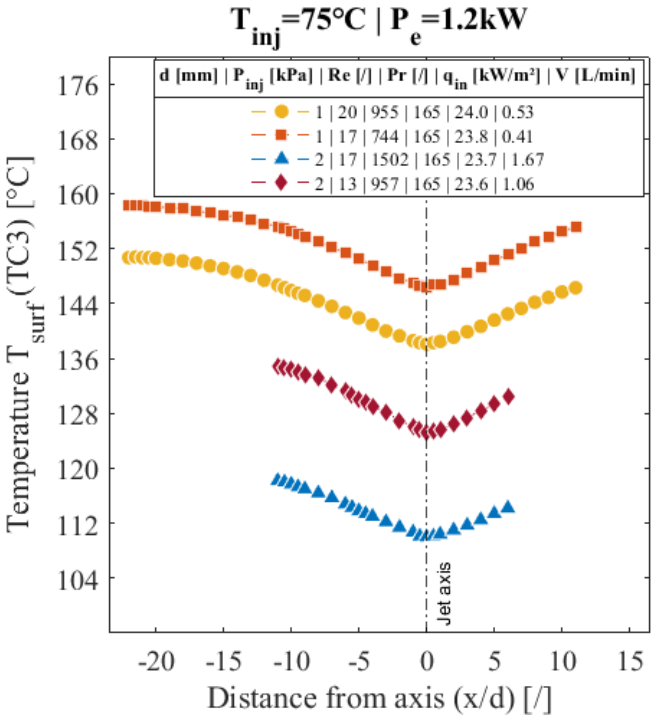

Figure 3.10 – Intermediate temperature range.

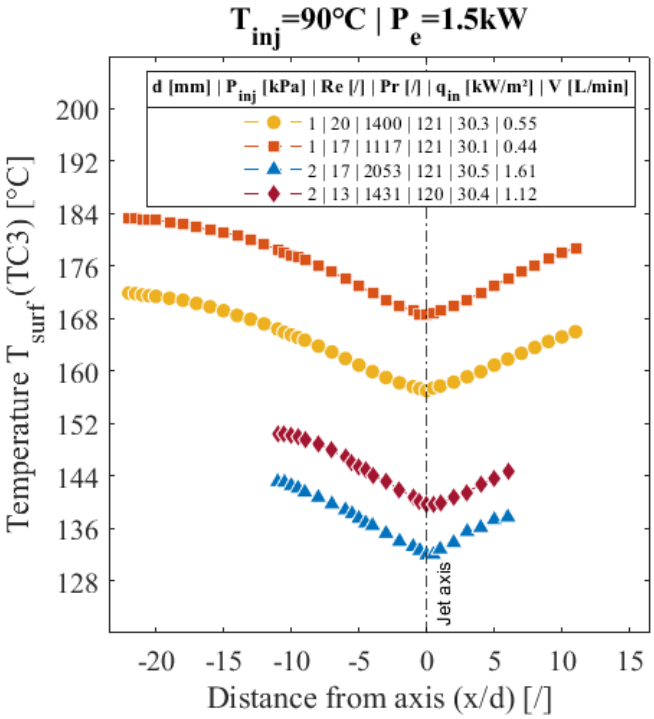

Figure 3.11 – Highest temperature range.

- **Temperature uniformity**

The uniformity of the surface temperature is expressed through the difference between the temperature measured at impingement point and the temperature at the edge of the profile. In such way, the temperature profiles are overlapped, and the relative variations can be observed. This is useful to obtain estimates of the temperature gradients along the jet-radial direction (*x* axis).

Figure 3.12 shows the difference $T_{surf}(x/d = 0) - T_{surf}(x/d = -22)$ for the experiments with d = 1 mm, T_{inj} = 60-75-90 °C, P_{inj} = 20 kPa and P_e = 0.9-1.2-1.5 kW. At first glance, the traces gather by groups of three with the same heating power and different injection temperature. At the impingement point the temperature difference is about – 8.6 °C for P_e = 0.9 kW, – 12.2 °C for P_e = 1.2 kW, and – 15.3 °C for P_e = 1.5 kW. The traces with the same injection temperature do not overlap and the higher the temperature, the larger the temperature difference between the impingement point and the edge of the profile.

Similar to the previous, Figure 3.13 illustrates the effects of the injection pressure, by plotting the difference $T_{surf}(x/d = 0) - T_{surf}(x/d = -22)$ for the experiments with d = 1 mm, T_{inj} = 60-75-90 °C, P_{inj} = 17-20 kPa and P_e = 1.2 kW. In this case, all the traces overlap, showing that the injection pressure poor influence on the extent of the profile.

From these two figures it seems clear that for a given heating power, the temperature gradients of the surface temperature are unchanged, regardless the injection parameters. In other words, the temperature profiles are simply shifted to a higher or lower temperature range. Conversely, increasing heating power increases the temperature difference between the impingement point and the edge of the profile. In this case, steeper temperature gradients appear, and the surface temperature become less uniform.

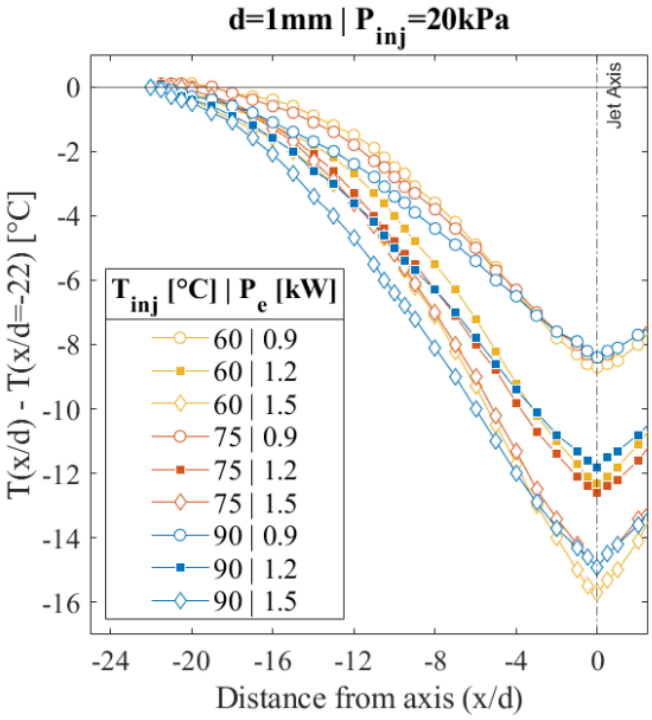

Figure 3.12 – Relative surface temperature of the plate measured by thermocouple TC3. Parametric study with the same diameter and injection pressure, and different injection temperature and heating power.

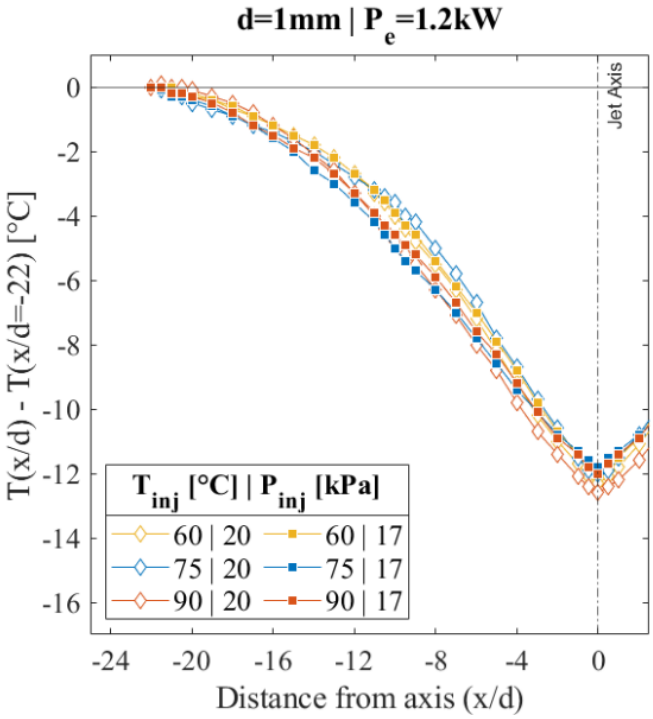

Figure 3.13 – Relative surface temperature of the plate measured by thermocouple TC3. Parametric study with the same diameter and heating power, and different injection pressure and temperature.

- **Discussion**

The parametric study shows that the surface temperature profile is lowered when decreasing T_{inj} and when increasing P_{inj} and d. In most of the experiments the increase of $\dot{V}$ reduces T_{surf}. Notice that the increase of $\dot{V}$ alone does not imply the decrease of T_{surf}, because in the present study the experiment where T_{inj} is increased leads to the increase of both T_{surf} and $\dot{V}$. The most effective way to mitigate surface temperature is by enlarging the diameter.

In terms of temperature uniformity, any change in the injection parameter simply shifts the T_{surf} profile to a higher or lower temperature range, without affecting the surface temperature gradients. What increases the steepness of the temperature gradients (along x) is the increase of P_e, therefore the surface temperature is less uniform.

Lastly, it is important to outline that the temperature range covered in the parametric study is fully representative of the electric insulation limit of the end-windings. Also, the database produced so far on the plate temperature is exploitable in the calculation of the convective coefficient (in chapter 5), and it is also necessary to compute the heat flux.

3.3 Simulation of the heat flux

3.3.1 Model validation and heat flux computation

The heat flux is simulated for the reference experiment d = 1 mm, T_{inj} = 75 °C, P_{inj} = 20 kPa and P_e = 1.2 kW. For technical details about the FEM model see section 2.2.2.

- **Validate model with internal temperature**

In Figure 3.14, the experimental (T_{TC1_exp}, T_{TC2_exp} and T_{TC3_exp}) and simulated (T_{TC1_sim}, T_{TC2_sim} and T_{TC3_sim}) temperatures are plotted. The boundary temperature $T_{boundary}$ used by

the solver CONVERGE is also traced, to verify whether the boundary used by the solver CONVERGE is correct. For almost every x/d in the range $-15 < x/d < +15$, it results $|T_{TC1\_exp} - T_{TC1\_sim}| < 0.3$ °C and $|T_{TC2\_exp} - T_{TC2\_sim}| < 0.2$ °C. Considering the typical uncertainty of the temperature measurement and the calibration of the thermocouples (see section 3.2.2), the figure shows that the FEM model replicates the plate temperature accurately. The simulation proves that the combination of experimental measurements and simulation allows evaluating the heat transfer, for generic thick solids targets.

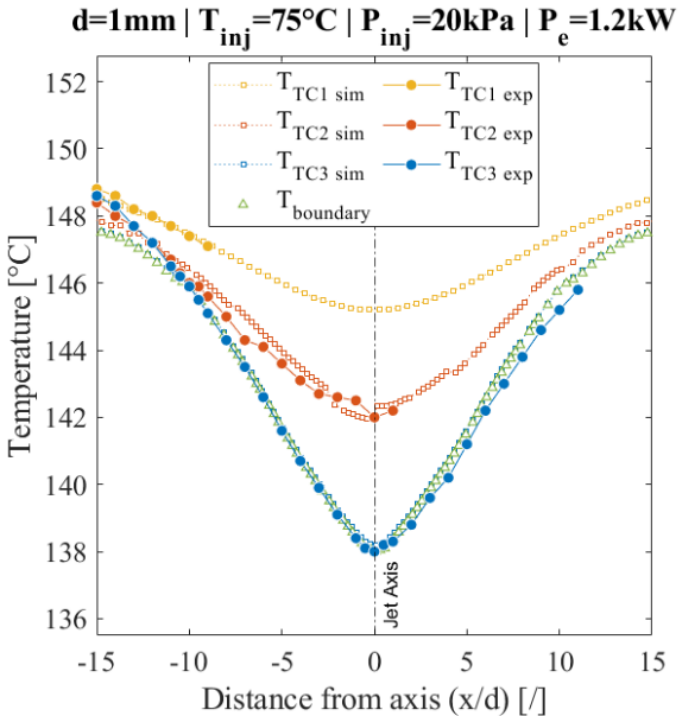

Figure 3.14 – Surface and internal temperature of the plate for the reference conditions. Comparison between experimental and simulated temperatures. TC1 and TC2 refer to the internal thermocouples. TC3 refers to the surface thermocouples.

- **Simulation of the heat flux**

Subsequent to the model validation, the heat flux q is calculated from the difference $T_{boundary} - T_{TC1\_sim}$. The result is plotted in Figure 3.15, normalised by the input heat flux q_{in} = 23.8 kW/m². The trace shows a very pronounced peak at the centre ($x/d = 0$), where the value $q/q_{in} = 18.1$ is reached. A steep decrease follows until $x/d = 10$, where the heat flux equals the input ($q/q_{in} = 1$). Unexpected fluctuations occur between $10 < x/d < 30$, which corresponds to the approximate position of the hydraulic jump. At greater distance ($x/d > 30$), the heat flux flattens until the edge of the plate. In this last region the heat flux is slightly smaller than the input heat flux, and it results $0.95 < q/q_{in} < 0.98$. Despite the presence of inconsistencies, the estimates of the heat flux are perfectly exploitable for calculating the convective coefficient within the range $0 < x/d < 10$, where the surface temperature measurements are also consistent. From this result, the heat flux exhibits significant variability within the investigated x/d range, showing that the assumption of a uniform heat flux at the solid-liquid interface (as for thermally thin targets, such as thin plates) would be misleading.

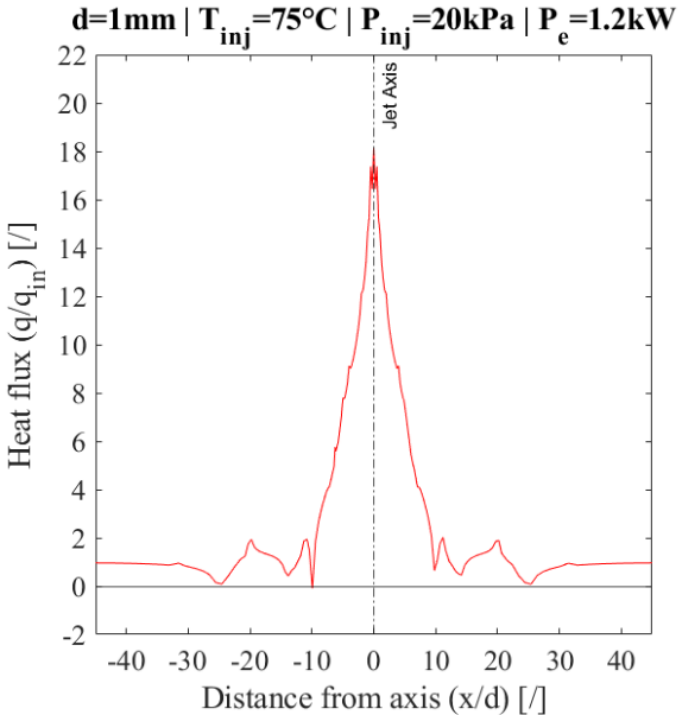

Figure 3.15 – Simulated heat flux q on the upper surface of the plate and normalised by the input heat flux on the bottom surface of the plate q_{in}.

3.3.2 Uncertainty analysis of heat flux evaluation

- **Influence of the mesh refinement level**

A sensitivity study is undertaken to verify the independence of the heat flux from the refinement level, and to determine the most appropriate refinement level to employ in this research. Four simulations of the reference experiment are run, setting identical boundary conditions. Referring to the mesh refinement described in section 2.2.2, the refinement level is increased progressively from L2 to L5. The result is plotted in Figure 3.16 and a zoom of the peak is given in Figure 3.17.

Figure 3.16 shows that the heat flux is essentially unaffected by the refinement level nearby the impingement point, as the traces overlap almost perfectly for $x > 1$ mm and $x < -1$ mm. More remarkable differences appear in the narrow range -1 mm $< x < +1$ mm, as illustrated by the zoom in Figure 3.17. Increasing the refinement level is, in fact, followed by the increase of the pick value and by the appearance of spatial fluctuations.

Since the pick does not appear to converge to any value, additional considerations are necessary to explain this this apparent incoherence. The first aspect relies in the boundary conditions: the mesh size ΔX_n should be shorter than the smallest nozzle repositioning to assure a correct interpolation of the experimental temperature over the boundary. Consequently, L3 and L2 do not fulfil the criterion. The second aspect relies on the accuracy of the prediction: the difference between the simulated and experimental temperatures is $|T_{TC2\_exp} - T_{TC2\_sim}| < 0.3$ °C for level L4 (as discussed in Figure 3.14), and $|T_{TC2\_exp} - T_{TC2\_sim}| < 0.2$ °C for level L5. A priori, the level L5 should be preferred to L4, however, the level L4 is used for the rest of the results presented in this research and this choice is motivated by technical and practical reasons. The heat flux with L5 is only 4 % higher than the one with L4, in favour of a 0.1 °C gain in accuracy in the temperature prediction. Moreover, the effort for computing the temperature map (with MATLAB) need for the boundary conditions, increases exponentially with the level of mesh refinement.

In conclusion, the accuracy of the simulated temperature improves with a more refined mesh. On the other side, the results show that calculating the heat flux as the difference between the boundary temperature at the boundary and at the cell-centre implies that the evaluation is inevitably bounded to the mesh size. Consequently, there is a limit to the smallest cell size, where the heat flux prediction become meaningless. In light of these considerations, the level L4 is considered a reasonable and adequate compromise between temperature prediction accuracy and computational effort. A finer mesh than L4, in fact, reduces the difference between simulated and experimental temperatures to about 0.1 °C, which is also the calibration of the thermocouple.

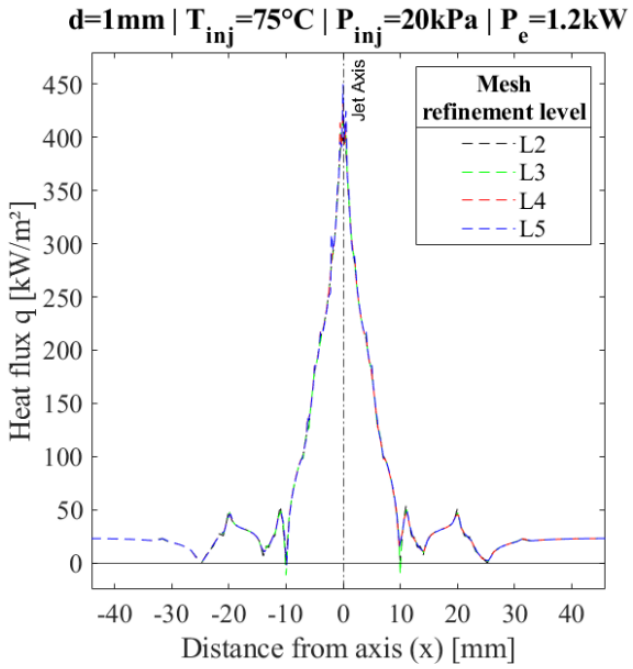

Figure 3.16 – Simulated heat flux on the upper surface of the plate. Parametric study on the level of mesh refinement level.

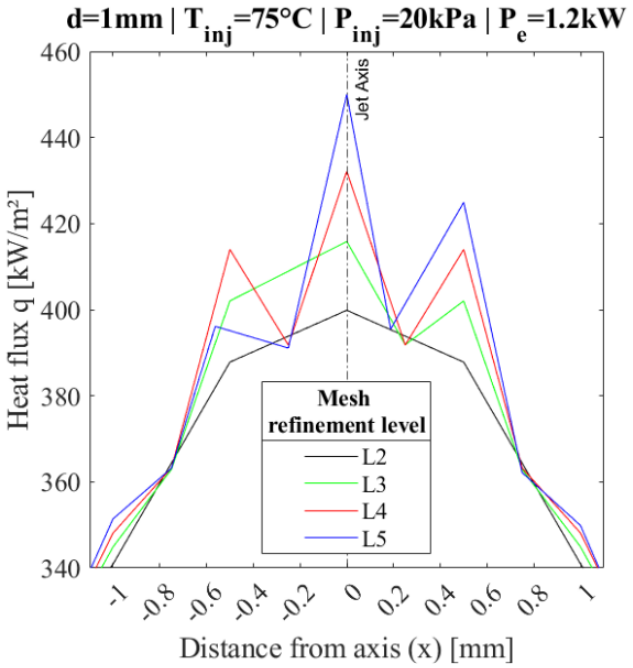

Figure 3.17 – Simulated heat flux on the upper surface of the plate. Parametric study on the level of mesh refinement level. Zoom on the jet axis.

- **Propagation of the uncertainty of the temperature measurements**

In the previous section 3.2.2 about the uncertainty of temperature measurements, it is explained that the inaccurate positioning of the thermocouples in the *z* axis leads to inaccuracy of the measurement, which is assumed as 1 °C (max 2 °C). The propagation of such inaccuracy to the heat flux is investigated hereby via a sensitivity study.

Four simulations are run with purposely alternated boundaries. Before applying the MATLAB routine to generate the temperature map, the experimental temperature is modified in range 0 mm < *x* < + 10 mm, so that the temperature of the impingement point (*x/d* = 0) is progressively diminished or incremented by 1 °C (see Figure 3.18). The same process is done by diminishing or incrementing 2 °C.

The heat flux issued from the four simulations Is plotted in Figure 3.19. The prediction on the impingement point (*x/d* = 0) shows large variability depending on the boundary condition. Decreasing or increasing the boundary temperature by 1 °C causes the heat flux to increase or decrease by 18 %. Similarly, a 2 °C alteration of the boundary alters the heat flux by 36 %. This sensitivity study shows that inaccuracy in the temperature measurements of the impingement point propagates significantly in the heat flux estimation.

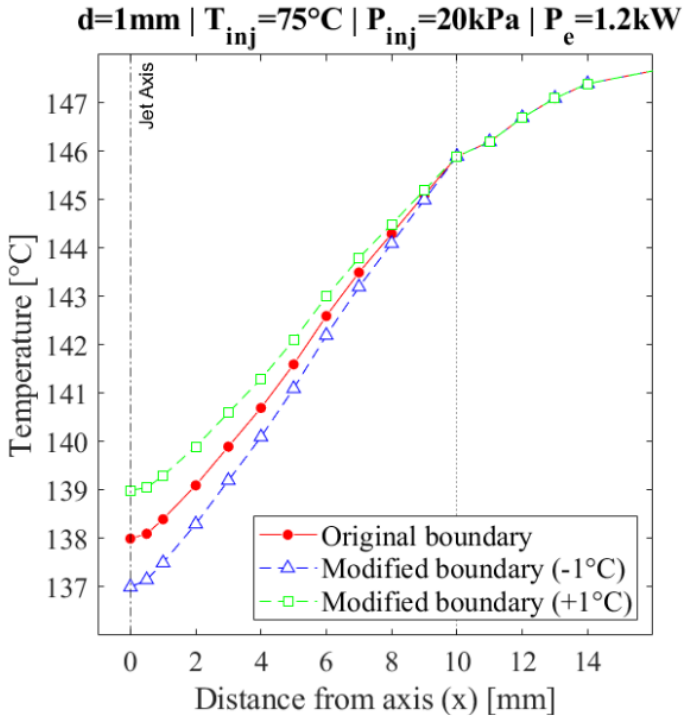

Figure 3.18 – Original and modified boundary condition to set on the upper surface of the plate. Parametric study on the propagation of measurement inaccuracy on the heat flux simulation.

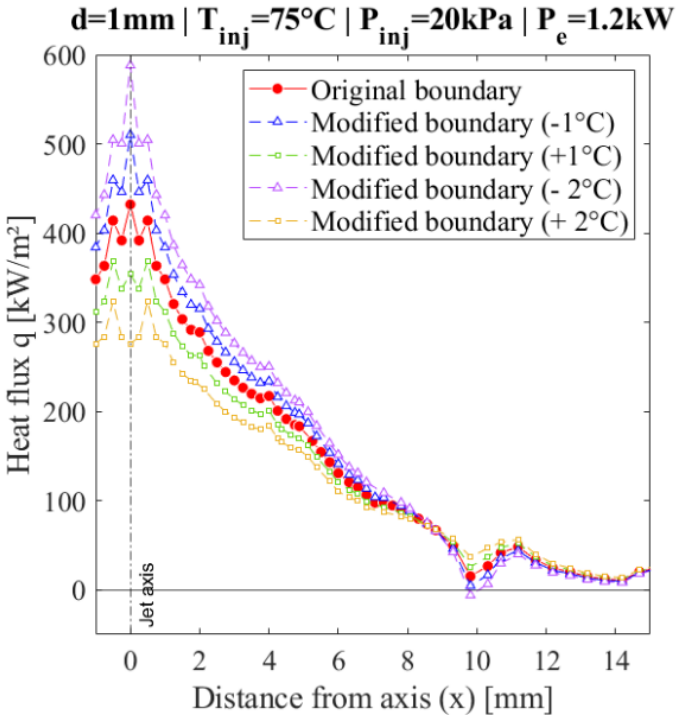

Figure 3.19 – Simulated heat flux on the upper surface of the plate. Parametric study on the propagation of measurement inaccuracy on the heat flux simulation, setting modified boundary conditions.

- **Total uncertainty**

The uncertainty is essentially given by the propagation of the uncertainty on temperature measurements. The analysis shows that the heat flux at the impingement point is significantly affected. Such uncertainty is very large, approximately with the following proportion: 1 °C of inaccuracy in the boundary implies 18 % of inaccuracy in the heat flux.

3.3.3 Parametric study for variable injection and heating

The heat flux is computed for all the experiments reported in Table 3.1 and Table 3.2. All these estimates are needed to calculate the convection coefficient, which is presented later in chapter 5. Only few of these parametric variations are presented and discussed in this section.

In Figure 3.20, the heating power P_e is varied while keeping the same injection parameters. The simulation based on the same experiments illustrated in Figure 3.6. The normalised heat flux q/q_{in} exhibits the same trend, regardless the heating power, as all traces overlap. This means that when the heating power is increased, the overall profile is shifted to higher ordinates, in a proportional trend with the input heat flux q_{in}.

In Figure 3.21 the injection temperature T_{inj} is varied, while keeping the same injection pressure P_{inj} and heating power P_e. The simulation based on the same experiments illustrated in Figure 3.7. The heat flux exhibits the same trend, regardless the injection, and all traces overlap.

More variability is exhibited at the impingement point, as in Table 3.3. For the same injection parameters (d, T_{inj} and P_{inj}) and increasing heating power P_e, the heat flux increases, coherently with the previous observations of Figure 3.12 section 3.2.3. Considering an increasing T_{inj} while keeping the other parameters (d, P_{inj} and P_e), the heat flux shows a coherent decrease, likely due the increase of the temperature of the fluid in the stagnation region. Lastly the increase of the injection pressure P_{inj}, without changing

the other parameters (d, T_{inj} and P_e), appears to produce a slight decrease of the heat flux (contrarily to the expectations).

The parametric study on the influence of the injection and heating parameters on the heat flux show that both the trend and the magnitude of the heat flux q are almost identical, regardless the injection or heating. This is observed especially in the range $x/d > +1$ and $x/d < -1$. Conversely, the value at the impingement point ($x/d = 0$) exhibits more variability with the heating power and the injection temperature, however the variations are small and the trend is not evident. In chapter 5, the effects of the injection and heating parameters are better investigated through the Nusselt number.

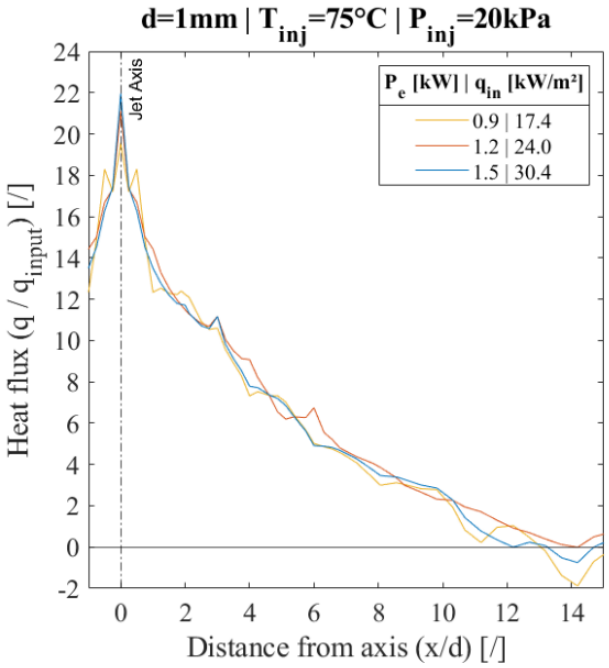

Figure 3.20 – Simulated heat flux q on the upper surface of the plate. Parametric study on the input heat flux q_{in} on the lower surface of the plate.

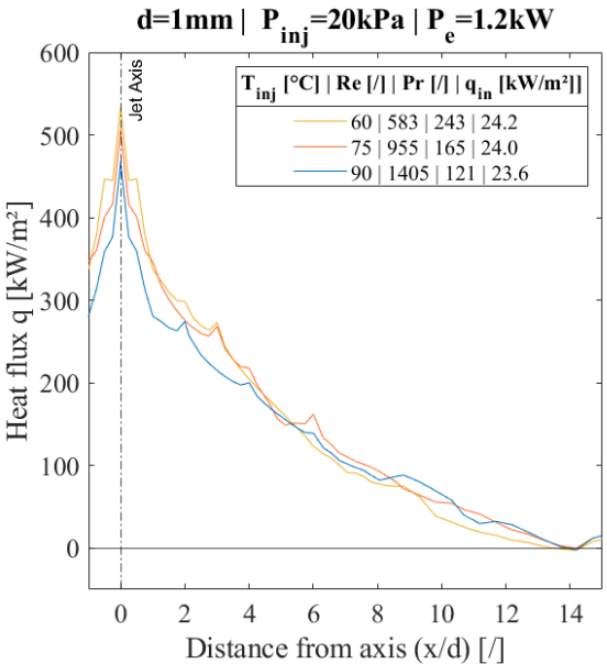

Figure 3.21 – Simulated heat flux q on the upper surface of the plate. Parametric study on the injection temperature.

Table 3.3 – Normalised heat flux q/q_{in} at the impingement point $x/d=0$, for various parametric variations.

d	P_{inj}	T_{inj}	P_e	q/q_{in}
[mm]	[kPa]	[°C]	[kW]	[/]
1	20	75	0.9	19.6
			1.2	21.1
			1.5	22.0
1	20	60	1.2	22.0
		75		21.1
		90		19.8
1	17	75	1.2	22.4

3.4 Chapter conclusions

- **Investigation overview**

In this chapter, the plate temperature is measured, the numerical method is validated, the fundamental parameters of the convective heat exchange (Reynolds and Prandtl numbers) are determined, and cooling effectiveness and temperature uniformity are evaluated.

An extensive parametric study is performed to observe the variation of the plate temperature for different combinations of the injection and heating parameters (i.e., T_{inj}, P_{inj}, d and P_e) in steady state. The injection and heating parameters are well characterised and are affected by small uncertainty. The Reynolds number covers a relatively wide laminar and transitional range (i.e., $449 < Re < 2138$) while the Prandtl number is varied up to a factor 2 (i.e., $120 < Pr < 240$). The plate temperature is significantly influenced by all the parameters investigated. Conversely, the heat flux is much less affected, except for the impingement point. The measured temperature range (90 °C < T_{surf} < 190 °C) is fully representative of the limits of the electric insulation in the winding of the electric motors.

- **Method limits and measurement uncertainty**

The experimental method for measuring the plate temperature is robust within $-10 < x/d < +10$, with a temperature sensitivity of 0.1 °C and a spatial resolution of 0.2 mm. The surface temperature denotes steep temperature gradients of about 0.1 °C/mm < $\Delta T/\Delta x$ < 1 °C/mm, coherent with the expectations and the known literature. The measurements are consistent and exploitable for the heat flux calculation.

The simulations replicate accurately the plate internal temperature distribution (within 0.3 °C and $-10 < x/d < +10$) and are validated through experimental measurements. The heat flux shows a very pronounced peak on the impingement point, which can be approximately 20 times larger than the input heat flux delivered by the heater underneath. Conversely, at about $x/d = 10$, the heat flux equals the input one, meaning that the cooling action of the jet impingement is localised within a relatively small region.

The plate temperature measurements are affected by relatively large uncertainty, with respect to their calibration. The precision plays a minor role because the standard deviation between experiments is similar or slightly larger than the thermocouple calibration. On the other hand, the accuracy plays a major role and is affected by diverse types of misalignments and imperfection in the experimental apparatus. The accuracy related to the measurement of the actual impingement point (i.e., the correct x-y alignment between the thermocouple tip and the jet axis) plays a non-negligible role, however it can be

characterised and corrected partially. The accuracy related to the measurement of the actual solid-liquid interface (i.e., the correct placement of the hot junction along the *z* direction) contributes the most to the uncertainty at the impingement point. Such accuracy cannot be fully characterised experimentally, and simulations are advised to complete this research as future work. For instance, it would be interesting to evaluate if and how the presence of the thermocouple perturbs the measurement and the role of the plate-thermocouple thermal contact resistance. Lastly, it is observed that the inaccuracy of the surface temperature measurement propagates considerably into the heat flux, especially at the impingement point. In conclusion, the final estimates of the uncertainty in this research are 1.4 °C (max 2.4 °C) for the surface temperature and 18 % (max 36 %) for the heat flux.

- **Cooling effectiveness and temperature uniformity**

In terms of cooling effectiveness, the increase of the injection pressure, the nozzle diameter and the reduction of the injection temperature leads to the decrease of the surface temperature. Considering the maximum variation of the injection parameters (allowed by the experimental apparatus), a simplified synthesis of the surface temperature reduction for obtained in this research follows below:

- ΔT_{inj} = – 30 °C leads to ΔT_{surf} = – 10 °C and $\Delta \dot{V}$ = – 8 %
- ΔP_{inj} = + 4 kPa leads to ΔT_{surf} = – 9 °C and $\Delta \dot{V}$ = + 30 %
- Δd = + 2 mm leads to ΔT_{surf} = – 35 °C and $\Delta \dot{V}$ = + 215 %

The increase of the nozzle diameter is the most effective for temperature mitigation, followed by the increase of the injection pressure and the decrease of the injection temperature. As known in the literature, the increase of the flowrate reduces the surface temperature, only if the injection temperature is unchanged (notice that increasing the injection temperature increases the flowrate but the surface temperature as well). For sizing cooling systems, these results suggest that increasing the flowrate through the nozzle diameter or the injection pressure is more or as effective as reducing the injection temperature.

Concerning cooling uniformity, any variation of the injection temperature or pressure does not modify the temperature gradients $\Delta T/\Delta x$ but rather shifts the surface temperature to a lower or higher temperature range. Conversely, the increase of the heating power steepens the gradients, thus the surface temperature is less uniform. These observations suggests that jet impingement is effective at reducing the surface temperature and is even more effective for very localised cooling (i.e., at the impingement point), confirming the potential applications for concentrated heat sources (e.g., power electronics and microprocessors). On the other hand, jet impingement is less effective at assuring a uniform surface temperature and, if this is the task, a multi-jet solution should be considered.

4 CHARACTERISATION OF THE LIQUID

- **Chapter introduction**

This chapter reports the pointwise or wide-field measurements of the temperature and thickness of the liquid film (after impingement), with optical and non-optical techniques. Large focus is given to the development of the imaging method based on 2-colour 2-dye LIF. The temperature measurements presented in the chapter are important for a more accurate characterisation of the local convective coefficient at the solid-liquid interface. The thickness measurements are not used directly for characterising convective heat transfer, but they are important because they provide complementary information about the hydrodynamic regions of the jet and about the fluid coverage of a solid surface. More generally, these evaluations are important to build an experimental database to support CFD. The chapter is structured into five parts.

In the first part, optical and non-optical techniques are used for pointwise measurements of temperature and thickness of the impinging jet. Thermocouples are used to measure the temperature. A laser for triangulation and a contact needle are used for measuring thickness. For all methods, an evaluation of the uncertainty is provided.

The second part describes the preliminary phase for the development of the imaging method. Three approaches are proposed and investigated (experimentally and theoretically) to measure: the film thickness, the temperature of the air-liquid interface, the mean temperature along the jet-radial direction, and the temperature along the plate-normal direction. Moreover, a spectroscopy study characterises the fluorescence behaviour of the dyes and their suitability for 2-colour 2-dye LIF.

In the third part, the imaging method is established for static liquid films. More specifically, simulations of detection with RGB camera are performed and compared with experimental measurements with the imaging method.

The fourth part presents the analysis of the uncertainty. The various sources of uncertainty affect the precision and the accuracy of the measurements for temperature and thickness. Such sources are identified, quantified, and analysed. Also, technical solutions are tested to reduce the uncertainty.

In the fifth, the optical method is calibrated on a static film and applied to the impingement jet, for measuring temperature and thickness. The results from the field measurements are compared to the pointwise measurements.

4.1 Pointwise measurements of temperature and thickness

4.1.1 Temperature measurements with thermocouple

- **Temperature measurement along z**

The local oil temperature (after impingement) is measured with thermocouples, by immersing the tip in the liquid film. The method and protocol are in detailed in section 2.3.1, while Figure 4.1 is a schematic view of the expected temperature evolution along the z axis for a generic x.

Figure 4.2 shows the local temperature $T_{oil}(z)$, at x/d = 20 (beyond the hydraulic jump, in the high-thickness region), that is, over the plate-embedded thermocouple TC5. The first measurement is taken in the air above the air-liquid interface (z = 3.6 mm) and the last

when the thermocouple tip touches the plate (z = 0 mm). The plate embedded thermocouple TC5 is used to report the temperature of the solid-liquid interface.

The trace decreases gradually in the whole range, without abrupt variations. During the experiment, it is observed that a meniscus forms when the tip of the thermocouple interacts with the liquid at the air-liquid interface, approximately between 2.7 mm < z < 3.0 mm. In the plot, there is no evidence of such event in the trace, but the increase of the standard deviation in this range suggests that the meniscus forms in this region.

From z = 3 mm to z = 0 mm, $T_{oil}(z)$ increases by about + 20 °C. At the solid-liquid interface z = 0 mm, the temperature measured by the thermocouple is 75 °C, that is, the same temperature measured at the nozzle. By comparison, the one measured by TC5 is T_{surf} = 129.1 °C.

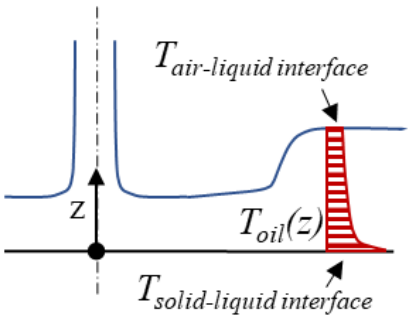

Figure 4.1 – Scheme of the temperature and thickness evolution along x and z.

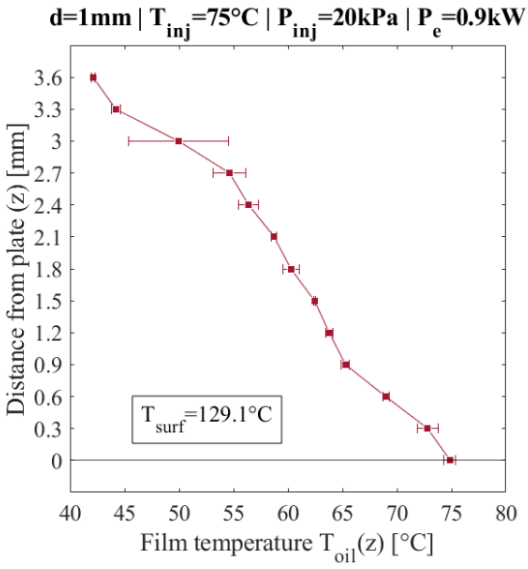

Figure 4.2– Temperature of the oil film along the plate-normal direction. A thermocouple is used for $T_{oil}(z)$ and the plate-embedded thermocouple TC5 for T_{surf}.

The results in Figure 4.2 show that the temperature evolution is coherent with the expectations, as the lowest temperature is measured within the air and the hottest the closer to the solid-liquid interface. The measurement is relatively precise, as overall small deviation is observed. The method shows some inaccuracy suggested by the large difference $T_{surf} - T_{oil}(z=0)$ = 54 °C and by the fact that $T_{oil}(z=0) = T_{inj}$. Since the exact position of the sensitive element is not known and the probe is big with respect to the film, the measurement is likely to be some averaged value of the fluid and air temperature. Moreover, it is not possible to detect the exact air-liquid interface due to the meniscus formation, thus the method cannot be use for simultaneous thickness measurement.

- **Temperature measurement along x**

Figure 4.3 and Figure 4.4 shows $T_{oil}(x)$ for two different injection temperatures T_{inj} = 60-75 °C, with the same heating power and injection pressure. Three more traces are drawn: the injection temperature T_{inj} (measured at the nozzle by TC0), the "end of the field of view" at x = 60 mm (of the RGB camera installed on bench 2), and the surface temperature T_{surf} (measured by the plate-embedded thermocouples TC3, TC4, TC5 and TC7, at x = 0-10-20-40-80 mm respectively). The position of the hydraulic jump is not reported, but it is located at approximately x = 20 mm and x = 30 mm, for Figure 4.3 and Figure 4.4 respectively.

In both figures, the oil temperature $T_{oil}(x)$ increases with the distance x, and difference between the two furthest measurements (x = 10 mm and x = 80 mm) is about 15 °C. The measured values appear relatively accurate because in both figures T_{oil} $(x = 10\ mm)$ is similar to the injection temperature (within 2-3 °C). The trend is coherent with the expectations because within the field of view (10 mm < x < 60 mm) both $T_{oil}(x)$ and T_{surf} increase (thus the liquid heats up) and such increase is similar (about + 10 °C).

The standard deviation of $T_{oil}(x)$ is relatively small before the hydraulic jump, while significant after. During the measurement, it is observed that before the hydraulic jump, the thermocouple perturbs the flow significantly, but deviation is smaller. The opposite (small perturbation and large deviation) is observed after the hydraulic jump.

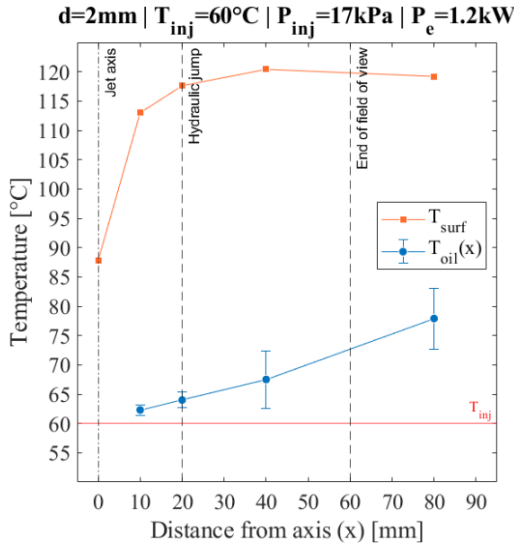

Figure 4.3 – Temperature of the oil film and of the solid-liquid interface after impingement. A thermocouple is used for $T_{oil}(x)$ and a plate-embedded thermocouple for T_{surf}. The injection temperature T_{inj} = 60 °C is measured by the circuit-embedded thermocouple TC0.

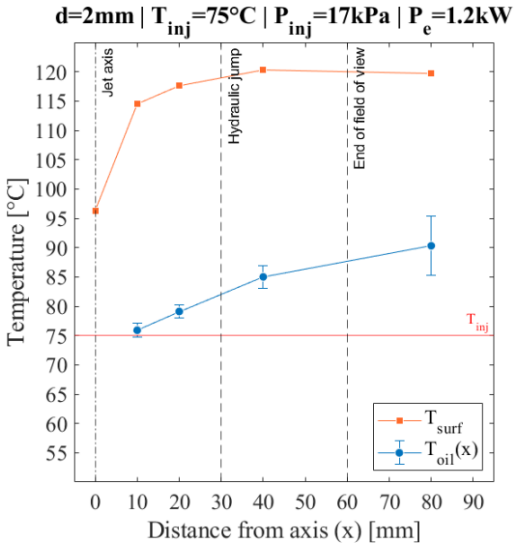

Figure 4.4 – Temperature of the oil film and of the solid-liquid interface after impingement. A thermocouple is used for $T_{oil}(x)$ and a plate-embedded thermocouple for T_{surf}. The injection temperature T_{inj} = 75 °C is measured by the circuit-embedded thermocouple TC0.

In general, the temperature measurements with thermocouples along z are coherent with the expectations because the temperature increases the closer to the plate with the rate ≈ 10 °C/mm. Although, the thermocouple perturbs the flow and measurement suffers from inaccuracy. When measuring the temperature along the plate-normal direction (z axis), it is not evident whether the temperature of the liquid film or the air or both are being measured. For measurements along the jet-radial direction (x axis), relevant flow perturbation is induced before the hydraulic jump, and large standard deviation after, likely due to inaccurate positioning. In the investigated injection temperature range and field of view, an increase of ≈ 0.2 °C/mm is therefore expected along x. In conclusions, there is room for improving accuracy and precision, however the measurements with thermocouples provide valuable information about the evolution of the temperature within the liquid film.

4.1.2 Thickness measurements with triangulation laser and contact needle

- **Thickness measurement with triangulation laser**

Figure 4.5 and Figure 4.6 show the film thickness measurements using the laser for triangulation (section 2.3.1 for technical details). A parametric study is undertaken by varying the injection and heating parameters. In Figure 4.5, the injection temperature T_{inj} is varied, keeping the same heating power P_e, while the opposite is done in Figure 4.6. For both figures, the nozzle diameter is fixed to d = 1 mm and the pressure to P_{inj} = 20 kPa.

For all traces in both figures, some common features are: a spike at x = 3 mm, and an abrupt transition between a low-thickness region and a high-thickness region. The origin of the spike is not clear because the liquid column is expected to be found at about x = 0.5 mm. Contrarily, the abrupt transition corresponds exactly to the hydraulic jump, and its position is confirmed by images taken with a camera (see annexe to chapter 4). In the low-thickness region, the thickness is approximately δ = 0.5 mm, while δ = 0.5 mm in the high-thickness region, therefore ratio between the two is 3.2.

The position x of the hydraulic jump increases with increasing injection temperature (Figure 4.5). This result appears consistent with the expectations, as temperature increase causes viscosity and surface tension to diminish, thus the hydraulic jump occurs at further distances from the jet axis. Contrarily, it appears unaffected by any variation of the heating power (Figure 4.6).

The overall results appear consistent with the expectations, however it not enough evidence that the measured thickness is accurate. As mentioned previously in section 2.3.1, the calibration is not performed on a liquid interface (but with solid objects) and the sensor is not perpendicular to the target surface (as recommended by the manufacturer). Despite that, this non-intrusive method has potential for future work.

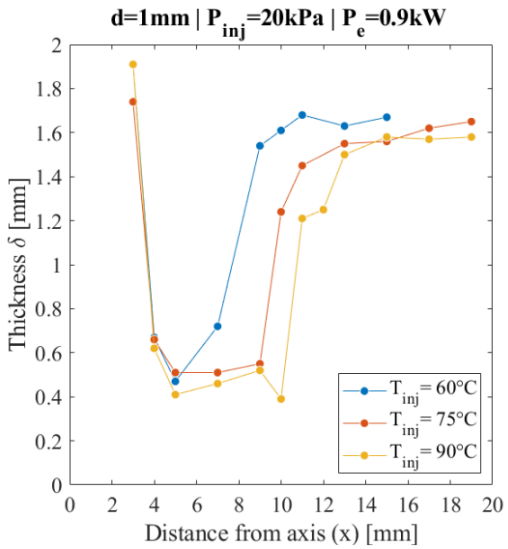

Figure 4.5 – Thickness of the oil film after impingement, for different injection temperatures T_{inj}, (same nozzle diameter d, injection pressure P_{inj} and heating power P_e). Measurement taken with the laser for triangulation.

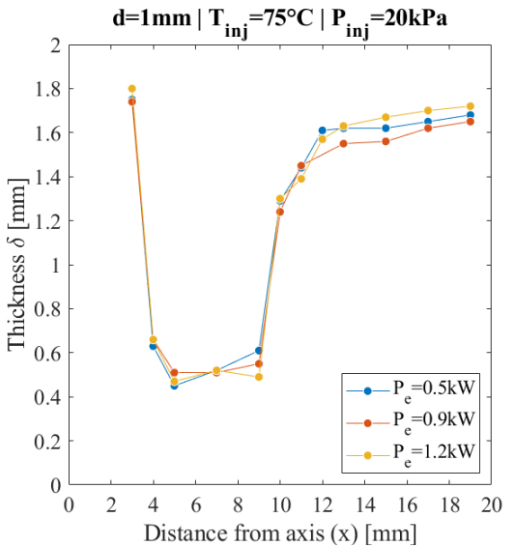

Figure 4.6 – Thickness of the oil film after impingement, for different heating powers P_e (same nozzle diameter d, injection temperature P_{inj} and injection temperature T_{inj}). Measurement taken with the laser for triangulation.

- **Thickness measurement with contact needle**

Figure 4.7 and Figure 4.8 show the thickness measurement obtained with the contact needle. In the first image, a parametric study is performed with fixed nozzle diameter d = 2 mm and different injection temperature T_{inj}, injection pressure and heating power P_e. In the second image, the heating power P_e is varied for the same injection d = 2 mm, T_{inj} = 60 °C and P_{inj} = 17 kPa.

In both figures, two distinct low- and high-thickness regions are observed, marked by an abrupt transition. For all the parametric variations, the lowest value is approximately δ = 0.2 mm (at x = 4 mm). The highest value is about δ = 3 mm, in the high-thickness region. Considering these two extreme values, the ratio between the thickness in the two regions is about 15, which is much larger than the one evaluated for the experiments in Figure 4.5 and Figure 4.6.

Figure 4.7, shows that increasing oil temperature and pressure shift the position of the hydraulic jump further from the jet axis. The influence of heating power also seems to affect the hydraulic jumps, but the effects are less pronounced than in Figure 4.8. The explanation to this observation is not evident but could be attributed to the reduction of the oil viscosity. Even though the experiment is slightly different, the same occurrence is not observed with the triangulation laser in Figure 4.6, suggesting that the contact needle is more sensitive for the same measurements.

The method uncertainty is simply quantified by the standard deviation between experiments represented by the error bars. The measurement accuracy is influenced by the operator. For the given protocol, taking a measurement means that the operator sees perturbation in the flow. Such perturbation takes the form of a combination between a meniscus formation (due to capillarity) and a small hydraulic jump over the needle (due to the transformation of kinetic energy into potential energy). The perturbation is evident for the low-thickness region because the velocity is larger and human error is less probable. Another source of inaccuracy is the impossibility to insert the needle perpendicularly along the hydraulic jump, causing the largest uncertainty along the hydraulic jump.

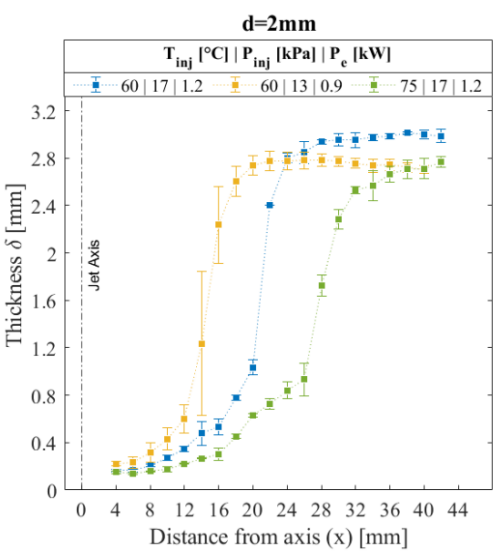

Figure 4.7 – Thickness of the oil film after impingement, for different injection temperature T_{inj}, injection pressure P_{inj} and heating power P_e (same nozzle diameter d). Measurement taken with the contact needle.

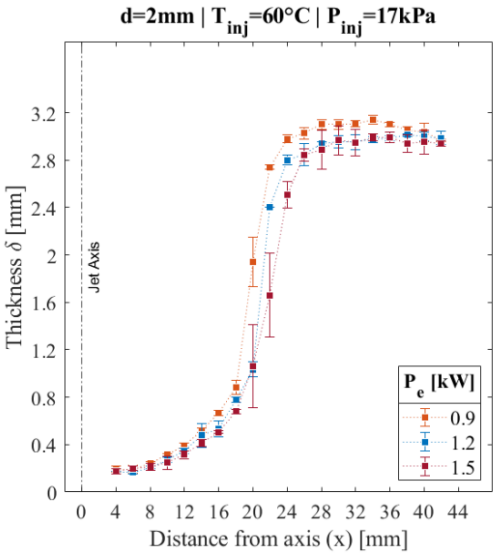

Figure 4.8 – Thickness of the oil film after impingement, for different heating power P_e, (same nozzle diameter d, injection temperature P_{inj} and injection temperature T_{inj}). Measurement taken with the contact needle.

4.2 Illumination, spectroscopy, and dye selection for LIF

4.2.1 Detection schemes and illumination

The possibility to measure the temperature and thickness of an oil film is examined in this preliminary phase by considering three different approaches. Referring to the previous Figure 4.1, the aim is to take field measurements of the temperature at the air-liquid interface, of the thickness and temperature along the plate-normal direction (z axis), and of the thickness and the mean temperature (within the film thickness) at different distances from the jet (along x).

- **Approach for evaluating the temperature of the air-liquid interface**

The approach consists in having such a high concentration of fluorescent dye that almost all the excitation light (coming from above the liquid) is absorbed within a very thin layer nearby the air-liquid interface. In this a way, the detected fluorescence signal can be considered as coming exclusively from the air-liquid interface. According to Beer-Lambert law of absorption and to the scheme in Figure 4.9, I_0 is the intensity of the excitation light and $I_0 e^{-\varepsilon C \Delta z}$ is the residual intensity after absorption within a thin layer Δz. Assuming that 90 % of the incident excitation light is absorbed within $\Delta z = 0.1$ mm, and assuming absorptivity $\varepsilon = 6 \cdot 10^4$ L/mol/cm (maximum experimental value for PYR597 when dissolved in Polyalphaolefin with $C = 0.1$ mmol/L and between 30-100 °C), the dye concentration must be $C = 23$ mmol/L. The solubility of the dye in oil is hence tested experimentally by preparing samples with large concentrations. Figure 4.10 is a photo of the samples with concentration $C = 10$ mmol/L, where traces of solid deposit can be observed on the bottom of the flasks and agglomerates on the upper part.

In conclusion, it is not possible produce a fluorescence signal from a very thin layer of a liquid film with high concentration of dye, because of the saturation limit. Consequently, the approach proposed for measuring the temperature of the air-liquid interface is not likely to work.

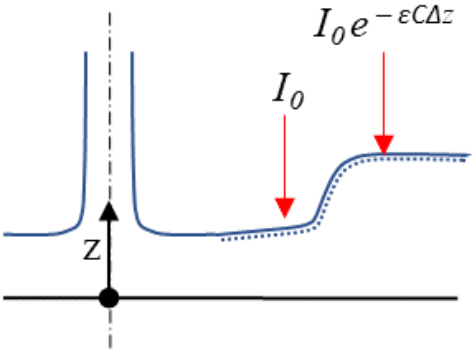

Figure 4.9 – Intensity of the excitation light before (I_0) and after absorption within a layer (Δz).

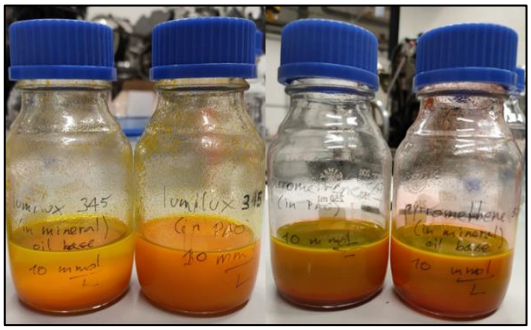

Figure 4.10 – Flasks with high-concentration of dye (C = 10 mmol/L). Presence of solid deposit and aggregates could be observed.

- **Approach for field measurements along z with a thin laser sheet**

The concept is to generate a thin excitation light sheet, which intersects the liquid film, and restrains the fluorescence emission to a cross section of the film. Previous studies have successfully developed this approach for free-falling films, with water-based solutions (see section 1.3.2), but it has never been tested on free jets with high-Prandtl fluids.

The phenomenon of total internal reflection must be considered. In Figure 4.11, a geometric construction shows the interactions of light with the two interfaces of the liquid film. The arrow I_1 is the excitation light and is incident with an angle Θ_1 with respect to the normal to the air-liquid interface. According to Snell's law, I_1 is refracted with the angle Θ_2. The resulting I_2 is absorbed by the dye in the oil and fluorescence is emitted isotropically. The component I_3 of the fluorescence emission (normal to the plane of I_2) is now considered. This is refracted at the air-liquid interface, hence I_4 represent the emission that can be detected.

The objective is to calculate the angle Θ_1 which prevents the fluorescence signal from the liquid to incur in total internal reflection (i.e., $\Theta_4 = 90°$). The exact value of the refraction index of the oil used in this research is unknown and the value 1.4 is assumed from similar lubricants. The outcome of the calculation is that the possible range is achieved by setting $79° < \Theta_1 < 89°$. It follows that $44.5° < \Theta_2 < 45.6°$, $44.4° < \Theta_3 < 45.5°$ and $78.5° < \Theta_4 < 86.8°$.

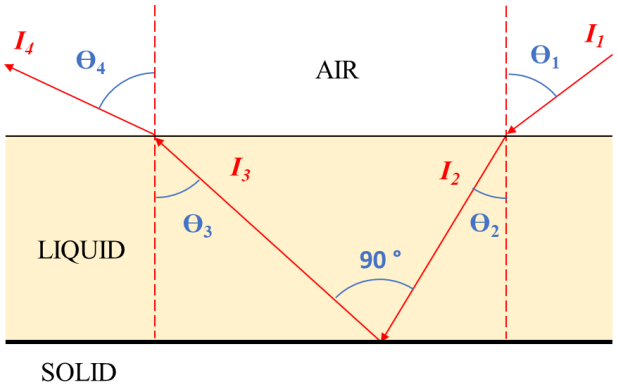

Figure 4.11 – Geometrical construction to calculate the angles for excitation and detection to avoid total internal reflection. I_1 is the incident light, I_2 is the refracted component of I_1, I_3 is the fluorescence emission perpendicular to I_2, and I_4 is the refracted component of I_3. Θ_1, Θ_2, Θ_3 and Θ_4 are the angles between the light component and the normal to the interface.

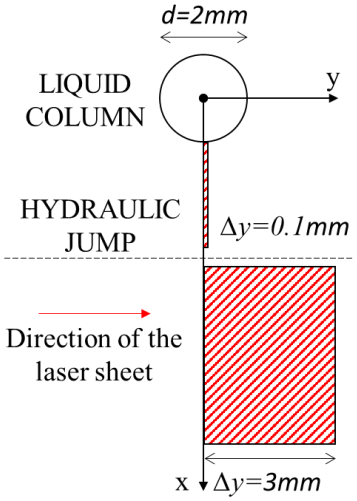

Figure 4.12 – Extent Δy of the illuminated cross section within the liquid film (seen from above the plate) if a laser sheet hits the liquid film along the x axis.

These angles are very inconvenient for two main reasons. From a technical point of view, the excitation and detection system must be placed almost at the same plane of the plate. More importantly, the illuminated cross section would not be perpendicular to the plane but would be tilted of approximately $\Theta_2 = 45°$. In other terms, the illumination sheet intersects the air-liquid interface, then travels within the liquid film, and hits the plate with a shift of approximately $\Delta y = \delta$ from the first intersection. Figure 4.12 helps visualise that. Before the hydraulic jump, where thickness is about $\delta = 0.1$ mm, Δy would be acceptable because relatively small compared to the jet (i.e., d =1-2 mm is much larger than $\Delta y = 0.1$ mm). After the hydraulic jump, where thickness is about $\delta = 3$ mm, this is problematic as Δy is larger than the jet (i.e., d =1-2 mm is smaller than $\Delta y = 3$ mm). Moreover, the geometry of the impinging jet does not provide an air-liquid interface that is always parallel to the plate, increasing the potential to have even more limitations.

In conclusion, illuminating a cross section of the liquid film is theoretically possible, but technically complex and inaccurate. The detection and illumination angles are ambitious, and the resulting illuminated cross section would be inappropriate given the geometry of the impinging jet. Consequently, measurements along z cannot be taken.

- **Approach for field measurement along *x* and *y* with flood illumination**

Flood illumination is examined. According to the schemes of bench 1 and bench 2 in section 2.3.2, the orientation of the RGB camera and of the laser are adjusted to assure simultaneously a large field of view and illumination of the liquid within the field of view. Two examples are given in Figure 4.13 and Figure 4.14 for a static film and for the impinging jet, respectively.

Figure 4.13 is taken with bench 1. The RGB camera is detecting the fluorescence signal of a static oil film with a dissolved fluorescent dye. Concerning the excitation system, the setup with the mechanical aperture and negative lens is used. In the image, the aperture is adjusted so that the illumination disk is contained within the camera field of view, and the illuminated and non-illuminated regions can be distinguished. In such a way, the non-illuminated region can be used as a control region.

Figure 4.14 is taken with bench 2. The camera is installed over the impinging jet, mounting a nozzle with $d = 2$ mm and $z/d = 10$. In this case, the excitation system is composed of a laser, a homogeniser, and a negative lens. As the image shows, it is possible to take images from the impingement point to about $x = 60$ mm, assuring flood illumination in the whole field of view and without noticeable distortion of the image. For nozzle $d = 1$ mm it is not possible to keep the same geometric settings without having the nozzle in the field of view or without increasing the nozzle-to-plate distance to $z/d = 20$ (see annexe to chapter 4). Consequently, the evaluations in this manuscript must be restrained to the injections with $d = 2$ mm.

These two images prove that bench 1 and 2 allow to take field measurements (*x*-*y* plane) of either static films and impinging jets. The fluorescence signal appears to be coming exclusively from the illuminated region and all the characteristic regions of the impinging jet can be investigated over the *x*-*y* plane and for a relatively wide field of view.

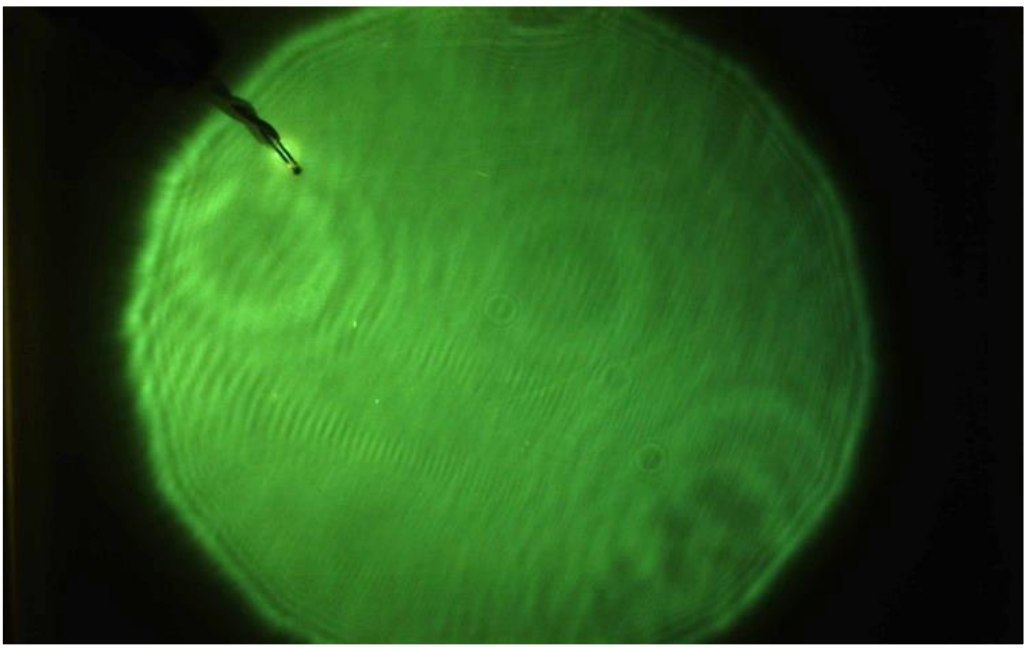

Figure 4.13 – Image (in real colours) of the fluorescence signal of a static film, detected by a RGB camera. The round region corresponds to the illumination disk. The tip of a thermocouple can be seen in the up left corner.

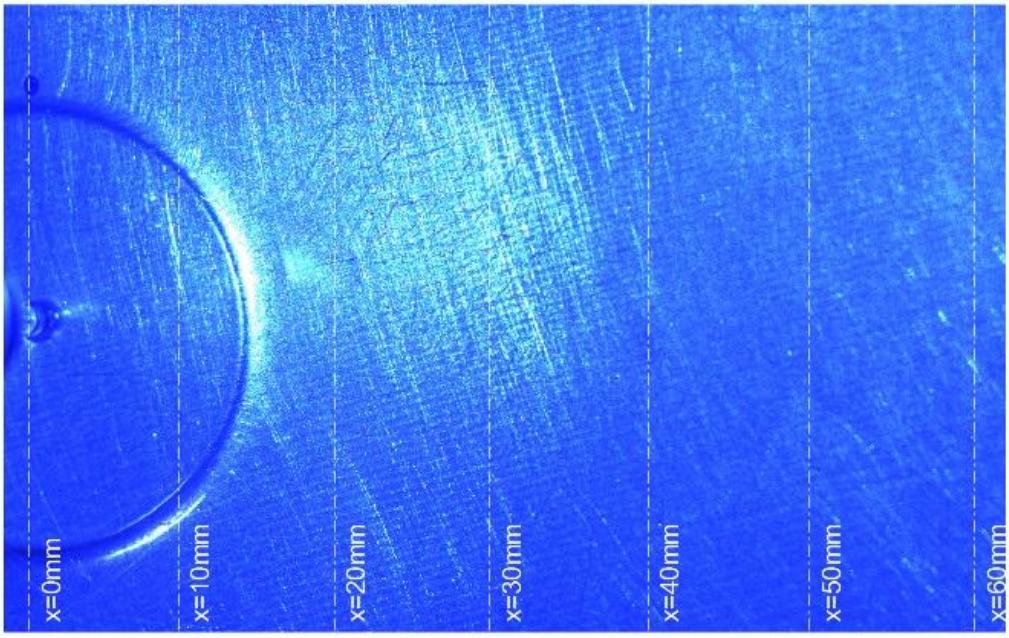

Figure 4.14 – Image (in real colours) of the impinging jet, detected by a RGB camera, without filters nor fluorescent dyes. The illuminated area is larger than the field of view of the camera.

4.2.2 Characterisation of the 2-dye mixtures

The aim of this section is to identify a potential fluorescence mixture for 2-colour 2-dye LIF. As introduced in section 2.3.2, the dyes are LUM345, PYR597 and PYR650. Their fluorescence spectrum is characterised with bench 1 and their absorption spectrum is measured with a cuvette spectrometer (Varian Cary 400 Spectrophotometer, *Spectralab Scientific Inc.*). A preliminary investigation with cuvette spectroscopy can be found in annexe to chapter 4.

- **Fluorescence spectrum, absorption spectrum and emission-reabsorption**

In Figure 4.15, the fluorescence spectra of the single dyes (LUM345, PYR597 and PYR650) are plotted for the concentration $C = 0.1$ mmol/L. The spectra of the 2-dye mixtures LUM345 + PYR597 and LUM345 + PYR650 are also plotted. All spectra are measured at 30 °C.

Considering the single dye emission, LUM345 has the highest intensity, followed by PYR650 and PYR597. These last two are poorly excited at $\lambda = 450$ nm with respect to LUM345, as their peak of intensity is only 20 % and 10 % of the LUM345 peak at $\lambda = 491$ nm.

Considering the mixture LUM345 + PYR597, the LUM345 local peak at $\lambda = 491$ nm is about 15 % than that of LUM345 alone. This is coherent as proportionality with the concentration is showed. Conversely, the LUM345 local peak at $\lambda = 523$ nm almost disappears, while the PYR597 peak at $\lambda = 573$ nm increases by 48 % with respect to the PYR597 alone. This occurrence is the evidence of emission-reabsorption between LUM345 and PYR597.

The same emission-reabsorption is less pronounced for the combination LUM345 + PYR650, for three reasons. First, the LUM345 peak at $\lambda = 491$ nm is about 20 % than that of LUM345 alone, thus proportional to the concentration of the single dye. Second, the LUM345 local peak at $\lambda = 523$ nm is still perceptible. Third, the PYR650 local peak at $\lambda = 612$ nm is only 8 % smaller than that of the single dye emission.

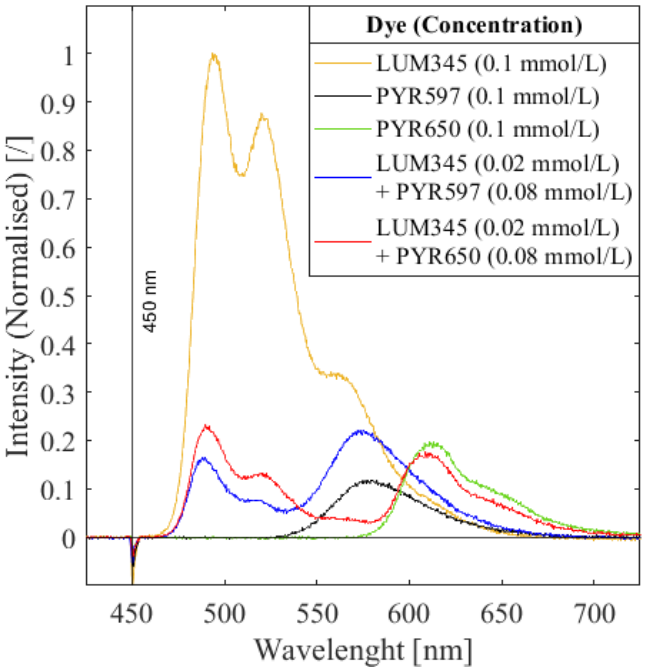

Figure 4.15 – Fluorescence spectrum of three individual dyes (LUM345, PYR597 and PYR650) and two 2-dye mixtures (LUM345 + PYR597 and LUM345 + PYR650), with 450 nm laser excitation and at 25°C

Figure 4.16 and Figure 4.17 show the absorption and emission spectra of each individual dye. These figures are complementary to the previous analysis and confirm the mutual interaction because the emission of LUM345 overlaps with the absorption of both PYR597 and PYR650. The overlapping band is larger for PYR597 than for PYR650 (about 85 nm and 130 nm respectively). The distance between the emission peak of LUM345 (λ = 520 nm) and the absorption peak of PYR597 (λ = 528 nm) is shorter than for PYR650 (λ = 590 nm). Consequently, even though the overlapping band is larger for PYR650, the proximity between the emission peak of LUM345 and the absorption peak of PYR597 suggests that the phenomenon of emission-reabsorption is expected to be more pronounced for a mixture of LUM345 and PYR597.

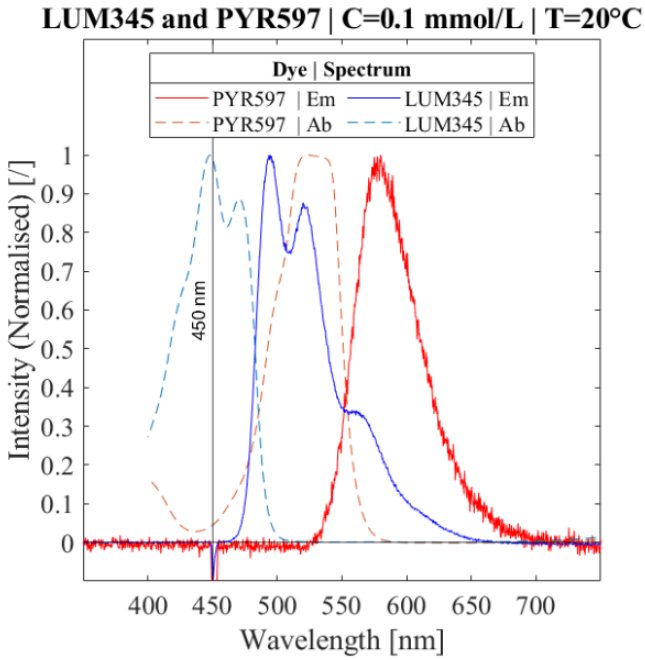

Figure 4.16 – Emission (Em) and absorption (Ab) spectra of two dyes LUM345 and PYR597.

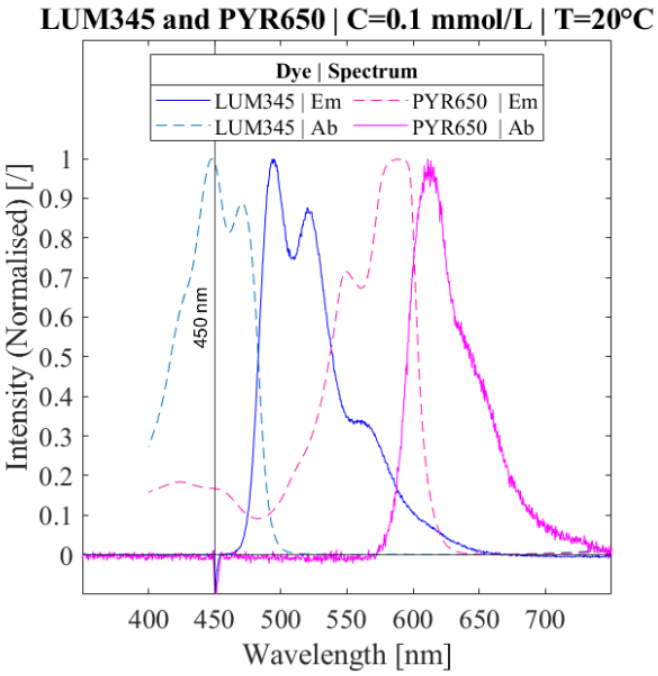

Figure 4.17 – Emission (Em) and absorption (Ab) spectra of two dyes LUM345 and PYR650.

In conclusion, the phenomenon of emission-reabsorption is more prominent in LUM345 + PYR597 than for LUM345 + PYR650. According to the observations by *Hidrovo* and *Hart* 2000 (see section1.3.3), the combination LUM345 + PYR650 is more suitable for temperature measurement whereas LUM345 + PYR597 is more suitable for thickness measurements. On the other hand, the emission of PYR650 is relatively weak (even if in larger proportions than LUM345) and the temperature sensitivity is smaller than that of PYR597. Nevertheless, both mixtures have potential for the 2-colour 2-dye LIF technique.

- **Thermal limits fluorescence loss**

In some experiments, not reported in this manuscript, inconsistencies in the fluorescence spectra are observed for $T > 110$ °C. The thermal endurance is therefore examined for each dye with the following protocol: (1) the fluorescence spectrum is measured at $T = 20$ °C, (2) the oil film is heated at $T = 130$ °C and the spectrum is measured at different time steps, (3) the oil film is cooled, and the spectrum is measured again at $T = 20$ °C. Figure 4.18 shows that LUM345 loses progressively its fluorescence and when restored to $T = 20$ °C the emission is almost zero.

The same test at $T = 130$ °C is performed for PYR597 and PYR650 and a loss of fluorescence is observed as well (results in annexe to chapter 4). The same test is performed for the three dyes at $T = 110$ °C, and in this case no fluorescence loss is observed (results in annexe to chapter 4). It follows that fluorescence degradation occurs permanently within $110\ °C < T < 130\ °C$.

Lastly, the fluorescence properties of LUM345 are lost when exposed to $T = 130$ °C. This could be a restricting factor for technical applications, as with jet impingement the local temperature of the fluid could pass the thermal limit of the dye.

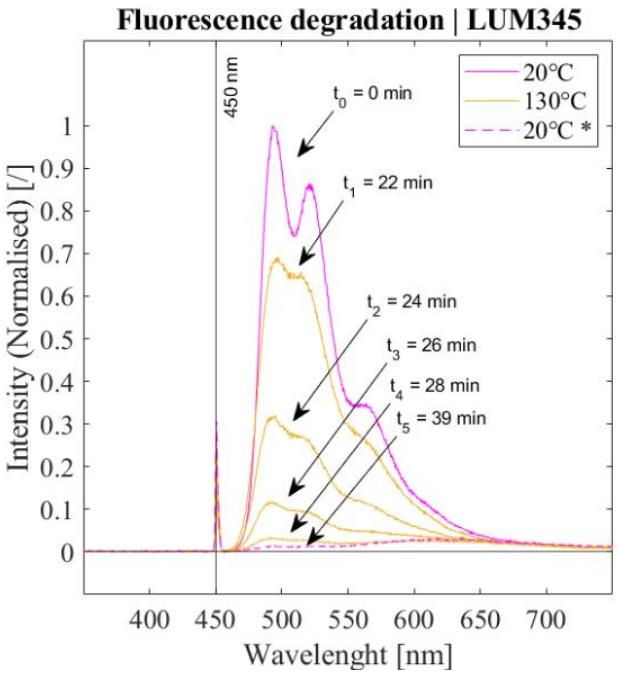

Figure 4.18 – Loss of fluorescence of the dye LUM345. Initial temperature T = 20 °C, exposure to T = 130 °C, and restoration to T = 20 °C (*).

- **Temperature dependence of the fluorescence spectra**

The fluorescence spectra of LUM345 + PYR597 and LUM345 + PYR650 are measured between T = 20 °C and T = 110 °C. The results are plotted in Figure 4.19 and Figure 4.20 respectively. The temperature sensitivity is evaluated through the ratio between the peak intensity at T = 110 °C and T = 20 °C. The ratio is about 0.7-0.8 for LUM345, 0.28 for PYR597 and 0.45 for PYR650. The variation of the peak intensity is therefore larger for the mixture LUM345 + PYR650. Additionally, this mixture features a wider separation of the local peaks of the two dyes. On the other hand, the peak of PYR650 is smaller than that of LUM345.

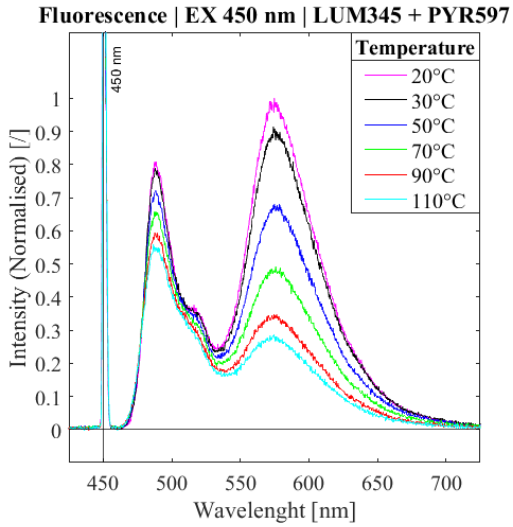

Figure 4.19 – Fluorescence spectrum at different temperatures of the mixture LUM345 + PYR597 (0.02 mmol/L and 0.08 mmol/L, respectively) measured with bench 1.

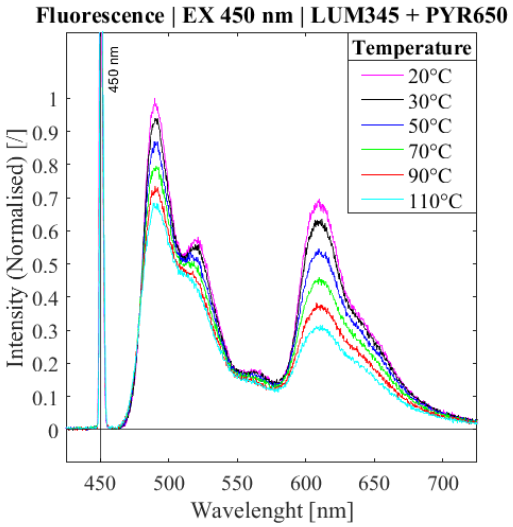

Figure 4.20 – Fluorescence spectrum at different temperatures of the mixture LUM345 + PYR650 (0.02 mmol/L and 0.08 mmol/L, respectively) measured with bench 1.

4.3 Temperature and thickness sensitivity with RGB camera on static films

4.3.1 Establishment of the imaging method

In this section the imaging method with the RGB camera is established, through a qualitative analysis of the images of a static film and by introducing a method for quantitative analysis based on a region of interest (ROI). The intensity collected in the individual channels and the channel ratio *Red/Blue* are examined. The details on the optical setups and the image processing are in the previous sections 2.3.2 and 2.3.3. Bench 1 is used (with the negative lenses and the aperture), along with the two fluorescent mixtures (LUM345 + PYR597 and LUM345 + PYR650, with relative dye concentration 0.02 mmol/L and 0.08 mmol/L), the exposure time is set to t_{exp} = 3 ms, 25 images are used for averaging, and the background images with pure oil are used.

- **Qualitative analysis**

Figure 4.21, Figure 4.22 and Figure 4.23 are examples of the averaged and background-corrected intensity *Red*, *Green* and *Blue*, at T = 20 °C. In the images the fluorescence signal comes from the illuminated region and is almost zero outside, showing overall coherence with the expectations. Diffraction patterns (e.g., ripples) are recognised along the contour of the illumination disk and within the illuminated region. These are attributed to the interaction of the excitation light with the mechanical aperture and some dust on the optics (before hitting the film). They can be reduced by enlarging the aperture and by cleaning the optics. Moreover, the thermocouple for measuring the film temperature can be seen on the upper left part of the image.

The ratio of *Red* and *Blue* is the channel ratio *Red/Blue*, as in Figure 4.24. The channel ratio is expected to be homogenous due to the principles of the ratiometric approach. The channel ratio is relatively homogenous in the centre of the image, even though some diffraction patterns are still present, while it is not close to the contour of the illumination disk. Outside the illumination disk, the value increases abruptly because the intensity in *Blue* is almost zero.

Figure 4.25 is the plot of the data points extracted from a thin horizontal strip of pixels at the centre of the images, extracted from Figure 4.21, Figure 4.22, Figure 4.23 and Figure 4.24. On the left side of the image, and within the range 200 < pixel < 1600, *Red*, *Green*, and *Blue* exhibit intensity fluctuations for the same pixel location, probably due to the diffraction patterns. Outside of this range, the signal is almost zero, because corresponding to the region outside the illumination disk. Within the illuminated region (200 < pixel < 1600), *Red/Blue* is relatively uniform, as confirmed by a ≈ 5 % standard deviation calculated along the profile between pixels.

This qualitative analysis indicates that the detected fluorescence signal comes almost exclusively from the fluorescent mixture and that the background correction is correct. Also, the channel ratio is coherent with the expectations as it shows independence from the intensity of the illumination. Lastly, the images show some noise and spatial fluctuations, which are investigated through dedicated analysis in the following sections.

Example of measurements for the experiment using bench 1 (with mechanical aperture and negative lenses), LUM345 + PYR597, camera acA1920-50gc, and exposure time t_{exp} = 3 ms.

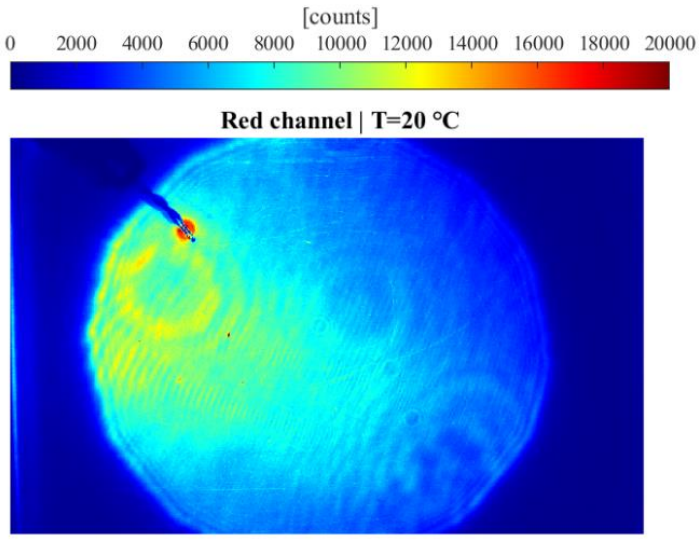

Figure 4.21 – *Red* channel.

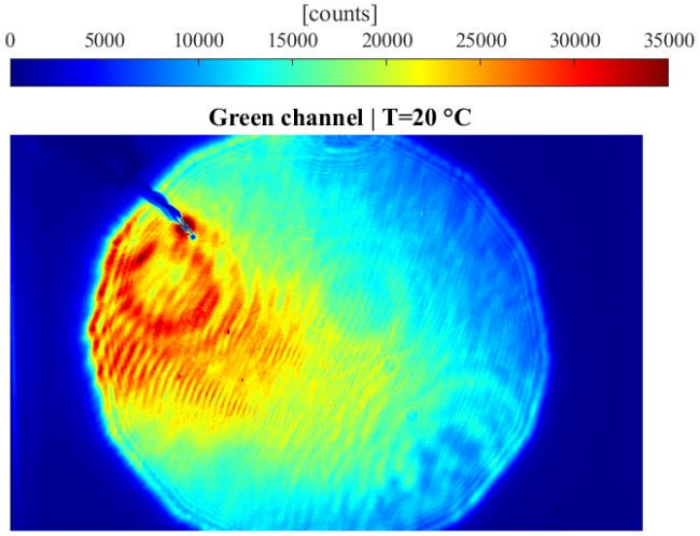

Figure 4.22 –*Green* channel.

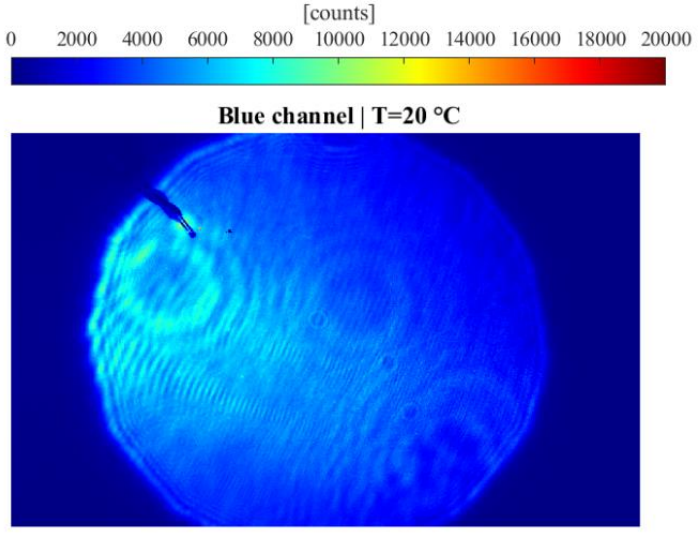

Figure 4.23 – *Blue* channel.

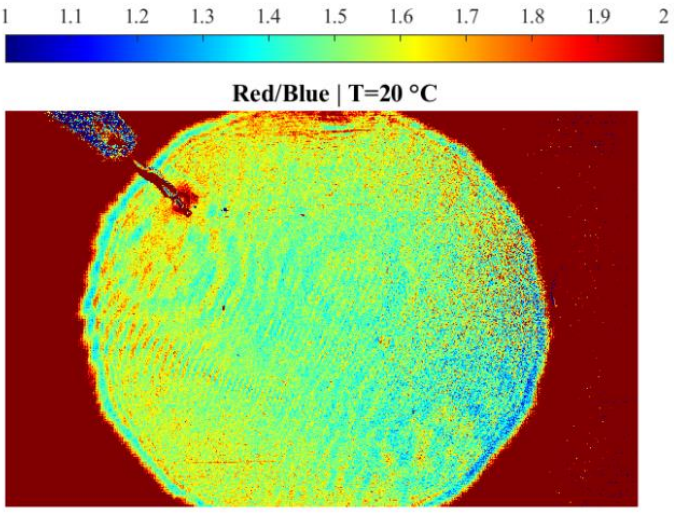

Figure 4.24 – Channel ratio *Red/Blue*.

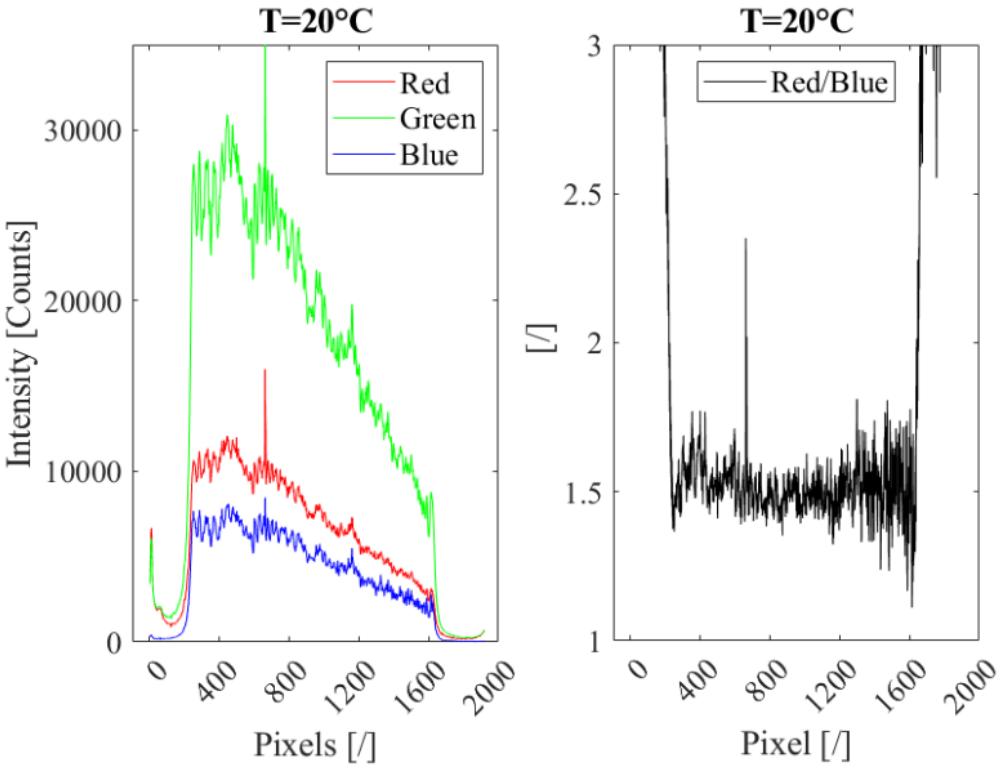

Figure 4.25 – Profile of *Red*, *Green* and *Blue* channel, and channel ratio *Red/Blue*.

- **Quantitative analysis for temperature sensitivity**

The pixel data are extracted from a 200 x 200 pixel ROI at the centre of the image (Figure 4.26). The mean and standard deviation between the pixels of the ROI is calculated for *Red*, *Green*, and *Blue* and is plotted in Figure 4.27 for different temperatures. Considering T = 20 °C, the intensity in *Red* and in *Blue* with LUM345 + PYR650 are 35 % and 25 % larger, than with LUM345 + PYR597. Considering sensitivity to temperature, Table 4.1 shows that temperature sensitivity is larger in *Red* than in *Blue* regardless the mixture. Additionally, the temperature sensitivity is larger with LUM345 + PYR597 than with LUM345 + PYR650 in channel *Green* and *Red*, and is similar in channel *Blue*. It

follows that even if the camera used in the given experiment detects a larger signal with LUM345 + PYR650, the temperature sensitivity of the individual channels is larger with LUM345 + PYR597.

This quantitative analysis using a ROI shows that the intensity of each channel varies with temperature, at different rates depending on the mixture and channel. In general, the sensitivity is larger in *Red* than in *Blue*. This outcome is encouraging for temperature and thickness measurements because *Red* is sensitive to temperature, thus it is useful for temperature measurements, while *Blue* is insensitive to temperature, thus it is useful for thickness measurement. Moreover, more temperature sensitivity is obtained using the mixture LUM345 + PYR597 rather than LUM345 + PYR650.

In conclusion, the imaging method is therefore established, the results are coherent with the expectations, on both a qualitative and quantitative point of view. From this step, a deeper analysis can be undertaken to evaluate the sensitivity of the method to temperature and thickness of the oil film.

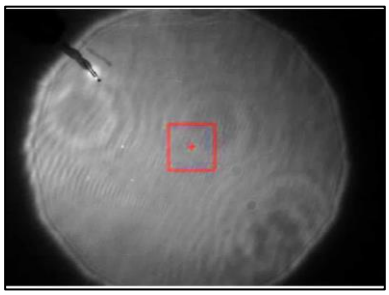

Figure 4.26 – Position and size of a 200 x 200 pixel ROI, for the experiment: LUM345 + PYR597 (0.02 mmol/L and 0.08 mmol/L), camera acA1920-50gc, and exposure time t_{exp} = 3 ms. Bench 1 is used.

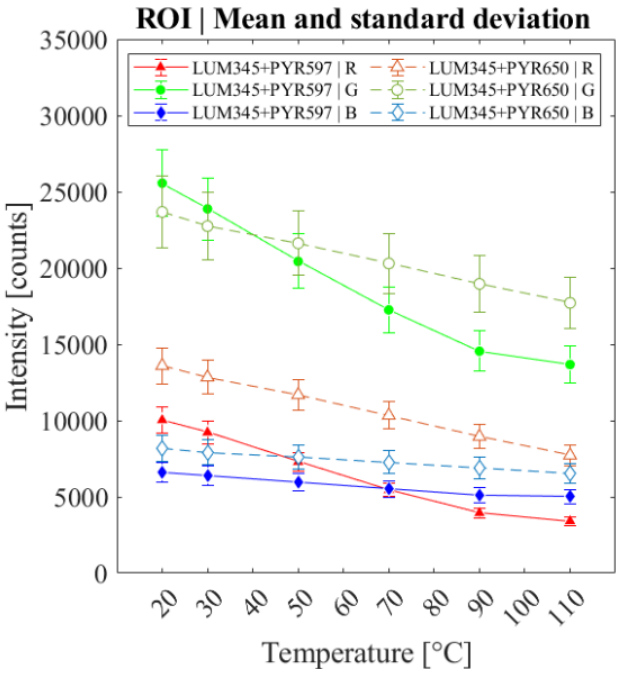

Figure 4.27 – Example of ROI analysis of *Red*, *Green* and *Blue* channel. The averaged and background-corrected intensity plotted, for two experiments: LUM345 + PYR597 and LUM345 + PYR650 (0.02 mmol/L and 0.08 mmol/L), camera acA1920-50gc, and exposure time t_{exp} = 3 ms. Bench 1 is used.

Table 4.1 – Temperature sensitivity for different dye mixtures. Example of ROI analysis for the channels *Red, Green, and Blue*. Experiments: LUM345 + PYR597 and LUM345 + PYR650 (0.02 mmol/L and 0.08 mmol/L), camera acA1920-50gc, and exposure time t_{exp} = 3 ms. Bench 1 is used.

CAMERA	MIXTURE	CHANNEL	TEMPERATURE SENSITIVITY
[model]	[dye 1 + dye 2]	[Red, Green , Blue]	[counts / °C / ms]
acA1920-50gc	LUM345+PYR597	Red	– 74
		Green	– 132
		Blue	– 35
	LUM345+PYR650	Red	– 65
		Green	– 66
		Blue	– 18

Temperature sensitivity = $\frac{Channel(110\,°C) - Channel(20\,°C)}{110\,°C - 20\,°C} \frac{1}{t_{exp}}$

4.3.2 Channel ratio and temperature sensitivity

As explained in section 1.3.3 and 2.3.4, the principle of the ratiometric approach is that the variation of the channel ratio *Red/Blue* can be associated with a variation of the temperature, thus it is important to have a large temperature sensitivity. In this section, the sensitivity to temperature of the channel ratio is therefore quantified with the aim of comparing the ideal sensitivity to the actual sensitivity obtained in this research. Relying on the experimental spectra of Figure 4.19 and Figure 4.20, the temperature sensitivity of the channel ratio *Red/Blue* is evaluated with three different approaches.

(i) Simulate detection with ideal camera

This approach considers an ideal camera, with 100 % detection efficiency regardless the wavelength, and whose two channels *Red* and *Blue* are perfectly separated by a cut-off wavelength.

(ii) Simulate detection with RGB camera

This approach is more representative of the real detection, which is simulated considering the nominal spectral response of a real RGB camera and the experimental fluorescence spectra. In this case, the channels *Red* and *Blue* partially overlap and the detection efficiency depends on the wavelength. Two camera models are considered: a2A1920-160ucPRO and acA1920-50gc (details in section 2.3.2).

(iii) Detect with real RGB camera

This approach is the output from experimental detection with a real RGB camera of the fluorescence emission of thin static films, obtained with bench 1.

- **Simulated detection with ideal camera and with RGB camera**

For approach (i), the cut-off wavelength of the channels *Blue* and *Red* of the ideal camera is defined as the wavelength which divides the high- and low-temperature sensitivity of the fluorescence spectrum. Referring to previous Figure 4.19 and Figure 4.20 the ratio of the fluorescence intensity at $T = 110$ °C and at $T = 20$ °C is calculated and plotted in Figure 4.28, for LUM345 + PYR597 and LUM345 + PYR650. The higher the ratio the more the more the temperature insensitivity, and conversely the lower the ratio the more the temperature sensitivity. Taking arbitrarily 0.7 as the discriminant value, the cut-off wavelength for LUM345 + PYR597 is set at $\lambda = 536$ nm and at $\lambda = 590$ nm for LUM345 + PYR650. If only one cut-off wavelength is to set for both mixtures, $\lambda = 536$ nm is considered. Consequently, the ideal camera features a channel *Blue* within 400 nm < λ < 536 nm and a channel *Red* within 536 nm < λ < 750 nm. Subsequently, the fluorescence spectra in Figure 4.19 and Figure 4.20 are interpolated between 400 nm < λ < 750 nm and integrated within the two channels. The result of the integration is plotted in Figure 4.30 as the channel ratio *Red/Blue* and the temperature.

For simulating camera detection with approach (ii), the nominal spectral response of the camera models a2A1920-160ucPRO and acA1920-50gc are considered, as well as the fluorescence emission of LUM345 +PYR597 and LUM345 +PYR650 from the previous Figure 4.19 and Figure 4.20. An example of spectral response is given in Figure 4.29, and all the camera-mixture combinations are found in annexe to chapter 4. First, every fluorescence spectrum and camera spectral response are interpolated between

400 nm < λ < 750 nm. Subsequently, the values at the same wavelength are multiplied to simulate the fluorescence intensity detected by the camera. This last is integrated within 400 nm < λ < 750 nm and the channel ratio *Red/Blue* is plotted against temperature in Figure 4.30. The traces of the intermediate calculations are in annexe to chapter 4.

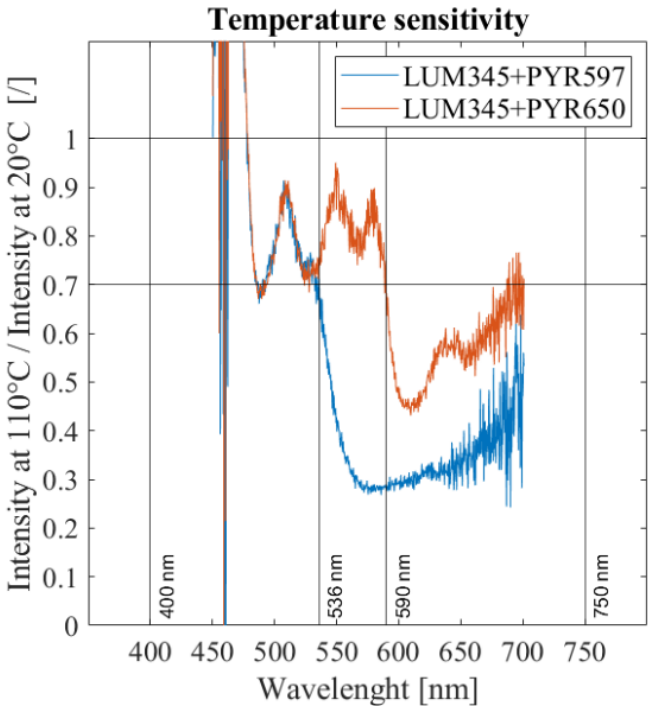

Figure 4.28 – Ratio between the fluorescence intensity at 110 °C and at 20 °C, for the mixtures LUM345 + PYR597 and LUM345 + PYR650 (Excitation λ = 450 nm).

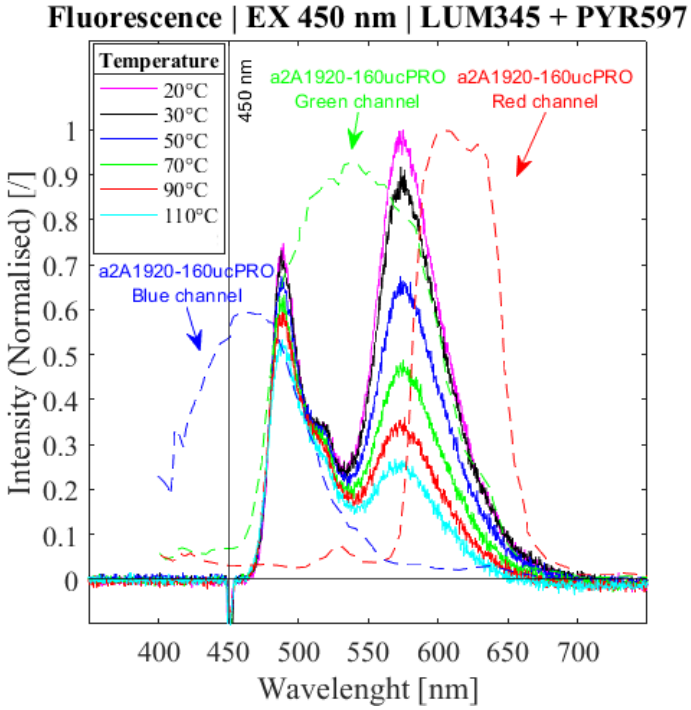

Figure 4.29 – Fluorescence spectrum of the mixture LUM345 + PYR597 (0.02 mmol/L and 0.08 mmol/L, respectively), excited with a 450 nm laser, and measured with bench 1. The nominal spectral response of the RGB camera a2A1920-160ucPRO is plotted over for each channel.

In Figure 4.30, the results from the two simulative approaches (i) and (ii) are plotted as *Red/Blue* for different temperatures and two observations can be made about the mixtures. The first observation is that if temperature increases, the *Red/Blue* ratio decreases, regardless the solutions used. This is coherent because the fluorescence emission of PYR597 and PYR650 decreases with increasing temperature. The second observation is that temperature sensitivity is larger with LUM345 + PYR597 than with LUM345 + PYR650, in reason of the larger variation (approximately 0.38 < *Red/Blue* < 1 and 0.60 < *Red/Blue* < 1 respectively).

Concerning the camera-mixture combinations, Figure 4.30 shows various outcomes. The three traces for LUM345 + PYR597 overlap in the whole temperature range, while more differences between the traces are exhibited for LUM345 + PYR650. In the case of LUM345 + PYR597, this means that detecting with a RGB camera is already as efficient as with the ideal camera with perfect filters and detection. In the case of LUM345 + PYR650, the ideal camera with perfect filters and detection has the smallest temperature sensitivity (0.72 < *Red/Blue* < 1), the camera a2A1920-160ucPRO has the largest sensitivity (0.60 < *Red/Blue* < 1), and the camera acA1920-50gc is between the two (0.66 < *Red/Blue* < 1).

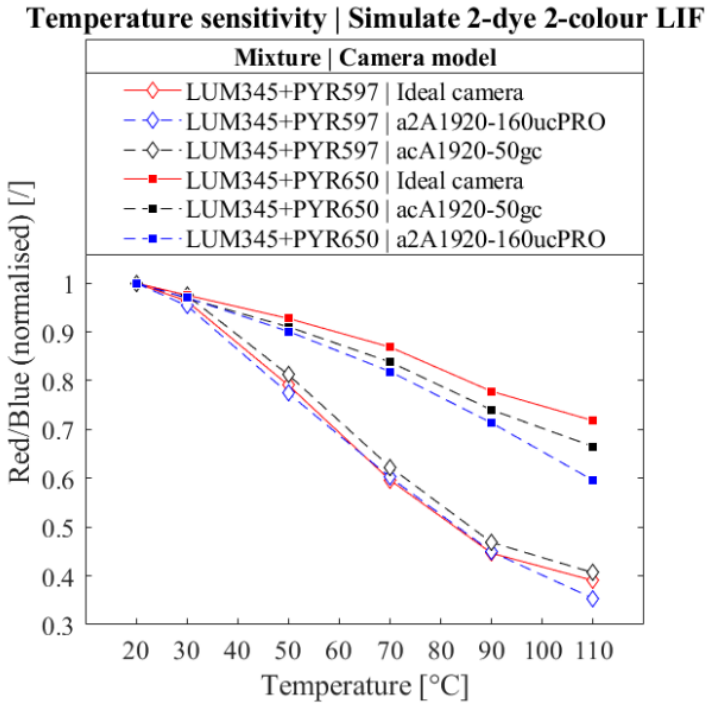

Figure 4.30 – Simulated temperature sensitivity combining two dye mixtures (LUM345 + PYR597 and LUM345 + PYR650) with three cameras (Ideal camera, a2A1920-160ucPRO and acA1920-50gc).

- **Temperature sensitivity in experimental detection with an RGB camera**

Using the imaging method established in previous section 4.3.1, the results from the experimental approach (iii) are hereby compared with the approaches (i) and (ii). In Figure 4.31 and Figure 4.32, the temperature variation of *Red/Blue* is plotted for different combinations of dye mixtures and approaches.

In both Figure 4.31 and Figure 4.32, all the traces have similar trend, as *Red/Blue* is the highest at T = 20 °C and the lowest at T = 110 °C. Concerning the experimental traces, the two overlap in the whole temperature range in Figure 4.31, while more differences are observed in Figure 4.32. Concerning the difference between the experimental traces and

the simulated traces is more pronounced for increasing temperature for both figures. Concerning temperature sensitivity, Table 4.2 shows that LUM345 + PYR597 has larger temperature sensitivity, regardless the approach.

To summarise the findings of Figure 4.31 and Figure 4.32, the figures show overall good agreement between the simulations and the experimental results. Moreover, they confirm that temperature sensitivity of the channel ratio *Red/Blue* is larger with LUM345 + PYR597, regardless the camera model.

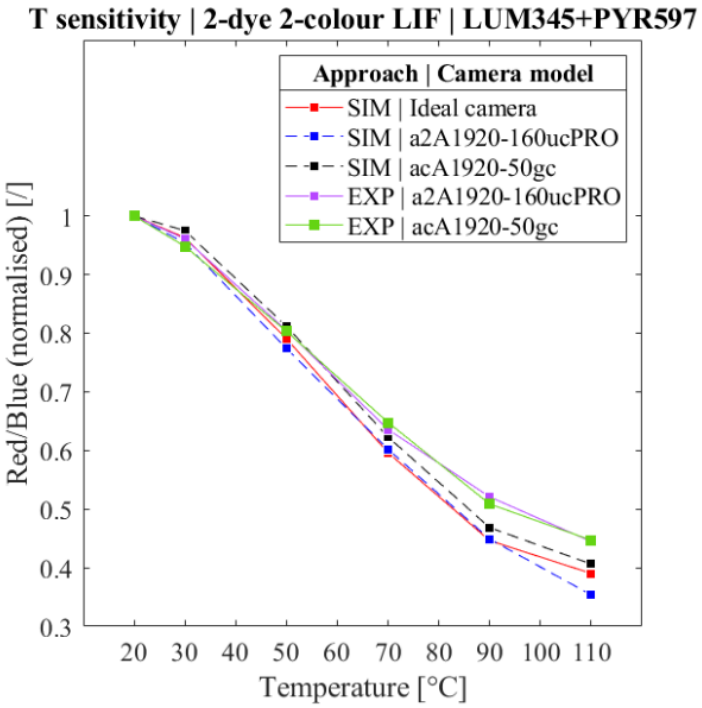

Figure 4.31 – Temperature sensitivity with LUM345 + PYR597 for different RGB cameras and approaches.

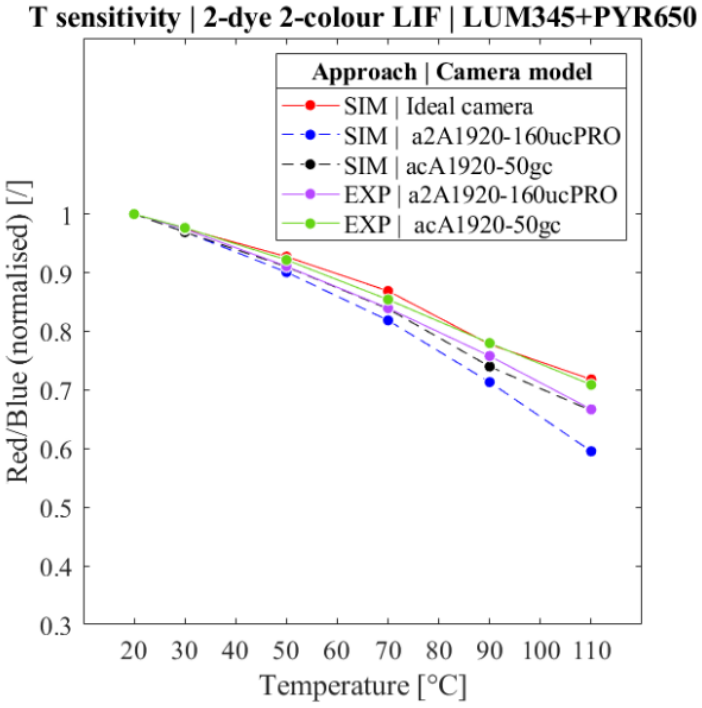

Figure 4.32 – Temperature sensitivity with LUM345 + PYR650 for different RGB cameras and approaches.

Table 4.2 – Temperature sensitivity for different combinations of mixture, RGB cameras and approaches.

MIXTURE	APPROACH	CAMERA	TEMPERATURE SENSITIVITY OF Red/Blue
[dye 1 + dye 2]	[SIM or EXP]	[model]	[1000 x °C $^{-1}$]
LUM345 + PYR597	SIM	Ideal camera	− 6.8
		a2A1920-160ucPRO	− 7.2
		acA1920-50gc	− 6.6
	EXP	a2A1920-160ucPRO	− 6.2
		acA1920-50gc	− 6.1
LUM345 + PYR650	SIM	Ideal camera	− 3.1
		a2A1920-160ucPRO	− 4.5
		acA1920-50gc	− 3.7
	EXP	a2A1920-160ucPRO	− 3.7
		acA1920-50gc	− 3.2
Temperature sensitivity = $\frac{R/B(110\,°C) - R/B(20\,°C)}{110\,°C - 20\,°C}$			

- **Discussion**

The temperature sensitivity is evaluated for the two dye mixtures LUM345 + PYR597 and LUM345 + PYR650 by comparing numerical and experimental approaches. Overall good agreement is found between the simulations and the experimental datapoints.

Two important achievements are reported in this section. The first is that the imaging method allows characterisation of the temperature from fluorescence intensity detection. The second is that simulating detection is a reasonable method for predicting the sensitivity of a fluorescent specimen, relying on representative experimental fluorescence spectra and nominal spectral response of the camera.

Concerning the temperature sensitivity of the optical method, this is influenced by the mixture and the RGB camera. The mixture LUM345 + PYR597 has always larger temperature sensitivity than LUM345 + PYR650, regardless of the camera. The camera acA1920-50gc detects more intensity with LUM345 + PYR650 than with LUM345 + PYR597 (with the same camera settings and experimental setup). The camera a2A1920-160ucPRO allows more temperature sensitivity than acA1920-50gc, when using the mixture LUM345 + PYR650 (for LUM345 + PYR597 minor differences are observed). The results help for the selection of the best mixture-camera combination for simultaneous temperature and thickness measurements.

4.3.3 Thickness and temperature sensitivity with step plate

This section provides a complementary analysis to the previous by taking into account the sensitivity to the thickness δ of the liquid film. The evaluation is undertaken with bench 1 and the step plate (see section 2.3.2). The experiments are performed with the camera

model acA1920-50gc, using mixture LUM345 + PYR597 and LUM345 + PYR650, within the temperature range 20 °C < T < 110 °C.

- **Thickness and temperature sensitivity of the channels *Red* and *Blue***

The intensity of *Red*, and *Blue* is extracted from ten different ROI, corresponding to each step plate, as illustrated in Figure 4.33. The mean value and standard deviation of the pixels of each ROI are plotted in Figure 4.34, Figure 4.35, Figure 4.36 and Figure 4.37, for the channels *Red* and *Blue*, for the mixtures LUM345 + PYR597 and LUM345 + PYR650, and for increasing temperature and thickness of the oil film.

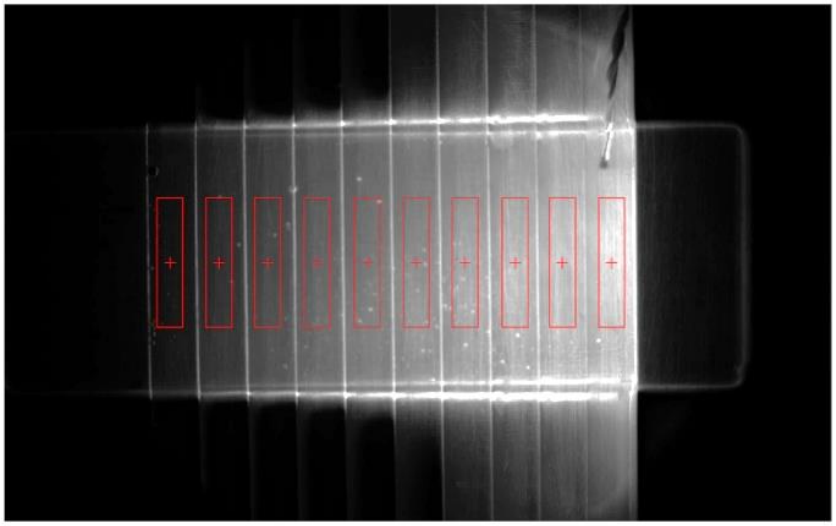

Figure 4.33 – Position and size of ten 60 x 300 pixel ROI. The film thickness increases from left to right.

For every figure and trace, increasing thickness increases the intensity, while increasing temperature decreases the intensity. The traces exhibit an almost linear trend within 0.2 mm < δ < 3 mm, thus optically thin behaviour is exhibited. Conversely, for δ > 3 mm, the trace is no longer proportional meaning that optically thick behaviour is shown.

The sensitivity to thickness and temperature of every channel is reported in

Table 4.3. For both mixtures, *Red* is more sensitive to thickness than *Blue* (by 1.8 times for LUM345 + PYR650 and 3.1 times for LUM345 + PYR597). LUM345 + PYR597 is about 1.1 times more sensitive to thickness in the *Red* channel, whereas LUM345 + PYR650 is 1.5 times more sensitive in the *Blue* channel. Increasing temperature reduces sensitivity in *Blue*: from T_{oil} = 20 °C to T_{oil} = 110 °C, – 21 % for LUM345 + PYR650 and – 32 % for LUM345 + PYR597. Considering the typical injection temperature investigated in this research (60 °C < T_{oil} < 110 °C) and the expected temperature variation along the x axis (about 10 °C), the increase in temperature should reduce slightly (about – 6%) the sensitivity to thickness in *Blue*. Consequently, *Blue* can be considered unaffected by temperature.

These results indicate that given the larger temperature sensitivity in *Red* of LUM345 + PYR597, this mixture is more suitable for temperature measurement, whereas larger thickness sensitivity in *Blue* of LUM345 + PYR650 is more suitable for thickness measurements.

Intensity measured for increasing thickness and temperature. Bench 1 is used with the step plate.

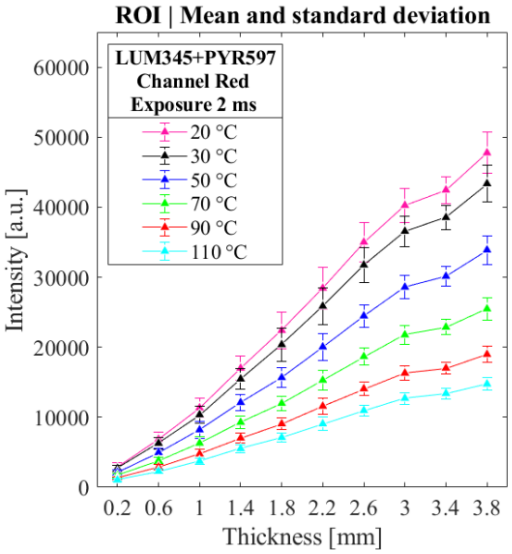

Figure 4.34 – Channel *Red* and LUM345 + PYR597.

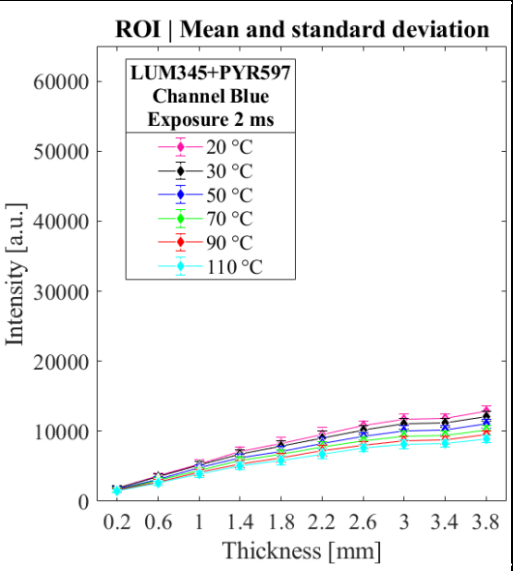

Figure 4.35 – Channel *Blue* and LUM345 + PYR597.

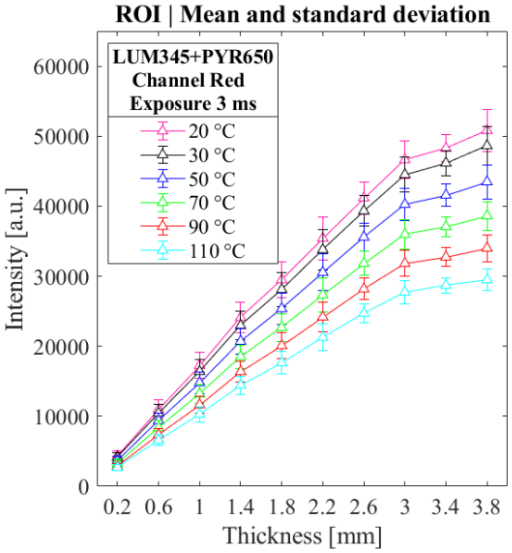

Figure 4.36 – Channel *Red* and LUM345 + PYR650.

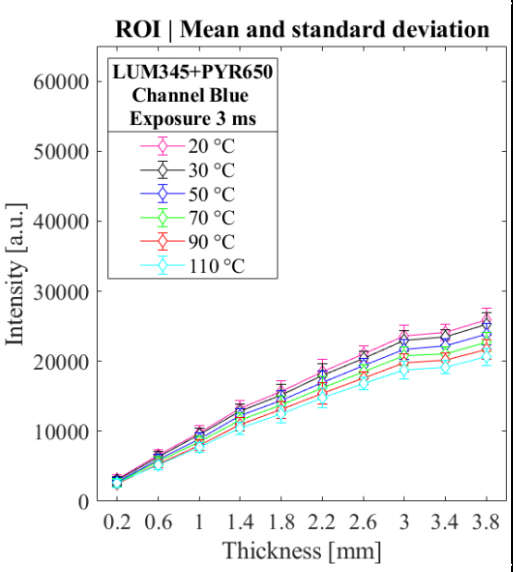

Figure 4.37 – Channel *Blue* and LUM345 + PYR650.

Table 4.3 – Mean thickness sensitivity in channels *Red* and *Blue*.

	LUM345+PYR597		LUM345+PYR650	
	Red	***Blue***	***Red***	***Blue***
Temperature	**THICKNESS SENSITIVITY**	**THICKNESS SENSITIVITY**	**THICKNESS SENSITIVITY**	**THICKNESS SENSITIVITY**
[°C]	**[Counts / mm / ms]**	**[Counts / mm / ms]**	**[Counts / mm / ms]**	**[Counts / mm / ms]**
20	6224	1516	4305	2108
30	5648	1425	4123	2066
50	4408	1288	3687	1947
70	3305	1184	3275	1860
90	2457	1102	2884	1779
110	1904	1035	2481	1669

Thickness sensitivity = $\frac{Channel(3.8\ mm) - Channel(0.2\ mm)}{3.8\ mm - 0.2\ mm} \frac{1}{t_{exp}}$

- **Sensitivity to thickness and temperature of the channel ratio *Red/Blue***

The thickness and temperature dependence of *Red/Blue* is shown in Figure 4.38 and Figure 4.39, for LUM345 + PYR597 and LUM345 + PYR650, respectively. Figure 4.38 shows that the typical trend is linear with thickness within 0.2 mm < δ < 3 mm, while the slope tends to flatten within 3 mm < δ < 3.8 mm. Similarly, in Figure 4.39 the typical trend is linear with thickness in most of the investigated range (0.2 mm < δ < 3.4 mm).

For a better comparative analysis, the sensitivity of *Red/Blue* to either thickness or temperature is evaluated and compared in a normalised form in Table 4.4 and Table 4.5 (using the data points from Figure 4.38 and Figure 4.39). The mixture LUM345 + PYR597 is twice as sensitive as LUM345 + PYR650 (about 1.8 times for temperature and 2.1 times for thickness). For increasing thickness, both mixtures lose sensitivity to temperature, but this is much more pronounced LUM345 + PYR597. Similarly, for increasing temperature, both mixtures lose sensitivity to thickness.

The variation of *Red/Blue* per unit of thickness or temperature can be exploited to evaluate the expected variation of the channel ratio for the impinging, combining the measurement of section 4.1 and the data from this section. Considering a nozzle diameter d = 2 mm and a field of view of 60 mm from the impingement point, the expected temperature and thickness variations are about + 10 °C and + 3 mm. If the mixture LUM345 + PYR597 is used, this corresponds to a variation of *Red/Blue* of – 0.045 due to temperature and + 0.48 due to thickness. For LUM345 + PYR650, the expected variation is – 0.025 due to temperature and + 0.22 due to thickness. In both cases, the variation of *Red/Blue* due to thickness is about 10 times larger than the variation due to temperature. Also, LUM345 + PYR597 is almost twice more sensitive than LUM345 + PYR650.

In conclusion, LUM345 + PYR597 is a better option given the expected variations of thickness and temperature of the impinging jet. Despite that, the measurements presented for the impinging jet in the following parts of this manuscript are taken using LUM345 + PYR650. At the time of the selection of one of the mixtures, there was lack of measurements of the typical variations of thickness and temperature of the impinging jet, thus the less pronounced mutual interaction was the main criterion for selection.

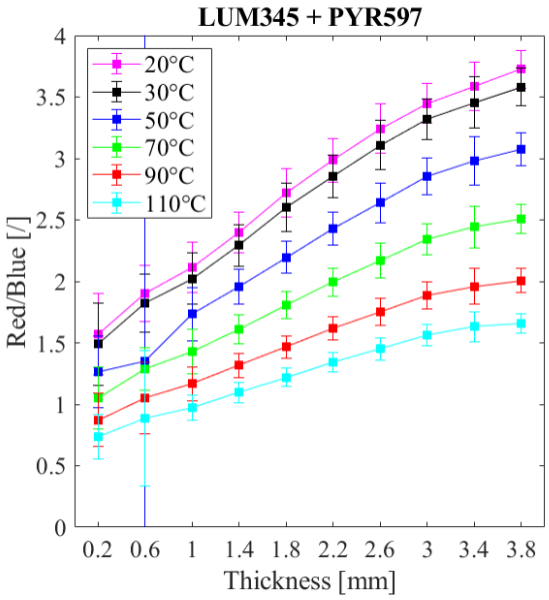

Figure 4.38 – Channel ratio *Red/Blue* for increasing temperature and thickness. Experiment: mixture LUM345 + PYR597, camera acA1920-50gc, and exposure time t_{exp} = 2 ms. Bench 1 is used, mounting the step plate.

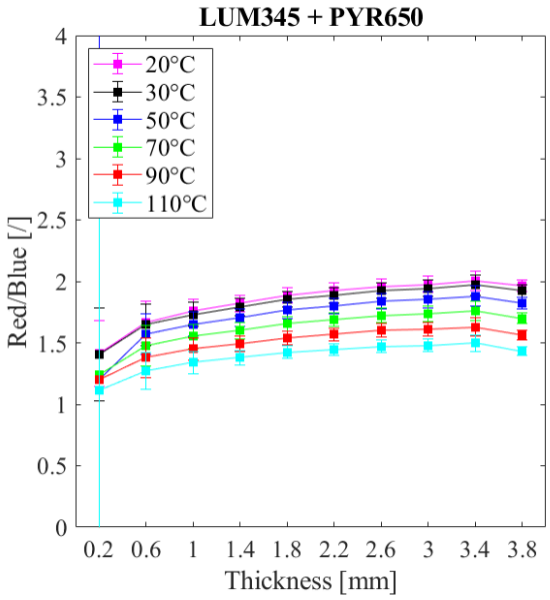

Figure 4.39 – Channel ratio *Red/Blue* for increasing temperature and thickness. Experiment: mixture LUM345 + PYR650, camera acA1920-50gc, and exposure time t_{exp} = 3 ms. Bench 1 is used, mounting the step plate.

Table 4.4 – Thickness sensitivity evaluated for the channel ratio *Red/Blue*, at different temperatures. Experiments: LUM345 + PYR597 and LUM345 + PYR650, camera acA1920-50gc, and exposure time t_{exp} = 2-3 ms. Bench 1 is used, mounting the step plate.

CAMERA	MIXTURE	T_{oil}	δ SENSITIVITY
[model]	**[dye 1 + dye 2]**	**[°C]**	**[mm $^{-1}$]**
acA1920-50gc	LUM345 + PYR597	20	0.1607
		30	0.1623
		50	0.1635
		70	0.1610
		90	0.1570
		110	0.1539
	LUM345 + PYR650	20	0.0780
		30	0.0750
		50	0.0945
		70	0.0750
		90	0.0640
		110	0.0623

Thickness sensitivity = $\frac{Red/Blue(3.8\ mm) - Red/Blue(0.2\ mm)}{(3.8\ mm - 0.2\ mm)\ (Red/Blue(3.8\ mm,\ \ 20\ °C))}$

Table 4.5 – Temperature sensitivity evaluated for the channel ratio *Red/Blue*, at different thicknesses. Experiments: LUM345 + PYR597 and LUM345 + PYR650, camera acA1920-50gc, and exposure time t_{exp} = 2-3 ms. Bench 1 is used, mounting the step plate.

CAMERA	MIXTURE	δ	T_{oil} SENSITIVITY
[model]	[dye 1 + dye 2]	[mm]	[1000 x °C^{-1}]
acA1920-50gc	LUM345+PYR597	0.2	– 6.2
		0.6	– 5.8
		1.0	– 5.6
		1.4	– 5.4
		1.8	– 4.9
		2.2	– 4.5
		2.6	– 3.9
		3.0	– 3.4
		3.4	– 3.0
		3.8	– 2.5
	LUM345+PYR650	0.2	– 3.0
		0.6	– 2.8
		1.0	– 2.8
		1.4	– 2.8
		1.8	– 2.6
		2.2	– 2.6
		2.6	– 2.4
		3.0	– 2.3
		3.4	– 2.2
		3.8	– 1.7
Temperature sensitivity = $\frac{Red/Blue(110\,°C) - Red/Blue(20°C)}{(110\,°C - 20\,°C)\,(Red/Blue(3.8\,mm,\ 20\,°C))}$			

4.4 Uncertainty analysis

4.4.1 Pointwise analysis of uncertainty

The uncertainty on temperature is evaluated with a pointwise analysis, that is, considering the intensity fluctuations of individual pixels. Bench 1 with the beam homogeniser (see section 2.3.2) and the mixture LUM345 + PYR650 are used.

- **Intensity fluctuation**

The data from six pixels located as in Figure 4.40 are extracted from 25 successive images of the oil film. The measured intensity *I* is background-corrected in every channel and no image averaging is performed, except for the images used for the background, according to the formulation below (for one of the three channels):

$$Red' = \left[I - \langle I_{background} \rangle\right]_{Red\ channel} \qquad (29)$$

The outcome is plotted in Figure 4.41 for every channel. Notice that one of the selected pixels is outside of the illuminated region and is used as a control pixel, where intensity is expected to be small and uncertainty significant. Considering the intensity of the individual pixels in Figure 4.41, the difference between successive images is relatively small. The typical standard deviation is 0.9-1.1 % regardless the channel, the temperature of the oil

film or the pixel. Conversely, the overall intensity varies significantly from a pixel to another (up to a factor 2) and cannot be attributed to photon noise but likely to a significant difference in the excitation light intensity. Notice that the pointwise analysis undertaken with *Red'* and *Blue'* is necessary to evaluate the uncertainty related to time variant phenomena. *Red* and *Blue* are time-averaged values but these two are actually used to evaluate thickness and temperature of liquid films (as in the following sections of the manuscript).

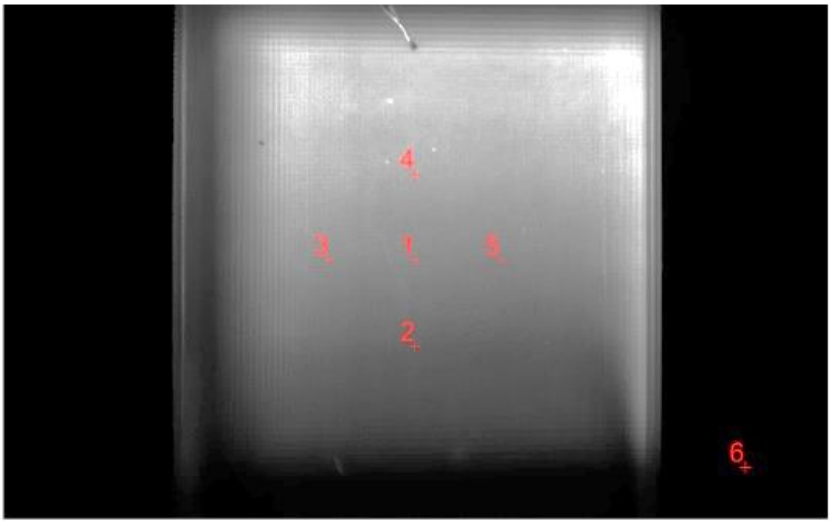

Figure 4.40 – Position of the six pixels used for the pointwise analysis.

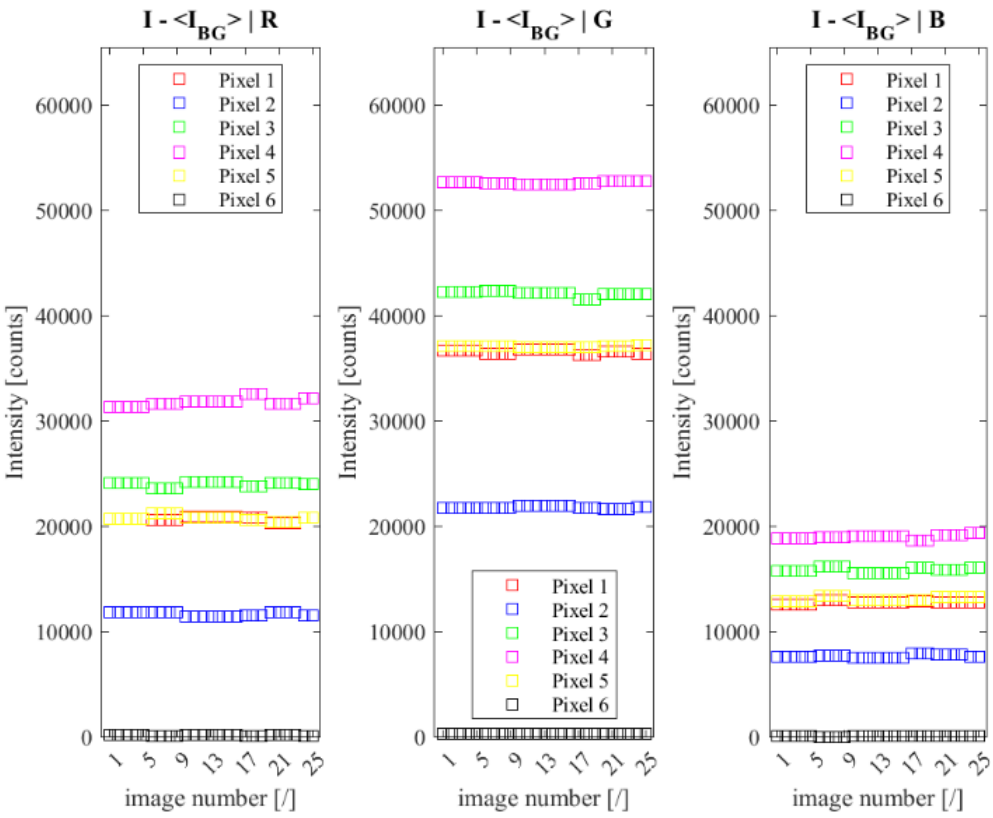

Figure 4.41 – Intensity measured during a sequence of 25 images by six different pixels, in the three channels *Red*, *Green* and *Blue*.

- **Methods for characterising pointwise uncertainty**

Using the data from Figure 4.41, two equivalent methods are used to evaluate the uncertainty of each pixel (in % of the intensity), namely, a direct method and an indirect method. In the direct method, the channel ratio *Red'/Blue'* is calculated for each pixel and image. Subsequently, the mean and standard deviation of *Red/Blue* between the 25 images is calculated, and their ratio gives the relative standard deviation (STD) is calculated. The formulations below are used for a single pixel:

$$STD = \frac{std\,(Red\prime/Blue\prime)}{mean\,(Red\prime/Blue\prime)} \tag{30}$$

The indirect method requires the signal-to-noise ratio (SNR) in *Red'* and *Blue'*, which is calculated as the ratio between the mean intensity and the standard deviation for each pixel and between the 25 images. Subsequently, the relative squared error (RSE) is applied. The formulations used are listed below for a single pixel:

$$SNR_{Red\prime} = \frac{mean\,(Red')}{std(Red')} \tag{31}$$

$$RSE = \left(SNR_{Red\prime}^{-2} + SNR_{Blue\prime}^{-2}\right)^{1/2} \tag{32}$$

- **Estimates of the uncertainty**

The outputs from the two methods are in Table 4.6. Concerning the signal-to-noise ratio SNR, large variability is exhibited from a pixel to another, regardless the temperature. The SNR in the channel *Red'* is slightly larger than that in *Blue'* (about 1.3 times). The SNR is at least 10 times larger for any pixel with respect to pixel 6 (the one outside the illuminated region), denoting overall good detection.

Concerning the estimates obtained through the STD and the RSE, three observations are made. The first is that the typical values are between 0.5 % and 2.2 % (excluding pixel 6). The second is that no evident trend with temperature or pixel location is exhibited. The third is that good agreement is found between the two methods, as they provide similar estimates for pairs of pixels and temperature. An equivalent table is presented in annexe to chapter 4 for bench 1, using the negative lens and mechanical aperture and the mixture LUM345+PYR597, and the same observations are valid. These estimates suggest that the uncertainty evaluated from the intensity fluctuations could be associated with photon noise, because it appears to be independent from the pixel location, the optical path, and the temperature.

In conclusion, the typical uncertainty on the channel ratio is $(\Delta Red/Blue)_{pn}$ = 1.6 %. This percentage can be associated with the precision of an individual pixel. The source of the intensity fluctuation in time is uncertain and can be attributed to either pixel noise or to unsteady illumination.

Table 4.6 – Estimates of the signal-to-noise ratio (SNR) for *Red'* and *Blue'*, of the standard deviation (STD) for the channel ratio *Red'/Blue'*, and of the relative squared error (RSE) for *Red'/Blue'*. Bench 2 is used, mounting the mechanical aperture and negative lenses. Six pixels are considered.

	T=25°C				T=30°C				T=50°C			
	Red'	Blue'	Red'/Blue'		Red'	Blue'	Red'/Blue'		Red'	Blue'	Red'/Blue'	
Pixel	SNR	SNR	STD	SNR	SNR	STD	SNR	SNR	STD	SNR	SNR	STD
[number]	[/]	[/]	[%]	[%]	[/]	[/]	[%]	[%]	[/]	[/]	[/]	[%]
1	94.9	106.1	1.4	1.4	110.1	63.2	2.1	1.8	102.5	104.5	1.5	1.4
2	62.6	60.1	1.8	2.3	65.5	90.9	1.9	1.9	61.0	81.5	1.3	2.0
3	111.6	68.4	2.3	1.7	109.8	78.6	1.3	1.6	91.0	92.7	0.4	1.5
4	85.6	109.4	1.7	1.5	107.5	82.8	1.8	1.5	171.0	193.6	1.1	0.8
5	89.3	67.8	1.6	1.9	118.7	77.7	0.9	1.5	153.6	81.7	0.8	1.4
6	6.1	4.6	15.7	27.3	14.4	6.1	17.0	17.8	5.1	5.2	29.9	27.3
	T=70°C				T=88°C				T=106°C			
	Red'	Blue'	Red'/Blue'		Red'	Blue'	Red'/Blue'		Red'	Blue'	Red'/Blue'	
Pixel	SNR	SNR	STD	SNR	SNR	STD	SNR	SNR	STD	SNR	SNR	STD
[number]	[/]	[/]	[%]	[%]	[/]	[/]	[%]	[%]	[/]	[/]	[/]	[%]
1	76.6	85.4	2.1	1.8	119.3	78.8	1.6	1.5	109.3	93.4	1.6	1.4
2	64.0	39.0	3.9	3.0	49.9	72.9	2.6	2.4	81.5	57.2	2.8	2.1
3	131.4	124.3	1.3	1.1	82.9	75.5	1.5	1.8	166.4	47.6	2.0	2.2
4	127.5	116.6	1.3	1.2	87.3	83.9	1.8	1.7	103.1	90.3	1.0	1.5
5	99.2	82.9	2.1	1.6	126.8	98.1	1.0	1.3	70.6	47.9	1.2	2.5
6	25.6	5.6	22.9	18.4	18.4	6.1	15.3	17.2	5.2	8.1	23.0	22.8

4.4.2 Analysis of uncertainty by region of interest

- **Method for characterising the uncertainty by region of interest**

In this section, the uncertainty is evaluated by considering the intensity measured by a cluster of neighbour pixels. This analysis aims to characterise the camera non-uniform response in the channel ratio *Red/Blue* to a uniform input, that is, a static film with uniform temperature and thickness. Bench 1 is used (with either the beam homogeniser or the negative lenses, as in section 2.3.2) and both mixtures LUM345 + PYR597 and LUM345 + PYR650.

The pixel data are extracted from a 200 x 200 pixel ROI at the centre of the image (as in the previously presented Figure 4.26). The mean and standard deviation of the channel ratio *Red/Blue* are calculated between the pixels of the ROI. Notice that the aim of the analysis by ROI is to evaluate the uncertainty from a small but representative sample of the pixels of the image, and annexe to chapter 4 reports a dedicated study which verifies the independence of the outcome from the ROI position and size.

For evaluating the uncertainty on the temperature measurement of the imaging method, the experimental variation of *Red/Blue* with *T* must be determined first (where *Red/Blue* is measured with the RGB camera and *T* is measured with a thermocouple in the liquid film). Consider a plot with *T* on the *x* axis, *Red/Blue* on the *y* axis, and *e* as the error bar of *Red/Blue*. Then consider three vectors [T_{i-1} , *Red/Blue* $_{i-1}$, e_{i-1}], [T_i , *Red/Blue* $_i$, e_i] and [T_{i+1} , *Red/Blue* $_{i+1}$, e_{i+1}]. The uncertainty on the temperature of the intermediate point ΔT_i is calculated by projecting the error bar e_i on the trace *Red/Blue(T)*, according to the following formulation:

$$\Delta T_i = e_i \, 2 \left(\frac{(Red/Blue)_{i+1} - (Red/Blue)_i}{T_{i+1} - T_i} + \frac{(Red/Blue)_i - (\Delta Red/Blue)_{i-1}}{T_i - T_{i-1}} \right)^{-1} \qquad (33)$$

If omitted, in this manuscript the error bar e_i is the standard deviation of *Red/Blue* between the pixels of the ROI, while $(Red/Blue)_i$ is their mean and T_i the temperature of the oil.

- **Effects of exposure time and number of images for averaging**

In Figure 4.42, the uncertainty associated with the dynamic range of the camera is examined for increasing exposure time t_{exp}. The experiment is performed at T = 20 °C with mixture LUM345 + PYR597 and 25 images are used for averaging. The trace increases slightly until when *Green* starts saturating at about t_{exp} = 8 ms. A plateau occurs up to t_{exp} = 14 ms, when *Red* starts saturating and an abrupt increase is observed. In the investigated range, the standard deviation is between 3-4 %, even if *Green* is saturated, meaning that there is no evidence of signal leakage from the pixels in *Green* to the pixels in *Red* or *Blue*. Since the standard deviation is essentially constant and increases abruptly close to the saturation of *Red*, this occurrence cannot be associated with photon noise, because photon noise is expected to diminish when increasing the exposure time.

In Figure 4.43, the uncertainty associated with the number of images used for averaging is examined by varying the number of images for averaging from 1 to 50 and keeping the same exposure time (t_{exp} = 7 ms). The experiment is performed at T = 20 °C with the mixture LUM345 + PYR597. The plot shows clearly that the standard deviation is identical for any number of images greater than 5.

The results showed in the two figures indicate that for the uniform input provided by the static film, the typical variability of *Red/Blue* between neighbour pixels is approximately 3-4 %. This value is essentially unaffected by the exposure time (when operating nearby the saturation of *Green*) and by the number of images used for averaging.

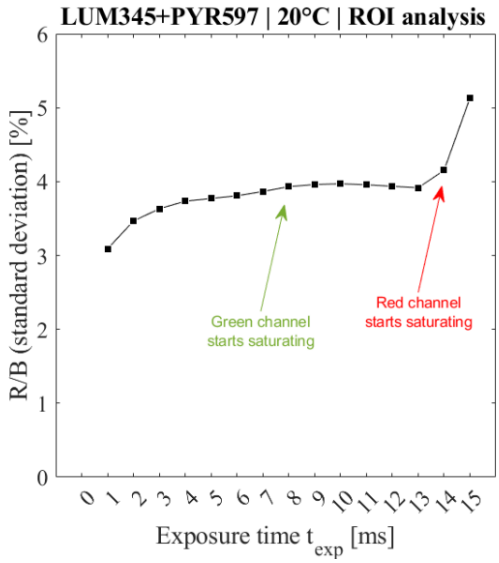

Figure 4.42 – Variation of the standard deviation of the channel ratio *Red/Blue* within ROI for increasing exposure time.

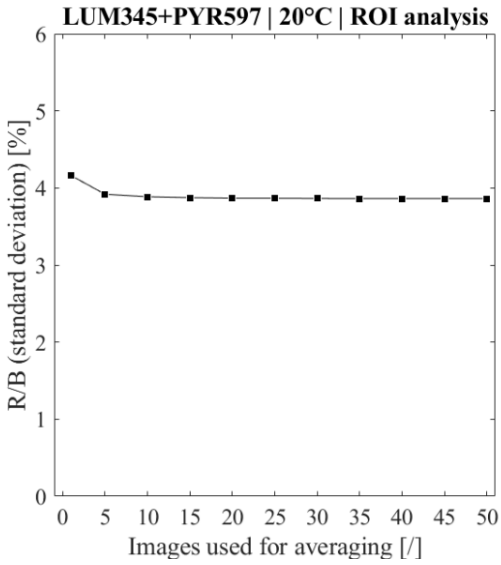

Figure 4.43 – Variation of the standard deviation of the channel ratio *Red/Blue* within ROI for increasing number of images used for averaging.

- **Experiment repetition**

The same experiment is repeated five times to evaluate the statistical uncertainty associated with repeatability. The temperature of the oil film is varied between 20 °C < T_{oil} < 110 °C and *Red/Blue* is evaluated. Subsequently, the mean and standard deviation of *Red/Blue* are calculated for the pixels defined in the ROI, for each of the five experiments. An example of one of the five experiments is given in Figure 4.44, showing the variation of *Red/Blue* with temperature.

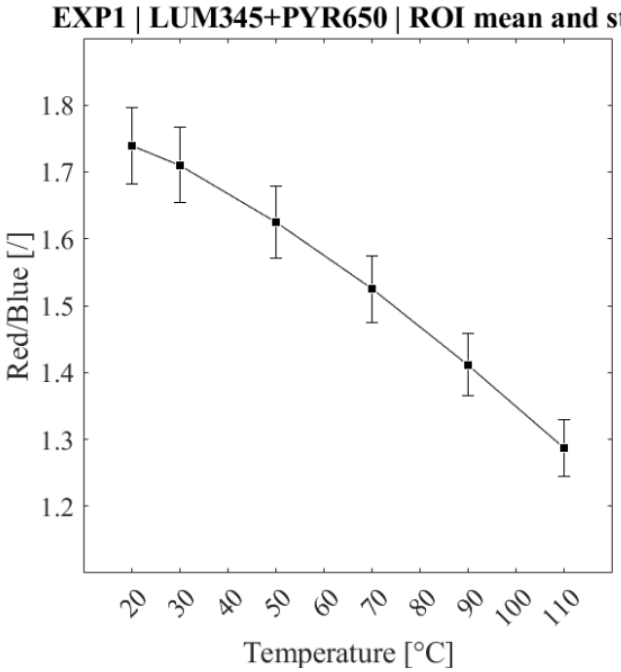

Figure 4.44 – Variation of the channel ratio *Red/Blue* with temperature, for LUM345 + PYR650. The datapoint and the error bars are the mean and standard deviation, within the pixels of ROI. Bench 1 is used (mounting the mechanical aperture and negative lens), with the mixture LUM345 + PYR650, exposure time t_{exp} = 8 ms, and 25 images for averaging.

In Table 4.7 the uncertainty is reported for the five experiments and is condensed within four types of estimates: standard deviation of *Red/Blue* calculated within the ROI, standard deviation of *Red/Blue* calculated between the experiments, uncertainty on temperature ΔT within the ROI, and uncertainty on temperature ΔT between experiments. The uncertainty on the temperature is calculated with (33).

Table 4.7 – Uncertainty on the channel ratio *Red/Blue* and the temperature of the oil film, within the pixels of the RPI and between five repetitions of the same experiment.

	EXP 1	**EXP 2**	**EXP 3**	**EXP 4**	**EXP 5**	**ALL EXPERIMENTS**
T_{oil}	***Red/Blue*** **(std within the ROI)**					***Red/Blue*** **(std between experiments)**
[°C]	**[%]**					**[%]**
20	3.3	3.3	3.1	3.6	3.6	0.9
30	3.3	3.4	3.2	3.6	3.6	1.0
50	3.3	3.5	3.2	3.6	3.7	1.0
70	3.3	3.5	3.3	3.6	3.6	1.0
90	3.3	3.5	3.2	3.6	3.6	0.7
110	3.3	3.4	3.2	3.5	3.5	0.9
T_{oil}	ΔT **(within the ROI)**					ΔT **(between experiments)**
[°C]	**[°C]**					**[/]**
20	19.4	16.3	15.5	19.2	19.8	5.1
30	16.3	14.9	13.8	16.5	17.0	4.5
50	11.7	11.9	11.3	11.8	12.8	3.3
70	9.4	10.1	9.3	9.5	10.0	2.5
90	7.9	8.6	7.7	7.8	8.4	1.6
110	6.7	7.1	6.7	8.2	7.8	1.6
	$\Delta T = 96.7\ (T_{oil})^{-0.546}$ $R^2=0.93$					$\Delta T = 55.2\ (T_{oil})^{-0.738}$ $R^2=0.95$

In the table, the typical standard deviation (due to camera non-uniform response) is 3 % < $(\Delta Red/Blue)_{nh}$ < 4 %, for every T_{oil} and experiment. This uncertainty can be associated with the accuracy of the measurement. The standard deviation of *Red/Blue* when repeating experiments is about $(\Delta Red/Blue)_r$ = 1 %. Consequently, the statistical uncertainty between experiments is smaller than the variability between neighbour pixels and is unaffected by temperature. Concerning the temperature uncertainty of individual experiments, ΔT within the ROI decreases significantly when the oil film is hotter, as showed by the power law fitting at the bottom of the table. For instance, from T_{oil} = 20 °C to T_{oil} = 110 °C, ΔT within the ROI is more than halved. The non-uniform response of neighbour pixels contributes significantly to the uncertainty, and the estimates are between 6 °C < $(\Delta T)_{nh}$ < 20 °C. Also, the lower the temperature of the oil film, the smaller the uncertainty. Between experiments, the uncertainty on temperature is about 2 °C < $(\Delta T)_r$ < 5 °C, which is 3-5 times smaller than the one due to the non-uniform response between neighbour pixels.

These results show that when given a uniform input (i.e., an oil film with uniform thickness and temperature), the output is considerably not uniform enough to allow fine measurements with respect to the expected temperature variation in the impinging jet (about 10 °C). Some strategies must be contemplated to reduce the camera non-uniform response.

4.4.3 Total uncertainty on temperature and thickness measurements

- **Total uncertainty on channel ratio *Red/Blue***

The total uncertainty on the channel ratio is calculated from the uncertainty associated with pixel noise, camera non-uniform response and experiment repeatability using the formulation below (relative squared error):

$$(\Delta Red/Blue)_{tot} = \left[(\Delta Red/Blue)_{pn} + (\Delta Red/Blue)_{nh} + (\Delta Red/Blue)_r\right]^{1/2} \qquad (34)$$

Assuming $(\Delta Red/Blue)_{pn}$ = 1.6 % (as in section 4.4.1), $(\Delta Red/Blue)_{nh}$ = 3.4 % (as in section 4.2.2) and $(\Delta Red/Blue)_r$ = 1 % (as in section 4.2.2), the estimate of the total uncertainty is $(\Delta Red/Blue)_{tot}$ = 3.9 %. This value represents the uncertainty of the measurement taken with the imaging method, regardless the fluorescent mixture and the film temperature.

- **Total uncertainty on temperature**

The total uncertainty ΔT_{tot} on the oil temperature is calculated form the total uncertainty $(\Delta Red/Blue)_{tot}$ and using equation (33). The nominal precision of the thermocouple for measuring the liquid film is added to the estimate (i.e., 0.5 °C, as mentioned in section 2.3.2). Table 4.8 reports the total uncertainty of the evaluation, depending on the temperature of the oil film. These values represent the uncertainty of the temperature evaluation with the imaging method, using the mixture LUM345 + PYR650.

The table shows that the estimates are between 8.2 °C < ΔT_{tot} < 20.6 °C, which are still significantly large for the application to the impinging jet. In the fitting function reported at the bottom of the table, the exponent is similar to the one obtained in previous Table 4.7, suggesting that the non-homogenous response plays an important role in the uncertainty.

Table 4.8 – Total uncertainty in temperature from LIF imaging. The temperature of the oil film is measured with a thermocouple. Bench 2 is used, with the beam homogeniser and LUM345 + PYR650.

T_{oil}	*Red/Blue* (total uncertainty)	ΔT (total uncertainty)
[°C]	[%]	[°C]
20	3.9	20.6
30	3.9	17.9
50	3.9	13.6
70	3.9	11.0
90	3.9	9.1
110	3.9	8.2
		$(\Delta T)_{tot} = 114.7\ (T_{oil})^{-0.557}$ $R^2=0.99$

- **Total uncertainty on *Blue* and on film thickness**

The estimate of the total uncertainty $(\Delta\delta)_{tot}$ and for the channel *Blue* is in Table 4.9 for different film thickness δ. The detailed calculations are not reported in this manuscript, but they are analogous to those for the channel ratio and the temperature. The pixel noise contributes for $(\Delta Blue)_{pn}$ = 1 % to the uncertainty on the intensity, the non-uniform response for $(\Delta Blue)_{nh}$ = 8.6 %, and the experiment repeatability for $(\Delta Blue)_r$ = 5.3 %. These estimates are obtained by the analysis of the previously described experiments in Figure 4.41 for pixel noise, in Figure 4.37 for non-uniform response, and Table 4.7 for experiment repetition. Moreover, as discussed in section 4.3.3, *Blue* is poorly influenced by temperature, thus the uncertainty on thickness is considered independent from temperature as well. The total uncertainty in the intensity measured in channel *Blue* is $(\Delta Blue)_{tot}$ = 10.2 %, via the relative square error, equivalent to equation (34). Using the traces of Figure 4.37 and equation (33) (where *Red/Blue* is replaced by *Blue* and T by δ), the uncertainty in the intensity is converted into uncertainty in thickness $(\Delta\delta)_{tot}$ and is reported in Table 4.9. From the thickness measurement of the impinging jet, the low-thickness region is expected to be approximate δ = 0.2 mm and the high-thickness region approximately δ = 3 mm (see section 4.1.2). With respect to these expected values, the table shows that for thin films δ < 1 mm the uncertainty is very large and for δ > 1 mm is smaller but still significant.

Table 4.9 – Total uncertainty $\Delta\delta$ on thickness using the LIF technique and the imaging method. The thickness of the oil film is determined by gauges. Bench 1 is used, with the beam homogeniser and LUM345 + PYR650.

Thickness δ	*Blue* (total uncertainty)	$\Delta\delta$ (total uncertainty)
[mm]	[%]	[mm]
0.2	10.2	0.1
0.6	10.2	0.1
1.0	10.2	0.1
1.4	10.2	0.1
1.8	10.2	0.2
2.2	10.2	0.2
2.6	10.2	0.3
3.0	10.2	0.3
3.4	10.2	0.9
3.8	10.2	0.8
		$(\Delta\delta)_{tot} = 0.126\ (\delta)^{-1.13}$ $R^2=0.80$

- **Reduction of the uncertainty**

Some strategies are proposed to reduce the uncertainty on the temperature, since the fluorescent mixture is more sensitive to thickness than to temperature. This includes the optimisation of the optical components and additional image processing.

Replacing the thermocouple by another with a finer calibration (0.1 °C) would not reduce the uncertainty in a significant way. The statistical error when repeating experiments is assumed identical. The uncertainty associated with pixel noise and with the camera non-uniform response could be reduced effectively through the image processing. The influence of binning is hence investigated.

An experiment is performed with bench 1 (with either the homogeniser or the negative lens) and the same images are processed by applying an increasing binning. A pointwise analysis and the analysis by region of interest are undertaken to characterise pixel noise and non-homogenous response, with the same procedures of calculation (described in 4.4.1 and 4.4.2, respectively).

Concerning the pointwise analysis (with bench 1, using the homogeniser, and at T_{oil} = 25 °C), it is calculated that STD = 0.8 % and RSE = 0.9% when applying 3 x 3 pixel binning, STD = 0.5 % and RSE = 0.6 % when applying 4 x 4 pixel binning, and STD = 0.3 % and RSE = 0.3 % when applying 8 x 8 pixel binning (table in annexe to chapter 4). Consequently, binning proves to be effective for reducing pixel noise for individual pixels.

Concerning the analysis by region of interest, Figure 4.45 shows the standard deviation of *Red/Blue* for increasing binning for the two setups of bench 1. Without binning, the standard deviation is about 4 % for both. The standard deviation decreases more significantly when combining binning and the setup with the homogeniser rather than the setup with the negative lens and mechanical aperture. This could be explained by the fact that the homogeniser generates a regular illumination pattern, whose characteristic size is imaged by a certain number of pixels. For a sufficiently large level of binning, all these pixels are counted as one and the pattern disappears (as in Figure 4.46). Additionally, such decrease is at the same rate for any temperature. Using the datapoints of Figure 4.45, that the uncertainty on the channel ratio *Red/Blue* (in %) associated with non-uniformity can be approximated (in %) by the fitting function $(\Delta Red/Blue)_{nh} = 3.55\ (binning)^{-0.567}$ with $R^2 = 0.95$. Similarly, the uncertainty on the oil temperature (in °C) associated with non-uniformity is fitted by $(\Delta T)_{nh} = (19 - 0.14\ T_{oil})\ (binning)^{-0.568}$ with $R^2 = 0.93$ (T_{oil} is the oil temperature measured by the thermocouple). These fitting functions are useful to predict the uncertainty for increasing binning when the imaging method is applied to unknown liquid films including the impinging jet.

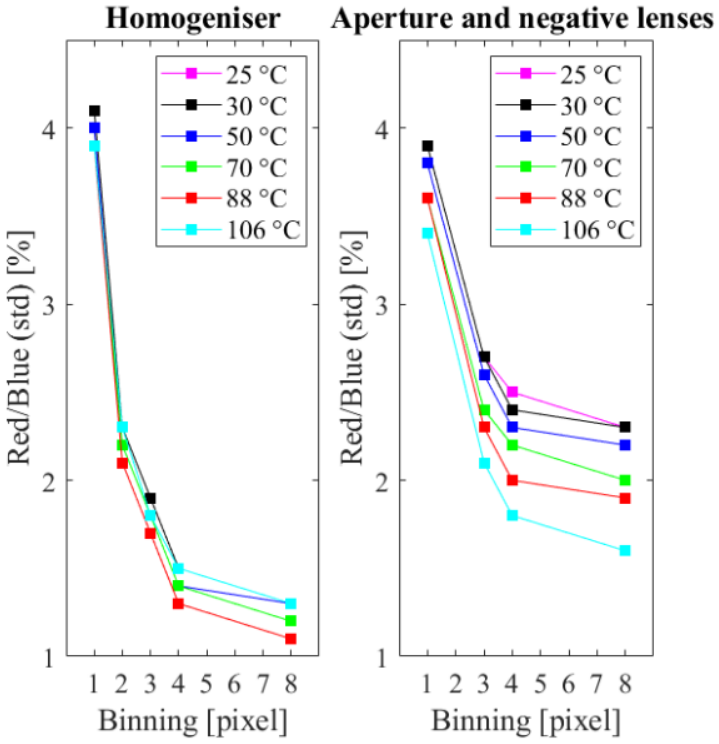

Figure 4.45 – Reduction of the uncertainty associated with the camera non-uniform response with increasing binning level. The standard deviation on the channel ratio *Red/Blue* between the pixels of ROI is considered. Bench 1 is used, with either the beam homogeniser, or the mechanical aperture and negative lens. Evaluation for LUM345 + PYR650.

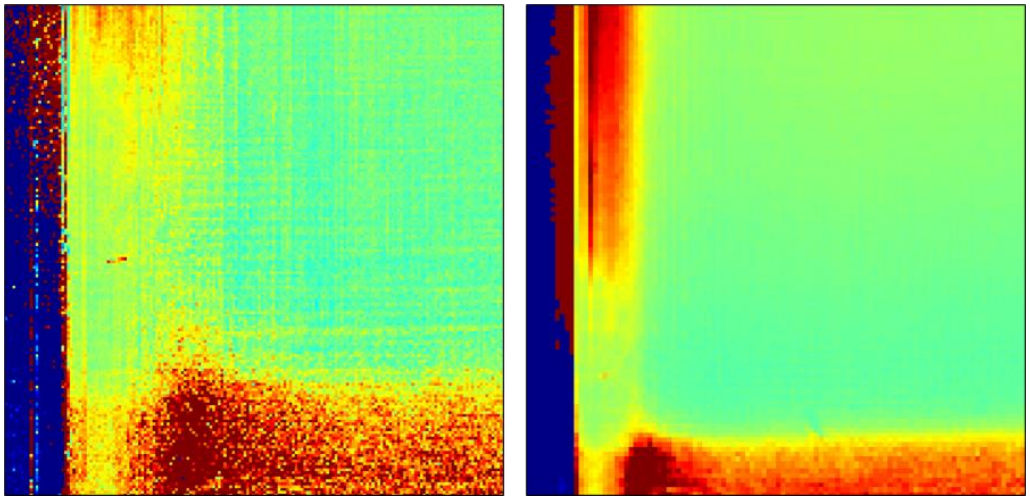

Figure 4.46 – Zoom of the bottom-left corner of the image of the channel ratio *Red/Blue*, taken with bench 1 mounting the homogeniser. (Left) No binning. (Right) 8 x 8 pixel binning.

- **Total uncertainty on channel ratio and temperature after improvement**

The total uncertainty $(\Delta Red/Blue)_{tot}$ and $(\Delta T)_{tot}$ are recalculated, including all sources of error and technical improvements. The total uncertainty on the channel ratio and temperature of the oil film are summarised in Table 4.10. The estimates are provided for several binning and refer to bench 1 with the homogeniser. With respect to the previous estimates in Table 4.8, the uncertainty is reduced significantly after the technical improvements. Considering the injection temperature investigated in this research (60 °C < T_{oil} < 90 °C) and the expected temperature variations along x (about 10 °C within

the field of view), the table suggests that a relevant binning level is necessary (at least more than 5 x 5 pixel).

Among all the strategies proposed to reduce the uncertainty on *Red/Blue* and T_{oil}, the most effective is given by the combined use of the beam homogeniser and a sufficiently large image binning. The homogeniser alone has no advantage for reducing pixel noise and non-uniform response, but as soon as binning is implemented, both are reduced.

Table 4.10 – Total uncertainty on the channel ratio *Red/Blue* and temperature, using the LIF technique and imaging method, for different levels of binning. The temperature of the oil film is measured with a thermocouple. Bench 1 is used, mounting the homogeniser, and using LUM345 + PYR650.

T_{oil} [°C]	Binning 1 x 1 pixels		Binning 3 x 3 pixels		Binning 5 x 5 pixels		Binning 9 x 9 pixels		Binning 15 x 15 pixels	
	ΔRed/Blue [%]	*ΔT* [°C]	*ΔRed/Blue* [%]	*ΔT* [°C]	*ΔRed/Blue* [%]	*ΔT* [°C]	*ΔRed/Blue* [%]	*ΔT* [°C]	*ΔRed/Blue* [%]	*ΔT* [°C]
20	4.0	20.6	2.3	10.6	1.8	8.2	1.4	6.5	1.3	5.7
30	4.0	17.9	2.3	9.6	1.8	7.5	1.4	6.0	1.3	5.2
50	4.0	13.6	2.3	7.8	1.8	6.1	1.4	4.8	1.3	4.2
70	4.0	11	2.3	6.0	1.8	4.7	1.4	3.7	1.3	3.3
90	4.0	9.1	2.3	4.2	1.8	3.2	1.4	2.6	1.3	2.3
110	4.0	8.2	2.3	2.3	1.8	1.8	1.4	1.5	1.3	1.3

4.4.4 Background subtraction

So far in this manuscript, the chosen background is the fluorescence signal from pure oil, obtained with an oil film without any fluorescent dye. In this section, the background correction is examined.

In a preliminary spectroscopy analysis, it is found that the colour long-pass filter of bench 1 (technical details in section 2.3.2) emits in the red (see spectrum in annexe to chapter 4) and it can be detected by the camera. This justifies the need for the high-optical density dichroic filter.

Concerning the image processing, four background corrections are considered: pure oil, dark images, bare plate, and none. The comparison is carried out considering the fluorescence intensity in the channels *Red*, *Green* and *Blue*, and the channel ratio *Red/Blue*. The four images of the *Red/Blue* ratio are reported in annexe to chapter 4, but they do not exhibit notable differences within the illuminated region. For a quantitative analysis, the pixels of a 200 x 200 pixels ROI in the centre of the image are considered, to obtain the mean value of the averaged and background-corrected images in every channel and the channel ratio *Red/Blue*. These values are in Table 4.11.

Table 4.11 – Averaged and background-corrected intensity and channel ratio *Red/Blue*, obtained with different background corrections. The values in the table are calculated as the mean between the pixels of ROI.

Background correction	*Red* [counts]		*Green* [counts]		*Blue* [counts]		*Red/Blue*
	I_{avg_cor}	I_{BG}	I_{avg_cor}	I_{BG}	I_{avg_cor}	I_{BG}	[/]
Pure oil	$2.08 \cdot 10^4$	495	$3.73 \cdot 10^4$	547	$1.37 \cdot 10^4$	657	1.53
Dark	$2.09 \cdot 10^4$	484	$3.73 \cdot 10^4$	495	$1.38 \cdot 10^4$	480	1.51
Bare plate	$2.08 \cdot 10^4$	509	$3.73 \cdot 10^4$	558	$1.36 \cdot 10^4$	733	1.54
None	$2.15 \cdot 10^4$	0	$3.80 \cdot 10^4$	0	$1.44 \cdot 10^4$	0	1.44

In Table 4.11, the background is always several orders of magnitude smaller than the measured intensity in the channels. The intensity and the channel ratio are the same (within less than 1 %) for any of the background corrections with pure oil, with the dark images or

with the bare plate. The only exception is when no correction is applied, as the channel intensity is 2-5% larger than with any correction, resulting in *Red/Blue* being 6 % larger.

The results point out that any type of background correction poorly affects the intensity in every channel and the channel ratio *Red/Blue*, however a background correction is always recommended instead of none. The most relevant outcome is that the background plays a minor role also for the impinging jet configuration. This is a practical advantage because it is not strictly necessary to measure the background with pure oil. For the following experiments, the dark images are used for the background correction.

4.5 Field measurements of temperature and thickness

4.5.1 Calibration and algorithm testing on a static film

In this section, the calibration is briefly explained. Subsequently, measurements of temperature and thickness are performed on static oil films, using the iterative and interpolative algorithms. The experiments presented in this section are performed with the mixture LUM345 + PYR650 and with bench 2, whose technical details are in section 2.3.2. The formulations of the image processing are in section 2.3.3. The explanation of the two algorithms for determining the temperature and the thickness from the intensity measurements is in section 2.3.4.

- **Calibration with glass-confined surface and sensitivity to temperature and thickness**

Before applying the 2-dye 2-colour LIF technique to the impinging jet, the method must be calibrated. Calibration is the association of specific values of the channel ratio *Red/Blue* and *Blue* to specific values of temperature T and thickness δ of the liquid film. A flat-field correction is applied to uniformise the brightness across the image and to correct small irregularities. The notation $Red_{FF}/Blue_{FF}$ and $Blue_{FF}$ are used in the following of the manuscript.

The temperature of the film is varied between 30 °C < T_{oil} < 110 °C and thickness between 0.1 mm < δ < 4.1 mm. The calibration is performed using a glass-confined static film, to assure a constant and uniform thickness during the measurement. Because of the introduction of a new optical element (i.e., the glass), a comparative study is undertaken between a glass-confined and a free-surface static film. The outcome of this study (reported in annexe to chapter 4) is that the glass produces a 0.2 % offset in the channel ratio $Red_{FF}/Blue_{FF}$ and a 6.5 % offset in channel $Blue_{FF}$ (6.5 %). Consequently, when the optical method is applied to the impinging jet, this offset must be taken into account.

The channel ratio $Red_{FF}/Blue_{FF}$ is plotted in Figure 4.47 and Figure 4.48, while the flat-field corrected intensity $Blue_{FF}$ is plotted in Figure 4.49 and Figure 4.50. The datapoints and the error bars are the mean and standard deviation between three repetitions of the calibration. The trace named "DARK" is the value of the dark images used as background and corresponds to δ = 0 mm.

All traces exhibit consistency in the variation of temperature and thickness, and they resemble those predicted by *Hidrovo* and *Hart* 2000 (see section 1.3.3). The sensitivity to temperature of $Red_{FF}/Blue_{FF}$ is about – 0.0026 °C^{-1} and for thickness it is + 0.0535 mm^{-1}. The sensitivity to temperature of $Blue_{FF}$, is about – 0.0019 °C^{-1} and for thickness it is + 0.1838 mm^{-1}.

These four figures present the dataset used for calibrating the iterative and interpolative algorithms. Concerning the first, a polynomial fit is used and the coefficients a, b and R^2

are in Table 4.12. Concerning the interpolated algorithm, the datapoints of the four figures are interpolated locally via MATLAB.

Calibration with bench 2, LUM345 + PYR650, glass-confined static films, flat-field correction.

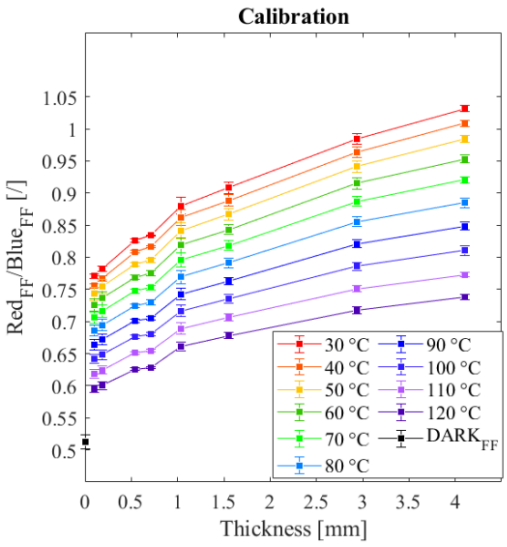

Figure 4.47 – Channel ratio *Red*$_{FF}$*/Blue*$_{FF}$, for increasing film temperature and thickness.

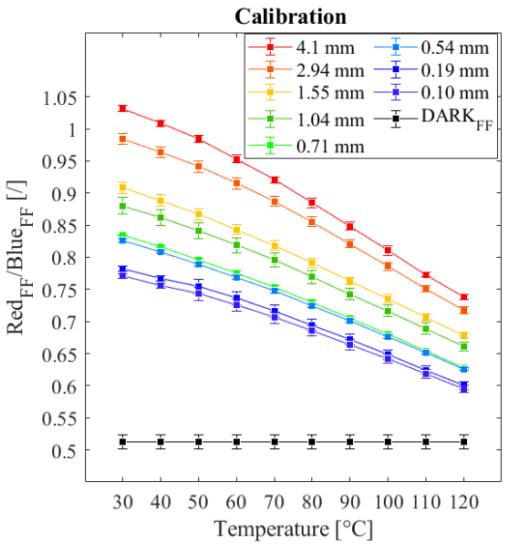

Figure 4.48 – Channel ratio *Red*$_{FF}$*/Blue*$_{FF}$, for increasing film temperature and thickness.

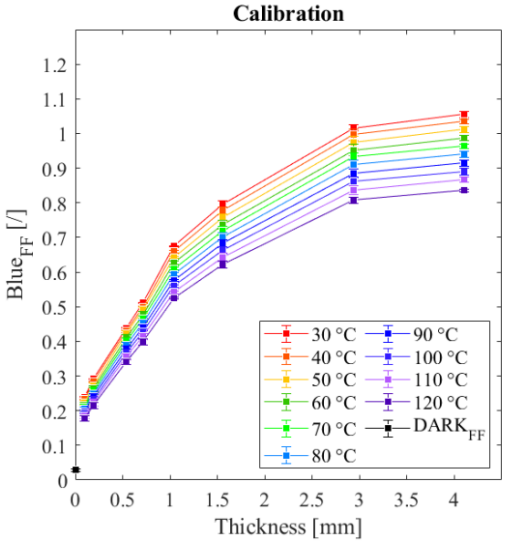

Figure 4.49 – Channel *Blue*$_{FF}$, for increasing film temperature and thickness.

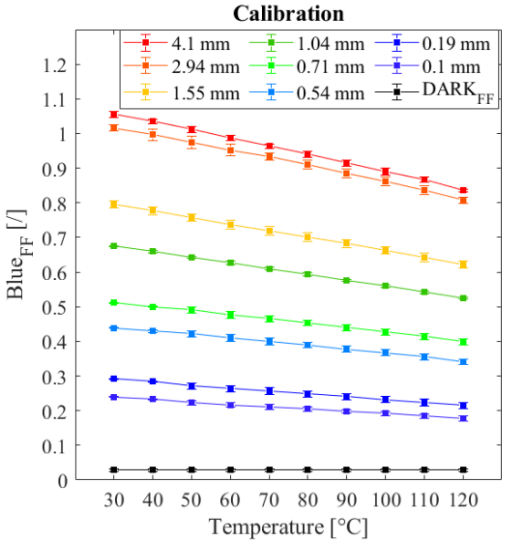

Figure 4.50 – Channel *Blue*$_{FF}$, for increasing film temperature and thickness.

Table 4.12 – Coefficients of the polynomial fitting functions, correlating the channel ratio *Red*$_{FF}$*/Blue*$_{FF}$, the oil film temperature T and oil film thickness δ. The coefficient of determination R^2 is also reported.

a_0	a_1	a_2	a_3	a_4	a_5	R^2
0.8030	0.1159	– 0.0010	– 0.0097	– 0.0003	$-6.825 \cdot 10^{-6}$	0.997
b_0	b_1	b_2	b_3	b_4	b_5	R^2
0.2350	0.4788	– 0.0007	– 0.0632	– 0.0004	$-1.461 \cdot 10^{-6}$	0.997

- **Testing the algorithms**

The algorithms are tested on static oil films. Three free-surface films are considered with known temperature T_{oil} = 60 °C (measured with the immersed thermocouple) and thickness δ = 0.54-1.00-2.91 mm (measured with the contact needle). $Red_{FF}/Blue_{FF}$ and $Blue_{FF}$ are extracted from a thin horizontal stripe of pixels and discretised, in such a way that a value is obtained for every millimetre of the field of view. Subsequently, the algorithms are run to determine T_{oil} and δ.

The temperature T_n and T_i (evaluated by the iterative and interpolative algorithm, respectively) are plotted in Figure 4.51. The iterative algorithm usually converges within $n = 15$ iterations when a 10^{-4} tolerance is set. From a qualitative observation, the predictions appear relatively close to the expected temperature $T_{oil} = 60$ °C, but wide fluctuations are exhibited. Similar observations can be made for the thickness δ_n and δ_i (from the iterative and interpolative algorithm, respectively), plotted in Figure 4.52.

For a more quantitative analysis, the mean and standard deviation are calculated along each trace and are reported in Table 4.13. The difference between the expected temperature and the algorithm output are $T_{oil} - \text{mean}(T_n) < 5$ °C and $T_{oil} - \text{mean}(T_i) < 2$ °C. Consequently, the interpolated algorithm is more accurate than the iterative one. Concerning the standard deviation T_n and T_i, similar values are obtained. In this case the precision is similar between the two algorithms. The differences between the expected thickness and the predictions are $\delta - \text{mean}(\delta_n) < 0.4$ mm and $\delta - \text{mean}(\delta_i) < 0.2$ mm. Consequently, the two algorithms have similar accuracy regardless the target thickness. Concerning the standard deviation of δ_n and of δ_i, they are very similar, regardless the expected thickness. The results indicate that that the two algorithms have similar precision as well.

In conclusion, the measurements are relatively accurate on a large scale (i.e., the whole field of view, which is about 60 mm wide) but very inaccurate at a smaller scale (i.e., within few millimetres). Since the two algorithms are independent but exploit the same calibration database, the inaccuracy and imprecision are attributed to insufficient sensitivity to temperature and thickness of the fluorescent mixture, and not to a numerical problem.

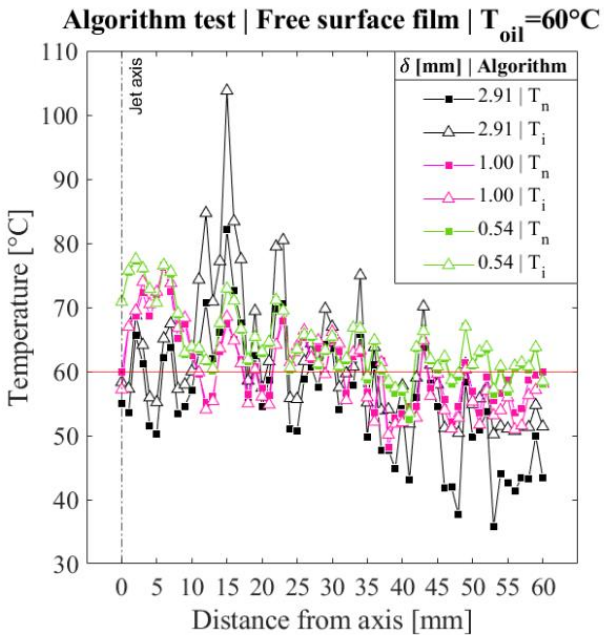

Figure 4.51 – Test of the algorithms at evaluating the temperature of three free-surface films, whose temperature is T_{oil} = 60 °C and thickness are δ = 0.54-1.00-2.91 mm. T_n is from the iterative algorithm and T_i from the interpolative one.

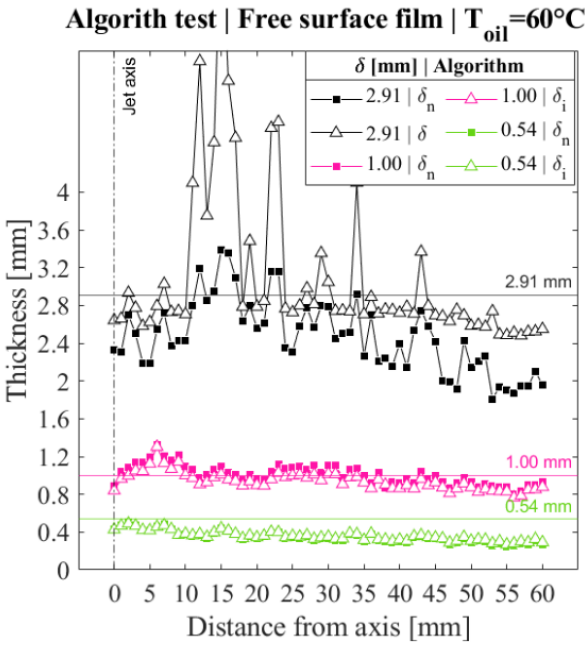

Figure 4.52 – Test of the algorithms at evaluating the thickness of three free-surface films, whose temperature is T_{oil} = 60 °C and thickness are δ = 0.54-1.00-2.91 mm. δ_n is from the iterative algorithm and δ_i from the interpolative one.

Table 4.13 – Test of the algorithms at evaluating the temperature of three free-surface films, whose temperature is T_{oil} = 60 °C and thickness are δ = 0.54-1.00-2.91 mm. Comparison through the mean and the standard deviation along an image profile.

Measurement technique		Iterative algorithm				Interpolative algorithm			
Thermocouple	Contact needle	Iterated temperature T_n		Iterated thickness δ_n		Interpolated temperature T_i		Interpolative thickness δ_i	
T_{oil}	δ	mean	std	mean	std	mean	std	mean	std
[°C]	[mm]	[°C]	[°C]	[mm]	[mm]	[°C]	[°C]	[mm]	[mm]
60	0.54	64.2	5.6	0.4	0.2	60.5	5.4	0.4	0.1
60	1.00	60.6	5.7	1.0	0.1	60.1	6.7	0.9	0.1
60	2.91	55.5	9.5	2.5	0.2	61.7	10.5	3.1	0.1

- **Testing the algorithms with binned images**

In previous section 4.4.3, binning is proven to reduce the uncertainty of *Red/Blue* and *Blue*. The same test of the algorithms, as the one described through Figure 4.51 and Figure 4.52, is hence performed with binned images. A film with T_{oil} = 60 °C and δ = 2.91 mm is considered. The results are shown in Figure 4.53 and Figure 4.54, where two binning levels are applied, 7 x 7 pixel and 11 x 11 pixels. These are considered a compromise between image resolution and limited uncertainty (see section 4.4.3 and annexe to chapter 4). More tests of the improvement of the image uniformity with binning are reported in annexe to chapter 4 for *Red/Blue*.

Binning does not show significant improvement in accuracy nor precision in the temperature and thickness measurement, as 10-20 °C wide spatial fluctuations are observed at the same distances from the jet axis. This is confirmed when calculating the mean and standard deviation of the datapoints of each trace. For the 7 x 7 pixel binning, T_n = 55.1 ± 9.0 °C and δ_n = 2.4 ± 0.4 mm are obtained. For the binning chunk 11 x 11 pixels it results T_n = 55.2 ± 8.7 °C and δ_n = 2.4 ± 0.4 mm. These values are similar to those obtained without binning. The lack of accuracy even after image binning is probably not due to the algorithms, because the two are independent and provide similar

results. Since the algorithms are based on the same calibration dataset, such inaccuracy is more likely to be attributed to the small sensitivity of the fluorescent mixture LUM345 + PYR650.

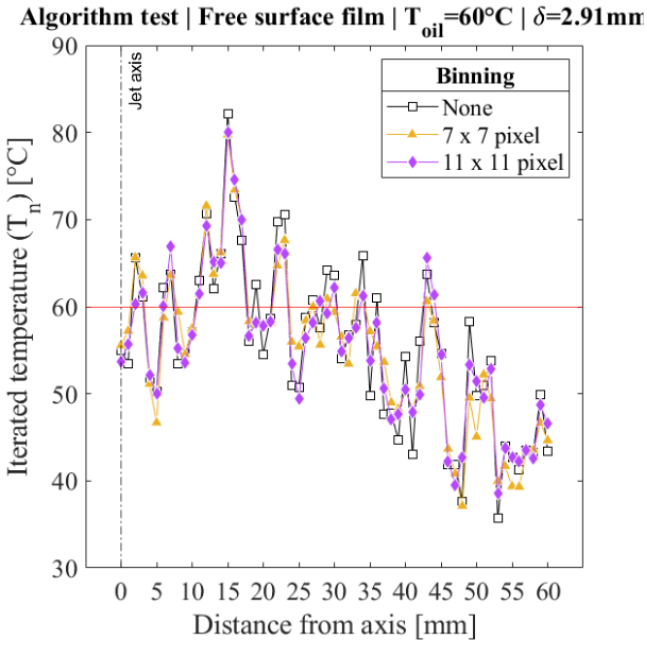

Figure 4.53 – Test of the iterative algorithm at evaluating the temperature of a free-surface films, whose temperature is T_{oil} = 60 °C and thickness is δ = 2.91 mm. Different levels of binning are applied.

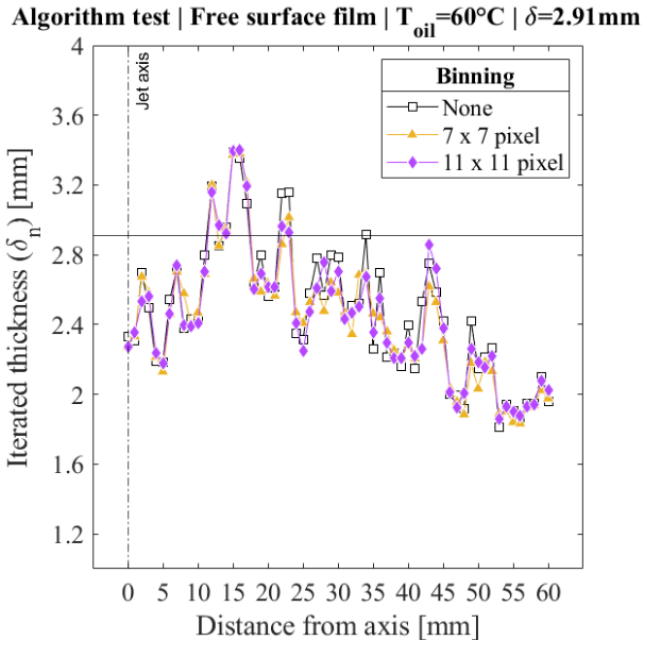

Figure 4.54 – Test of the iterative algorithm at evaluating the thickness of a free-surface films, whose temperature is T_{oil} = 60 °C and thickness is δ = 2.91 mm. Different levels of binning are applied.

4.5.2 Temperature and thickness measurements of the impinging jet

- ***Red*$_{FF}$*/Blue*$_{FF}$ and *Blue*$_{FF}$**

Wide field measurements of the temperature and thickness are taken using the imaging method for several injection and heating parameters. Figure 4.55 shows the flat-field

corrected channel ratio $Red_{FF}/Blue_{FF}$, along a radial profile, while Figure 4.56 shows the flat-field corrected intensity in channel $Blue_{FF}$. All traces in Figure 4.55 present four similar features: a first spike is found nearby the jet axis (x = 1 mm), a second spike (15 mm < x < 30 mm), the channel ratio always increases, and the increase is more pronounced before the hydraulic jump. The first spike corresponds to the liquid column, whereas the second spike to the hydraulic jump. The second spike is detected in Red_{FF} for every experiment (not shown in this manuscript), but not in $Blue_{FF}$ (see Figure 4.56). The first spike is attributed to the increase of thickness due to the liquid column, however the origin of the second is not evident yet. Similarly, all the traces in Figure 4.56 have the same features as the ones in Figure 4.55, with the only difference that the second spike is replaced by an abrupt increase of the intensity. Concerning the overall increase of the channel ratio $Red_{FF}/Blue_{FF}$, this is mostly attributed to the increase of thickness. As discussed in section 4.3, the channel ratio is sensitive to both temperature and thickness, but with opposite trends (increasing with thickness and decreasing with temperature) but the variation due to thickness is expected to be greater. At this stage it is not possible to distinguish information about temperature and thickness yet.

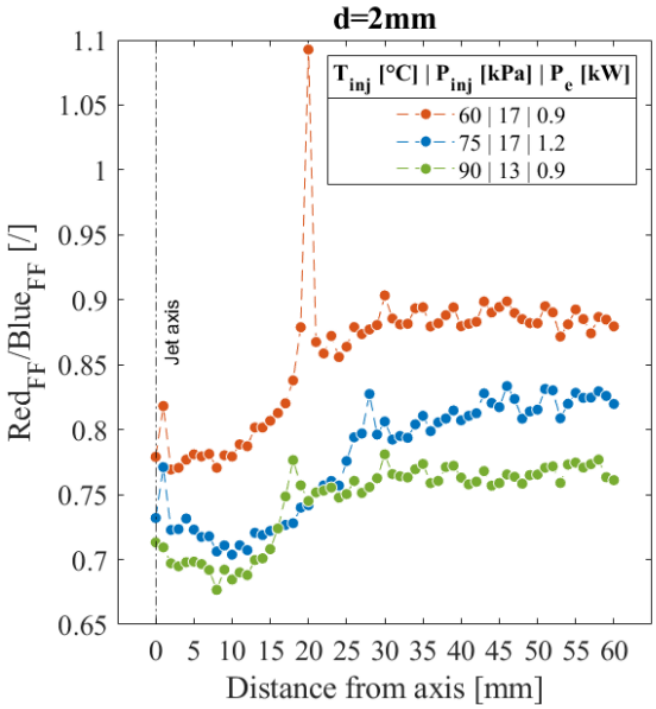

Figure 4.55 – Flat-field corrected channel ratio $Red_{FF}/Blue_{FF}$ for an impinging jet, for different injection and heating parameters. Evaluation along a radial profile and discretisation for every x = 1 mm.

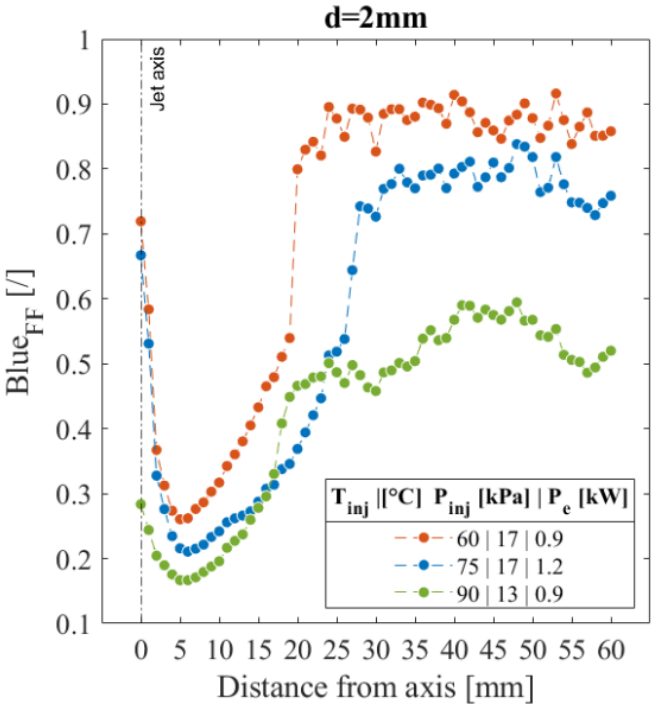

Figure 4.56 – Flat-field corrected $Blue_{FF}$ for an impinging jet, for different injection and heating parameters. Evaluation along a radial profile and discretisation for every x = 1 mm.

- **Temperature**

The temperature is measured via the iterative and interpolative algorithms. The temperature T_n is plotted in Figure 4.57 and the one from the interpolation T_i is plotted in Figure 4.58. Considering the experiment at T_{inj} = 60 °C, the traces T_n and T_i are below the injection temperature in the region x < 20 mm, showing large inaccuracy. There is no reasonable explanation to justify how the oil could lower its temperature down to 20-30 °C (and even negative temperatures at x = 20 mm) and then increase above 60 °C, within few millimetres from the impingement. Also, the fluid has some thermal inertia, and the air convection is not significant enough to justify such temperature drop. Conversely, the algorithms provide a plausible temperature range, within 60 °C < T < 70 °C for x > 20 mm (larger than the injection temperature). In particular, the measurement with the iterative algorithm shows more accuracy, as its spatial fluctuations are limited to about 10 °C while they are about 20 °C for the interpolative one.

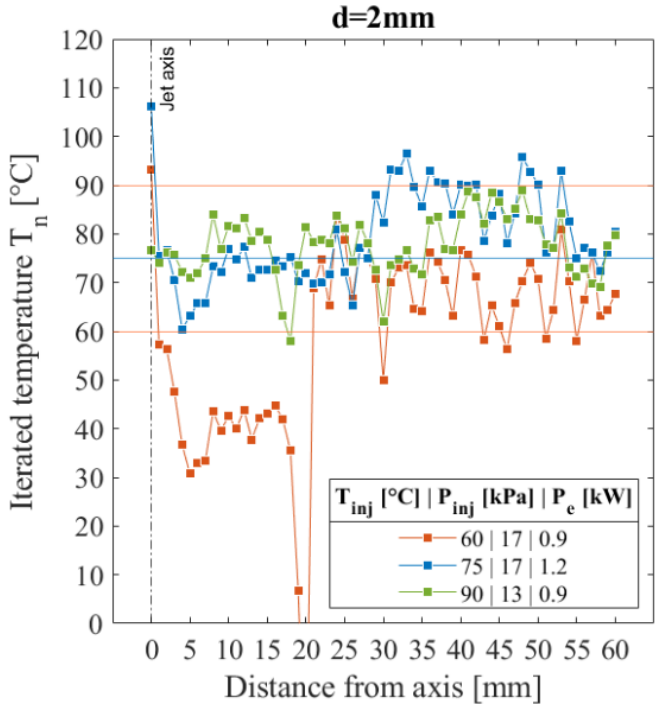

Figure 4.57 – Measurement of temperature with the iterative algorithm, for an impinging jet, with different injection and heating parameters. Evaluation along a radial profile and discretisation for every x = 1 mm.

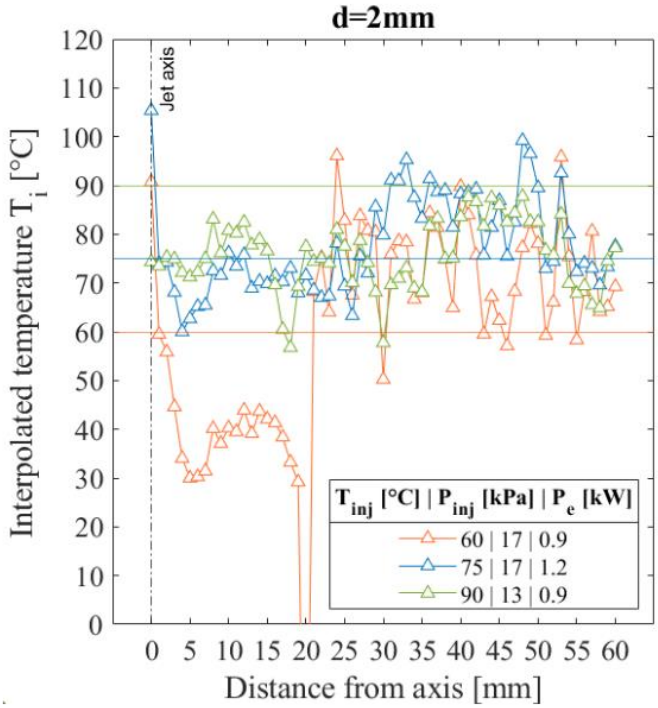

Figure 4.58 – Measurement of temperature with the interpolative algorithm, for an impinging jet, for different injection and heating parameters. Evaluation along a radial profile and discretisation for every x = 1 mm.

Considering the experiment at T_{inj} = 75 °C, the traces T_n and T_i are the most plausible of all, because the whole range is equal or above the injection temperature, and because the overall trend is to increase. In contrast, the traces T_n and T_i with injection temperature T_{inj} = 90 °C exhibit inaccuracy, because lower than the injection temperature in the whole

range. Additionally, the interpolative algorithm is less accurate than the iterative one, contrarily to the expectations.

- **Thickness**

The thickness is measured via the iterative and interpolative algorithms. The thickness δ_n is plotted in Figure 4.59 and the one from the interpolation δ_i is plotted in Figure 4.60. As seen previously for the temperature, the two measurements taken with the different algorithms are similar. Both algorithms enable to identify the expected low- and high-thickness regions which characterise the impinging jets are well-defined. Contrarily to what is shown in the algorithm testing phase (section 4.5.2), the interpolative algorithm is more imprecise than the iterative one, given the extent of the spatial fluctuations for T_{inj} = 75 °C. Moreover, both algorithms appear to perform better within the low-thickness region as the spatial fluctuations are less pronounced. Concerning the x position of the hydraulic jump, the measurements with both algorithms agree on x = 20 mm with injection temperature T_{inj} = 60 °C, and on x = 27 mm for the injection temperature T_{inj} = 75 °C. The hydraulic jump is not well-defined for the traces with injection temperature T_{inj} = 90 °C, contrarily to what observed for $Blue_{FF}$ in Figure 4.56.

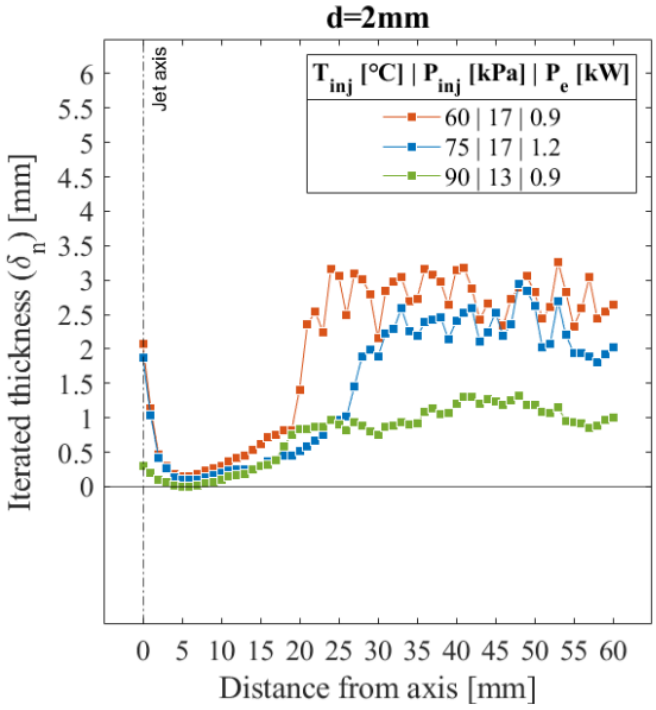

Figure 4.59 – Measurement of thickness with the iterative algorithm, for an impinging jet, for different injection/heating parameters. Evaluation along a radial profile and discretisation for every x = 1 mm.

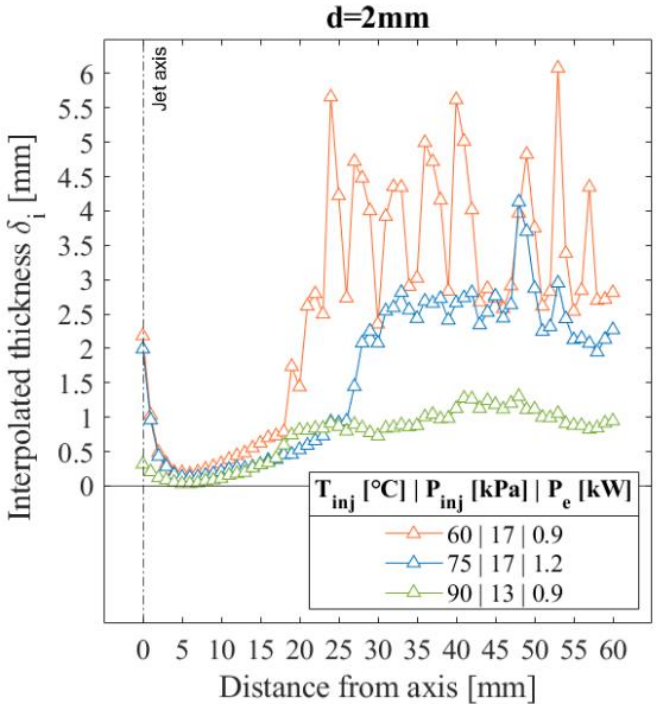

Figure 4.60 – Measurement of thickness with the interpolative algorithm, for an impinging jet, for different injection/heating parameters. Evaluation along a radial profile and discretisation for every x = 1 mm.

- **Comparison between field and pointwise measurements**

In Figure 4.61, the temperatures measured via the iterative algorithm are compared to the pointwise measurements from the thermocouple measurements in 4.1.1 (traces from Figure 4.3 and Figure 4.4), for two experiments with the same injection and heating parameters. From previously discussed results, it is observed that the iterative algorithm is very imprecise and incoherent in most of the domain, while the measurements with the thermocouple perturb the flow and are also characterised by large inaccuracy. Despite that, the two types of evaluation agree in the overall temperature range (especially for T_{inj} = 75 °C) and both show an increasing trend along the jet-radial profile.

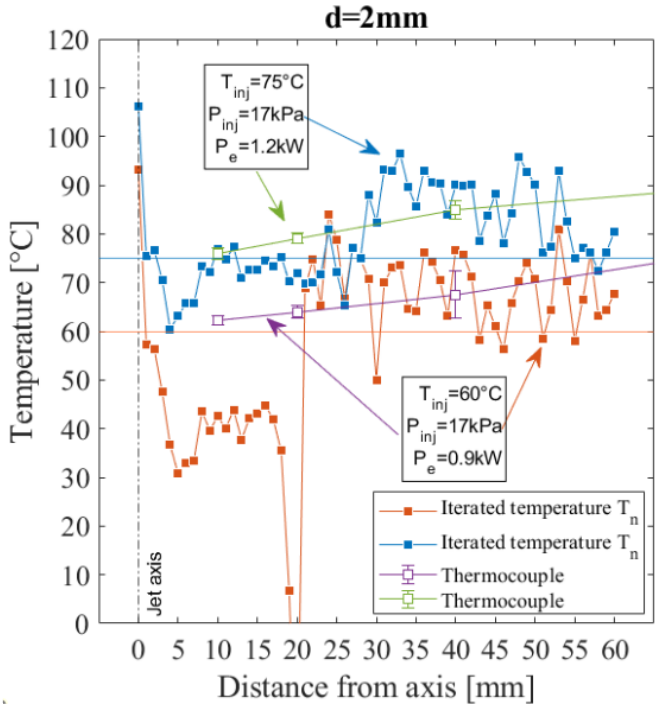

Figure 4.61 – Temperature of an impinging jet along a radial profile. Comparison between the thermocouple and the iterative algorithm.

The same type of comparison is carried out for thickness and for the same experiments. Figure 4.62 illustrates the thickness measured by the contact needle from section 4.1.2 (Figure 4.59, Figure 4.7 and Figure 4.8), and the one with the iterative algorithm δ_n. Good agreement is found, especially before and along the hydraulic jump, where the traces overlap. It follows that in this region both the trend and the values are similar from the two methods.

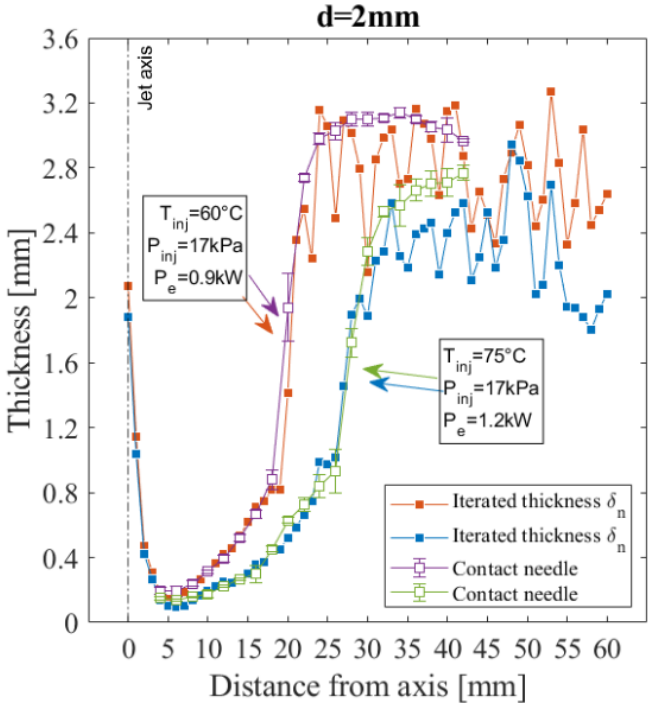

Figure 4.62 – Thickness of an impinging jet along a radial profile. Comparison between the contact needle and the iterative algorithm.

- **Wide-field imaging of thickness**

Figure 4.63, Figure 4.64 and Figure 4.65 are examples of wide-field measurements of the thickness of the impinging jet, evaluated with the iterative algorithm. In every image, all the regions with different thickness are clearly distinguished, including the position of the hydraulic jump and the impingement point. In the first two figures, the hydraulic jump is round, while in the third it is more irregular, likely due to some imperfections of the plate surface which deviates the liquid when at high temperature, thus low viscosity.

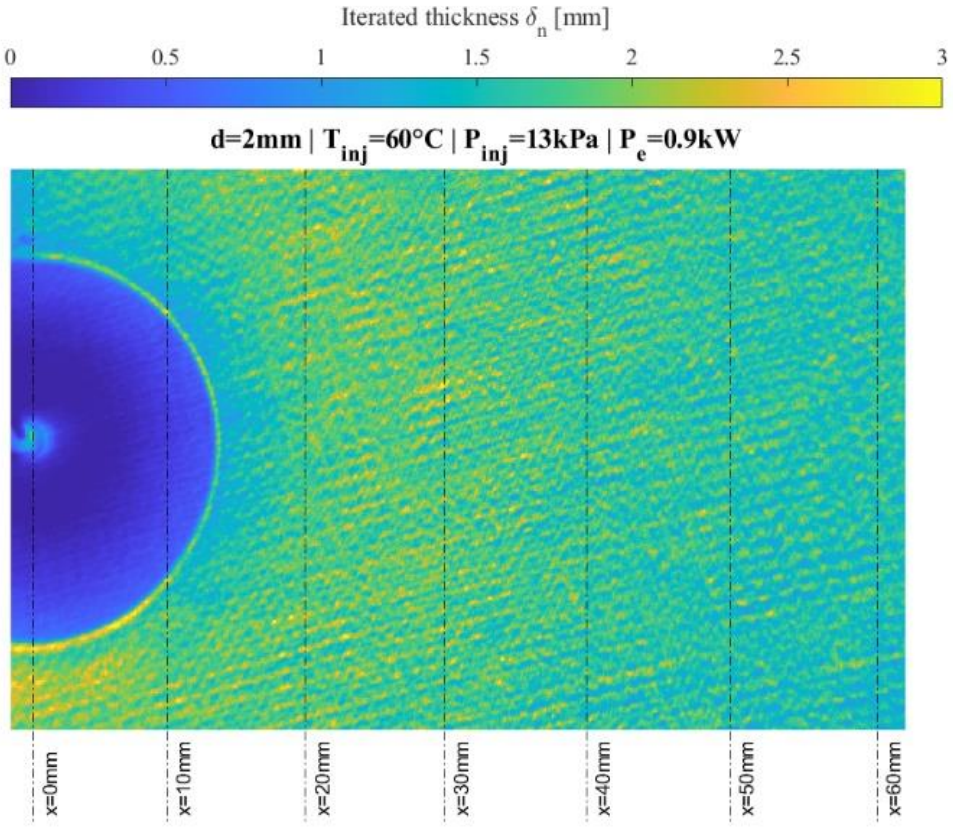

Figure 4.63 – Injection and heating parameters: d = 2 mm, T_{inj} = 60 °C, P_{inj} = 13 kPa, P_e = 0.9 kW.

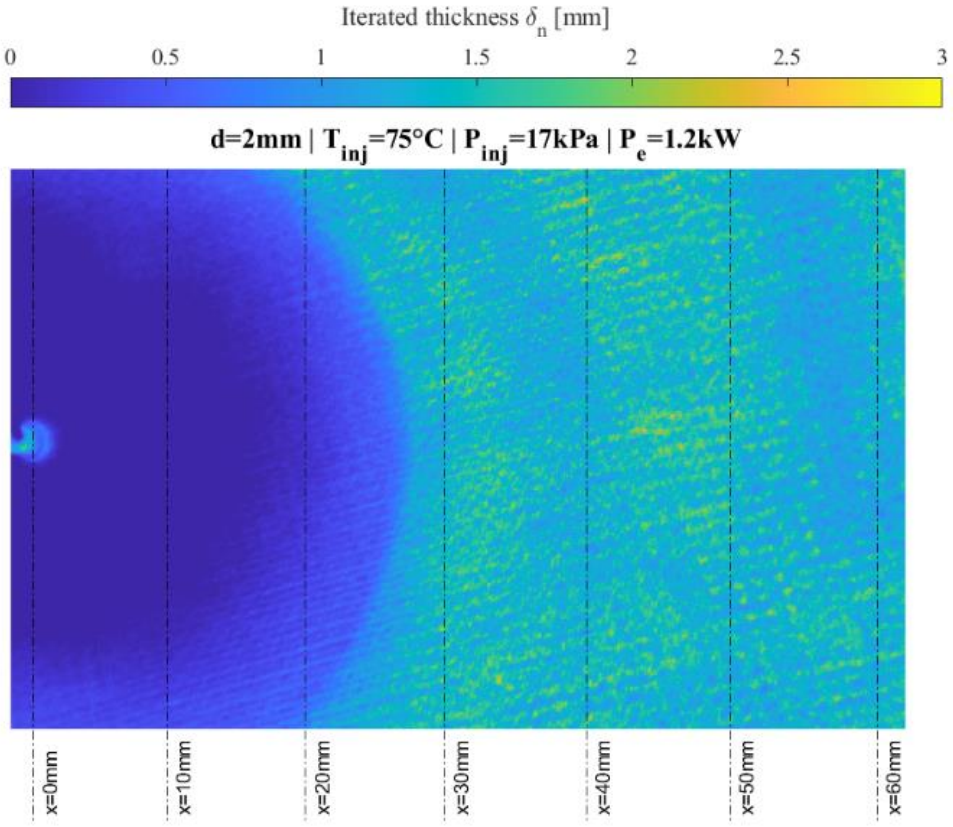

Figure 4.64 – Injection and heating parameters: d = 2 mm, T_{inj} = 75 °C, P_{inj} = 17 kPa, P_e = 1.2 kW.

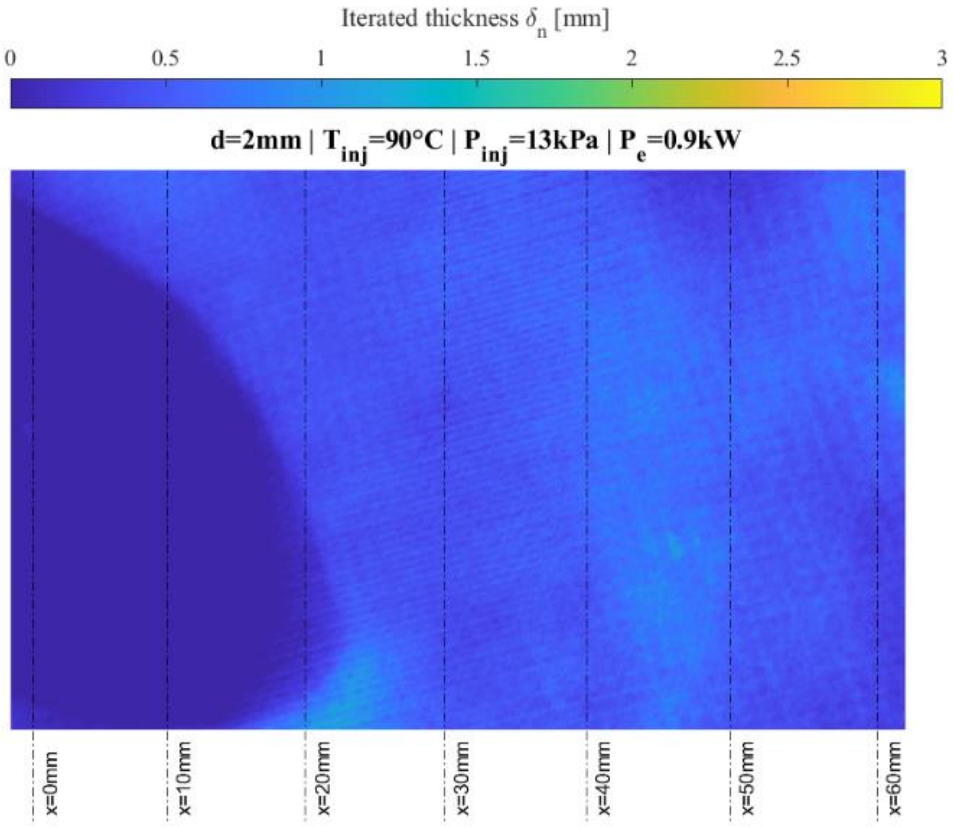

Figure 4.65 – Injection and heating parameters: d = 2 mm, T_{inj} = 90 °C, P_{inj} = 13 kPa, P_e = 0.9 kW.

4.6 Chapter conclusions

- **Preliminary characterisation of thickness and temperature of the jet**

In the very first part of the chapter, several methods are tested to measure the local temperature and thickness. From all these temperature and thickness measurements, the different regions after impingement are well-characterised for various experiments with different injection and heating parameters.

Thermocouples are used to measure temperature along both the plate-normal direction (*z* axis) or along the jet-radial direction (*x* axis). Because of the size of the sensor and the perturbation of the flow, relevant inaccuracy affects the measurement and difficulty is encountered at measuring the temperature of the air-liquid interface and, more generally, along the *z* axis. On the other hand, it is possible to measure the mean temperature along the *x* axis quite accurately, despite the perturbation of the flow and the relevant imprecision. The measurements show that the temperature of the liquid film evolves significantly within the liquid film (approximately 20-30 °C/mm along the *z* axis), and very slightly along the jet-radial direction (approximately 0.2 °C/mm along the *x* axis). A high level of precision is needed to measure such variations. For future work, the use of very small thermocouples is encouraged, given the good reliability of this sensor type.

Concerning thickness, optical and non-optical methods are tested, that is, a laser for triangulation and a contact needle. The laser for triangulation has potential, as measurements are relatively coherent between different experiments, but accuracy is limited by optical access and sensor positioning. The sensor, in fact, must be tilted and recalibrated, and cannot operate as recommended by the furnisher. On the other hand, the contact needle technique shows relatively good accuracy, precision and, more generally, reliability. There are some limitations to the use of the contact needle, in particular the fact that a visible perturbation of the flow must be induced to take the measurement, and the difficulty in measuring if the jet is not steady state. The contact needle is effective for basic and rapid measurements.

- **Spectroscopy and 2-colour 2-dye LIF**

In the second and more extensive part of this chapter, an optical method, based on LIF imaging, is described. In a preliminary phase, the possibility to measure the temperature of the air-liquid interface and the temperature evolution along the *z* axis is considered. For the first, the use of high-concentration fluorescent solutions is investigated experimentally. The aim is to produce a fluorescence signal from a very thin layer of the liquid film. This approach is discarded though, because the theoretical concentration required is much larger than the solubility limit of the dye in the oil. For the second measurement type, the use of planar LIF is examined theoretically. The strategy is to intersect the jet with a thin laser sheet and produce a fluorescence signal from a plane that is perpendicular to the plate. It is calculated that with this approach it is possible to avoid total internal reflection within a very narrow range of angles. More specifically, the theoretical angles for excitation and detection are almost 80 ° (with respect to the *z* axis) and the illumination plane would a 45 ° angle. Given these angles and the further difficulty induced by the jet impingement hydrodynamics, this approach is also discarded. Consequently, flood illumination from above the plate is examined. This represents the starting point for developing the LIF technique for measuring the thickness and the mean temperature of the oil film, and for developing a wide-field imaging method for taking measurements of all the characteristic regions of the impinging jet.

The spectroscopic analysis shows that both dye mixtures (LUM345 + PYR597 and LUM345 + PYR650) in uneven proportions (4 times more PYR than LUM345) are potential candidates for 2-colour 2-dye LIF, because of the sensitivity to temperature and thickness. Their fluorescence spectra are characterised, and it is observed that the mutual interaction is present in both mixtures and is much stronger for LUM345 + PYR597. The spectroscopy is supported by an analysis of the sensitivity to temperature and thickness which includes the detection system. Different combinations of dye mixtures and RGB cameras are simulated and validated experimentally. An important observation is that that both dye mixtures are suitable, but LUM345 + PYR597 is more sensitive to both temperature and thickness than LUM345 + PYR650. Another observation is that that the results from the imaging method agree with the predictions from the spectral simulations. Consequently, since the simulation method (which combines the fluorescence spectra with the camera spectral response) is a useful and effective tool for predicting detection sensitivity, it can be generalised for selecting dyes and cameras for future work. Finally, the mixture LUM345 + PYR650 is selected for the application on the jet impingement configuration, despite the smaller sensitivity than with LUM345 + PYR597.

The uncertainty of the imaging method is characterised with different approaches. Focus is given to the evaluation of the uncertainty related to temperature, and to technical solutions to reduce such uncertainty. The largest contribution to uncertainty is given by photon noise (intensity fluctuations in time in individual pixels) and by the non-uniform response (intensity fluctuations in space between neighbour pixels). The contribution of all these factors leads to about 3.9 % of uncertainty on the channel ratio *Red/Blue* (regardless the temperature) and 10.2 % uncertainty in the channel *Blue* (regardless the thickness). In reason of the small sensitivity to temperature of the mixture LUM345 + PYR650, the uncertainty on the temperature becomes much larger, approximately $(\Delta T)_{tot}$ = 9 °C for films between 60 °C < T_{oil} < 110 °C. With the implementation of a high-optical density filter, a beam homogeniser and image binning, the uncertainty is reduced to approximately $(\Delta T)_{tot}$ = 3 °C for films between 60 °C < T_{oil} < 110 °C. Concerning thickness, uncertainty estimates are between 0.1 mm < $(\Delta\delta)_{tot}$ < 0.9 mm for films between 0.1 mm < δ < 3.8 mm.

Lastly, the algorithms are tested by taking measurements of the temperature and thickness of static films, with known and uniform temperature and thickness. The measurements taken using both algorithms are globally accurate within a field of view of 60 mm (± 1-5 °C from the expected temperature and ± 0.1-0.2 mm from the expected thickness), however they are very inaccurate on a local scale (within few millimetres). Concerning image binning, if on one side it diminishes the uncertainty in the channel $Blue_{FF}$ and channel ratio $Red_{FF}/Blue_{FF}$, it is not effective for improving the measurement of temperature and thickness, probably because of the low sensitivity of the fluorescent mixture.

- **Application to the impinging jet**

The imaging method is applied to the impinging jet, allowing measurements over a wide field of view. The measurement of the local temperature is globally inaccurate and sometimes incoherent, especially in the low-thickness region before the hydraulic jump. For such reasons, the data are not exploitable for evaluating the convective heat transfer between the plate and the oil. Despite that, the overall temperature range is plausible (with respect to the injection temperature) and the overall trend agrees with the measurements taken by the thermocouples. For what concerns thickness, very good agreement is found between the measurements with the contact needle and those from the imaging method.

5 CONVECTIVE HEAT TRANSFER FOR AN IMPINGING JET

- **Chapter introduction**

In the previous chapter 3 and chapter 4, the injection, the plate and the liquid are characterised. Various diagnostics and methods are developed to measure and evaluate the fundamental parameters of conjugated heat transfer. In this chapter, the results from the previous two are retrieved and combined to calculate the convective coefficient, the Nusselt number and the Nusselt correlations. The chapter is divided in two parts.

In the first part, estimates of the convective coefficient and of the Nusselt number are given, using the formulations from section 2.1.1. In the second part, the Nusselt correlations are determined. A first correlation is deduced at the impingement point, via a fitting process. Similarly, a second correlation is deduced along the radial direction. Great focus is given to the correlation at the impingement point and details are provided about the computation method and the validity range. Lastly, the results from the present study are compared with the known literature, to better understand the contribution of the present study within the literature on jet impingement with high-Prandtl fluids.

5.1 Convective coefficient and Nusselt number

5.1.1 Uncertainty analysis

The uncertainty on the convective coefficient and Nusselt number is evaluated using the results from chapter 3 and 4. First, the error induced on the convective coefficient when assuming a uniform oil temperature is calculated, with respect to the evaluation with a locally variable oil temperature. Once established which oil temperature is more appropriate for the calculation, estimates of the uncertainty on the convective coefficient and the Nusselt number are given.

- **Uniform or locally variable oil temperature**

In chapter 4, the oil temperature T_{oil} is evaluated with three techniques: with the circuit-embedded thermocouple (at the injection), with a thermocouple immersed in the liquid (after impingement), with laser induced fluorescence (after impingement). The first technique provides accurate and precise measurements of the bulk oil temperature only at the injection. The second provides measurements for several *x/d*, but temperature is affected by considerable uncertainty (as the method is not suitable for thin liquid films). The third provides field measurements after impingement, but the results are restrained to a limited number of experiments and are not exploitable for calculating the convective coefficient, in reason of major discrepancies (as detailed in chapter 4). Consequently, the convective coefficient can be calculated in two ways: assuming a uniform oil temperature (i.e., the one at the injection) or using local measurements after impingement.

In Figure 5.1, the convective coefficient is shown for the injection and heating: d = 2 mm, T_{inj} = 75 °C, P_{inj} = 17 kPa and P_e = 1.2 kW. Notice that this experiment is not the reference experiment (with d = 1 mm) because the thermocouple measurements are taken only for d = 2 mm. The two traces are calculated with the same surface temperature T_{surf} and heat flux q, but with a different approach for the local oil temperature $T_{oil}(x)$. For the trace "*Uniform* $T_{oil}(x)$", the oil temperature is assumed uniform everywhere (i.e.,

"adiabatic fluid" assumption) and is equal to the injection temperature. For the trace "*Variable $T_{oil}(x)$*", the local oil temperature $T_{oil}(x)$ is the one measured by the thermocouple immersed in the liquid (see section 4.1.1). The only exception is $x/d = 0$, where the injection temperature is used.

In Figure 5.1, within the range $0 < x/d < 6$, adopting variable $T_{oil}(x)$ increases the estimate of h up to 4.2 % with respect to uniform $T_{oil}(x)$. The increase is more relevant at $x/d = 10$ where 10.1 % is calculated. For the furthest data point, $x/d = 29$, the increase is 29.6 %. Despite the measurements with the thermocouple immersed in the fluid are affected by large uncertainty, the small difference between the traces for $x/d < 10$ suggests that the adiabatic fluid assumption is valid for $x/d < 10$. This corresponds to the range where the surface temperature measurements and the heat flux evaluation are consistent, and where the overall method is also robust.

This result proves that assuming a uniform oil temperature induces negligible error in the convective coefficient within $0 < x/d < 10$, which is also the range where the experimental method is robust. Consequently, all the results presented in the rest of this manuscript can be calculated with the injection temperature and the adiabatic fluid assumption. On the other hand, the result highlights that not-so-far from the impingement point, accurate measurement of the local oil temperature allows more accurate evaluation of the convective coefficient. Even though the present study has limited reliable datapoints for $x/d > 10$, the evaluation of the local oil temperature could play a relevant role over the farthest regions from the nozzle, on the peripheral regions of end-windings with respect to the injector position.

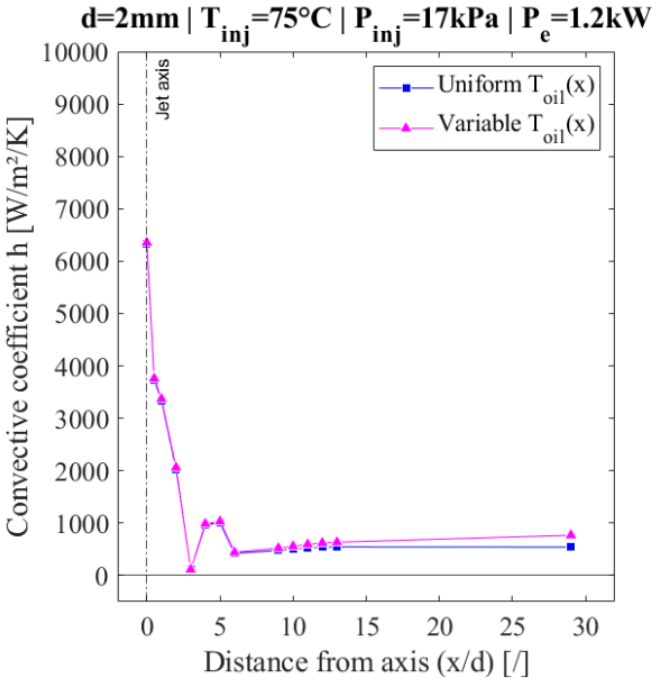

Figure 5.1 – Radial variation of the convective coefficient. "Uniform $T_{oil}(x)$" is calculated assuming uniform oil temperature, equal to the injection temperature. "Variable $T_{oil}(x)$" calculated with measurement of the local oil temperature. Both traces are calculated with the same surface temperature and heat flux.

- **Uncertainty of the convective coefficient and Nusselt number**

The uncertainty associated with the convective coefficient in Figure 5.2 is evaluated for the reference experiment: $d = 1$ mm, $T_{inj} = 75$ °C, $P_{inj} = 20$ kPa and $P_e = 1.2$ kW. The trace has resembling characteristic as the ones observed for the heat flux (in section 3.3): a pronounced peak at the impingement point, a relevant decrease up to $x/d \approx 10$, a flattening

for greater distances. The same inconsistencies from the heat flux evaluation appear within $10 < x/d < 30$ (see section 3.3).

The relative squared error is used for calculating the uncertainty on the convective coefficient $\Delta h/h$, as below:

$$\frac{\Delta h}{h} = \left[\left(\frac{\Delta T}{T}\right)^2 + \left(\frac{\Delta q}{q}\right)^2\right]^{1/2} \qquad (35)$$

The parameters $\Delta T/T$ and $\Delta q/q$ are the relative uncertainties associated with the temperature difference $T_{surf} - T_{inj}$ and to the heat flux q, respectively. The values ΔT and Δq used in the formula come for the uncertainty analysis undertaken in chapter 3. Notice that to use equation (35), ΔT and Δq are assumed independent. In section 3.2.2 it is shown that part of the uncertainty of the surface temperature (associated with the thermocouple placement) propagates into the heat flux. This implies that there is a dependence between the two (a linear one in this case), however two aspects are to take into account. First, the uncertainty of the temperature is quantified and its propagation into the heat flux is also quantified (i.e., typical and maximum values are given). Second, the estimates of the uncertainty are unlikely to increase or decrease, thus they variation is limited. After these considerations, ΔT and Δq can be considered independent.

The estimate of the total uncertainty on temperature difference $T_{surf} - T_{inj}$ is $\Delta T = \pm 2.1$ °C (max ± 3.2 °C), according to previous section 3.1.1 and 3.2.2. For a mean difference $T_{surf} - T_{inj} = 69.6$ °C, it results $\Delta T/T = 3$ %. The uncertainty of the heat flux is $\Delta q/q = \pm 18.0$ % (max ± 36.0 %) for every x/d (see section 3.3.2). By applying equation (35) to the data points of Figure 5.2, it results $\Delta h/h = \pm 18.3$ % (max ± 36.3 %).

Notice that the surface temperature contributes in two ways to the uncertainty: there is a direct contribution (in the term $T_{surf} - T_{inj}$) and an indirect one (through q). This last is amplified during by the simulation of the heat flux and represents almost the totality of the uncertainty of the convective coefficient. Since the method is affected primarily by T_{surf} rather than T_{inj}, this is the key parameter where to reduce uncertainty.

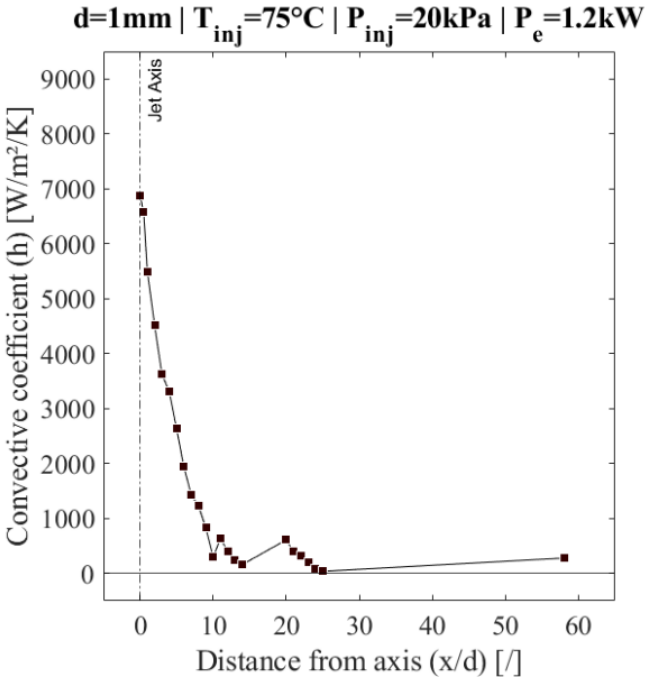

Figure 5.2 – Jet-radial distribution of the convective coefficient for the reference experiment.

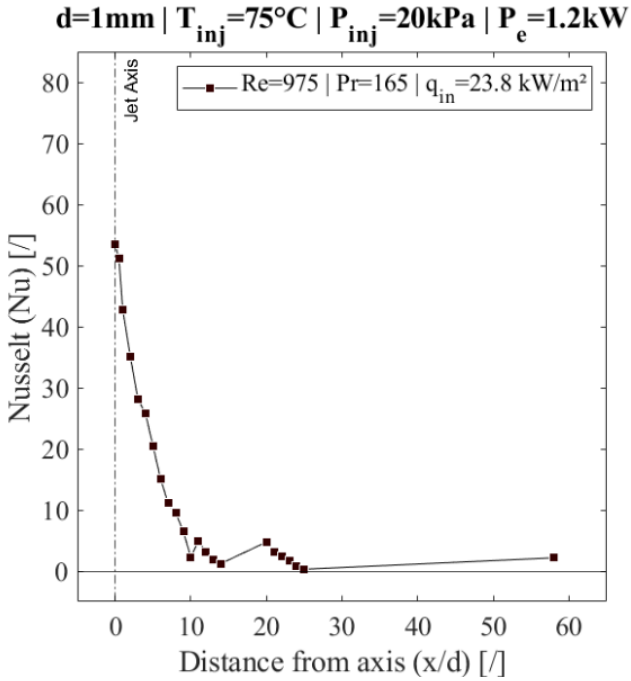

Figure 5.3 – Jet-radial distribution of the Nusselt number for the reference experiment.

The same data points of Figure 5.2 are used to calculate the Nusselt number and the results is in Figure 5.3. Concerning uncertainty, the Nusselt number is calculated from the nozzle diameter d, the thermal conductivity k and the convective coefficient h. The uncertainty associated with the measurement of the nozzle diameter d is considered negligible. The thermal conductivity k varies by 2.3 % in the whole injection range (60 °C < T_{inj} < 90 °C), including the uncertainty on the injection temperature. Consequently, the contribution of the thermal conductivity is also negligible, and the uncertainty on the Nusselt number is equivalent the one of the convective coefficient, that is, $\Delta Nu/Nu$ = ± 18.3 % (max ± 36.3 %).

5.1.2 Parametric study on the injection and heating parameters

The data from the same parametric study on the injection and heating parameters presented in chapter 3 are used to calculate the jet-radial distribution of the Nusselt number.

- **Variable heating power**

In Figure 5.4 the heating power P_e is varied while keeping the same injection parameters. All traces show similar features and overlap for most of the x/d range. The largest value of Nusselt is always obtained at the impingement point. A monotonic decrease follows up to $x/d \approx 10$. Complementary to Figure 5.4, the difference $\Delta Nu/Nu$ between the traces is reported in Figure 5.5 for every x/d. Notice that the uncertainty value ± 18.3% is also drawn. The plot shows that $(Nu_B - Nu_A)/Nu_B$ is mostly in the positive quadrant while $(Nu_B - Nu_C)/Nu_B$ is mostly in the negative quadrant. This suggests that the heating power has a slight effect on the convective coefficient, probably in reason of a localised reduction of viscosity close to the solid, however this outcome needs more investigation as the uncertainty is too large to confirm such occurrence.

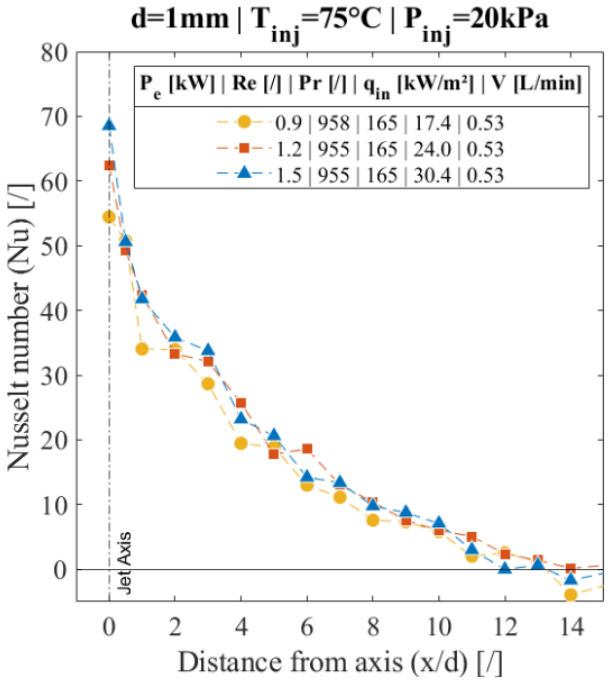

Figure 5.4 – Radial variation of the Nusselt number. Parametric variation of the injection and heating. In this case the heating power P_e is varied while keeping the same injection parameters.

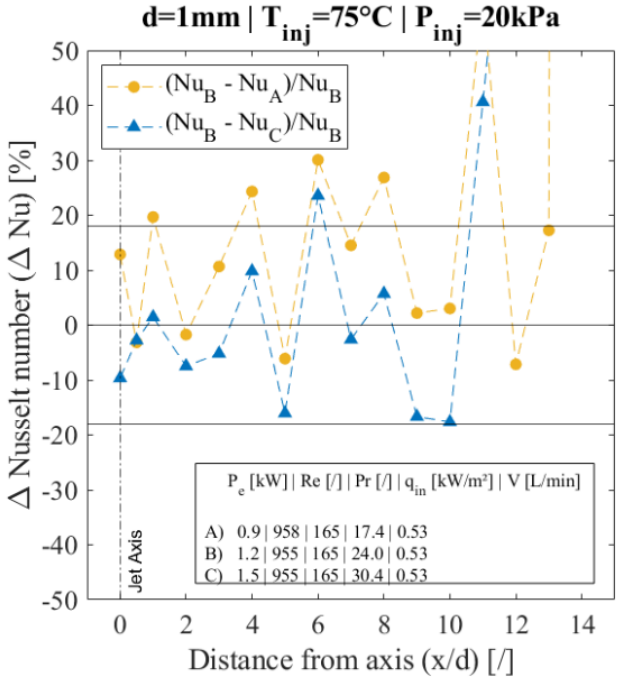

Figure 5.5 – Difference between the local Nusselt Number, referring to the traces in Figure 5.4.

- **Variable injection temperature**

In Figure 5.6 the injection temperature T_{inj} is varied while keeping the same nozzle diameter d, injection pressure P_{inj} and heating power P_e. Notice that the increase of T_{inj} from 60 °C to 90 °C leads to the increase of the flowrate $\dot{V}$ by 12.5 %, the increase of Re by a factor 2.4, and a decrease of Pr by a factor 2.0. The injection parameters vary significantly, but the Nusselt number is slightly affected, because all the traces of Figure 5.6 almost overlap. With the aid of Figure 5.7 (showing the relative difference ΔNu between the traces of Figure 5.6 of for every x/d), the effects of the temperature variation are more visible.

The datapoints $(Nu_B - Nu_A)/Nu_B$ are mostly negative and those $(Nu_B - Nu_C)/Nu_B$ are mostly positive. The horizontal lines in Figure 5.7 represents the uncertainty of the evaluation.

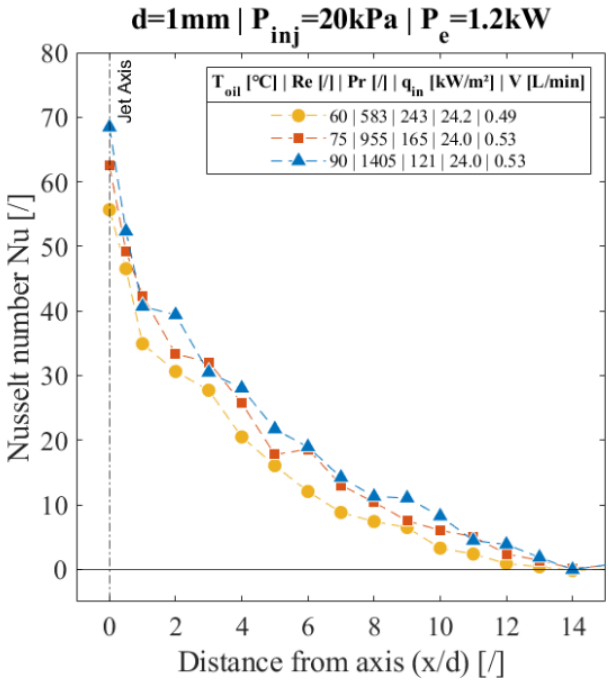

Figure 5.6 – Radial variation of the Nusselt number. Parametric variation of the injection and heating. In this case the injection temperature T_{inj} is varied while keeping the other injection parameters and heating power.

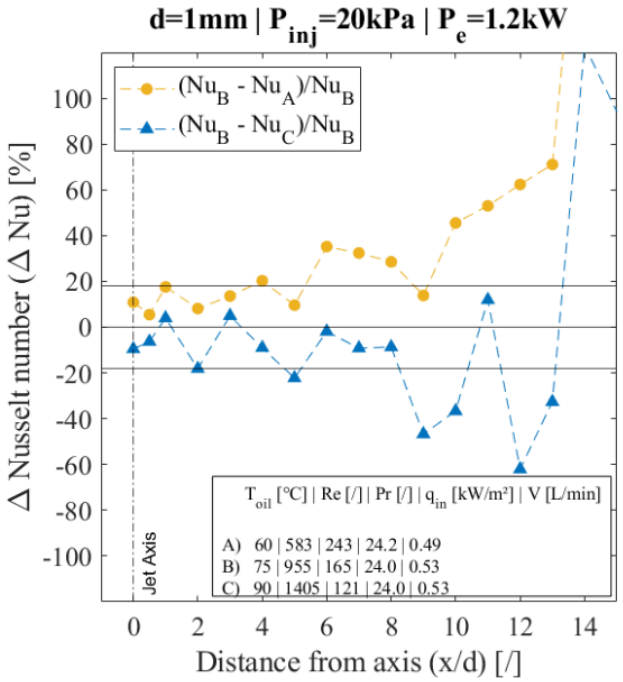

Figure 5.7 – Difference between the local Nusselt Number, referring to the traces in Figure 5.6.

- **Variable injection pressure**

In Figure 5.8, the injection pressure P_{inj} is varied while keeping the same nozzle diameter d, injection temperature T_{inj} and heating power P_e. The increase of P_{inj} from 17k Pa to 20 kPa leads to the increase of the flowrate $\dot{V}$ by 1.3 %. The Reynolds Re number also

increases by a factor 1.3 while the Prandtl *Pr* is unchanged. The Nusselt number increases slightly and everywhere in the plotted range. This is more evident in Figure 5.9, which shows the relative difference *ΔNu* between the traces of Figure 5.8 of for every *x/d*. In the plot, in fact, the data points *ΔNu* between the injection at P_{inj} = 17 kPa and those at P_{inj} = 20 kPa are mostly negative and larger than the uncertainty (represented by the horizontal line). In this case the result is coherent with the expectation because the increase of the flowrate or Reynolds, for the same P_e and *Pr*, should increase the heat transfer towards the liquid.

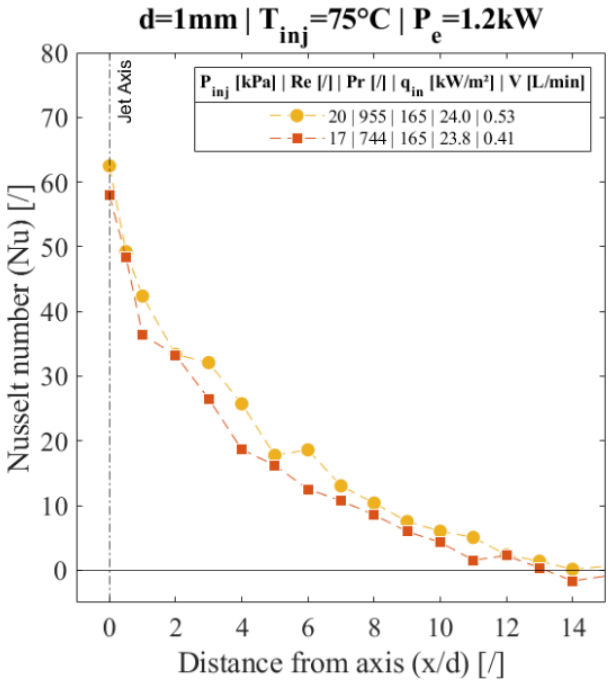

Figure 5.8 – Radial variation of the Nusselt number. Parametric variation of the injection and heating. In this case the injection pressure P_{inj} is varied while keeping the other injection parameters and heating power.

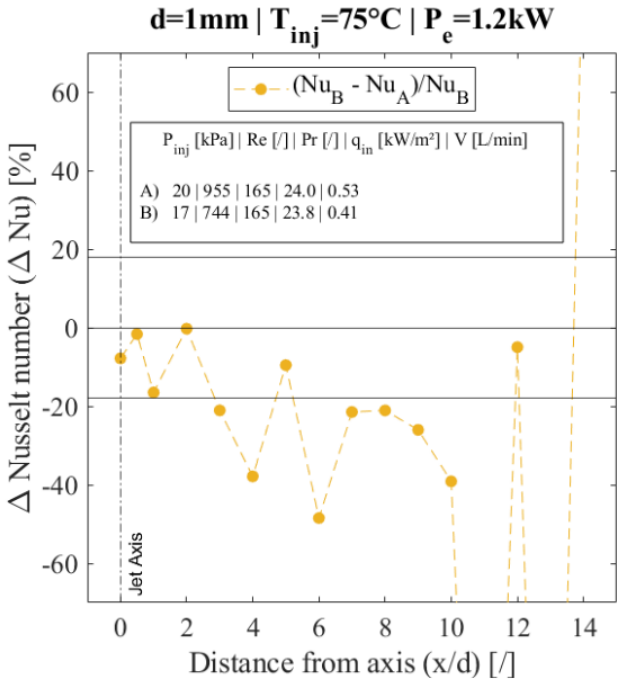

Figure 5.9 – Difference between the local Nusselt Number, referring to the traces A and B in Figure 5.8.

- **Variable nozzle diameter and injection pressure**

In Figure 5.10, the nozzle diameter d is doubled and the injection pressure P_{inj} is varied, while keeping the same injection temperature T_{inj} and heating power P_e. To complete the analysis, Figure 5.11 is added, showing the difference ΔNu between the traces of Figure 5.10 for every x/d. At first glance, all traces in Figure 5.10 have similar trend and tend to overlap, even though the traces with d = 2 mm exhibit more irregularities, inherited from the heat flux prediction. In particular, if the data points at x/d = 3 and x/d = 6 could be excluded, the traces would resemble those obtained with d = 1 mm.

Concerning the two traces with d = 2 mm in Figure 5.10, the increase of P_{inj} (thus $\dot{V}$) leads to the slight increase of the Nusselt number because the traces with P_{inj} = 17 kPa are above those with P_{inj} = 13 kPa. This occurrence is coherent and analogous to what discussed previously in Figure 5.8 using d = 1 mm.

The two injections with the same P_{inj} = 17 kPa and different diameter, correspond to a largest variation of the Reynolds number and flowrate. For these two injections, the relative ΔNu is plotted in Figure 5.11. The trace $(Nu_B - Nu_C)/Nu_B$ is mostly in the negative sector, when excluding the irregular data points at x/d = 3 and x/d = 6. This suggests that the increase of the nozzle diameter also increases the Nusselt number. The increase is rather evident because larger than the uncertainty range (represented by the two horizontal lines) and is more pronounced nearby the impingement point.

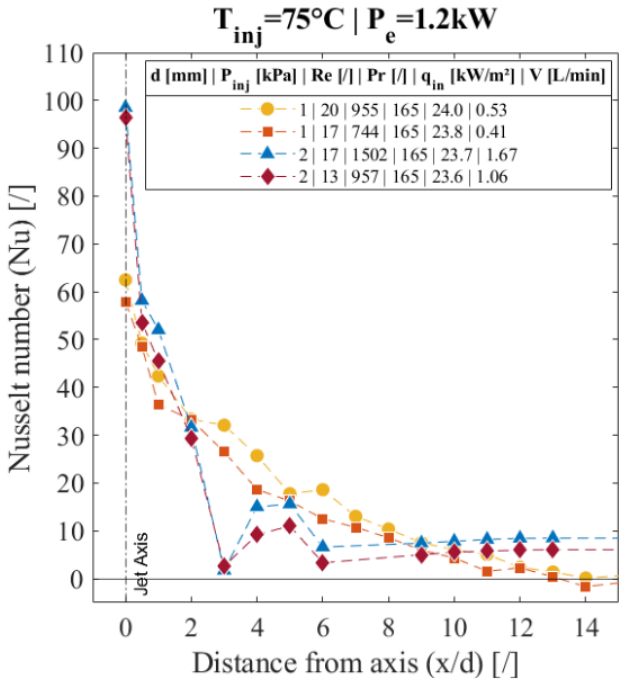

Figure 5.10 – Radial variation of the Nusselt number. Parametric variation of the injection and heating. In this case the nozzle diameter d and the injection pressure P_{inj} are varied while keeping the other injection parameters and heating power.

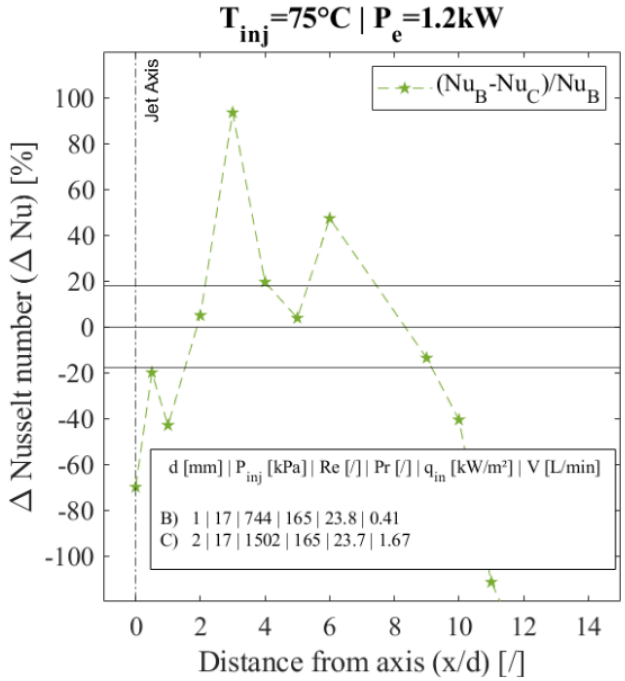

Figure 5.11 – Difference between the local Nusselt Number, referring to the traces Figure 5.10.

- **Discussion**

The plots from Figure 5.4 to Figure 5.11 show that the Nusselt number exhibits variations within the order of 10-20%, for the given injection and heating range investigated in this research. It is difficult to clearly understand the influence of the investigated parameters though. On one side, the overall uncertainty of the method is quite large (about 18 %), meaning that the extent of the variations is inevitably smaller than the uncertainty. On the other, the traces exhibit many irregularities (coming from the evaluation of the heat flux), especially for those obtained with diameter d = 2 mm.

Considering the largest variation of the injection and heating parameters (allowed by the experimental apparatus), a synthesis of the variations of the Nusselt number and other meaningful variables observed in this study (average between $0 < x/d < 10$) is reported in Table 5.1. According to such synthesis, in this study, the most significant variations of the Nusselt number are observed for variable injection temperature and pressure. The heating power appears to have mild effects on the Nusselt number. The effects of the diameter are difficult to observe because of the irregularity of the results with d = 2 mm.

Table 5.1 – Synthesis of the variations of the dimensionless numbers, flowrate and input heat flux induced by the largest variations of the injection and heating parameters allowed by the experimental apparatus.

LARGEST VARIATION OF THE INJECTION AND HEATING PARAMETERS	**MAXIMUM VARIATION INDUCED (Max – Min) / Min**				
Max – Min	***ΔNu*** **[%]**	***ΔRe*** **[%]**	***ΔPr*** **[%]**	$\Delta\dot{V}$ **[%]**	Δq_{in} **[%]**
ΔT_{inj} = 30 °C	37	141	-50	-8	0
ΔP_{inj} = 4 kPa	21	28	0	30	0
Δd = 2 mm	NA	102	0	215	0
ΔP_e = 0.6 kW	16	0	0	0	67

5.1.3 Literature comparison

- **Compare magnitude and trend**

The results from the present study are compared to those from *Ma et al.* 1997a and *Renon et al.* 2021, for what concerns the magnitude and the trend along the jet-radial direction. The *Nu* for most similar injection and heating parameters are extracted and examined. Notice that the mentioned authors use different methods and formulations for calculating the convective coefficient (see section 1.2.2). Moreover, assumptions are made for the missing parameters. In light of these considerations, direct comparison of the magnitude is not exhaustive but important to understand if the estimates are reasonably similar with the literature. Conversely, the trend is expected to be similar. In Figure 5.12 two traces from this study and two from the literature are plotted and compared.

The results from *Ma et al.* 1997a are typically 3-7 times larger than the ones from the present study, while those from *Renon et al.* 2021 are 1-2 times larger. Since the diameter is the same for the three traces and the thermal conductivity is similar between the fluids, the convective coefficient is the parameter making the difference in the Nusselt number.

Concerning the trend, all traces show a peak at the impingement point and a subsequent decrease for growing *x/d*. To evaluate such decrease, the values from two distant *x/d* are selected and the ratio *Nu* (*x/d* = 0) / *Nu* (*x/d* = 10) is calculated. For *Ma et al.* 1997a it is 13.1, for *Renon et al.* 2021 it is 8.3, for the present study it is 10.4 and 18.8 for the traces T_{inj} = 75 °C and T_{inj} = 60 °C, respectively. Such comparison indicates that despite the difference in the magnitude between the present study and those from the literature, the relative variation along *x* is similar.

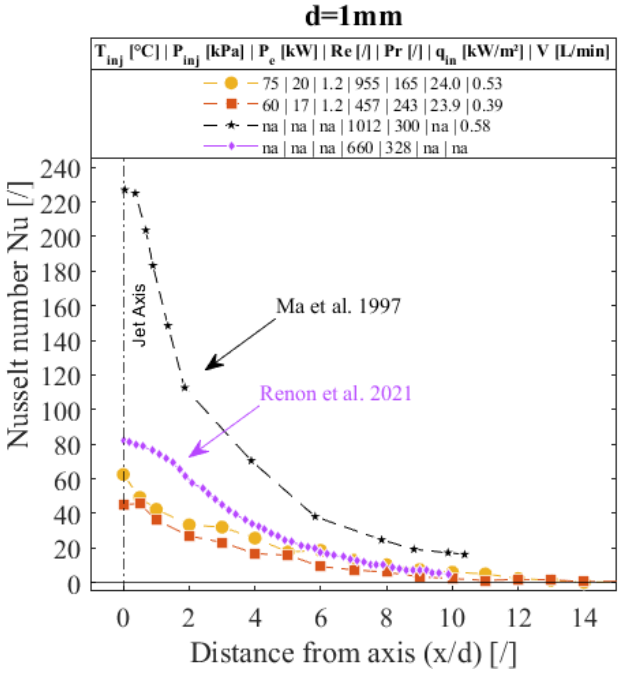

Figure 5.12 – Radial variation of the Nusselt number. Comparison with Ma et al. 1997 and Renon et al. 2021.

- **Compare effects of Reynolds and Prandtl**

The study by *Renon et al.* 2021 is considered to examine the expected variations of the Nusselt number induced by the input heat flux and the Reynolds and Prandtl numbers. Table 5.2 reports the variation of *Nu* for *x/d* = 0 and *x/d* = 5, obtained varying the injection

and heating parameters. The plots by *Renon et al.* 2021 are reported in annexe to chapter 5 for the range $0 < x/d < 5$.

For a given *Re* and *Pr*, in *Renon et al.* 2021 a positive variation of q_{in} leads to a positive variation of *Nu*. Such increase is less pronounced at the impingement point and more pronounced at greater distances. In the present study, *Nu* also increases when q_{in} is increased, but the variation is larger at the impingement point, therefore only partial agreement is found.

In *Renon et al.* 2021, the variation of *Nu* is positive and significant with a positive variation of *Pr* (for the same q_{in} and *Re*). Similarely, a positive variation of *Re* implies a positve variation of *Nu* (for the same q_{in} and *Pr*). For the cited study, the table shows that the variation on *Nu* induced by *Re* or *Pr* are similar, that *Nu* at $x/d = 0$ is less affcted than at $x/d = 5$, and that the *Re* variation affects *Nu* at $x/d = 5$ more significantly than *Pr*.

Concerning the present study, the table reports the individual variation of *Re* (obtained by varying P_{inj}), the opposite and simultaneous variation of *Re* and *Pr* (obtained by varying T_{inj}), but not the individual effects of *Pr*. For any variation of *Re* and *Pr* in the table, the *Nu* variation is always positive, and at $x/d = 5$ it is more pronounced than at $x/d = 0$. In these terms, the results are coherent with the reference study *Renon et al.* 2021.

Table 5.2 – Variations of the Nusselt number (*Nu*) induced by a parametric variation of the heat flux (q_{in}), the Reynolds number (*Re*) and the Prandtl number (*Pr*). Comparison with *Renon et al.* 2021 for two *x/d*.

Renon e al. 2021 (d = 2 mm)				**Present study (d = 1 mm)**				**Present study (d = 2 mm)**			
Parametric variation		**Variation of Nu**		**Parametric variation**		**Variation of Nu**		**Parametric variation**		**Variation of Nu**	
		x/d = 0	**x/d=5**			**x/d = 0**	**x/d=5**			**x/d = 0**	**x/d=5**
Re	0 %			Re	0 %			Re	0 %		
Pr	0 %	4%	45 %	Pr	0 %	26 %	9.0 %	Pr	0 %	25 %	17 %
q_{in}	300 %			q_{in}	70 %			q_{in}	70 %		
Pr	250 %			Pr	– 100 %			Pr	– 100 %		
Re	0 %	108 %	115 %	Re	+ 140 %	21 %	31 %	Re	+ 170 %	4 %	83 %
q_{in}	0 %			q_{in}	0 %			q_{in}	0 %		
Pr	0 %			Pr	0 %			Pr	0 %		
Re	280 %	115 %	194 %	Re	30%	8 %	13 %	Re	60 %	2 %	42 %
q_{in}	0 %			q_{in}	0 %			q_{in}	0 %		

5.2 Nusselt correlations

5.2.1 Nusselt correlations

- **Method**

The fundamental correlation (at the impingement point) has the typical formulation $Nu = C\, Re^{m}\, Pr^{n}$. The dimensionless numbers *Nu*, *Re* and *Pr* are determined from the experiments, whereas *C*, *m* and *n* are obtained empirically with data fitting. The *Pr* exponent is set to $n = 1/3$, as it is proved to fit well for high-Prandtl fluids (see section 1.2.3). The fitting algorithm is the least-squares and the fitting function is a power law (i.e., $y = a\, x^{b}$), as it consents simplification when transformed to logarithmic notation. For the correlation along the jet-radial direction, the overall method is analogous, but the formulations are slightly more complex. When applying the fitting algorithm, the coefficient of determination R^2 is also calculated: $R^2 > 0.9$ is considered very good fitting, $R^2 > 70$ still good fitting and $R^2 < 70$ not good fitting. Notice that this parameter represents

the error made when approximating data points with a continuous function, which is different and independent from the uncertainty of the experimental method.

- **Independence from the heating power**

The datapoints from the impingement point are considered: the Nusselt number *Nu* at the impingement point (*x/d* = 0) is extracted from all the experiments performed in this research, as well as the corresponding *Re*, *Pr* and P_e. The quantity $Nu\ Pr^{-1/3}$ is calculated and plotted as a function of *Re* and P_e. The outcome is illustrated in Figure 5.13. This pre-treatment is needed for several reasons: to prepare data for the calculation of the correlations, to facilitate comparison with the literature, and to avoid three-dimensional plotting. In the plot, $Nu\ Pr^{-1/3}$ increases with *Re*, for every nozzle diameter *d* and injection pressure P_{inj}. Conversely, the trend with the heating power P_e is unclear, because the data points are scattered, especially those with *d* = 2 mm. Given that, $Nu\ Pr^{-1/3}$ is considered independent from P_e for the following analysis.

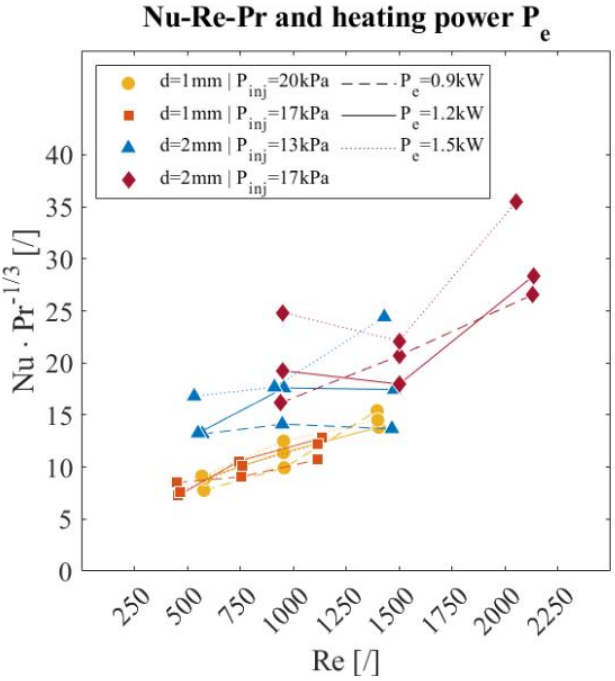

Figure 5.13 – Variation of the parameter $Nu\ Pr^{-1/3}$ with the Reynolds number *Re* and the heating power P_e. Nusselt number *Nu* is evaluated at the impingement point (*x/d* = 0).

- **Correlation at the impingement point**

In Figure 5.14, $Nu\ Pr^{-1/3}$ is fitted with a power law and the coefficient of determination R^2 is reported for every trace. The fitting is performed for every pair of nozzle diameter *d* and injection pressure P_{inj}, and for all the datapoints. For both traces with *d* = 1 mm, good fitting is obtained. Not good fitting is shown for *d* = 2 mm and P_{inj} = 17 kPa and poor fitting denotes the trace with *d* = 2 mm and P_{inj} = 13 kPa. Consequently, the fitting is not excellent (R^2 = 0.58) as affected by the relatively large dispersion of the datapoints with *d* = 2 mm. As showed in annexe to chapter 5, fitting can be improved by setting *n* > 1/3, however no convergence on a specific value of *n* is shown as the datapoints simply squeeze on the *x* axis. The value *n* = 1/3 is therefore kept since confirmed by the literature.

In Figure 5.15, the fitting process is improved through the scaling factor by involving the diameter *d* in the calculation, in order to increase the coefficient R^2. A similar strategy

is found in *Renon et al.* 2021. In this way, the same $Nu\ Pr^{-1/3}$ of Figure 5.14 is first multiplied by the term $(d/d_{ref})^{p}$ and then fitted. Notice that the value d_{ref} = 1 mm is chosen arbitrarily as the reference diameter. Via a trial-by-error process, the best fitting of all the data points is obtained when setting p = 0.50. Notice that C and m must be the same in both Figure 5.14 and Figure 5.15. The resulting Nusselt correlation is:

$$Nu = 0.31\ Re^{0.53}\ Pr^{1/3}\left(d/d_{ref}\right)^{0.50} \qquad (36)$$

In conclusion, this correlation is valid for the impingement point x/d = 0, within the range 449 < Re < 2138 and 120 < Pr < 240. The correlation approximates the datapoints with the determination coefficient R^2 = 0.70.

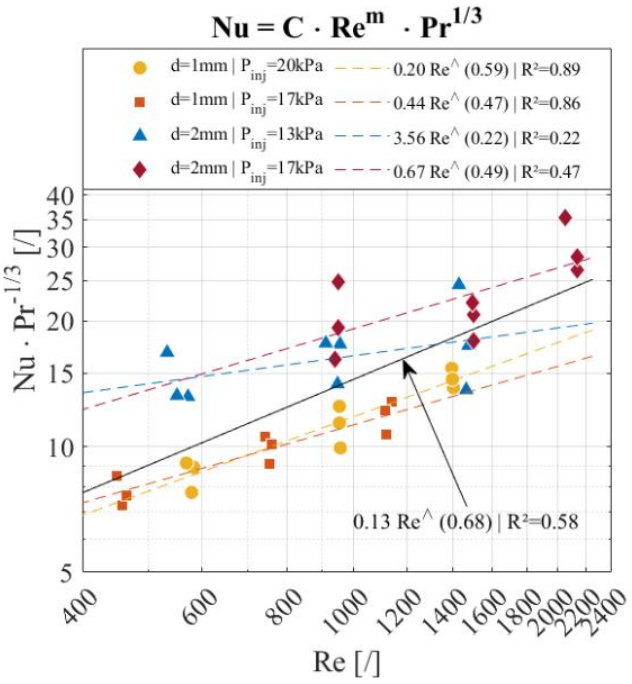

Figure 5.14 – Nusselt correlations at the impingement point. The coefficients C, m and R^2 are determined from a fitting process, and the Pr exponent is set as 1/3. The dashed traces refer to a pair of nozzle diameter d and injection pressure P_{inj}. The continuous trace refers to all the data points.

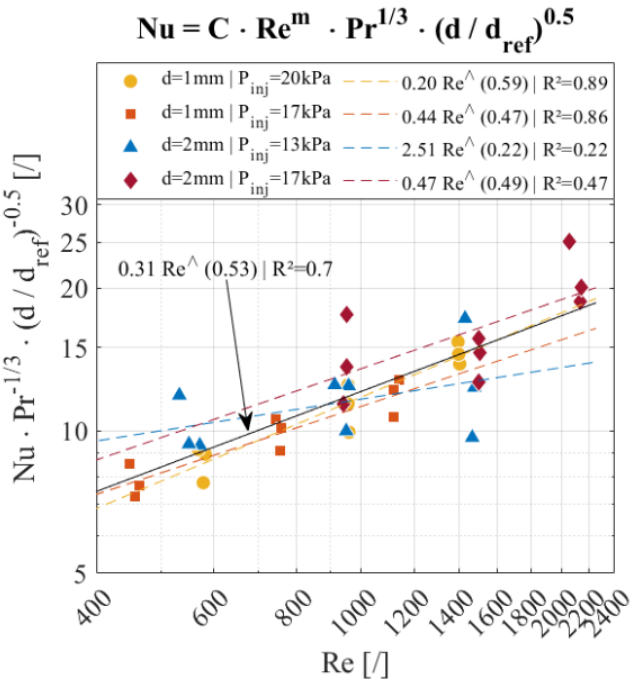

Figure 5.15 – Nusselt correlations at the impingement point. The coefficients *C*, *m* and R^2 are determined from a fitting process. The *Pr* exponent is set as 1/3, the d/d_{ref} exponent is set as 0.5, and d_{ref} =1 mm. The dashed traces refer to a pair of nozzle diameter *d* and injection pressure P_{inj}. The continuous trace refers to all the data points.

- **Correlation along the jet-radial direction**

The formulation below is borrowed from *Ma et al.* 1997a, to correlate the datapoints between $1 < x/d < 10$, with the addition of the term $(d/d_{ref})^{p}$ for a better fitting (as done previously for the correlation at the impingement point):

$$\frac{Nu}{Nu_0} = \frac{(A \cdot Re)^{B \cdot x/d}}{1 + a \cdot (x/d)^b} \left(\frac{d}{d_{ref}}\right)^p \qquad (37)$$

The formulation approximates the radial variation of the Nusselt number with a hyperbole, and a normalisation is also applied by the Nusselt number at the impingement point Nu_0 (approximated by a power-law). The five parameters *A*, *B*, *a*, *b* and *p* must be determined empirically, via a trial-by-error process which requires three steps. In the first step, the parameters *p*, *A* and *B* are fixed, by assigning an arbitrary seed value. In the second step, *a* and *b* are determined from the least-squared fitting (also R^2). The third step consists in repeating the first and the second, by assigning different values to *p*, *A* and *B* from the seed ones, until the highest R^2 is obtained for *a* and *b*. In the present study, the best fitting is obtained with the following:

$$\frac{Nu}{Nu_0} = \frac{(7.5\,Re)^{0.05\,x/d}}{1 + 0.58\,(x/d)^{2.89}} \left(\frac{d}{d_{ref}}\right)^{0.85} \qquad (38)$$

The correlation is valid for $449 < Re < 2138$ and $120 < Pr < 240$, and is plotted in Figure 5.16. The datapoints in the figure show that the normalised function of the Nusselt number decreases the further from the impingement point.

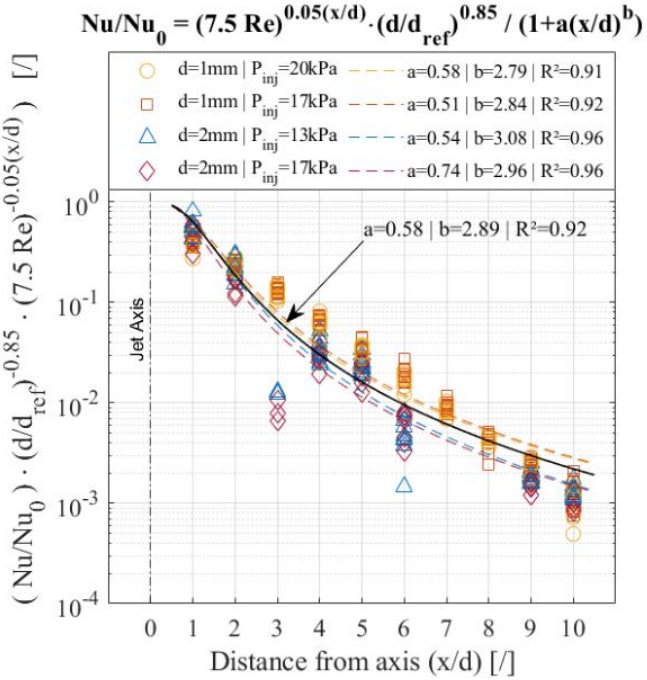

Figure 5.16 – Nusselt correlations along *x/d*. The parameters $p = 0.85$, $A = 7.5$ and $B = 0.05$ are fixed. The parameters *a*, *b* and R^2, are obtained from the fitting process. The dashed traces refer to each pair of nozzle diameter *d* and injection pressure P_{inj}. The continuous trace refers to all the data points.

5.2.2 Literature comparison

- **Compare by magnitude**

To best compare the results from different studies, the quantity $Nu\ Pr^{-1/3}$ is plotted as function of *Re* in Figure 5.17. The results from the present study (from Figure 5.14) and the three most similar studies on high-Prandtl fluids are plotted (*Bennion* and *Moreno*, 2015; *Leland* and *Pais*, 1999; *Ma et al.*, 1997a; *Renon et al.*, 2021). The trace from *Ma et al.* 1997a corresponds to the Nusselt correlation obtained using a pipe nozzle of diameter $d = 1$ mm and injecting transformer oil with $Pr = 300$. The experimental *Nu* from *Leland* and *Pais* 1999 are extracted from their plots. They used a $d = 1$ mm nozzle, injecting an unspecified lubricant oil, within the range $160 < Re < 2193$, $54 < Pr < 346$, 30 °C < T_{inj} < 100 °C, and 0.3 L/min < $\dot{V}$ < 0.57 L/min. Concerning *Bennion* and *Moreno* 2015, the experimental convective coefficient, injection temperature and bulk velocity are extracted from their plots. Successively, the dimensionless numbers are calculated while assuming the thermal properties of a typical ATF. They injected with a $d = 2$ mm nozzle within the range 50 °C < T_{inj} < 90 °C, and 0.5 m/s < U < 0.10 m/s. Notice that the mentioned authors use different methods and formulations for calculating the convective coefficient (see section 1.2.2).

The experimental data from this study do not agree with those from *Ma et al.* 1997a in terms of magnitude. In the whole range, *Ma et al.* 1997a is about 3 times higher than the data with $d = 1$ mm, and about 2 times higher for the data with $d = 2$ mm. Despite that, it is observed that the offset is almost identical in the whole range. This shows that the trend is very similar between the reference study and the present study.

On the other hand, good agreement is observed with the other two studies. More specifically, good agreement is found between data points with similar diameters, as they overlap in a large part of the investigated *Re* range.

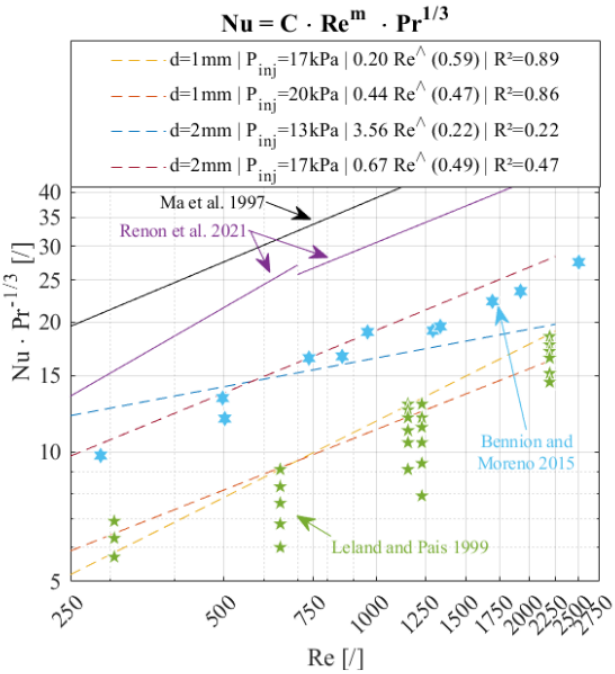

Figure 5.17 – Comparison between the parameter $Nu\ Pr^{-1/3}$ evaluated in the present study and those from the most similar injections from the literature: *Ma et al.* 1997a ($Nu\ Pr^{-1/3} = 1.27\ Re^{0.495}$), *Leland* and *Pais* 1999 (datapoints with $d = 0.838$ mm), *Bennion* and *Moreno* 2015 (datapoints with $d = 2$ mm), *Renon et al.* 2021 ($Nu\ Pr^{-1/3} = 0.315\ Re^{0.68}$ and $Nu\ Pr^{-1/3} = 1.11\ Re^{0.48}$, with $d = 2$ mm). Note: missing fluid properties are assumed from similar fluids.

- **Compare by correlation coefficients**

In Table 5.3, the Nusselt correlations (at the impingement point) are listed from similar studies, including the Reynolds and Prandtl number. The correlation (36) from the present study is at the bottom of the table. For the comparison, the coefficients m and n are to consider as they are associated with the relative variation of the Nusselt number. Concerning the scaling factor C, this parameter is less significative because it strongly depends on the formulation of the correlation. Every Author considers diverse physical variables for improving the whole correlation, involving for example fluid properties or injection parameters. The table shows that other authors proceed in a similar way and determine values between $0.2 < n < 0.4$. The coefficient $m = 0.53$ is obtain in this research, for a wide range of initially laminar injections. In literature, the value $m = 1/2$ is obtained for the laminar regime from analytical calculation and is generally confirmed by studies in the same regime. More discrepancy arises between the authors and typical values are $0.4 < m < 0.8$. More significant dependence on the nozzle diameter is found in the present study, as the exponent $p = 0.5$ is much smaller than the $p = 0.94$-0.98 found by *Renon et al.* 2021.

Concerning the correlation along the jet-radial direction, Table 5.4 reports the parameters of equation (38) along with those from *Ma et al.* 1997a. The parameters A and a are much different from those of the literature, but they are less relevant for the comparison, as they represent some sort of scaling factor. B and b are more relevant as they are related to the local slope of the function. In this case B is approximately the same and b is within the same order of magnitude.

In conclusion, both correlations are in relatively good agreement with similar findings from the literature.

Table 5.3 – Comparison between the Nusselt correlation evaluated in the present study and those from the most similar literature.

REFERENCE	CORRELATION	REYNOLDS	PRANDTL
Metzeger et al. 1974	$Nu = 2.65\ Re^{0.47} Pr^{0.24}\ (d_{tgt}/d)^{-0.68}$	*1200<Re<2200*	*85<Pr<151*
Liu et. al 1991	$Nu = 0.745\ Re^{1/2} Pr^{1/3}$	*Re>350*	*Pr>3*
Stevens and Webb 1994	$Nu = 2.67\ Re^{0.567} Pr^{0.4}\ (z_0/d)^{-0.0336} (\dot{V}/d)^{-0.237}$	*4000<Re<52000*	*Pr≈10*
Ma et al. 1997	$Nu = 1.27\ Re^{0.495} Pr^{1/3}$	*183<Re<2600*	*82<Pr<337*
Leland and Pais 1999	$Nu = 0.28\ Re^{0.84} Pr^{0.32}\ \left[(d_{tgt}/d)^{-0.64} - 0.10\right] (\mu_{aw}/\mu_w)^{0.04}$ $Nu = 1.78\ Re^{0.58} Pr^{0.22}\ \left[(d_{tgt}/d)^{-0.32} - 0.30\right] (\mu_{aw}/\mu_w)^{0.7}$	*110<Re<800* *1110<Re<8600*	*48<Pr<445* *48<Pr<445*
Renon et al. 2021	$Nu = 0.315\ Re^{0.68} Pr^{1/3}\ (d/d_{ref})^{0.98}$ $Nu = 1.11\ Re^{0.48} Pr^{1/3}\ (d/d_{ref})^{0.94}$	*170<Re<500* *700<Re<2225*	*148<Pr<925* *148<Pr<925*
Present study	$Nu = 0.31\ Re^{0.53} Pr^{1/3}\ (d/d_{ref})^{0.5}$	*449<Re<2138*	*120<Pr<240*

Table 5.4 – Empirical parameters obtained for the Nusselt correlation along the jet-radial direction.

REFERENCE	A	B	a	b	p
Pipe type nozzle (Ma et al. 1997)	0.00137	0.0538	0.168	1.65	0
Orifice type nozzle (Ma et al. 1997)	0.00180	0.0530	0.00709	2.00	0
Custom nozzles (Present study)	7.5	0.05	0.58	2.89	0.85

- **Compare by investigated injection range**

Figure 5.18 is a replotting from *Feng et al.* 2021. They provide comprehensive picture of the investigated *Re* range available in the literature, for a wide range of fluid types (thus Prandtl number). The correlation obtained in this study is added to the plot. The picture show that this study is coherent with general trend and has contributed to extend the investigation towards ATF and, more generally, lubricant fluids (for typical *Pr* values of these fluids, see Table 1.4). Notice that the authors mentioned in the plot use different methods and formulations for calculating the convective coefficient, which are not specified by the Author of the plot.

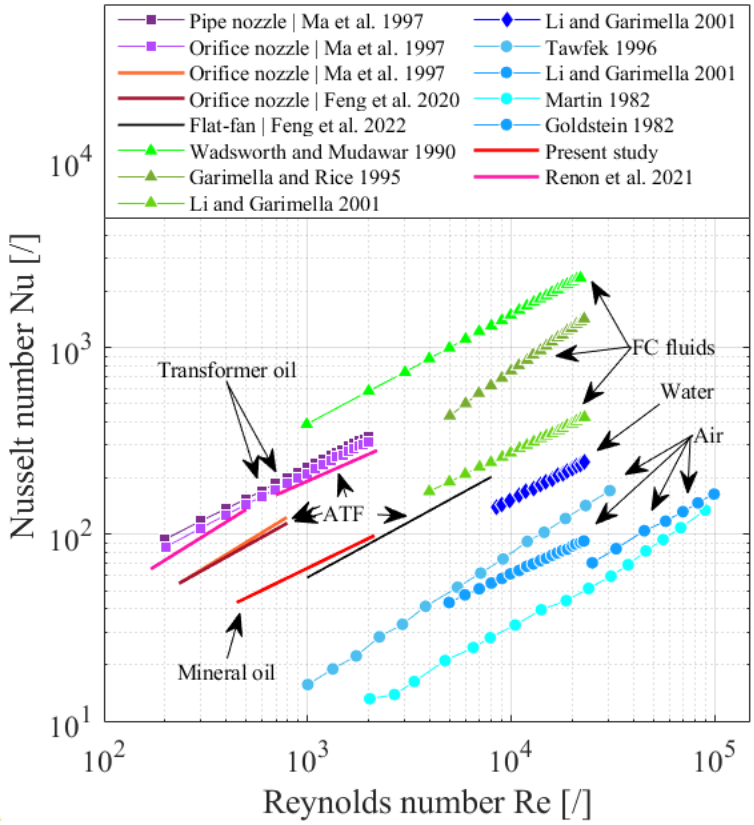

Figure 5.18 – Redrawing of the of the figure from *Feng et al.* 2021, comparing the investigated Nusselt range in the literature, for different flow regime and fluid types. The correlation obtained in the present study is plotted over the original graphic (with Pr = 165 and d = 1 mm) and those from *Renon et al.* 2021 (with Pr = 250 and d = 1 mm).

5.3 Chapter conclusions

In this chapter, it is shown that all the deliverable outputs of the method are obtained: the convective coefficient, the Nusselt number and the Nusselt correlations. This is important because the method proves to be able to characterise generic thermally thick targets, relying on temperature measurements of the surface temperature.

Concerning the convective coefficient and the Nusselt number, it is shown that the key parameter is the surface temperature, because the whole method relies directly or indirectly on it. Various observations support this conclusion First, it is observed that the oil temperature plays a minor role within $0 < x/d < 10$. In this range (where the surface temperature measurements and heat flux predictions are consistent, and the overall method is robust), it is observed that evaluating a local oil temperature after impingement, or simply assuming the temperature uniform everywhere, does not affect the convective coefficient significantly. Second, the measurement uncertainty associated with the surface temperature propagates directly and indirectly in the uncertainty of the convective coefficient. More specifically, through the heat flux prediction. It follows that the overall method would benefit by reducing the measurement uncertainty on temperature, thus improving the simulation approach.

The uncertainty of the method is quite large and makes comparison difficult between different injection and heating conditions. Despite that, the results are coherent with the expected variations, as observed from similar literature. As a matter of fact, the method provides solid estimates in the investigated range of injection and heating, which are representative for real applications on end-windings and manages to characterise jet

impingement for generic thermally thick solid targets, without the need of simplifying assumptions on heat transfer.

Two Nusselt correlation are determined at the impingement point and along the jet-radial direction, contributing to extend the knowledge about jet impingement with high-Prandtl fluids, within a representative thermal range for electric mobility and with a typical fluid. The correlation covers a quite large Reynolds and Prandtl range (i.e., $449 < Re < 2138$ and $120 < Pr < 240$), a significant dependence with the nozzle diameter is observed. Good agreement with similar studies from the literature, in particular for the one at the impingement point, where the typical $Re^{1/2}$ dependence of high-Prandtl fluids is observed (when setting the Prandtl exponent as 1/3).

The results from the present study are compared to the most similar literature in terms of magnitude, trend and correlations. Despite comparison is difficult when authors use different methods, formulations and injection parameters, relatively good agreement is found.

With these concluding remarks the present research is hoped to be useful for motivating future research, for extending the knowledge on lubricant fluids, for validating CFD simulations, for evaluating thermal transfer with thermally thick objects and for technical assessments on the cooling of the electric motors.

CONCLUSIONS AND SUMMARY

Driven by the increasing demand for electric mobility, is transforming the automotive industry. The strict requirements for traction require motors with high power density, high torque density and reduced bulk, leading to more complexity at evacuating the heat generated by the motor. The thermal management is hence important to preserve the lifespan of the motor and more efficient solutions are needed. Cooling systems are becoming more integrated in the motor architecture to better address individual localised heat sources. Among the critical components of the electric motor, the stator end-windings are likely to fail due to the degradation of the electrical insulation. Direct cooling by injection of dielectric lubricant oil is effective for preventing excessive temperature rise, thanks to the direct contact between coolant fluid and the hot surface. Also, direct cooling allows the motor to stay longer under high-torque operating conditions and lubricant oil is already available in the vehicle (e.g., in the transmission).

When considering jet impingement, better characterisation of the convective heat transfer is needed for the so-called high-Prandtl fluids, such as oil. High-Prandtl fluids have thermal and rheological properties which are strongly dependent from the temperature (viscosity in particular), and their thermal boundary layer is much thinner than the dynamic one. Modelling the injection is difficult and expensive because of the peculiar characteristics of these fluids. The intricate morphology of the end-windings and the multiple air-solid-liquid interactions, add further complexity to the simulations. More experimental characterisation is hence necessary to validate numerical models.

The experimental literature on jet impingement with lubricant oils is limited and even scarcer for representative fluids, injection parameters and temperatures of electric mobility. Experimental characterisations are typically carried out at a fundamental level, using thin plates or cylinders as solid targets. These shapes are commonly used because they enable simplifying assumptions on the heat flux and advantages for diagnostic.

The present doctoral research aims to extend the investigation on high-Prandtl fluids for representative fluids and temperatures of electric motors, by developing a method for characterising convective heat transfer with generic thick solid target. An experimental apparatus is used, composed of an impinging jet and an aluminium heated plate. A diagnostic system is built to measure, monitor, and control the parameters of the injection (before the nozzle), the local plate temperature (with embedded thermocouples), and the liquid temperature and liquid thickness (after impingement). The local heat flux is evaluated via a numerical simulation and the liquid temperature and thickness are measured with diverse diagnostic techniques. Concerning this last, an imaging method is also developed for wide-field and simultaneous measurements of temperature and thickness. The technique is based on 2-colour 2-dye laser induced fluorescence (LIF) and a colour camera (RGB camera). The aim is to evaluate oil coverage and temperature with a relatively compact optical setup which can be used in real electric motors. Lastly, heat transfer is characterised by through the local convective coefficient, the local Nusselt number and the Nusselt correlations at the impingement point and along the jet-radial direction.

- **Characterisation of the injection and the solid**

The solid plate is characterised for a numerous combination of injections and heating parameters (i.e., diameter d = 1-2 mm, injection temperature T_{inj} = 60-75-90 °C, injection pressure P_{inj} = 13-17-20 kPa, heating power P_e = 0.9-1.2-1.5 kW). The Prandtl and Reynolds numbers are determined for the laminar and transitional regimes

($449 < Re < 2138$) and with relatively large variations of the fluid properties ($120 < Pr < 240$), which are likely to be found in electric powertrain motors. The typical surface and internal temperature temperatures of the plate (T_{surf} and T_{int}) are between 90 °C < T_{surf} and T_{int} < 190 °C, a representative range of the thermal limits of the electrical insulation of the windings. Thanks to plate-embedded thermocouples and an experimental protocol based on regular nozzle repositioning along the jet-radial coordinate x, consistent measurements within $-10 < x/d < +10$ are taken, with a temperature sensitivity of 0.1 °C and a spatial discretisation of 0.2 mm. After a dedicated analysis, the estimate of the uncertainty associated with the temperature measurements is 1.4 °C (max 2.4 °C). Concerning the heat flux, the simulations replicate the internal temperature distribution of the plate, within 0.2 °C with respect to the experimental temperatures. The resulting heat flux at the solid-liquid interface exhibits a pronounced peak at the impingement point (roughly 20 times larger than the heat flux from the heater).

An extensive parametric study with different injection and heating parameters shows that significant temperature variations characterise the investigated region nearby the impingement point ($x/d = 0$), where typical gradients measured along the surface are between 0.1 °C/mm < $\Delta T_{surf}/\Delta x$ < 1 °C/mm. In terms of temperature mitigation, an enlargement of the nozzle diameter, an increase in the injection pressure and the reduction of the injection temperature lower the surface temperature. The first two are the most effective, as the surface temperature decreases approximately by – 1 °C per – 3 °C decrease of T_{inj}, by – 4 °C per + 1 kPa increase of P_{inj}, and by – 35 °C per doubling of d. Typically, any increase of the flowrate lowers the surface temperature, as it is commonly observed in similar literature. Nevertheless, the increase of the flowrate does not always imply a decrease of the surface temperature, because the increase of the injection temperature increases the flowrate but also the surface temperature. Concerning the mitigation of the surface temperature and the uniformity of cooling, a variation of any injection parameter simply shifts the surface temperature to a higher or lower range, without affecting the surface temperature gradients $\Delta T/\Delta x$. Conversely, increasing the heating power steepens the gradients nearby the impingement point. Concerning the heat flux, very small variability is observed throughout the parametric study for different injection and heating. For industrial cooling applications, jet impingement proves its efficacy for concentrated heat sources whose size is comparable to the stagnation region (e.g., processors, power electronics) but for assuring uniform surface temperature the use of a multi-jet or a spray is advised.

- **Characterisation of the liquid**

Various methods are used to measure the temperature of the air-liquid interface, the temperature evolution along the plate-normal direction (z axis), and the mean temperature (within the film) along the jet-radial direction (x axis). Pointwise and wide-field measurements are taken with non-optical and optical techniques. Thermocouples for temperature measurements along the jet-radial and plate-normal direction are inaccurate and imprecise, however they suggest that the oil temperature evolves mildly along the jet-radial direction (about 0.2 °C/mm) and significantly along the plate-normal direction (at least 7 °C/mm). Thickness measurements with a contact needle are found to be relatively more accurate and precise, with respect to a laser sensor for triangulation. Using the contact needle, the ratio between the thickness before and after the hydraulic jump is about 15, regardless the injection or heating. The position of the hydraulic jump moves outwardly (with respect to the impingement point) for increasing injection temperature, injection temperature and heating power (this last is not detected by the laser).

A large part of the research is dedicated to the development of an imaging LIF method with flood illumination. In a preliminary phase, several approaches are proposed to measure the temperatures of interest of the liquid film, however only the mean temperature within the film thickness can be measured, because of technical and physical limits. Subsequently, a spectroscopic analysis proposes two fluorescent 2-dye mixtures as potential candidates for the 2-dye 2-colour LIF technique. The mixtures are made of Lumilux 345 + Pyrromethene 597 and Lumilux 345 + Pyrromethene 650, with smaller proportions Lumilux 345 (i.e., C_{LUM345} = 0.02 mmol/L and $C_{PYR597} = C_{PYR650}$ = 0.08 mmol/L). The spectroscopic analysis reveals that the first mixture has a more pronounced emission-reabsorption spectral conflict than the other. Eventually, the mixture Lumilux 345 + Pyrromethene 650 is used for measurements with the impinging jet.

The spectroscopic analysis is supported by a study on temperature sensitivity of static films, which compares simulations of detection with ideal and RGB cameras and experiments with RGB cameras. Good agreement is found between simulations and experiments (proving that simulation approach is a valid tool and can be generalised). Although the mixture with more spectral conflict has larger temperature and thickness sensitivity, the mixture with lower spectral conflict is eventually employed for the experiments with the impinging jet.

An analysis of the uncertainty is carried out considering the temporal intensity fluctuations of individual pixels, and the spatial intensity fluctuations of neighbour pixels. The total uncertainty is estimated to 10.2 % for the fluorescence intensity in the channel *Blue*, 3.9% for the intensity ratio between the channels *Red* and *Blue*, within the order of 10 °C for temperature, and within the order of 0.4 mm for thickness. Image binning (i.e., between 7 x 7 pixel and 15 x 15 pixel) can reduce the uncertainty on temperature to 3 °C.

The optical method is then applied to the impinging jet and wide-field measurements are taken within a relatively large field of view (about 60 mm), covering all the characteristic regions of the impinging jet. Two independent algorithms are developed to convert the information on fluorescence intensity into information on thickness and temperature. For static oil films, the measurements taken with the two algorithms are relatively accurate within the whole field of view, but generally inaccurate and imprecise at a smaller scale.

A similar outcome is observed for the impinging jet. More specifically, the measured temperature agrees with the one measured by the thermocouple, in terms of overall range and growing trend along x. At a smaller scale, large inaccuracy and imprecision are observed, especially in the low-thickness region (before the hydraulic jump) and with high injection temperature. The large inaccuracy is probably a consequence of the small sensitivity to temperature of the fluorescent mixture, causing the data not to be exploitable for calculating the convective coefficient. Conversely, the thickness measurements are relatively accurate everywhere in the field of view and in very good agreement with those obtained by the contact needle.

- **Characterisation of convective heat transfer**

Estimates of the convective coefficient and Nusselt number are provided along the jet-radial direction for different combinations of injection and heating parameters. The Nusselt number is always the largest at the impingement point, where typical values are $80 < Nu < 110$, whereas at about $x/d = 10$ it decreases to $5 < Nu < 10$. The variations of the Nusselt number for different injection and heating parameters are smaller (or similar) to the uncertainty of the method, which is evaluated to be 18 % (max 36 %). This large uncertainty is mostly due to the propagation of the uncertainty in the measurement of the surface temperature. This occurs in a direct way, since the surface temperature is in the

formulation of the convective coefficient, and in an indirect way, because the surface temperature is needed to calculate the het flux. The indirect contribution is the most significant, especially at the impingement point. More accurate and precise measurements could reduce the uncertainty in the estimate of the convective coefficient.

Despite the large uncertainty, the results suggest that increasing the injection temperature and the injection pressure leads to the increase of the Nusselt number. Moreover, the variation of the Nusselt number, for variable Reynolds, Prandtl numbers and along x are similar to the expected ones, calculated from analogous studies.

The Nusselt correlation determined at the impingement point is $Nu = 0.31\ Re^{0.53}\ Pr^{1/3}\ (d/d_{ref})^{0.5}$, where $d_{ref} = 1$ mm. The correlation shows that the exponent of the Reynolds number is coherent with similar studies on high-Prandtl fluids when the exponent of the Prandtl number is set to 1/3. Moreover, a strong dependence with the nozzle diameter is observed, probably because the nozzles are custom-made and the velocity profile at the injection may be different from a nozzle diameter to another. A correlation is also determined for the datapoints between $1 < x/d < 10$, showing good agreement with the most similar literature and a strong dependence with the nozzle diameter as well. The correlations are valid for $449 < Re < 2138$ and $120 < Pr < 240$.

With the determination of the local distribution of the Nusselt number and the Nusselt correlations, this work manages to deliver a new experimental method for characterising convective heat transfer between high-Prandtl fluids generic solid targets, and to provide new data for a representative fluid and thermal range for electric mobility.

- **Perspectives for future work**

As observed in this research, measuring the surface temperature of generic thick plates requires embedded sensors, inserted from the unwetted side of the plate. The accuracy of the measurement depends on the proximity of the sensitive element to the actual solid-liquid interface, on the probe size, materials and embedding process. These are all limiting factors in this study which could affect accuracy. In particular, the thermocouple diameter in this study is too similar to the jet diameter and also larger than the spatial resolution of the measurements along x/d. A priori this is problematic for the measurement but driven by technical constraints. Since thermocouples are very reliable sensors, it would be interesting to use thermocouples with grounded junction, possibly much smaller than the jet diameter. Moreover, the uncertainty analysis of this study is evaluated experimentally only and should be completed numerically to evaluate the measurement error due to the presence of the thermocouple. Alternatively, optical diagnostic would also be interesting with thin layers of phosphors. In this case, a non-intrusive solution for optical access is to position the detection system above the oil-wetted side of the plate. A more intrusive solution is to provide access from the unwetted side of the plate through hollow canals.

The numerical simulations in this research use the experimental temperature as boundary condition to determine the heat flux, thus the convective coefficient. This is known as an inverse problem of heat transfer, as the goal is to evaluate the causes of some known effects, for example: the cooling action of the impinging jet (the cause) induces a temperature distribution within the plate (the effect). Since the boundaries of inverse problems are intrinsically “ill-conceived”, it would be interesting to improve the calculation of the heat flux, by creating a loop, where the surface temperature and the convective coefficient are alternatively used as boundary conditions.

The plate used in this research is a uniform aluminium slab, whose thermal properties are not fully representative of the strong anisotropy of the thermal conductivity of the end-windings. In particular, the literature shows that in distributed windings the axial thermal conductivity is about 100-200 times larger than the radial one, mostly due to the electrical

insulation of individual wires. Further investigation should be carried out to consider the properties of the solid, for example by replicating an anisotropic structure.

The optical method developed in this research and based on LIF shows good potential, but it is important to improve the temperature measurement of the liquid film. The most practical and quickest way would be to use the other fluorescent mixture investigated in this study (Lumilux 345 + Pyrromethene 597), because of the larger temperature and thickness sensitivity. Another way is through a more pondered selection of the dyes. It is difficult to find a pair of dyes which can be excited simultaneously with the same wavelength, with both a large quantum yield, and featuring low emission-reabsorption. A technical solution could be the use of two delayed and different excitation wavelengths, to effectively excite one dye at the time. A second way is by modifying the detection system. A RGB camera is practical in terms of compactness but restrains the options in terms of wavelength separation when using multiple dyes. Conversely, detection with two cameras (black/white or RGB) would provide more flexibility for filtering the fluorescence emission but it would require more optical components. Alternatively, different optical technics could be developed. A starting point is the use of thin thermocouples with exposed junction, and a more refined method could be the use of phosphor particles dispersed in the liquid.

In terms of investigation topics within the framework of the end-windings, more representative studies should be undertaken to evaluate the influence of the curved and grooved surfaces, the surface interaction between the fluid and the insulation material (e.g., polar interaction and wettability), and the influence of the air flow induced by the spinning rotor. Within the more general framework of the direct cooling of electric components, the experimental method and the experimental apparatus have potential for characterising other types of injections (i.e., spray) and concentrated heat sources (e.g., power electronics).

This page intentionally left blank.

ANNEXE TO CHAPTER 2

- **Nozzle scheme**

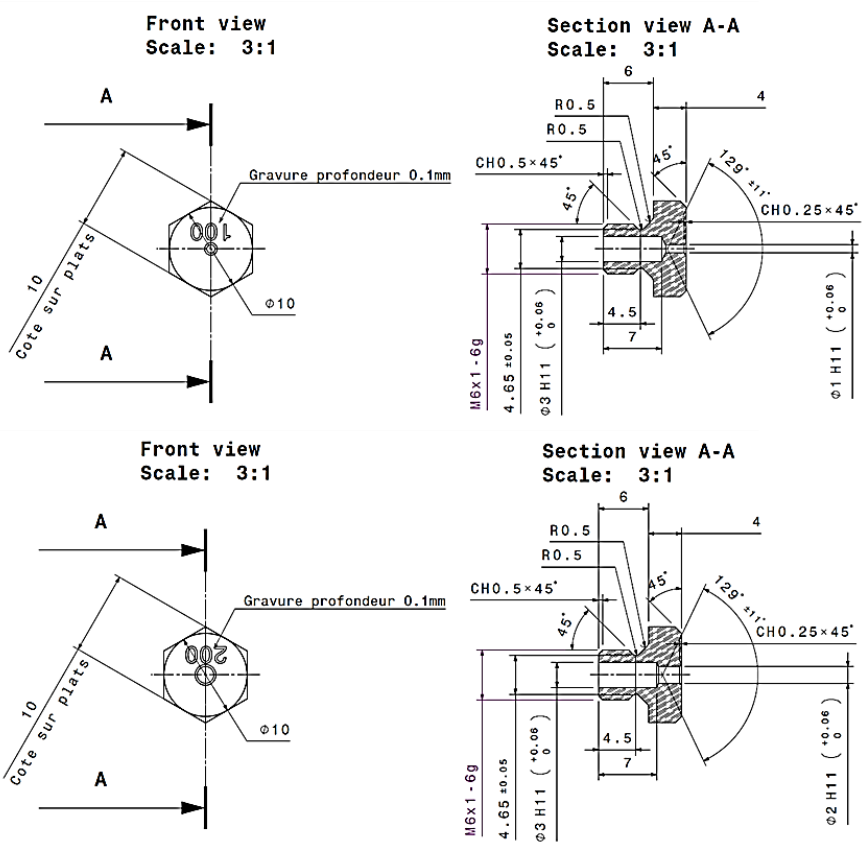

- **Adaptation of the boundary conditions to mesh**

The experiments provide measurements by different thermocouples, at different times and positions along *x*. Not all data points are useful for setting the boundary conditions, therefore a generalised and empirically calibrated sorting algorithm restrains the number of meaningful data points.

The sorted data points come as *T(x)*. Assuming perfect symmetry around the *z* axis, the profile is rotated and interpolated to generate a *T(x,y)* map, with an interpolation step (distance between interpolation coordinates). For an effective adaptation of the map to the mesh (of the FEM model of the plate), the interpolation step should be smaller than the smallest cell size. The best adaptation is observed empirically when the interpolation step is half of the smallest cell size.

Once given the map *T(x,y)*, the software assigns a boundary temperature T_b to each cell of the boundary surface. It is observed that the experimental impingement point corresponds to the map coordinate [*x*,*y*] = [0,0], but also to the common corner of four neighbour cells in the mesh. When given such map, the software assigns incorrect boundary temperatures to the four cells, none of which is the experimental one. Consequently, the evaluation of the heat flux at the impingement point is usually underestimated significantly. To prevent this occurrence, the [*x*,*y*] coordinate system of the temperature map is shifted by half of the smallest cell size, thus $[x + \Delta x_n/2,\ y + \Delta x_n/2]$. With such adjustment, the boundary temperature is equal to the experimental temperature in one of the four neighbour cells.

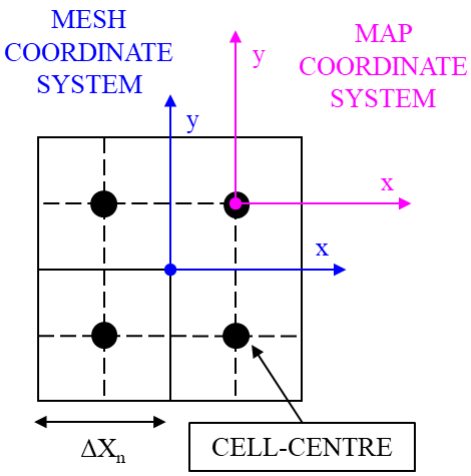

Shift of the coordinate system of the temperature map with respect to the one of the mesh. Thereby, the correct boundary temperature is assigned to the cell-centre of one of the cells.

Nozzle section

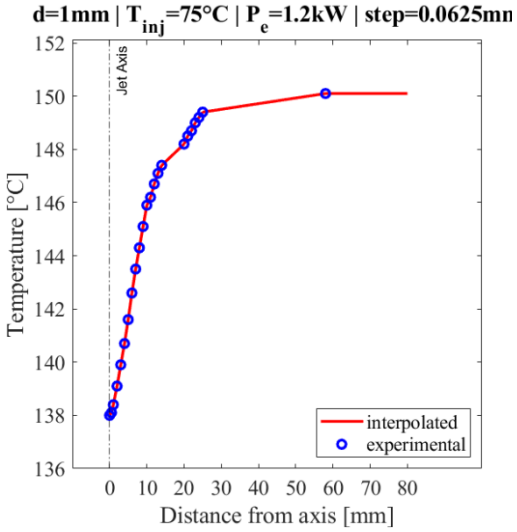

Surface temperature profile *T(x)* after data sorting.

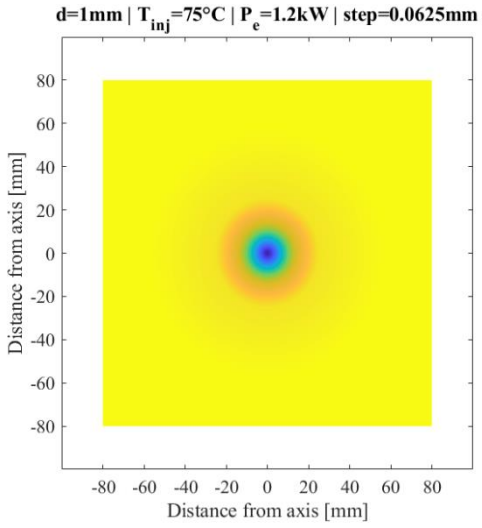

Temperature map *T(x,y)*.

- **Algorithms for temperature and thickness**

EQUATIONS OF THE ITERATIVE ALGORITHM

Eq1: $Blue_{FF} = a_1 + a_2T + a_3\delta + a_4T\delta + a_5T^2 + a_6\delta^2$

Eq2: $Red_{FF}/Blue_{FF} = b_1 + b_2T + b_3\delta + b_4T\delta + b_5T^2 + b_6\delta^2$

EQUATIONS OF THE INTERPOLATIVE ALGORITHM

$$T = f_1(Blue_{FF}\ ,\ Red_{FF}/Blue_{FF})$$
$$\delta = f_2(Blue_{FF}\ ,\ Red_{FF}/Blue_{FF})$$

SCHEMES OF THE ALGORITHMS

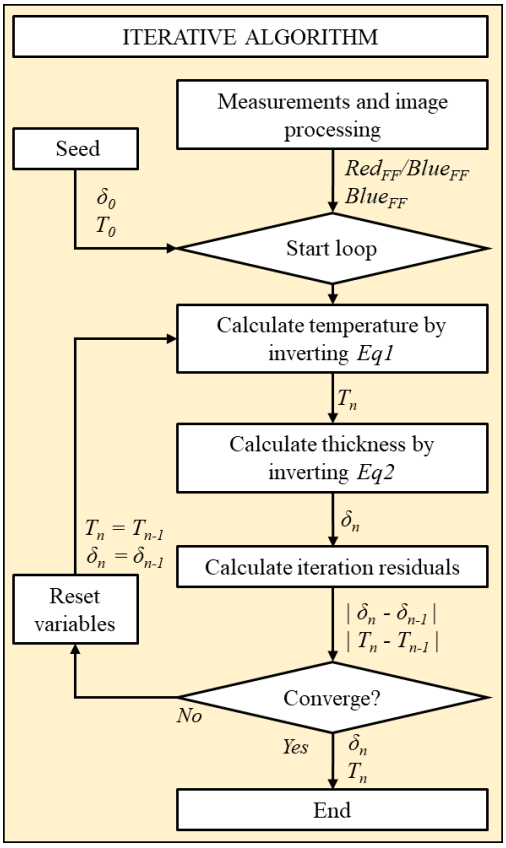

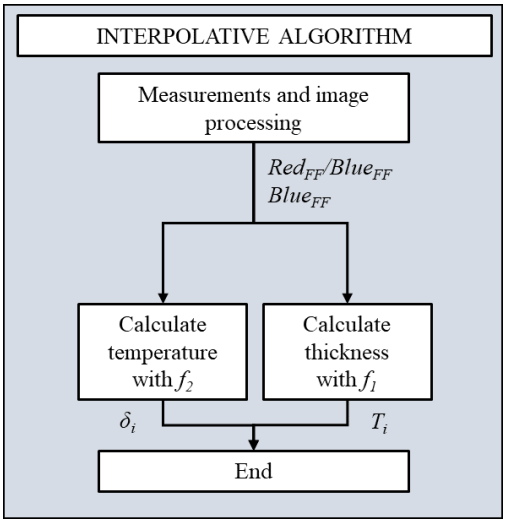

ANNEXE TO CHAPTER 3

- **Raw measurement of the surface temperature**

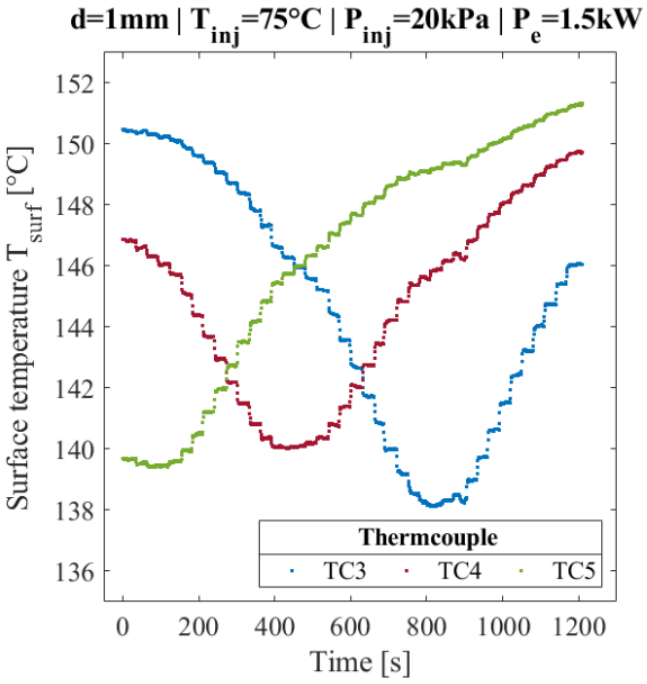

Raw measurement of the surface temperature with thermocouples TC3, TC4 and TC5. The nozzle is repositioned every 30 s.

- **Time between nozzle repositioning**

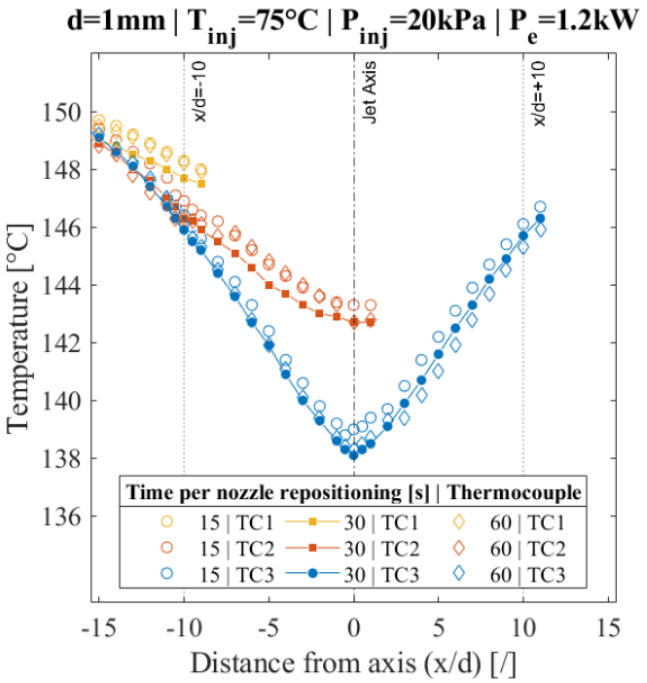

Surface and internal temperature of the plate for the reference experiment. Parametric study on the time for nozzle repositioning.

ANNEXE TO CHAPTER 4

- **Imaging of the impinging jet with flood illumination**

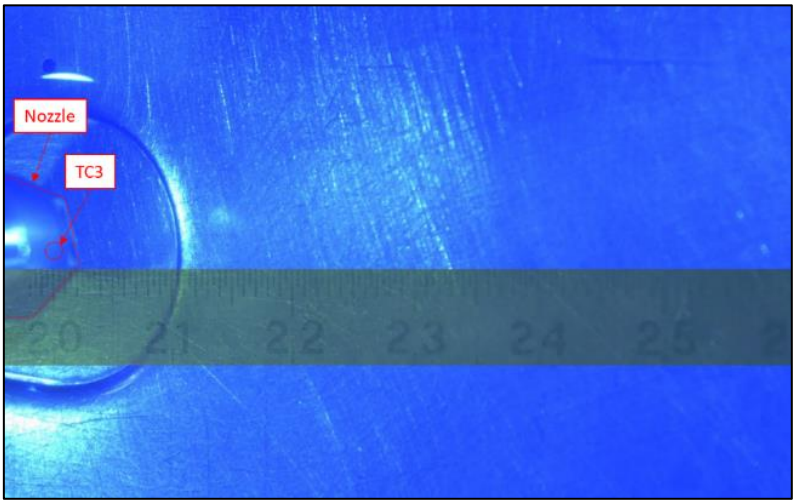

d = 1 mm, z = 10 mm | Θ_{camera} = 15 ° | P_{inj} = 20 kPa | T_{inj} = 75 °C | P_e = 1.2 kW

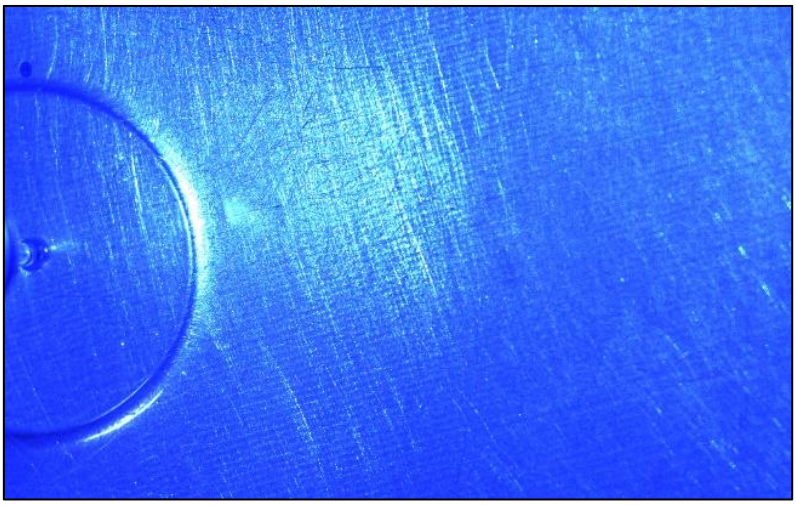

d = 2 mm, z = 20 mm | Θ_{camera} = 15 ° | P_{inj} = 13 kPa | T_{inj} = 60 °C | P_e = 1.2 kW

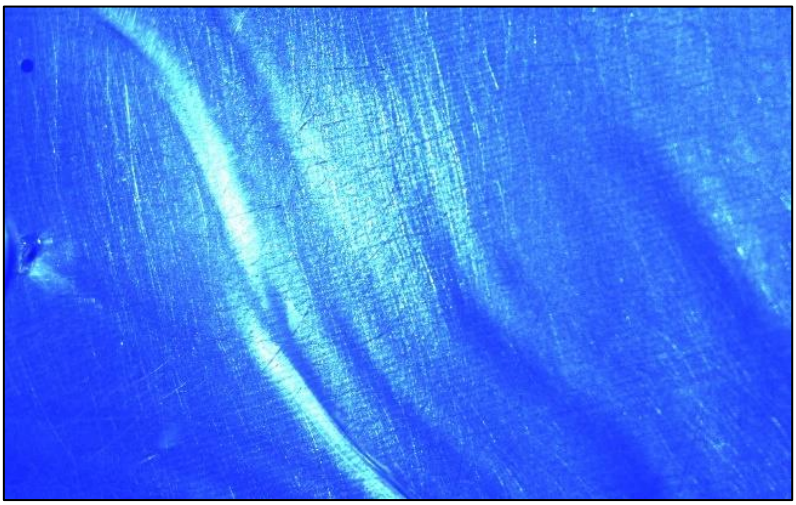

d = 2 mm, z = 20 mm | Θ_{camera} = 15 ° | P_{inj} = 17 kPa | T_{inj} = 75 °C | P_e = 1.2 kW

- **Preliminary study with cuvette spectroscopy**

  - Bench for cuvette spectroscopy with heated cell

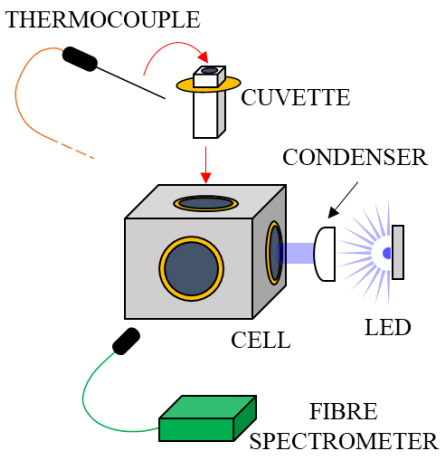

Scheme of the experimental bench.

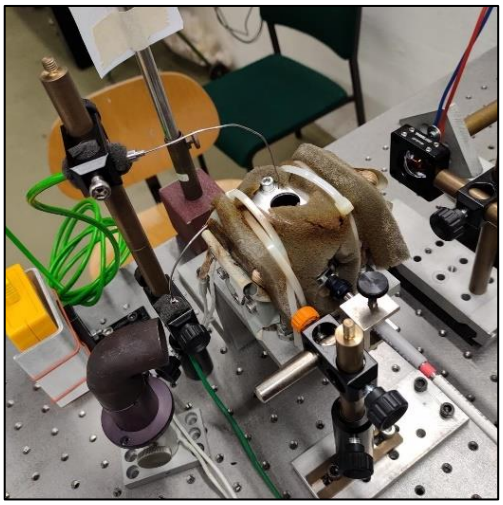

Photo of the experimental bench.

COMPONENT	SPECIFICATIONS
LIGHT SOURCE	LED λ = 450 nm (WEPRB1-S1, *Winger Electronics GmbH & Co. KG*).
CONDENSER	Focal length 16 mm (ACL25416U-A, *Thorlabs Inc.*)
THERMOCOUPLE	K type, insulated hot junction (397-1236, Ø = 1.5 mm, *RS Group plc*)
HETAED CELL	Custom-made cell for 90 ° and 180 ° spectroscopy, with heating system (electric coil, temperature regulator and thermocouple) up to 200 °C
SPECTROMETER	Fibre spectrometer (Flame, *Ocean Optics Inc.*)

- Parametric study and comparison with Schweizer et al. 2021

PRESENT STUDY – single dye emission

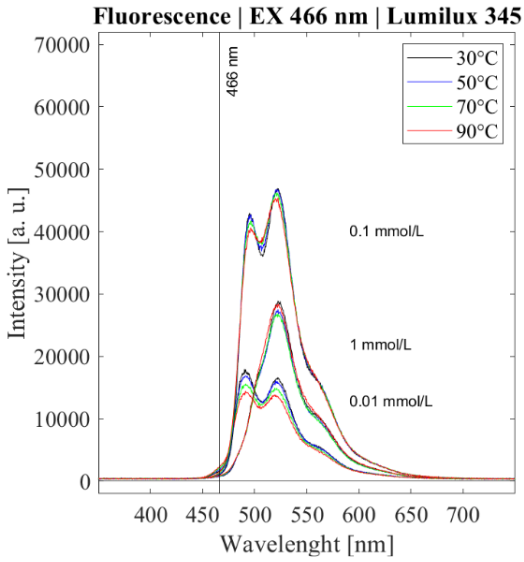

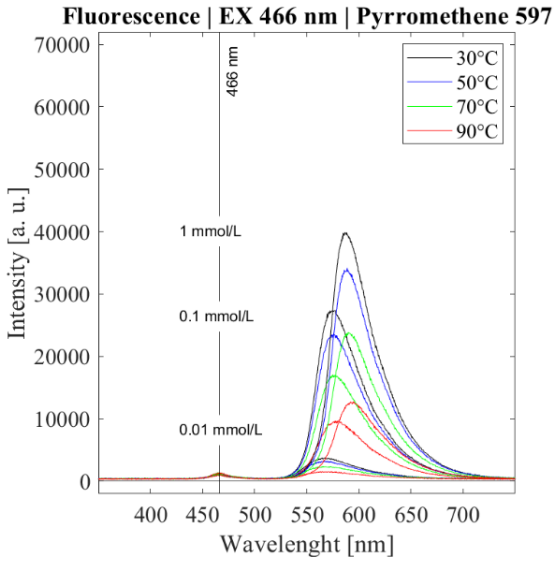

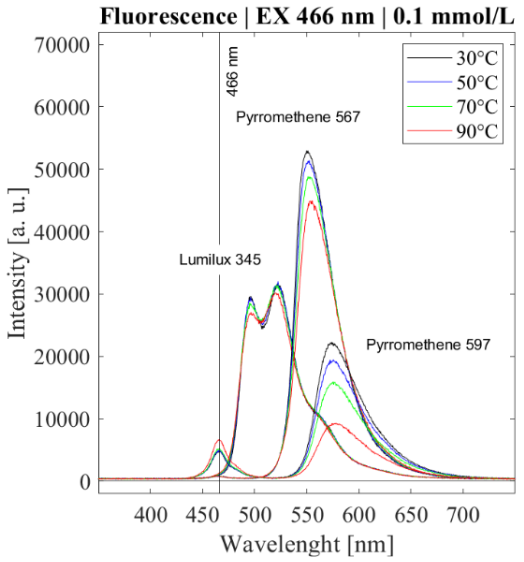

PRESENT STUDY – 2-dye mixture emission

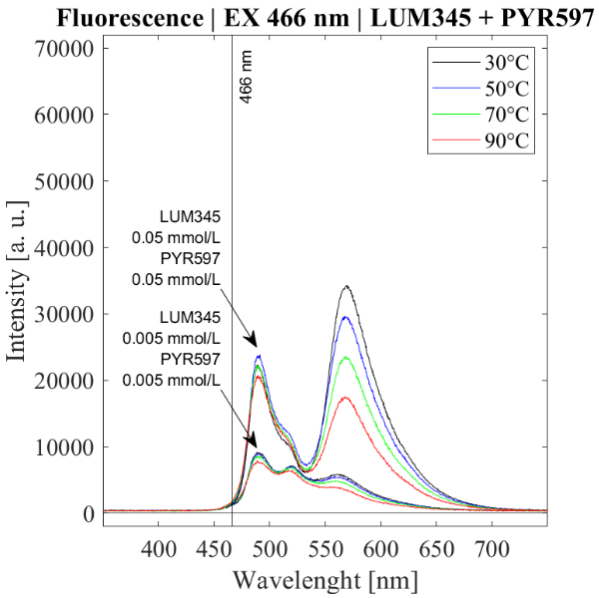

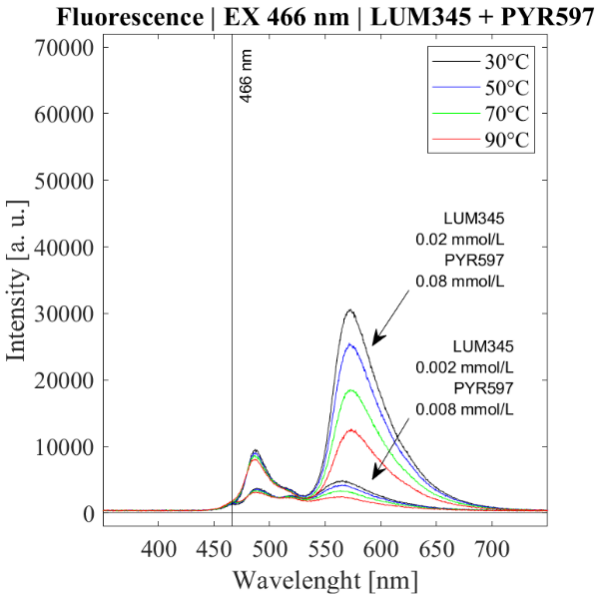

EXTRACTS FROM SCHWEIZER ET AL. 2021

Schweizer, T., Kubach, H., & Koch, T. (2021). Investigations to characterize the interactions of light radiation, engine operating media and fluorescence tracers for the use of qualitative light-induced fluorescence in engine systems. Automotive and Engine Technology, 6, 275-287.

NOTE: the concentrations are recalculated from mg/L to mmol/L and the lubricant used is Fuchs 5W20

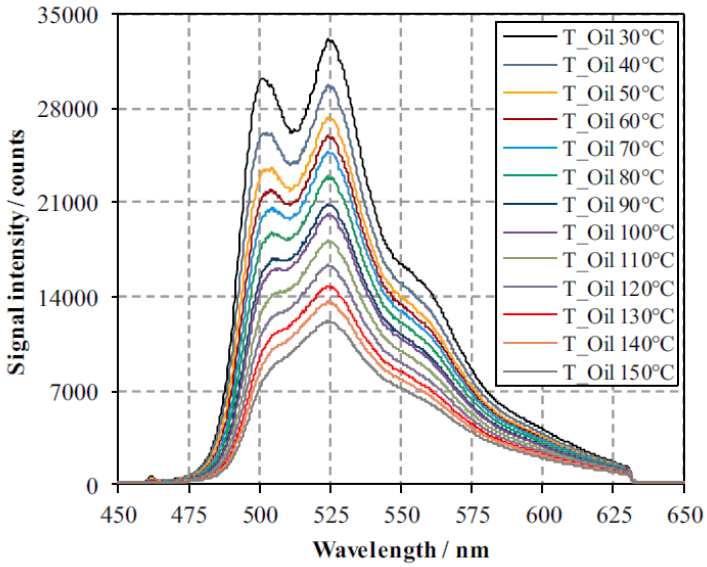

Emission spectra of Lumilux CD 345 (C = 0.099 mmol/L).

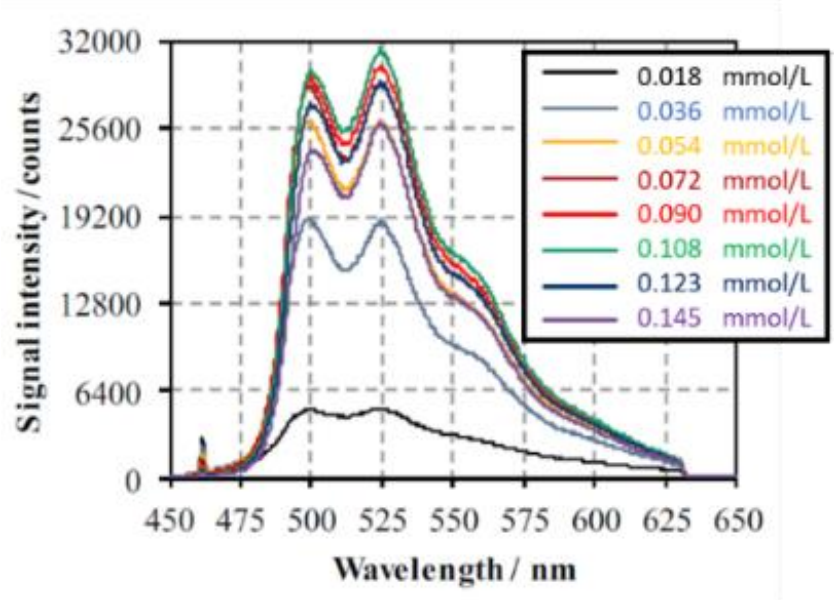

Emission spectra of Lumilux CD 345 at T = 30 °C.

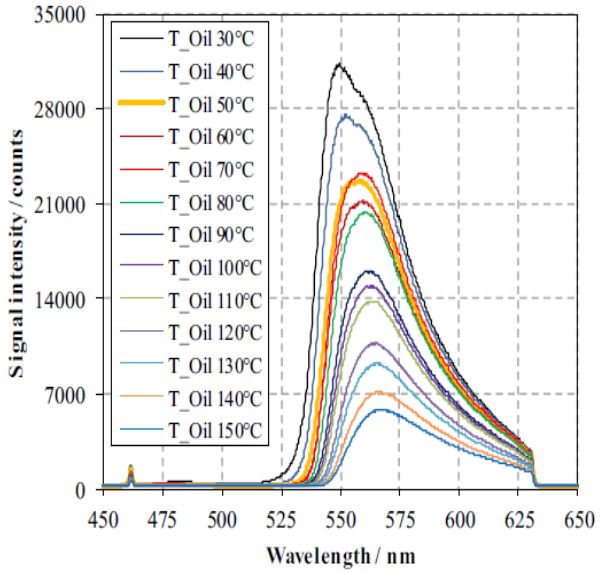

Emission spectra of Pyrromethene 567 (C = 0.214 mmol/L).

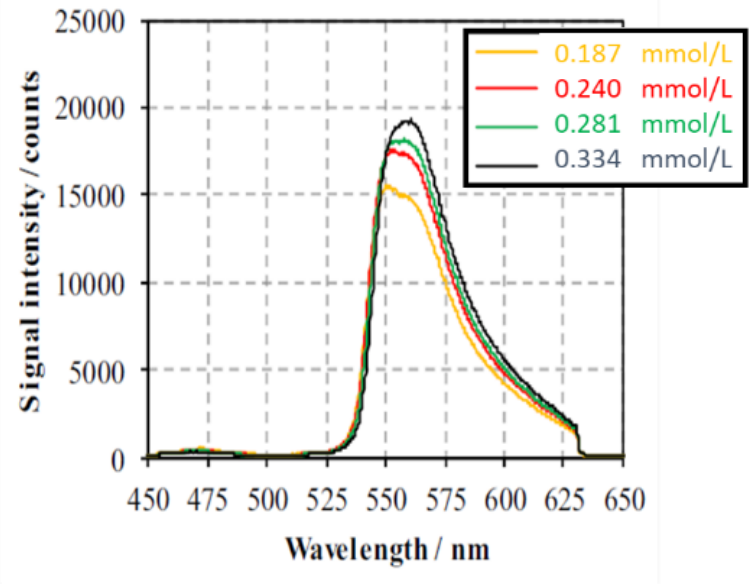

Emission spectra of Pyrromethene 567 at T = 30 °C.

- Optimise excitation and detection

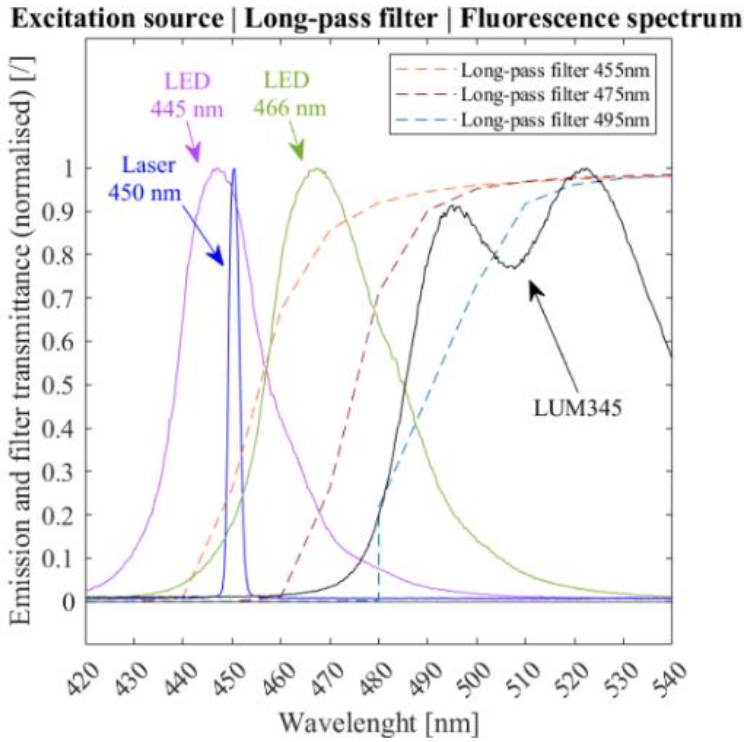

Zoom of the characteristic traces of the fluorescent dye LUM345, three excitation sources (LED λ_{ex} = 445 nm, LED λ_{ex} = 466 nm and laser λ_{ex} = 450 nm), and three commercial long pass filters ($\lambda_{cut\text{-}off}$ = 455-475-495 nm).

- **Exposure to high temperature and fluorescence loss**

Exposure to 110°C	Exposure to 130°C
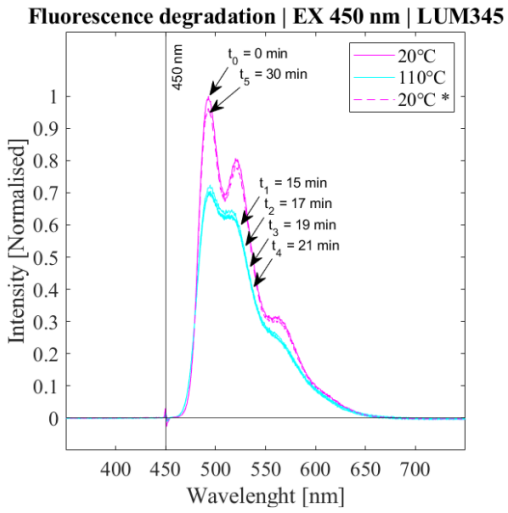	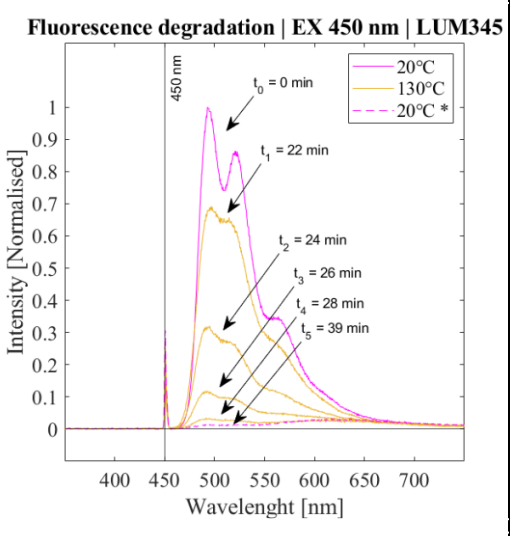
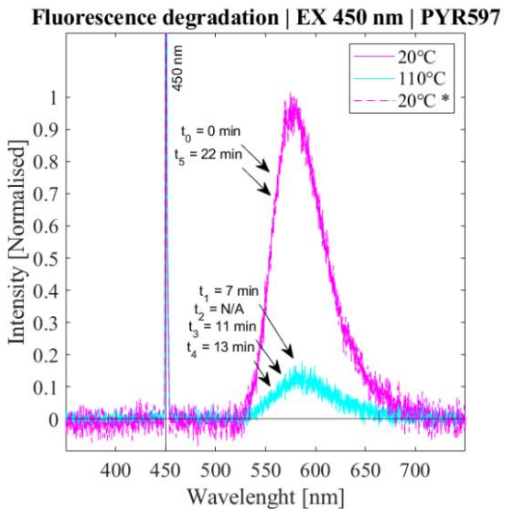	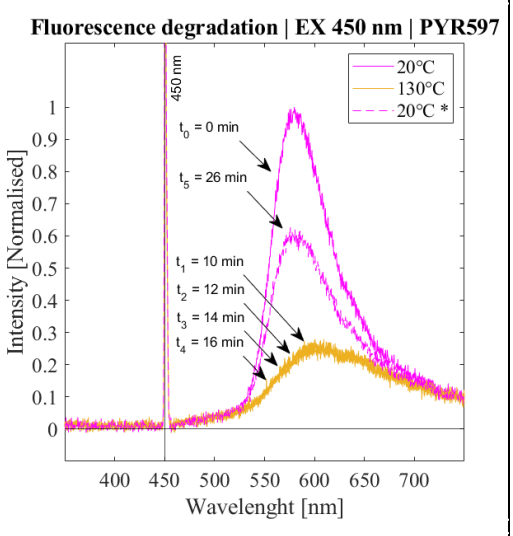
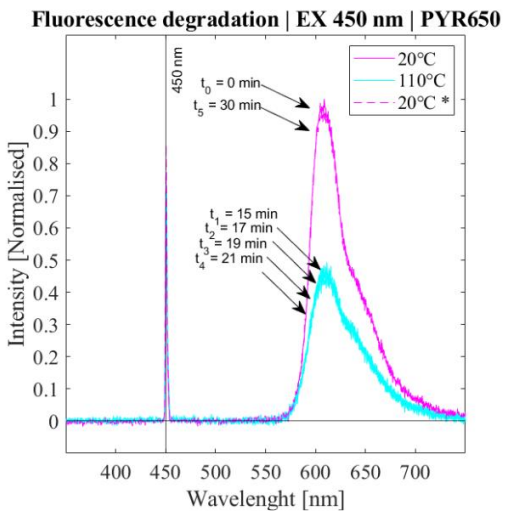	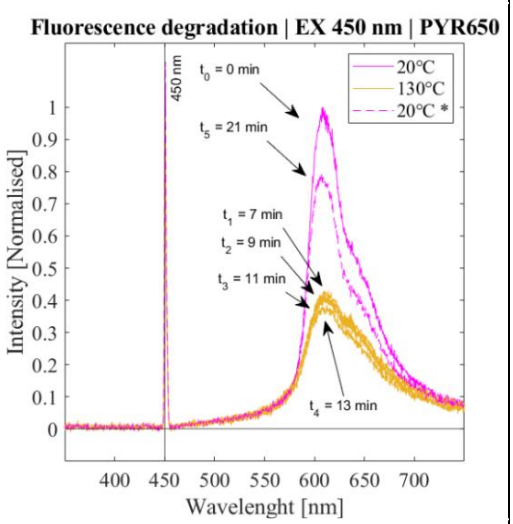

- **Fluorescence spectrum and RGB camera spectral response**

RGB CAMERA: a2A1920-160ucPRO

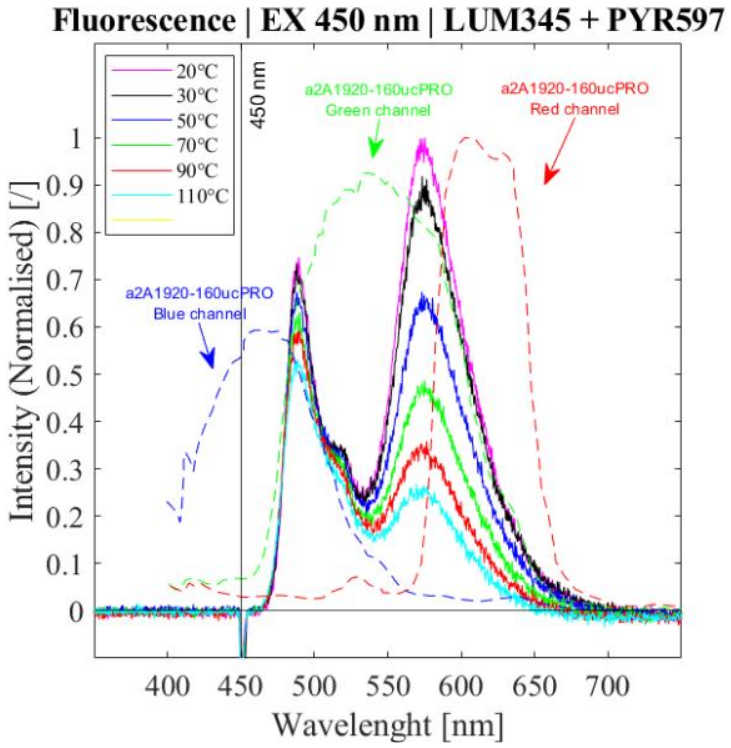

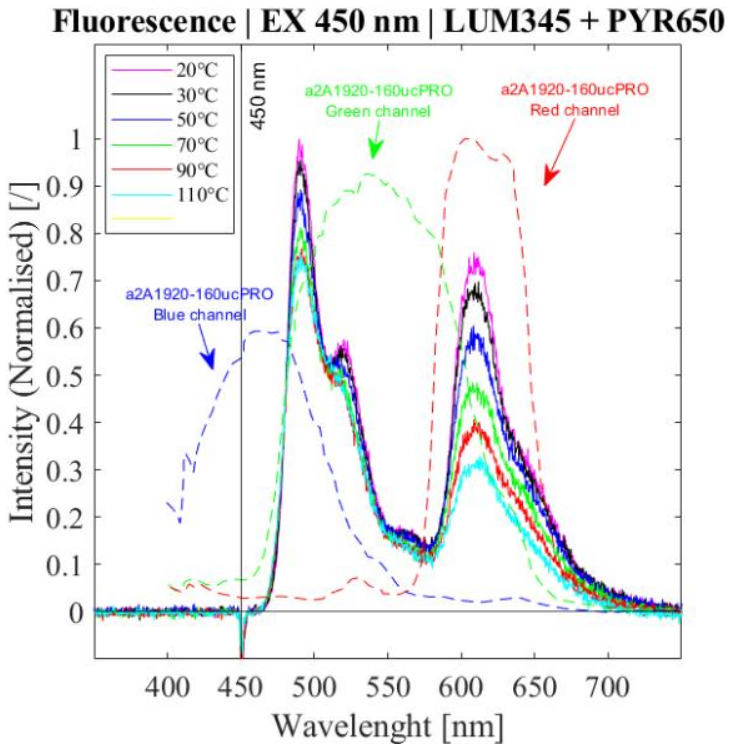

RGB CAMERA: acA1920-50gc

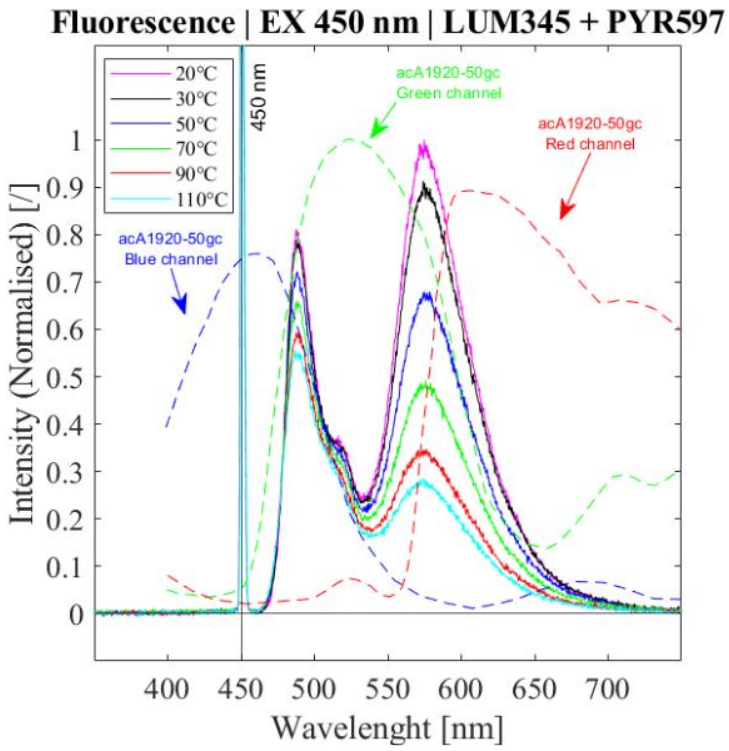

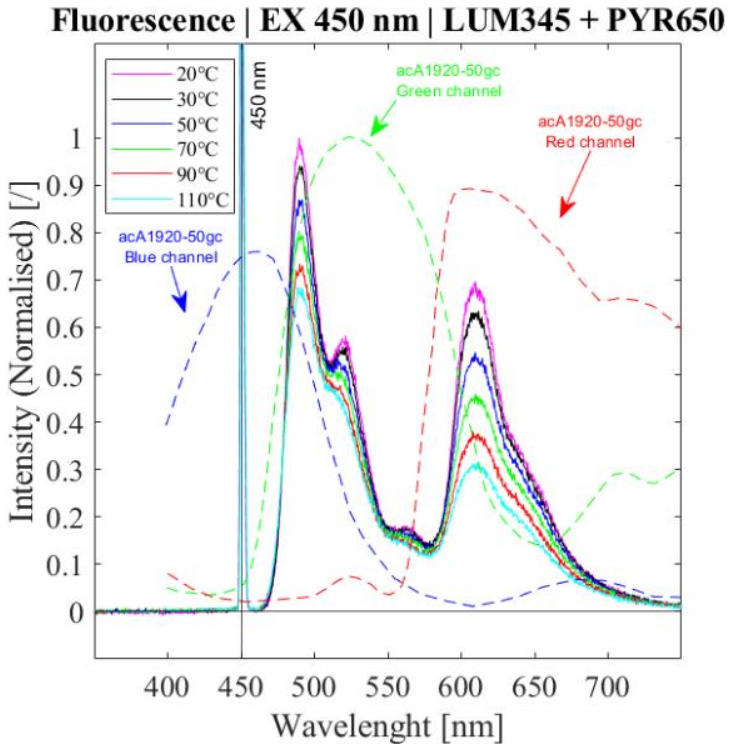

- **Simulate detection with RGB camera**

RGB CAMERA: ideal camera	
MIXTURE: LUM345 + PYR597	MIXTURE: LUM345 + PYR650
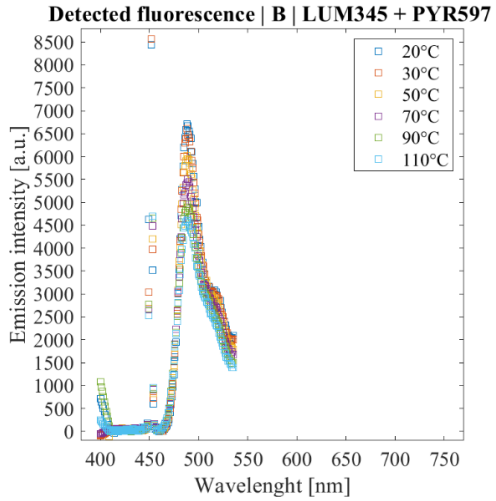	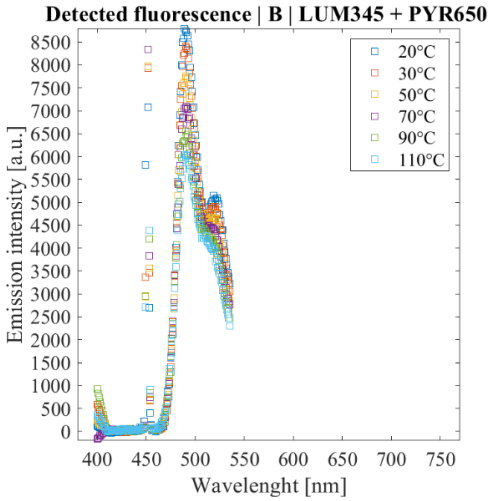
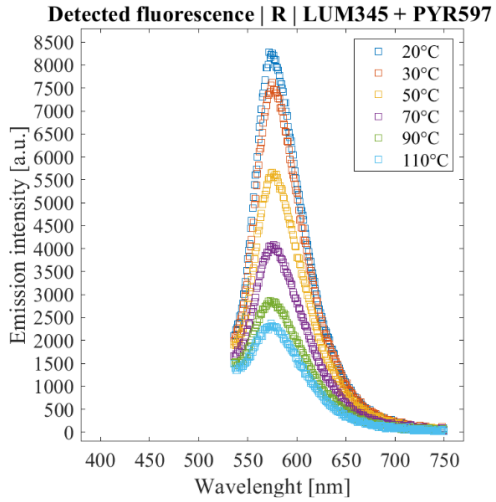	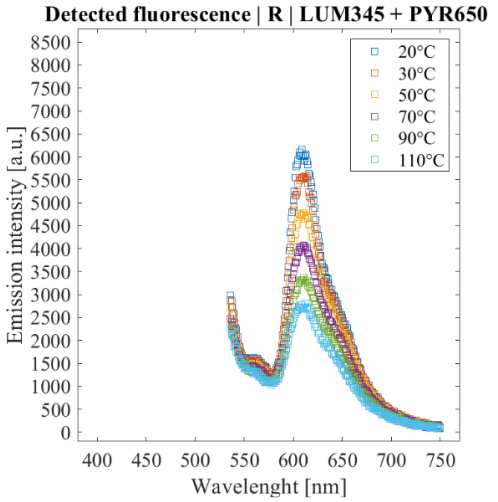
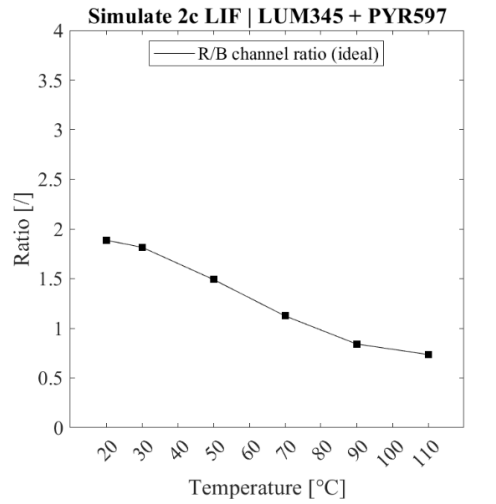	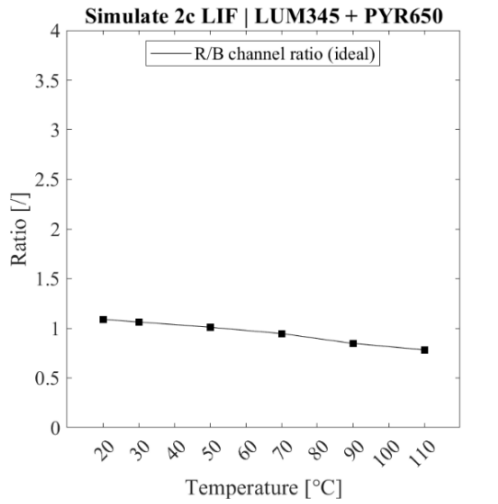

RGB CAMERA: acA1920-50gc
MIXTURE: LUM345 + PYR597

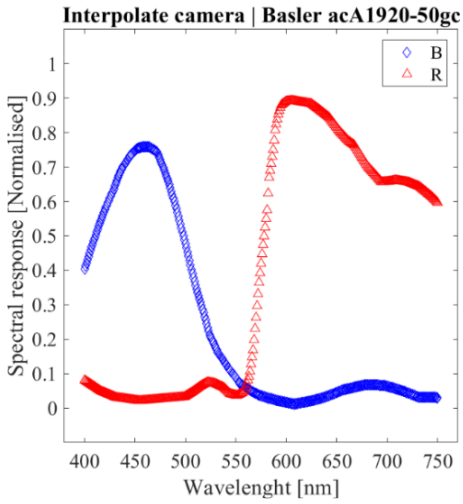

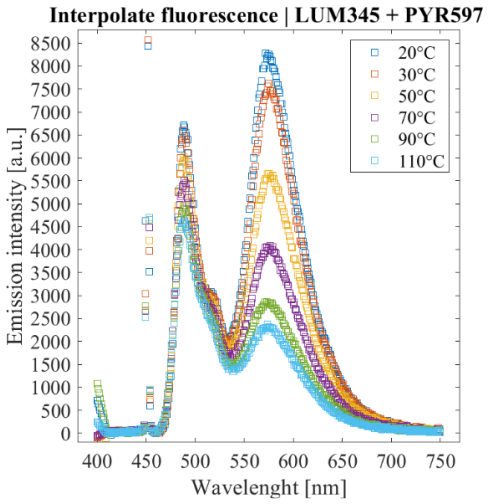

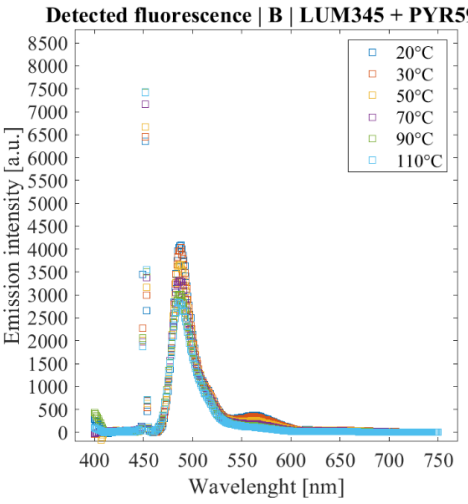

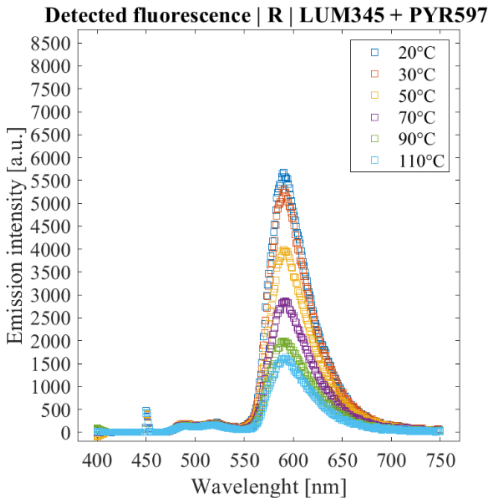

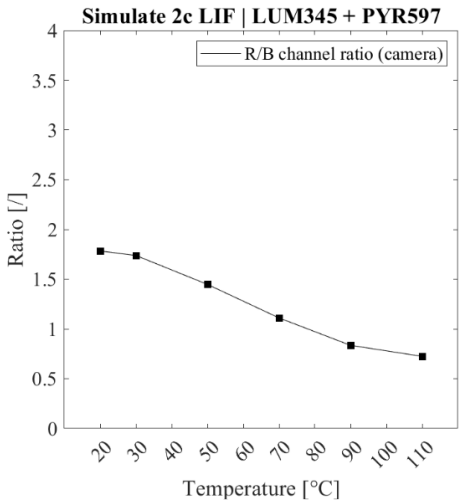

RGB CAMERA: acA1920-50gc
MIXTURE: LUM345 + PYR650

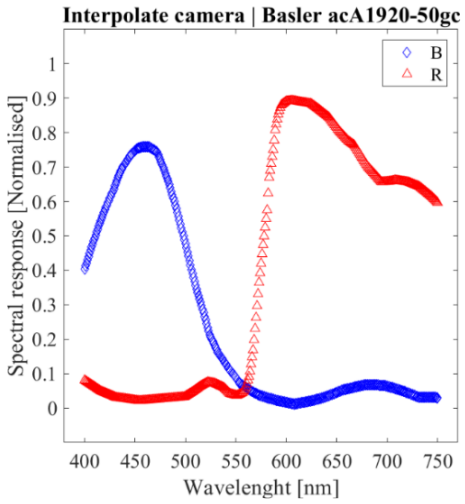

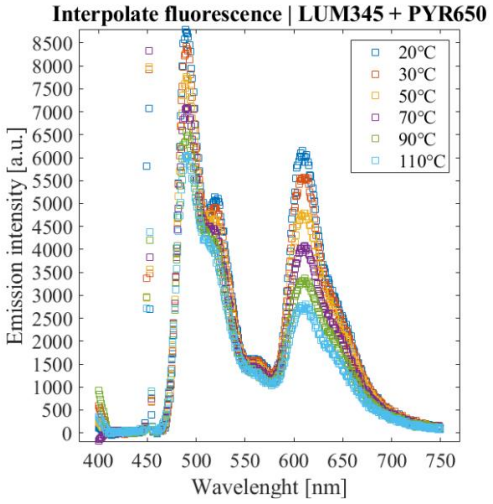

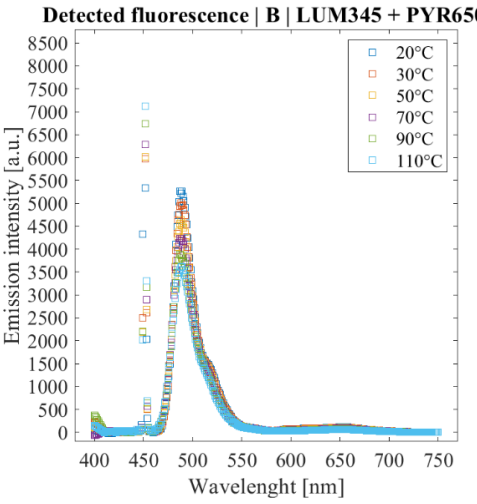

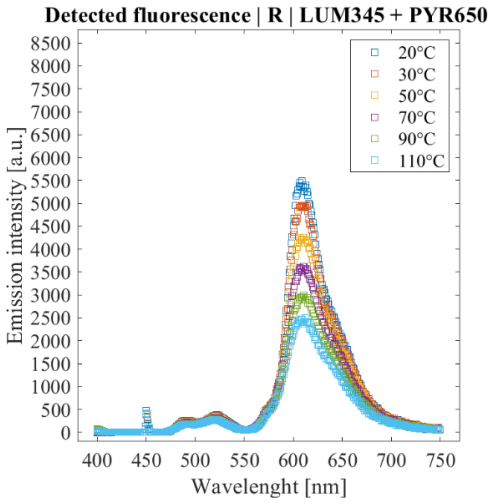

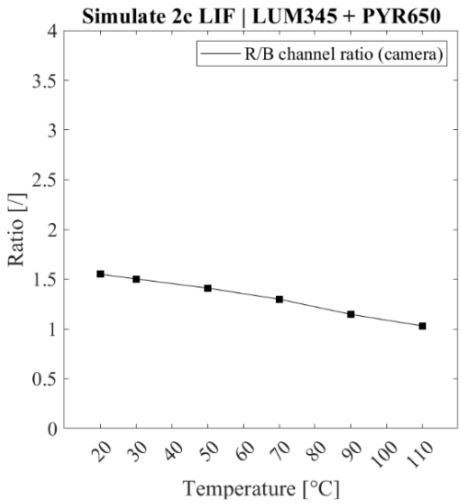

RGB CAMERA: a2A1920-160ucPRO
MIXTURE: LUM345 + PYR597

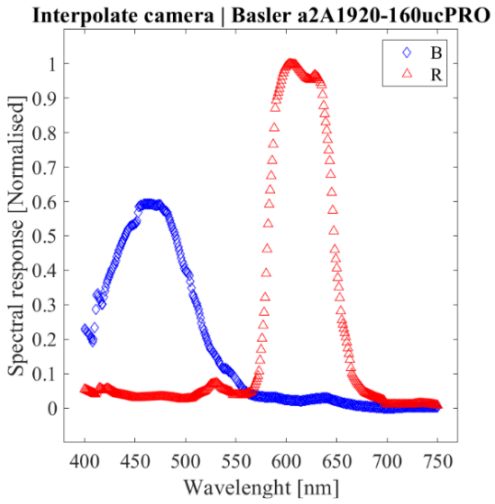

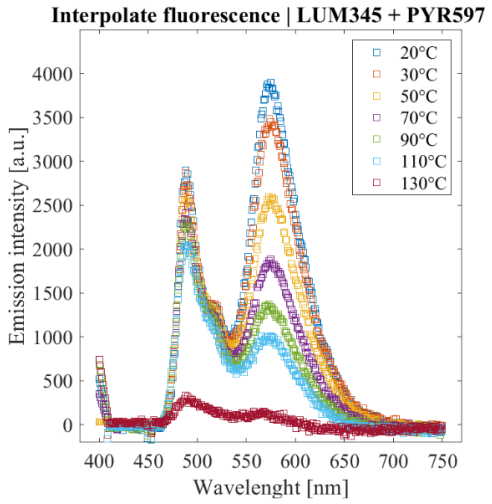

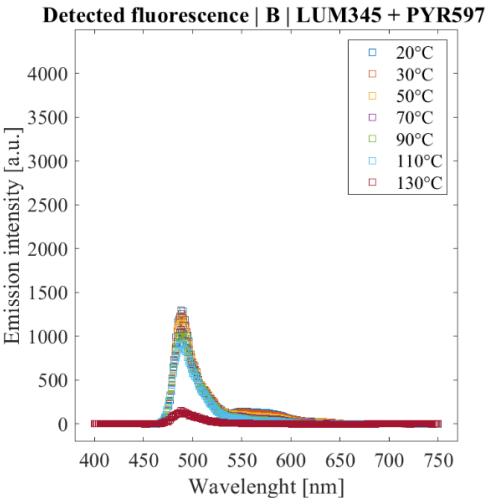

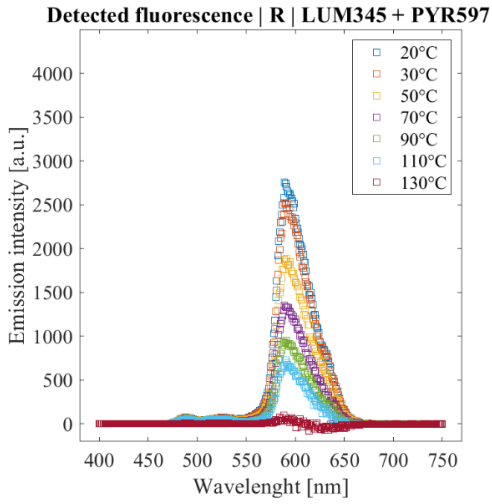

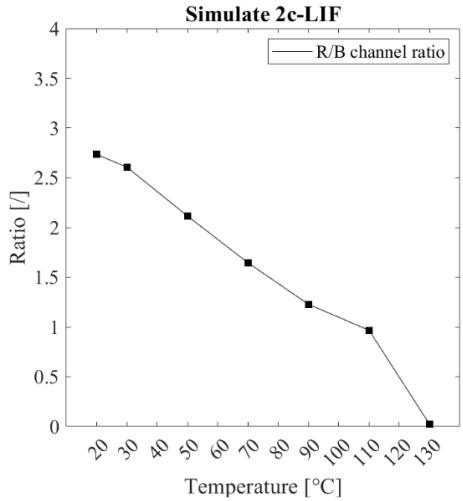

RGB CAMERA: a2A1920-160ucPRO
MIXTURE: LUM345 + PYR650

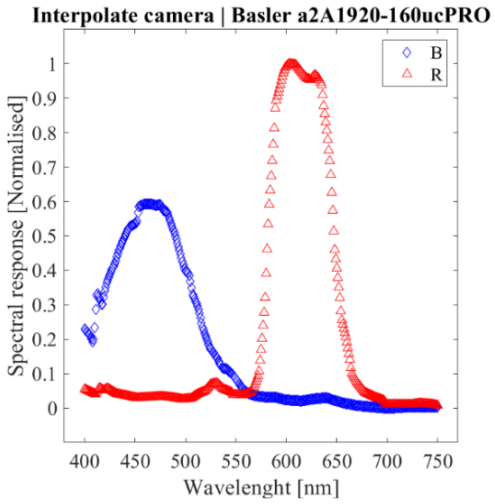

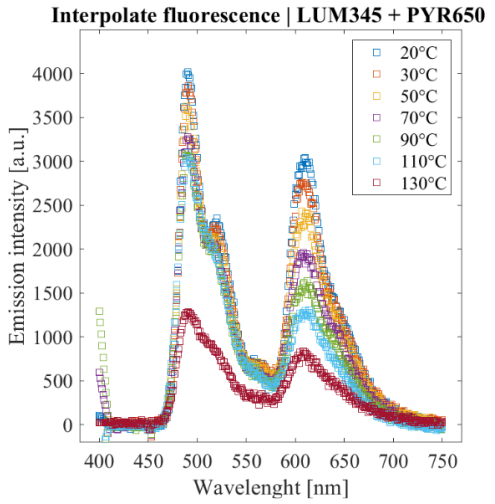

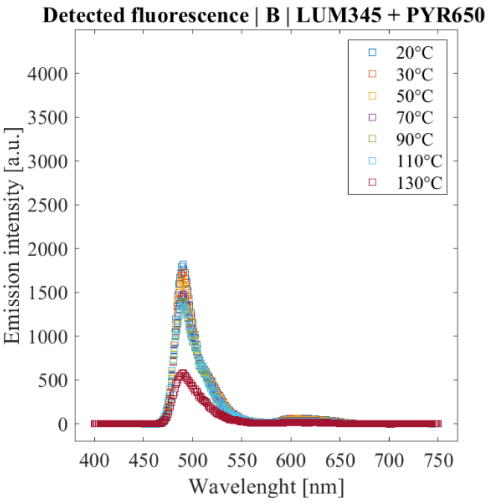

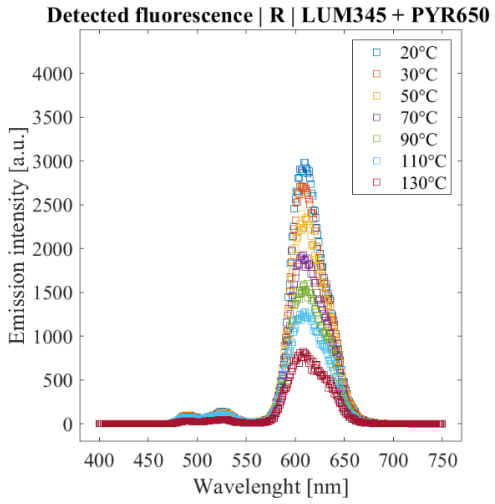

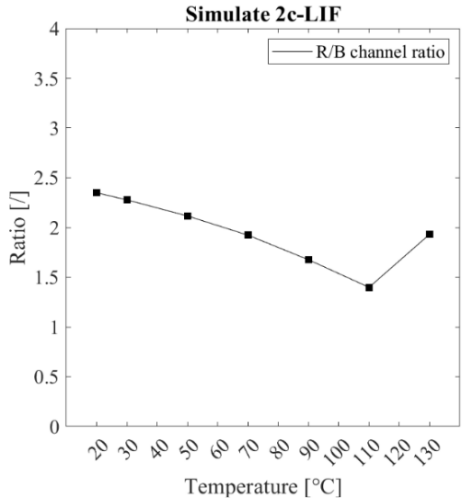

- **Measurements with LUM345 + PYR650 and bench 1 (with homogeniser)**

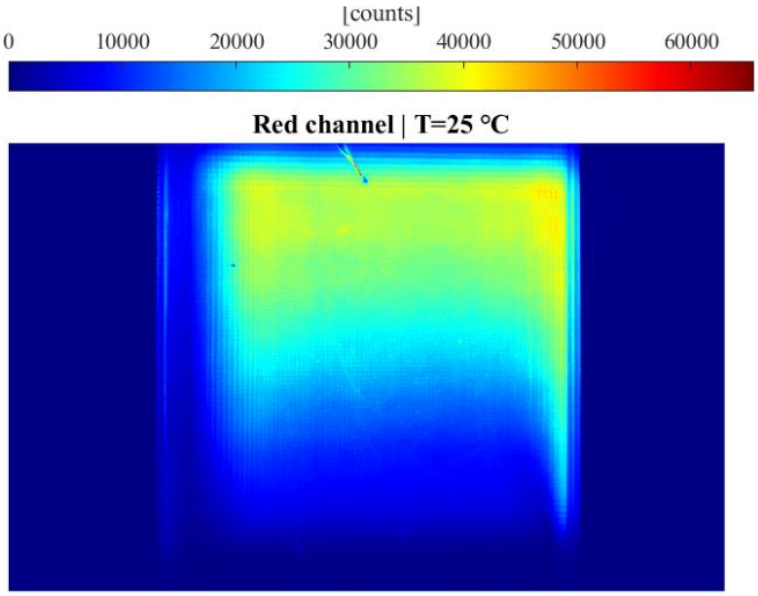

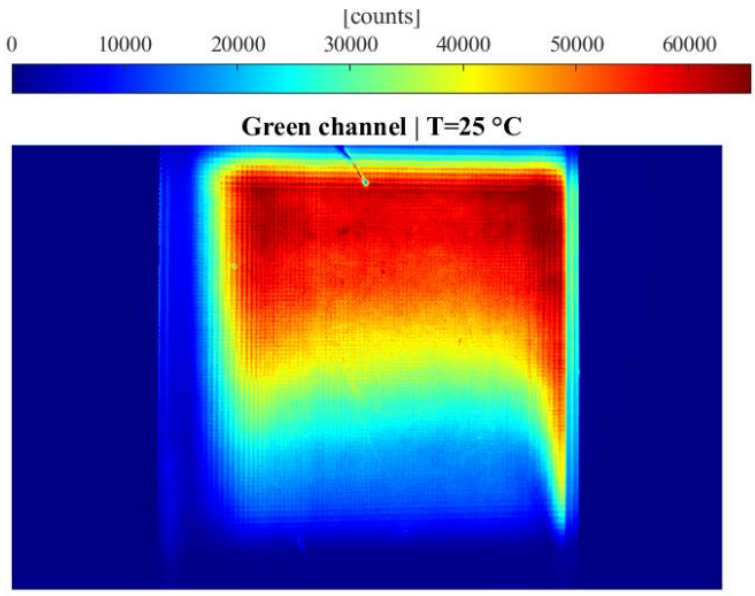

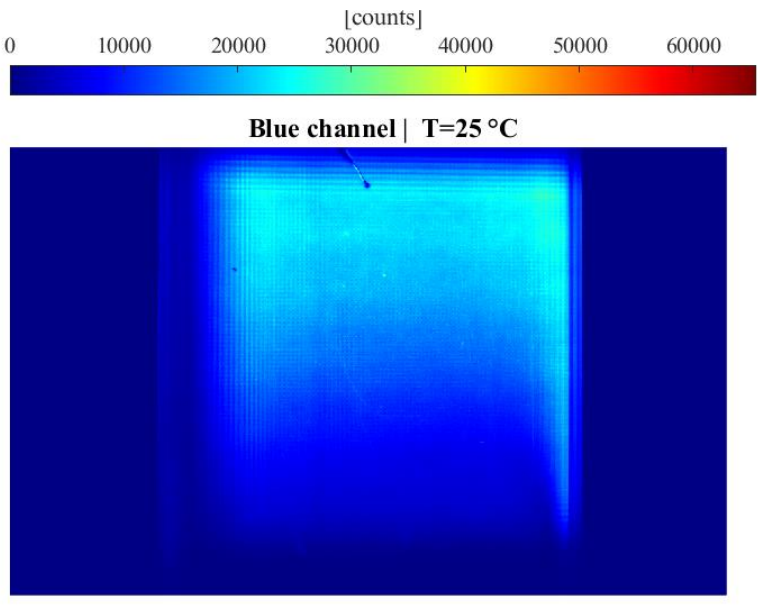

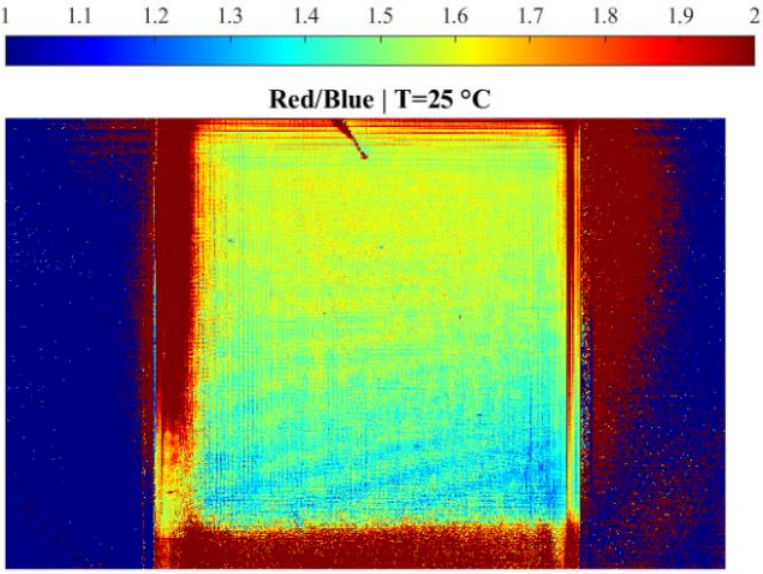

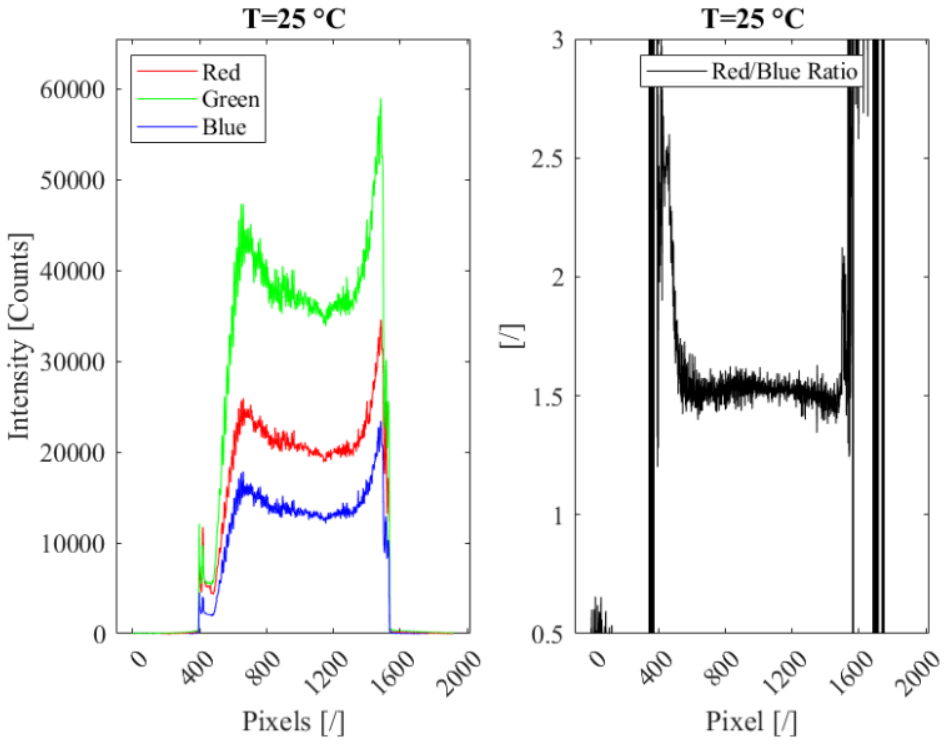

- **Analysis of uncertainty with ROI: independence from the ROI position and size**

Seven ROI with different positions and dimensions are considered in a central region of the image. The mean and standard deviation (between the pixels of every ROI) are calculated for an experiment undertaken with bench 1 and the mixture LUM345 + LUM597. The mean value of *Red/Blue* is the same regardless the ROI, because within ± 1.5 %. The typical standard deviation is between 3-5 %. The standard deviation is almost identical for ROI 1, ROI 2 and ROI 3.

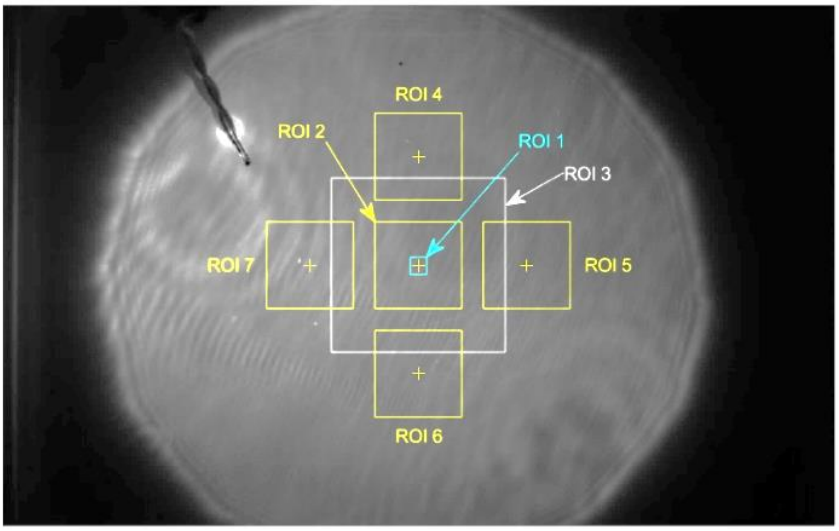

ROI	ROI (size)	*Red/Blue* (mean)	*Red/Blue* (standard deviation)
[number]	[pixels]	[/]	[%]
1	40 x 40	1.8624	3.9
2	200 x 200	1.8307	3.9
3	400 x 400	1.8325	4.0
4	200 x 200	1.8422	3.2
5	200 x 200	1.8346	5.8
6	200 x 200	1.8169	4.8
7	200 x 200	1.8254	3.7

▪ Reduction of uncertainty with binning

Reduction of uncertainty (associated with non-uniform response) on the channel ratio *Red/Blue* and the temperature ΔT, with increasing binning. The mean and standard deviation between the pixels of ROI is calculated. Bench 1 is used, mounting the beam homogeniser and using the mixture LUM345 + PYR650.

	No binning			3 x 3 pixels binning			8 x 8 pixels binning		
	Red/Blue		ΔT	Red/Blue		ΔT	Red/Blue		ΔT
T_{oil}	mean within ROI	std within ROI	within ROI	mean within ROI	std within ROI	within ROI	mean within ROI	std within ROI	within ROI
[°C]	[/]	[%]	[°C]	[/]	[%]	[°C]	[/]	[%]	[°C]
20	1.529	4.1	17.4	1.528	1.9	8.0	1.529	1.3	5.5
30	1.511	4.1	17.0	1.510	1.9	7.9	1.511	1.3	5.6
50	1.439	4.0	13.8	1.438	1.8	6.3	1.439	1.3	4.3
70	1.344	3.9	10.0	1.343	1.8	4.5	1.344	1.2	3.1
88	1.234	3.9	7.1	1.233	1.7	3.0	1.234	1.1	2.0
106	1.086	3.9	5.2	1.085	1.8	2.4	1.086	1.3	1.8

- **Background subtraction**

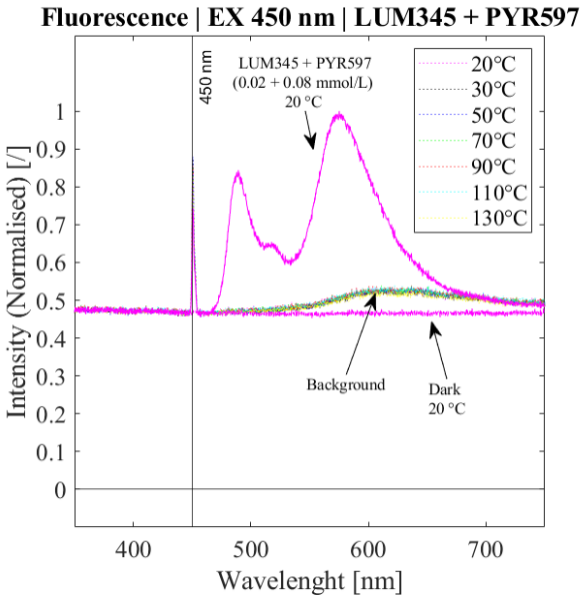

Raw fluorescence spectrum LUM345 + PYR650, the dark signal (no illumination), and the background (pure oil). The bump in the red wavelength in the background is generated by the colour filter.

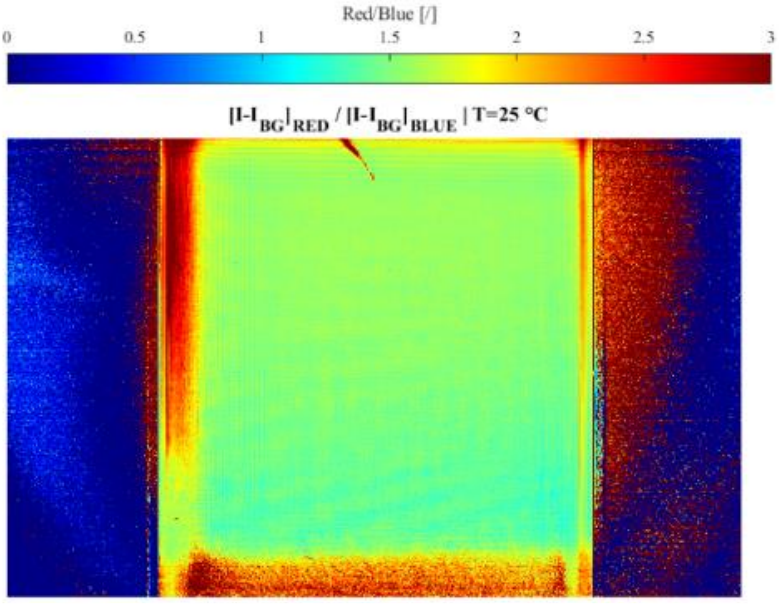

Channel ratio *R/B* obtained using pure oil for the background correction.

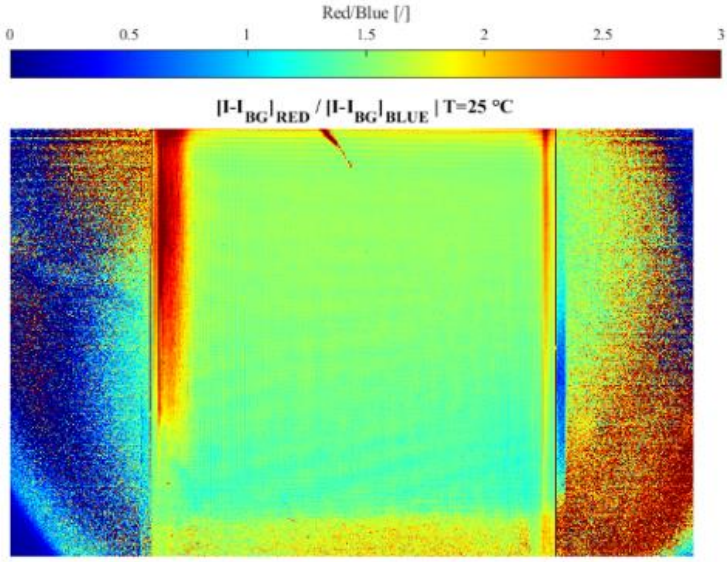

Channel ratio *R/B* obtained using the dark images for the background correction.

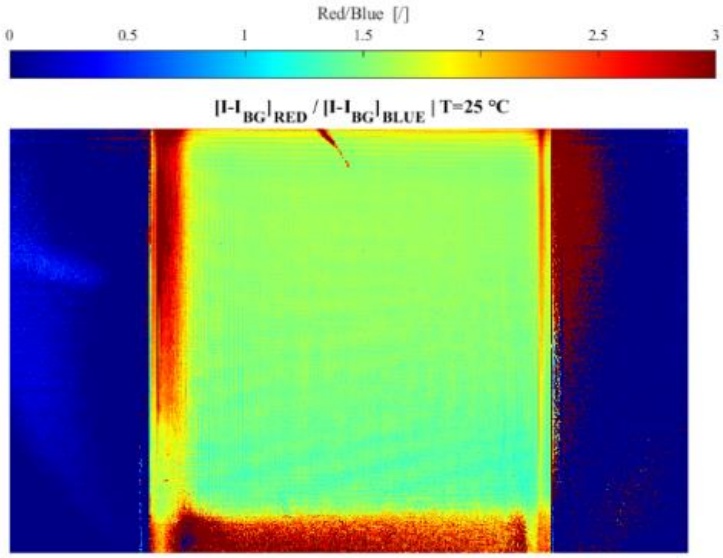

Channel ratio *R/B* obtained using the bare plate for the background correction.

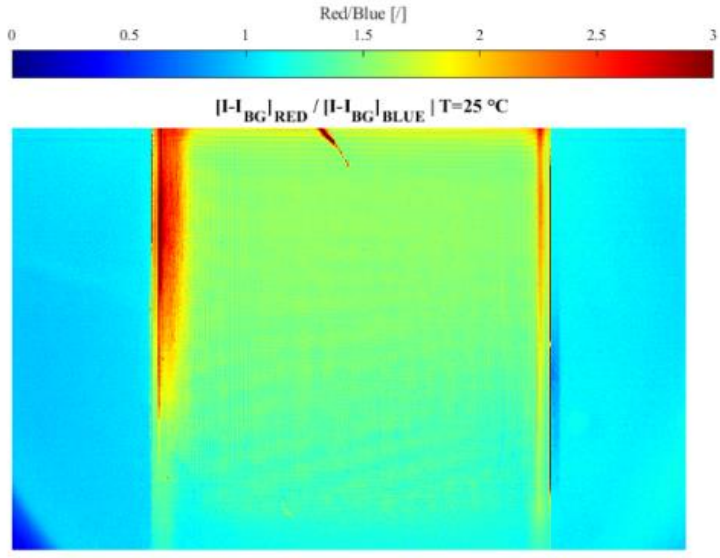

Channel ratio *R/B* obtained without background correction.

- **Calibration**

  - Without flat-field correction

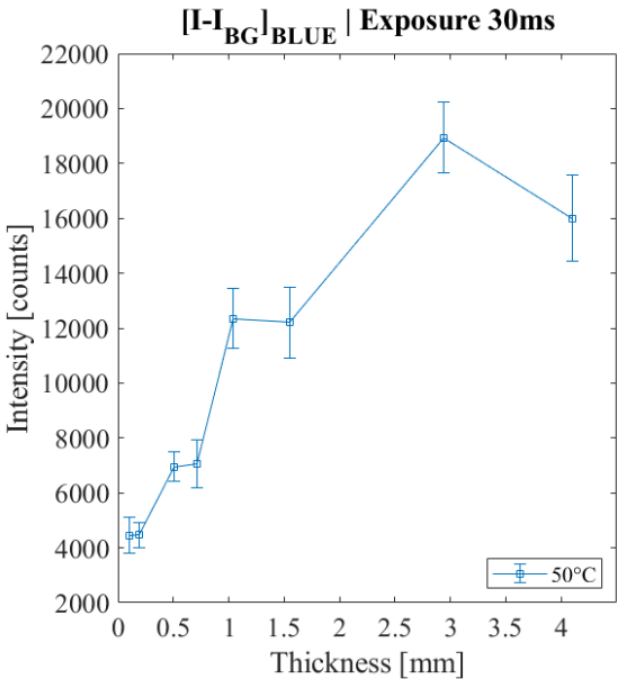

Averaged and background-corrected intensity for increasing film thickness without flat-field correction.

  - Free-surface vs glass-confined liquid films: bench and FOV

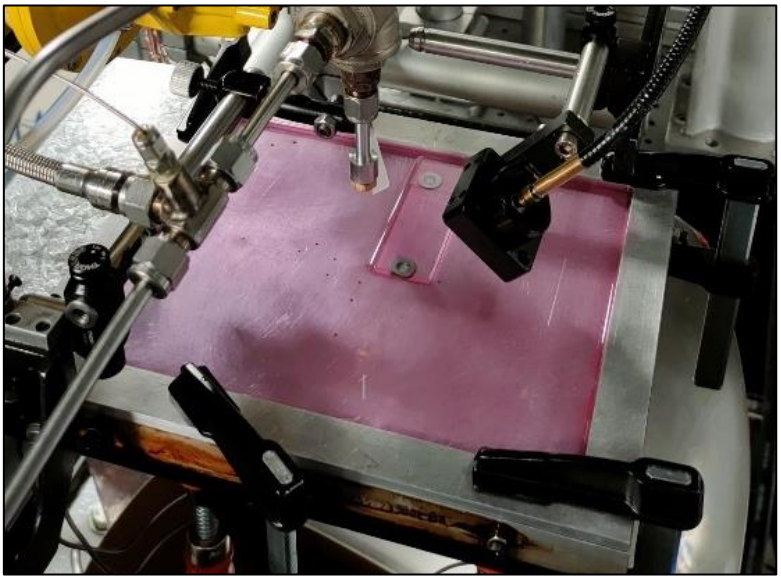

Bench 2 for static film characterisation.

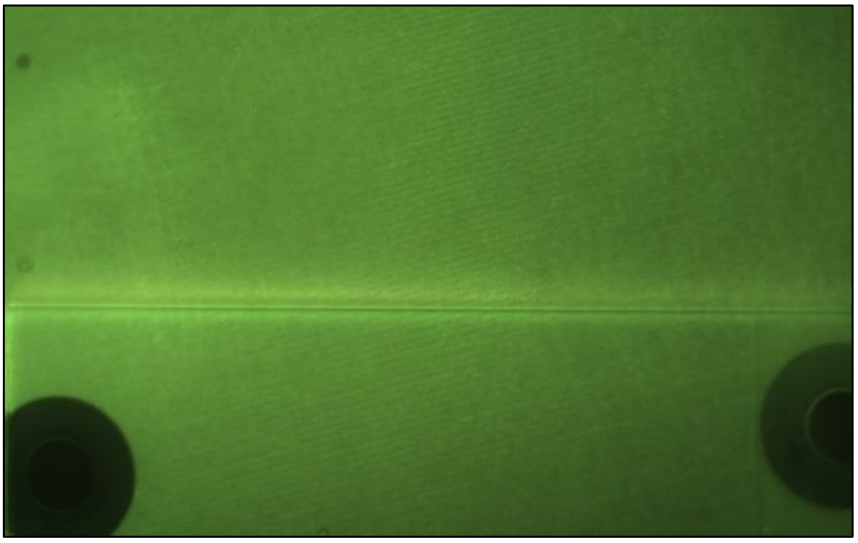

Field of view of the camera for characterising free-surface films (above) and glass-confined films (below).

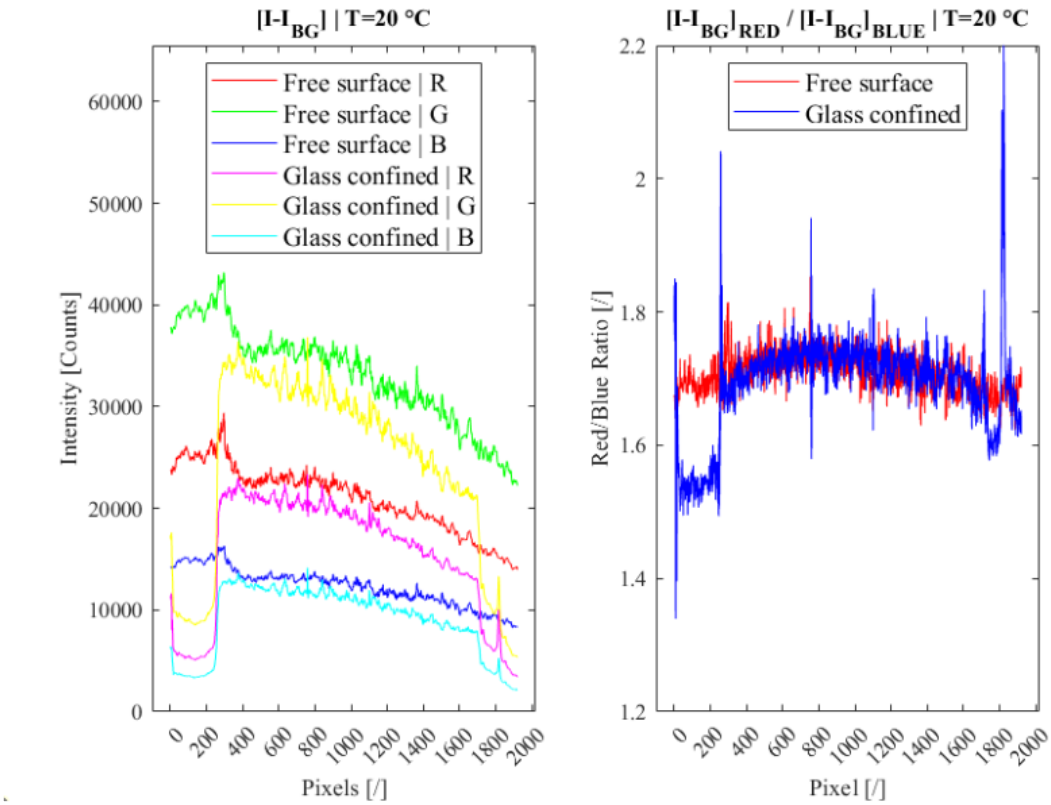

Profiles of intensity in channel of *Red*, *Green* and *Blue*, and channel ratio *Red/Blue* (without flat-field correction).

- Free-surface vs glass-confined: validate method and verify offset

The thickness of the free-surface film is $\delta = 0.92$ mm (measured with the contact needle). The thickness of the glass-confined film is $\delta = 0.91$ mm, given by the thickness of the two washers (measured with a calliper). Consider the mean and standard deviation (between the pixels of the two ROI) Concerning the channels (Red_{FF}, $Green_{FF}$ and $Blue_{FF}$) the traces of the free-surface film have the same slope as those of the glass-confined film, but they are always above it by a constant offset (about 6.5 % for $Blue_{FF}$). The same is observed for the channel ratio R/B_{FF} and the offset is 0.24 %.

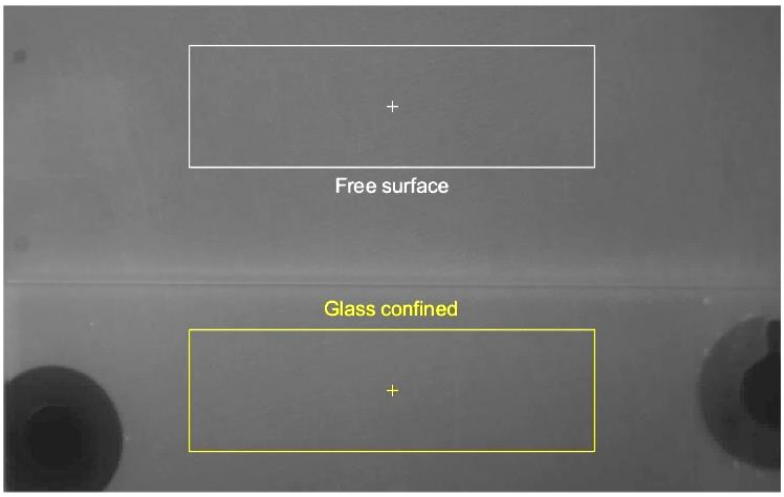

Position of two 1000 x 500 pixels ROI for characterising free-surface films and glass-confined films.

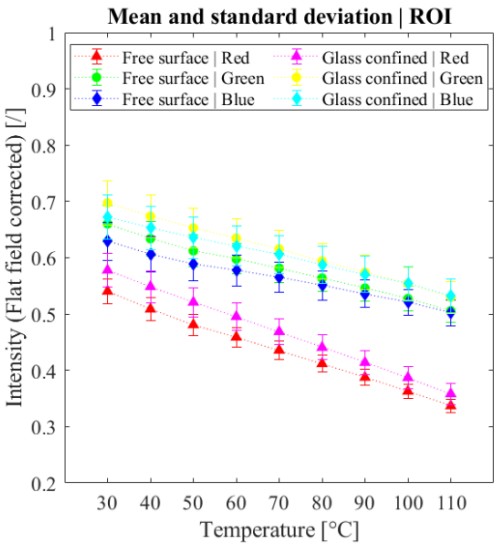

Flat-field corrected intensity of the channels Red_{FF}, $Green_{FF}$ and $Blue_{FF}$. Evaluation for free-surface and glass-confined films. The mean and standard deviations are calculated between the pixels of ROI.

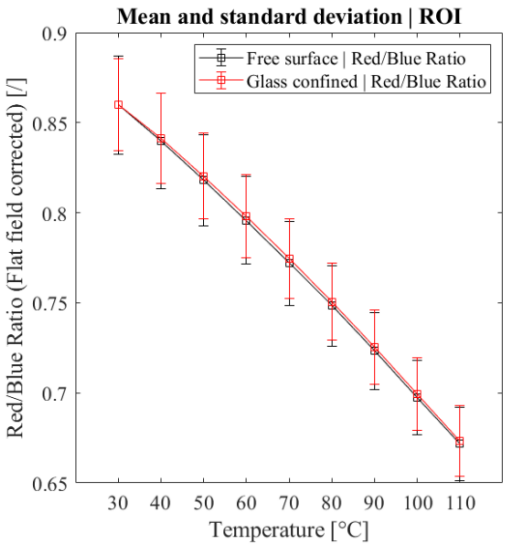

Flat-field corrected channel ratio R/B_{FF}. Evaluation for free-surface and glass-confined films. The mean and standard deviations are calculated between the pixels of ROI.

Flat-field corrected channel ratio R/B_{FF} and intensity in channel *Blue*. Measurements for free-surface and glass-confined films. The mean and standard deviations are calculated between the pixels of ROI.

T_{oil}	Free surface				Glass confined			
	$Red_{FF}/Blue_{FF}$		$Blue_{FF}$		$Red_{FF}/Blue_{FF}$		$Blue_{FF}$	
	mean	std	mean	std	mean	std	mean	std
[°C]	[/]	[%]	[/]	[%]	[/]	[%]	[/]	[%]
30	0.8598	3.2	0.6292	5.3	0.8600	3.0	0.6726	5.9
40	0.8398	3.1	0.6064	5.1	0.8413	3.0	0.6527	5.9
50	0.8181	3.1	0.5883	5.0	0.8204	2.9	0.6355	5.7
60	0.7958	3.1	0.5773	4.8	0.7982	2.9	0.6211	5.7
70	0.7719	3.0	0.5650	4.7	0.7744	2.8	0.6056	5.6
80	0.7483	3.0	0.5506	4.6	0.7505	2.8	0.5876	5.6
90	0.7232	3.0	0.5362	4.5	0.7256	2.8	0.5707	5.6
100	0.6974	3.0	0.5207	4.5	0.6994	2.9	0.5537	5.6
110	0.6717	3.0	0.5019	4.5	0.6733	2.9	0.5325	5.6

- **Algorithm testing on static films: verify input**

The two algorithms (iterative and interpolative) are given three free-surface static film as input, at T_{oil} = 60 °C and δ = 0.54-1.00-2.91 mm. Measurements are taken and the detected intensity and channel ratio are plotted.

In the left side of the figure, the flat-field corrected intensity is plotted for the three channels Red_{FF}, $Green_{FF}$ and $Blue_{FF}$. The traces gather by groups of three and the intensity is larger for increasing thickness. The mean value and standard deviation of each trace is calculated for $Blue_{FF}$. The mean intensity is $Blue_{FF}$ = 0.3145-0.5409-0.8566 for thickness δ = 0.54-1.00-2.91 mm, respectively, while the standard deviation of $Blue_{FF}$ is 6.3-5.6-5.2%. The same is done for the channel ratio, resulting in $Red_{FF}/Blue_{FF}$ = 0.7412-0.8025-0.9047 for thickness δ = 0.54-1.00-2.91 mm, respectively. In this case, the standard deviation of R/B_{FF} is 2.0-1.8-1.7 %.

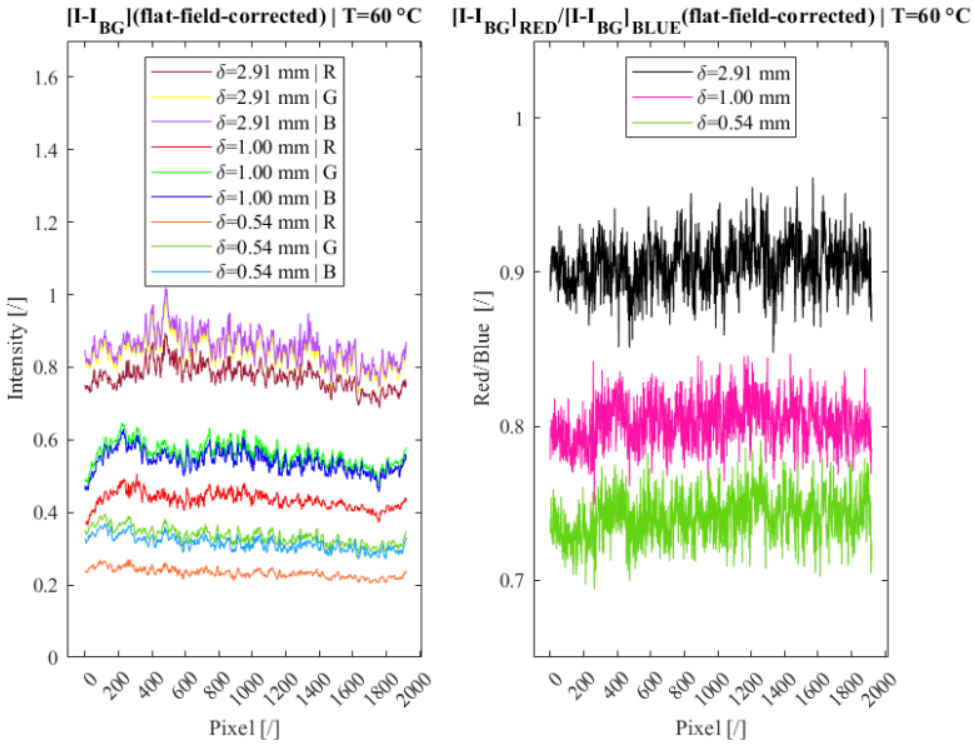

- **Binning**

  - Static film: image binning and improvement of the image uniformity

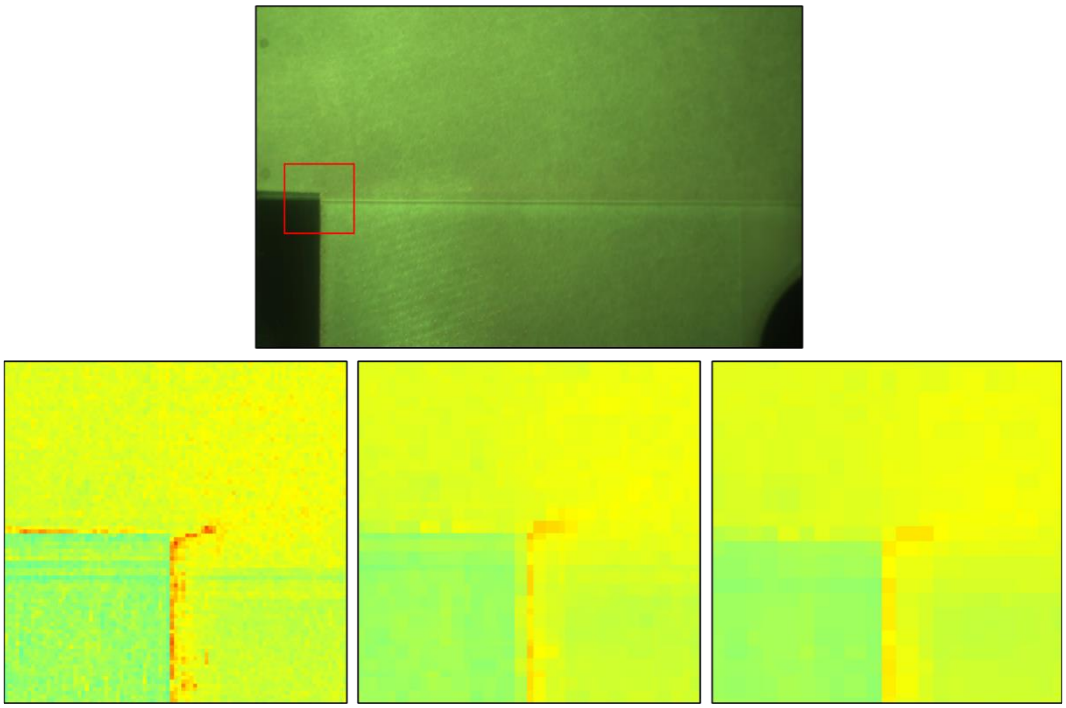

Application of binning on the images of a static film. (Above) Raw image of a static oil film, where the upper part is free-surface and the lower is glass-confined. (Below) Channel ratio $Red_{FF}/Blue_{FF}$ with increasing level of binning (from left to right none, 7 x 7 pixel and 11 x 11 pixel).

  - Suitable binning for the impinging jet

The table indicates that 7 x 7 pixel binning is roughly equivalent to 1/8 of a nozzle repositioning when d = 2 mm, while 15 x 15 pixels binning corresponds to roughly 1/4 With such levels of binning, the definition of the image is significantly reduced. With a binning chunk of 7 x 7 pixels, the image would have the 2 % of the resolution of the original image without binning. For a binning chunk of 15 x 15 pixels, that would decrease to 0.4 %. Considering that the typical length of the nozzle repositioning is equal to the nozzle diameter itself and that more than 5 x 5 pixel binning is needed to reduce the uncertainty, a binning between 7 and 15 pixels is reasonable.

Binning	Image size	Projected length
[pixel x pixel]	[pixel x pixel]	[mm / pixel]
None	[1200 x 1920]	0.03
3 x 3	[400 x 640]	0.10
5 x 5	[240 x 384]	0.17
7 x 7	[171 x 274]	0.23
9 x 9	[133 x 213]	0.30
11 x 11	[109 x 174]	0.36
13 x 13	[92 x 148]	0.43
15 x 15	[80 x 128]	0.50

- **Jet impingement: temperature and thickness evaluation with binning applied**

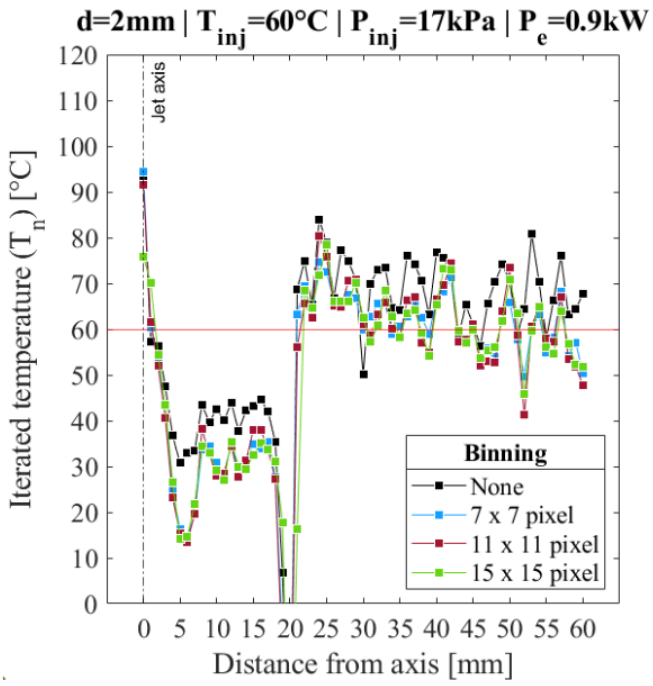

Temperature measurement with the iterative algorithm, for an impinging jet, for different binning levels. Evaluation along a radial profile and discretisation for every x = 1 mm.

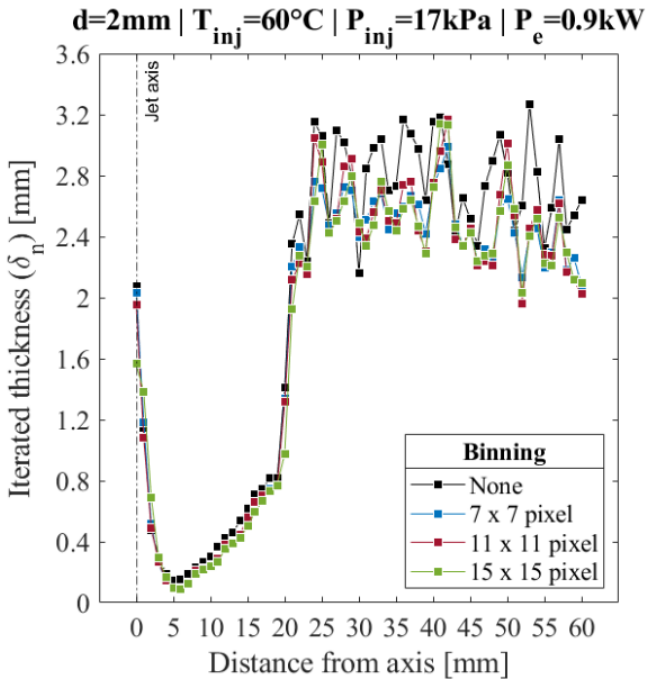

Thickness measurement with the iterative algorithm, for an impinging jet, for different binning levels. Evaluation along a radial profile and discretisation for every x = 1 mm.

ANNEXE TO CHAPTER 5

- **Radial distribution of the Nusselt for different injection and heating parameters**

Extract from Renon et al. 2012

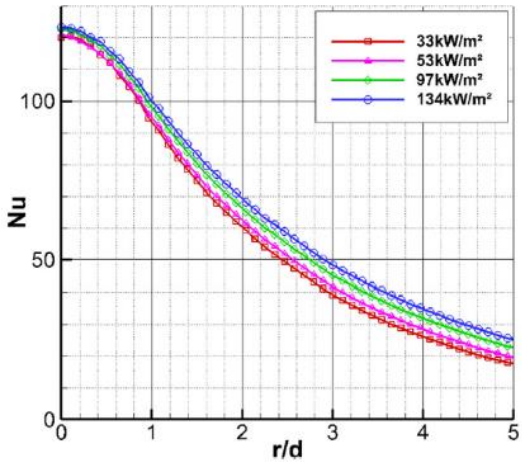

Variation of the Nusselt number with the input heat flux q_{in}. Re= 230 and Pr = 925.

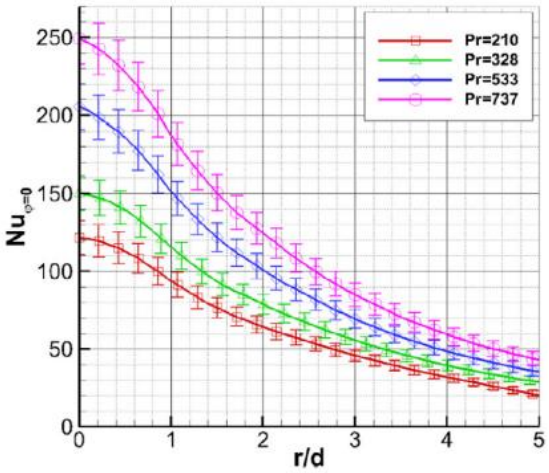

Radial variation of the Nusselt number for variable Prandtl. Re = 660, *d* = 2 mm.

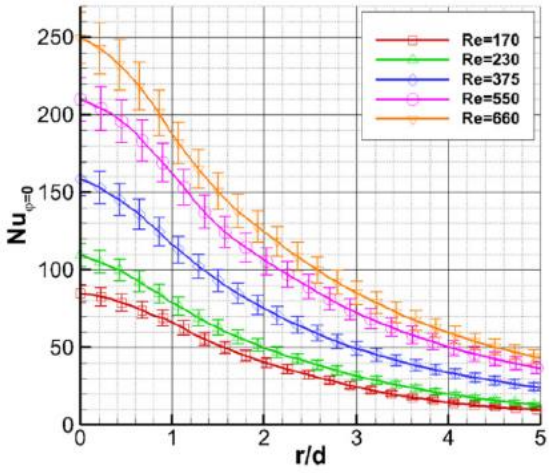

Radial variation of the Nusselt number for variable Reynolds. Pr = 737, d = 2 mm.

- **Nusselt correlation: variation of the exponent n=0.2-0.4-0.5**

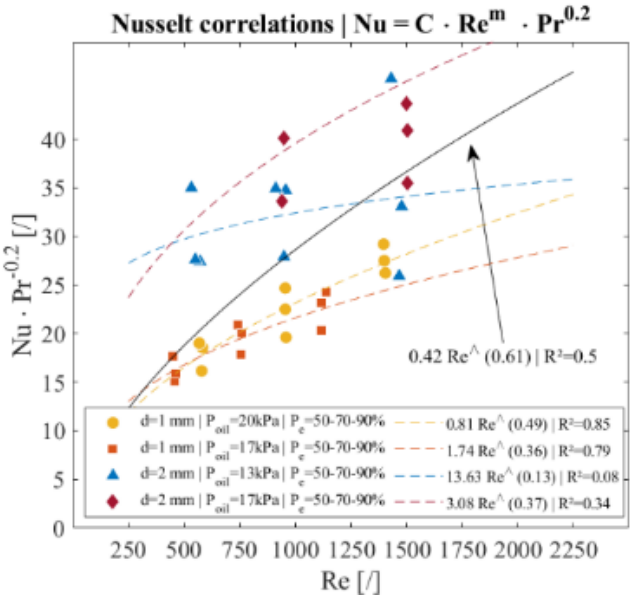

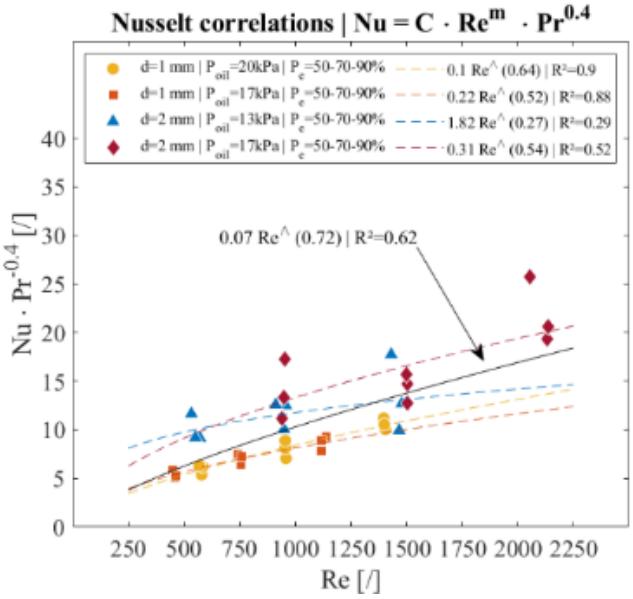

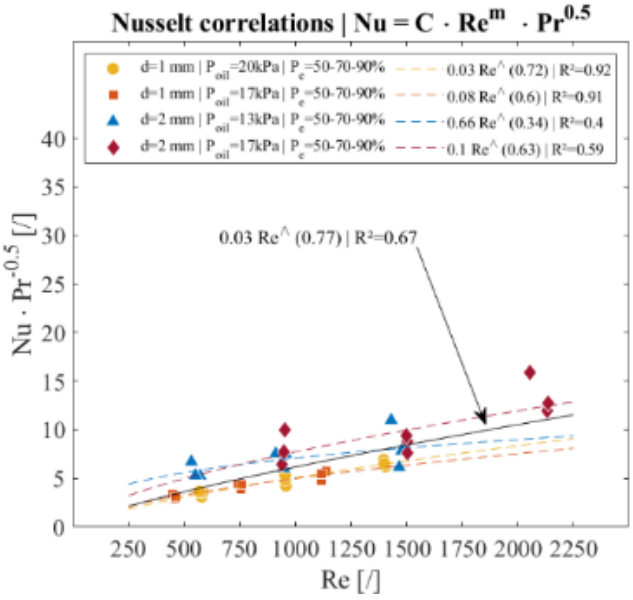

List of Figures

List of Tables

Nomenclature

Latin

Blue	[counts]	Intensity in channel Blue
C_P	[J kg^{-1} K^{-1}]	Heat capacity
d	[m]	Nozzle diameter
Green	[counts]	Intensity in channel Green
h	[W m^{-2} K^{-1}]	Convective coefficient
I	[counts]	Intensity
k	[W m^{-1} K^{-1}]	Conductivity
Nu	[/]	Nusselt number
P	[Pa]	Pressure
P_e	[W]	Electric power
Pr	[/]	Prandtl number
Re	[/]	Reynolds number
Red	[counts]	Intensity in channel Red
q	[W m^{-2}]	Heat flux at the air-liquid interface
q_{in}	[W m^{-2}]	Heat flux input for simulations
S	[m^2]	Plate surface (25 cm x 20 cm)
t_{exp}	[s]	Exposure time
T	[K]	Temperature
T_{int}	[K]	Internal temperature (within the solid plate)
T_{surf}	[K]	Surface temperature (solid-liquid interface)
U	[m s^{-1}]	Bulk velocity

Greek

δ	[m]	Liquid film thickness
μ	[kg m^{-1} s^{-1}]	Dynamic viscosity
ρ	[kg m^{-3}]	Density

Subscripts

aw	Adiabatic wall
b	Boundary surface
cc	Cell centre
FF	Flat-field corrected
inj	Referred to injection
oil	Referred to oil
plate	Referred to plate

References

Abram C, Fond B, Beyrau F (2018) Temperature measurement techniques for gas and liquid flows using thermographic phosphor tracer particles. Progress in Energy and Combustion Science 64: 93–156.

Akansu Y E, Sarioglu M, Kuvvet K, Yavuz T (2008) Flow field and heat transfer characteristics in an oblique slot jet impinging on a flat plate. International Communications in Heat and Mass Transfer 35 (7): 873–880.

Aldén M, Omrane A, Richter M, Särner G (2011) Thermographic phosphors for thermometry: A survey of combustion applications. Progress in Energy and Combustion Science 37 (4): 422–461.

Ashforth-Frost S, Rudel U W (2002) Thermal and hydrodynamic visualisation of a water jet impinging on a flat surface using microencapsulated liquid crystals. International Journal of Fluid Dynamics, 2002.

Azomaterial (accessed May 2023) Motor Rewind Using Zeus PEEK Insulation Products. Azomaterial. https://www.azom.com/article.aspx?ArticleID=13041.

Benhaddadi M, Olivier G, Ibtiouen R, Yelle J, Tremblay J-F (2011) Premium Efficiency Motors. In: Chomat M (ed) Electric Machines and Drives. InTech.

Bennion, K, Moreno, G (2015). Convective heat transfer coefficients of automatic transmission fluid jets with implications for electric machine thermal management. In International Electronic Packaging Technical Conference and Exhibition (Vol. 56901, p. V003T04A010). American Society of Mechanical Engineers.

Bizzak D J, Chyu M K (1995) Use of a laser-induced fluorescence thermal imaging system for local jet impingement heat transfer measurement. International Journal of Heat and Mass Transfer 38 (2): 267–274.

Bochenkov B, Lutz S (2004) A review of modern materials of permanent magnets. In: Proceedings, KORUS 2004. 8th Korea-Russia International Symposium on Science and Technology June 26-July 3, 2004 at Tomsk Polytechnic University, Russia. IEEE, Piscataway NJ. S. 201–203.

Broomfield D, Marvin R (2019) Design of Liquid Cooled IPM Motor for High Torque Density Applications. In: 2019 IEEE International Electric Machines & Drives Conference (IEMDC) May 12-15, 2019, Westin San Diego, San Diego, CA. IEEE, [Piscataway, New Jersey]. S. 2152–2159.

Bruchhausen M, Guillard F, Lemoine F (2005) Instantaneous measurement of two-dimensional temperature distributions by means of two-color planar laser induced fluorescence (PLIF) Exp Fluids 38 (1): 123–131.

Bula A J, Rahman M M, Leland J E (2000) Numerical Modeling of Conjugate Heat Transfer During Impingement of Free Liquid Jet Issuing from a Slot Nozzle. Numerical Heat Transfer, Part A: Applications 38 (1): 45–66.

Camilleri R, Howey D A, McCulloch M D (2016) Predicting the Temperature and Flow Distribution in a Direct Oil-Cooled Electrical Machine With Segmented Stator. IEEE Trans. Ind. Electron. 63 (1): 82–91.

Carriero A, Locatelli M, Ramakrishnan K, Mastinu G, Gobbi M (2018) A Review of the State of the Art of Electric Traction Motors Cooling Techniques. SAE technical paper 2018-01-0057.

Charogiannis A, An J S, Markides C N (2015) A simultaneous planar laser-induced fluorescence, particle image velocimetry and particle tracking velocimetry technique for the investigation of thin liquid-film flows. Experimental Thermal and Fluid Science 68: 516–536.

Charogiannis A, Denner F, van Wachem B G M, Kalliadasis S, Markides C N (2017) Detailed hydrodynamic characterization of harmonically excited falling-film flows: A combined experimental and computational study. Phys. Rev. Fluids 2 (1).

Charogiannis A, Markides C N (2019) Spatiotemporally resolved heat transfer measurements in falling liquid-films by simultaneous application of planar laser-induced fluorescence (PLIF), particle tracking velocimetry (PTV) and infrared (IR) thermography. Experimental Thermal and Fluid Science 107: 169–191.
Chaze W, Caballina O, Castanet G, Lemoine F (2016) The saturation of the fluorescence and its consequences for laser-induced fluorescence thermometry in liquid flows. Exp Fluids 57 (4): 1–18.
Coey J (2002) Permanent magnet applications. Journal of Magnetism and Magnetic Materials 248 (3): 441–456.
Collignon R, Caballina O, Lemoine F, Castanet G (2021) Temperature distribution in the cross section of wavy and falling thin liquid films. Exp Fluids 62 (5).
Coppeta J, Rogers C (1998) Dual emission laser induced fluorescence for direct planar scalar behavior measurements. Exp Fluids 25 (1): 1–15.
Cornacchia I, Pilla G, Chareyron B, Bruneaux G, Kaiser S, Poubeau A (2021) Development of an Experimental Methodology to Characterize Liquid Cooling Systems for Electric Motors. In: 2021 IEEE International Electric Machines & Drives Conference (IEMDC) IEEE.
Cousineau J E, Bennion K, DeVoto D, Mihalic M, Narumanchi S (2015) Characterization of Contact and Bulk Thermal Resistance of Laminations for Electric Machines.
Davin T, Pellé J, Harmand S, Yu R (2015) Experimental study of oil cooling systems for electric motors. Applied Thermal Engineering 75: 1–13.
Deisenroth D C, Ohadi M (2019) Thermal Management of High-Power Density Electric Motors for Electrification of Aviation and Beyond. Energies 12 (19): 3594.
Deriszadeh A, Monte F de, Villani M, Di Leonardo L (Eds.) (2019) Hydrothermal Performance of Ethylene Glycol and Water Mixture in a Spiral Channel for Electric Motor Cooling.
Dreisilker (accessed May 2023). Ultra-Sealed Winding. Dreisilker. https://dreisilker.com/electric-motor-repair-services/ultra-sealed-winding/.
Eggers J, Villermaux E (2008) Physics of liquid jets. Rep. Prog. Phys. 71 (3): 36601.
Eiamsa-ard S, Nanan K, Wongcharee K (2015) Heat transfer visualization of co/counter-dual swirling impinging jets by thermochromic liquid crystal method. International Journal of Heat and Mass Transfer 86: 600–621.
Elantas (accessed May 2023a) Insulation and Protection of Motors. Elantas. https://www.elantas.de/fileadmin/elantas/companies/elantas_europe/press_events/downloadcenter/2019-1917_en-brochure-a4_motors_web-einzel.pdf.
Elantas (accessed May 2023b) Solid Insulation Solutions for Motors and Motor Repair. Elantas. https://www.elantas.com/fileadmin/elantas/companies/elantas_pgd/products/sales_brochures/elan-film_brochure__2-15_.pdf.
Electricalaxis (accessed May 2023) What are the Basic Factors When Selecting AC Induction Motors?. Electricalaxis. http://www.electricalaxis.com/2020/11/what-are-basic-factors-when-selecting.html.
Elison B, Webb B W (1994) Local heat transfer to impinging liquid jets in the initially laminar, transitional, and turbulent regimes. International Journal of Heat and Mass Transfer 37 (8): 1207–1216.
Feng X, Cousineau E, Bennion K, Moreno G, Kekelia B, Narumanchi S (2021) Experimental and numerical study of heat transfer characteristics of single-phase free-surface fan jet impingement with automatic transmission fluid. International Journal of Heat and Mass Transfer 166: 120731.
Fenot M, Vullierme J-J, Dorignac E (2005) Local heat transfer due to several configurations of circular air jets impinging on a flat plate with and without semi-confinement. International Journal of Thermal Sciences 44 (7): 665–675.

Fond B, Abram C, Heyes A L, Kempf A M, Beyrau F (2012) Simultaneous temperature, mixture fraction and velocity imaging in turbulent flows using thermographic phosphor tracer particles. Opt. Express 20 (20): 22118–22133.
Funatani S, Fujisawa N, Ikeda H (2004) Simultaneous measurement of temperature and velocity using two-colour LIF combined with PIV with a colour CCD camera and its application to the turbulent buoyant plume. Meas. Sci. Technol. 15 (5): 983–990.
Gabour L A, Lienhard J H (1994) Wall Roughness Effects on Stagnation-Point Heat Transfer Beneath an Impinging Liquid Jet. Journal of Heat Transfer 116 (1): 81–87.
Gai Y, Kimiabeigi M, Chuan Chong Y, Widmer J D, Deng X, Popescu M, Goss J, Staton D A, Steven A (2019) Cooling of Automotive Traction Motors. Schemes, Examples, and Computation Methods. IEEE Trans. Ind. Electron. 66 (3): 1681–1692.
Galea M, Gerada C, Raminosoa T, Wheeler P (2012) A Thermal Improvement Technique for the Phase Windings of Electrical Machines. IEEE Trans. on Ind. Applicat. 48 (1): 79–87.
Garimella S V, Nenaydykh B (1996) Nozzle-geometry effects in liquid jet impingement heat transfer. International Journal of Heat and Mass Transfer 39 (14): 2915–2923.
Gavrilenko, V. (2020). Characterization of winding insulation of electrical machines fed by voltage waves with high dV/dt (Doctoral dissertation, Université Paris-Saclay; Université polytechnique de Tomsk (Russie)).
Gieras J F, Bianchi N (2004) Electric Motors for Light Traction. EPE Journal 14 (1): 12–23.
Glynn C, O'Donovan T, Murray D B, Feidt M (Eds.) (2005) Jet impingement cooling.
Goldstein R J, Behbahani A I, Heppelmann K (1986) Streamwise distribution of the recovery factor and the local heat transfer coefficient to an impinging circular air jet. International Journal of Heat and Mass Transfer 29 (8): 1227–1235.
Gundabattini E, Kuppan R, Solomon D G, Kalam A, Kothari D P, Abu Bakar R (2020) A review on methods of finding losses and cooling methods to increase efficiency of electric machines. Ain Shams Engineering Journal.
Guo F, Zhang C (2019) Oil-Cooling Method of the Permanent Magnet Synchronous Motor for Electric Vehicle. Energies 12 (15): 2984.
Haustein H D, Tebrügge G, Rohlfs W, Kneer R (2012) Local heat transfer coefficient measurement through a visibly-transparent heater under jet-impingement cooling. International Journal of Heat and Mass Transfer 55 (23-24): 6410–6424.
Herold K, Klute F, Kamps J, Monissen C, Ramones A I, Maiterth J M, Pischinger S (Eds.) (2020) Cost Optimization of E-Drives for Traction Applications.
Hidrovo C H (2002) 2D Thickness and Temperature Mapping of Fluids by Means of a Two-Dye Laser Induced Fluorescence Ratiometric Scheme. J Flow Vis Image Proc 9 (2-3): 21.
Hidrovo C H, Hart D P (Eds.) (2000) Dual emission laser induced fluorescence technique (DELIF) for oil film thickness and temperature measurement. InJul (pp. 23-28).
Hidrovo C H, Hart D P (2001) Emission reabsorption laser induced fluorescence (ERLIF) film thickness measurement. Meas. Sci. Technol. 12 (4): 467–477.
Huang J, Shoai Naini S, Miller R, Rizzo D, Sebeck K, Shurin S, Wagner J (2019) A Hybrid Electric Vehicle Motor Cooling System—Design, Model, and Control. IEEE Trans. Veh. Technol. 68 (5): 4467–4478.
Hultman E, Leijon M. (2013) Utilizing cable winding and industrial robots to facilitate the manufacturing of electric machines. Robotics and Computer-Integrated Manufacturing, 29(1), 246-256.

Iciek J (1982) The hydrodynamics of a free, liquid jet and their influence on direct contact heat transfer—II Conditions of change of liquid outflow type through sharp inlet edged orifice. International Journal of Multiphase Flow 8 (3): 251–260.
IEA (2020) Global EV Outlook 2020. Entering the decade of electric drive. International Energy Agency.
IEA (2022) Global EV Outlook 2022. Securing supplies for an electric future. International Energy Agency.
IEC, 2019 60034 - 2019, Rotating electrical machines.
Ingole S B, Sundaram K K (2018) Investigation of maximum Nusselt number with inclined and non-confined offset jet impingement cooling. International Journal of Heat and Technology (IJHT) 36(3), 869-876.
IRENA (2019) Innovation outlook: Smart charging for electric vehicles. International Renewable Energy Agency, Abu Dhabi.
Jambunathan K, Lai E, Moss M A, Button B L (1992) A review of heat transfer data for single circular jet impingement. International Journal of Heat and Fluid Flow 13 (2): 106–115.
Kato T, Mizutani R, Matsumoto H, Yamamoto K (2013) Advanced technologies of traction motor for automobile. In: 2013 IEEE ECCE Asia Downunder. IEEE. S. 147–152.
Kawamura T, Atarashi H, Miyoshi T, (2011 High-Power Density Motor for Racing Use. SAE Technical Paper Series No. 2011-39-7221.
Kekelia, B, Bennion K, Feng X, Moreno G., Cousineau J E, Narumanchi S, Tomerlin J (2019). Surface Temperature Effect on Convective Heat Transfer Coefficients for Jet Impingement Cooling of Electric Machines with Automatic Transmission Fluid. In International Electronic Packaging Technical Conference and Exhibition (Vol. 59322, p. V001T08A004). American Society of Mechanical Engineers.
Kemp S P, Linden J L (1990) Physical and Chemical Properties of a Typical Automatic Transmission Fluid. SAE technical paper 902148.
Kim H. J., Kihm K. D. (Eds.) (2001) Application of a Two-Color Laser Induced Fluorescence Technique (LIF) for Temperature Mapping. American Society of Mechanical Engineers.
Kramer M J, McCallum R W, Anderson I A, Constantinides S (2012) Prospects for Non-Rare Earth Permanent Magnets for Traction Motors and Generators. JOM 64 (7): 752–763.
Kulan M C, Sahin S, Baker N J (2020) An Overview of Modern Thermo-Conductive Materials for Heat Extraction in Electrical Machines. IEEE Access 8: 212114–212129.
Kulkarni D P, Rupertus G, Chen E (2012) Experimental Investigation of Contact Resistance for Water Cooled Jacket for Electric Motors and Generators. IEEE Trans. Energy Convers. 27 (1): 204–210.
Kurganov V A (2011) Adiabatic Wall Temperature. Thermopedia. https://www.thermopedia.com/content/291/.
Lavieille P, Delconte A, Blondel D, Lebouch M, Lemoine F (2004) Non-intrusive temperature measurements using three-color laser-induced fluorescence. Exp Fluids 36 (5): 706–716.
Lavieille P, Lemoine F, Lavergne G, Lebouché M (2001) Evaporating and combusting droplet temperature measurements using two-color laser-induced fluorescence. Exp Fluids 31 (1): 45–55.
Lawrence, R. R. (1920). Principles of alternating-current machinery. McGraw-Hill Book Company, Incorporated.
Lee J, Lee S-J (1999) Stagnation Region Heat Transfer of a Turbulent Axisymmetric Jet Impingement. Experimental Heat Transfer 12 (2): 137–156.

Lee K-H, Cha H-R, Kim Y-B (2016) Development of an interior permanent magnet motor through rotor cooling for electric vehicles. Applied Thermal Engineering 95: 348–356.
Lee X C, Ma C F, Zheng Q, Zhuang Y, Tian Y Q (1997) Numerical study of recovery effect and impingement heat transfer with submerged circular jets of large Prandtl number liquid. International Journal of Heat and Mass Transfer 40 (11): 2647–2653.
Leland J E, Pais M R (1999) Free Jet Impingement Heat Transfer of a High Prandtl Number Fluid Under Conditions of Highly Varying Properties. Journal of Heat Transfer 121 (3): 592–597.
Li H, Klontz K W, Ferrell V E, Barber D (2017) Thermal Models and Electrical Machine Performance Improvement Using Encapsulation Material. IEEE Trans. on Ind. Applicat. 53 (2): 1063–1069.
Lienhard J H (Ed.) (2006) Heat transfer by impingement of circular free-surface liquid jets.
Lim D H, Kim S C (2014) Thermal performance of oil spray cooling system for in-wheel motor in electric vehicles. Applied Thermal Engineering 63 (2): 577–587.
Lindh P M, Petrov I, Niemela M, Scherman E, Wallmark O, Pyrhonen J J (2019) Investigation of a Direct Liquid Cooling System in a Permanent Magnet Synchronous Machine. IEEE Trans. Energy Convers.: 1.
Liu C, Zhang H, Xu Z, Gerada D, Li J, Gerada C, Chong Y C, Popescu M, Goss J, Staton D (2019a) Experimental Investigation on Oil Spray Cooling with Hairpin Windings. IEEE Trans. Ind. Electron.: 1.
Liu H, Ayat S, Wrobel R, Zhang C (2019b) Comparative study of thermal properties of electrical windings impregnated with alternative varnish materials. The Journal of Engineering 2019 (17): 3736–3741.
Liu M, Li Y, Ding H, Sarlioglu B (2017) Thermal management and cooling of windings in electrical machines for electric vehicle and traction application. In: 2017 IEEE Transportation and Electrification Conference and Expo (ITEC) Chicago, Illinois, June 22-24, 2017. IEEE, [Piscataway, NJ]. S. 668–673.
Liu X, Lienhard J H, Lombara J S (1991) Convective Heat Transfer by Impingement of Circular Liquid Jets. Journal of Heat Transfer 113 (3): 571–582.
Ma C F, Zheng Q, Ko S Y (1997a) Local heat transfer and recovery factor with impinging free-surface circular jets of transformer oil. International Journal of Heat and Mass Transfer 40 (18): 4295–4308.
Ma C F, Zheng Q, Lee S C, Gomi T (1997b) Impingement heat transfer and recovery effect with submerged jets of large Prandtl number liquid—I. Unconfined circular jets. International Journal of Heat and Mass Transfer 40 (6): 1481–1490.
Ma C F, Zheng Q, Sun H, Wu K, Gomi T, Webb B W (1997c) Local characteristics of impingement heat transfer with oblique round free-surface jets of large Prandtl number liquid. International Journal of Heat and Mass Transfer 40 (10): 2249–2259.
Magnussen F, Thelin P, Sadarangani C (Eds.) (2004) Performance evaluation of permanent magnet synchronous machines with concentrated and distributed windings including the effect of field-weakening, IET ed.
Markides C N, Mathie R, Charogiannis A (2016) An experimental study of spatiotemporally resolved heat transfer in thin liquid-film flows falling over an inclined heated foil. International Journal of Heat and Mass Transfer 93: 872–888.
Metzger D E, Cummings K N, Ruby W A (Eds.) (1974) Effects of Prandtl number on heat transfer characteristics of impinging liquid jets.
Miyamoto T, Matsusaka S, Kato K (2017) U.S. Patent No. 9,729,027. Washington, DC: U.S. Patent and Trademark Office.

Mohanty A K, Tawfek A A (1993) Heat transfer due to a round jet impinging normal to a flat surface. International Journal of Heat and Mass Transfer 36 (6): 1639–1647.
Molana M, Banooni S (2013) Investigation of heat transfer processes involved liquid impingement jets: a review. Braz. J. Chem. Eng. 30 (3): 413–435.
Mouza A A, Vlachos N A, Paras S V, Karabelas A J (2000) Measurement of liquid film thickness using a laser light absorption method. Experiments in Fluids 28 (4): 355–359.
Myant C, Reddyhoff T, Spikes H A (2010) Laser-induced fluorescence for film thickness mapping in pure sliding lubricated, compliant, contacts. Tribology International 43 (11): 1960–1969.
Nategh S, Krings A, Wallmark O, Leksell M (2014) Evaluation of Impregnation Materials for Thermal Management of Liquid-Cooled Electric Machines. IEEE Trans. Ind. Electron. 61 (11): 5956–5965.
Nebuchinov A S, Lozhkin Y A, Bilsky A V, Markovich D M (2017) Combination of PIV and PLIF methods to study convective heat transfer in an impinging jet. Experimental Thermal and Fluid Science 80: 139–146.
NEMA, 2016 M. MG 1-2016, Motors and Generators.
O'Donovan T S, Murray D B (2007) Jet impingement heat transfer – Part I: Mean and root-mean-square heat transfer and velocity distributions. International Journal of Heat and Mass Transfer 50 (17-18): 3291–3301.
Owos (accessed May 2023) Reluctance Motor Types Overview and detailed Function. Owos. https://oswos.com/reluctance-motor/.
Park M H, Kim S C (2019) Thermal characteristics and effects of oil spray cooling on in-wheel motors in electric vehicles. Applied Thermal Engineering 152: 582–593.
Pawar S, Patel D K (2020) The Impingement Heat Transfer Data of Inclined Jet in Cooling Applications. A Review. J. Therm. Sci. 29 (1): 1–12.
Popescu M, Staton D, Boglietti A, Cavagnino A, Hawkins D, Goss J (2015) Modern heat extraction systems for electrical machines - A review. In: Electrical Machines Design, Control and Diagnosis (WEMDCD), 2015 IEEE Workshop on. IEEE. S. 289–296.
Poubeau A, Vinay G, Kekelia B, Bennion K (2022) Conjugate Heat Transfer Simulations of High Prandtl Number Liquid Jets Impinging on a Flat Plate. SSRN Journal.
Rahman M M, Bula A J, Leland J E (1999) Conjugate Heat Transfer During Free Jet Impingement of a High Prandtl Number Fluid. Numerical Heat Transfer, Part B: Fundamentals 36 (2): 139–162.
Ren J, Wang L, Huang Z, Wang X, Li H, Lu J (2020) Study of 2CLIF Based on Simultaneous Measurement of Temperature and Concentration Using Single Color-Camera. In: 2020 5th International Conference on Electromechanical Control Technology and Transportation (ICECTT) IEEE.
Renon C, Fénot M, Girault M, Guilain S, Assaad B (2021) An experimental study of local heat transfer using high Prandtl number liquid jets. International Journal of Heat and Mass Transfer 180: 121727.
Rivière N, Volpe G, Villani M, Fabri G, Di Leonardo L, Popescu M (2019) Design analysis of a high speed copper rotor induction motor for a traction application. In May 2019 IEEE International Electric Machines & Drives Conference (IEMDC) (pp. 1024-1031). IEEE.
Sakakibara J, Adrian R J (1999) Whole field measurement of temperature in water using two-color laser induced fluorescence. Exp Fluids 26 (1-2): 7–15.
Sakakibara J, Hishida K, Maeda M (1997) Vortex structure and heat transfer in the stagnation region of an impinging plane jet (simultaneous measurements of velocity and temperature fields by digital particle image velocimetry and laser-

induced fluorescence) International Journal of Heat and Mass Transfer 40 (13): 3163–3176.
Saldarriaga-Zuluaga S D, López-Lezama J M, Zuluaga Ríos C D, Villa Jaramillo A (2022) Effects of the Incorporation of Electric Vehicles on Protection Coordination in Microgrids. World Electric Vehicle Journal, 13(9), 163.
Sarlioglu B, Morris C T, Han D, Li S (2016) Driving toward accessibility: a review of technological improvements for electric machines, power electronics, and batteries for electric and hybrid vehicles. IEEE Industry Applications Magazine, *23*(1), 14-25.
Schiefer M, Doppelbauer M (2015) Indirect slot cooling for high-power-density machines with concentrated winding. In: Proceedings, 2015 IEEE International Electric Machines and Drives Conference (IEMDC) Coeur d'Alene Resort, Coeur d'Alene, ID, U.S.A., 11-13 May, 2015. IEEE, Piscataway, NJ. S. 1820–1825.
Schröder M, Monissen C, Wahl A, Herold K (2022) Active Thermal Field Weakening in Electric Machines. MTZ Worldw 83 (7-8): 28–33.
Shah R, Hope K, Law A (2020) ATF: 2020 status and where we go from here.
Stevens J, Webb B W (1991a) Local Heat Transfer Coefficients Under an Axisymmetric, Single-Phase Liquid Jet. Journal of Heat Transfer 113 (1): 71–78.
Stevens J, Webb B W (1991b) The effect of inclination on local heat transfer under an axisymmetric, free liquid jet. International Journal of Heat and Mass Transfer 34 (4-5): 1227–1236.
Sun H, Ma C F, Chen Y C (1998) Prandtl number dependence of impingement heat transfer with circular free-surface liquid jets. International Journal of Heat and Mass Transfer 41 (10).
Sun Y, Zhang S, Yuan W, Tang Y, Li J, Tang K (2019) Applicability study of the potting material based thermal management strategy for permanent magnet synchronous motors. Applied Thermal Engineering 149: 1370–1378.
Tabbache B, Djebarri S, Kheloui A, Benbouzid M (2013) A Power Presizing Methodology for Electric Vehicle Traction Motors. International Review on Modelling and Simulations 6 (1): 29–32.
Todorov G, Stoev, B (2015) Analytical model for sizing the magnets of permanent magnet synchronous machines. Journal of Electrical Engineering, 3(3), 134-141.
Trout S R (2001) Material selection of permanent magnets, considering thermal properties correctly. In: Proceedings. Electrical Insulation Conference and Electrical Manufacturing & Coil Winding Conference, Cincinnati Convention Center, Cincinnati, Ohio, October 16-18, 2001. Institute of Electrical and Electronics Engineers; Electrical Manufacturing & Coil Winding Association, Piscataway NJ, Imperial Beach CA. S. 365–370.
Tuysuz A, Meyer F, Steichen M, Zwyssig C, Kolar J W (2017) Advanced Cooling Methods for High-Speed Electrical Machines. IEEE Trans. on Ind. Applicat. 53 (3): 2077–2087.
Wang H, Liu X, Kang M, Guo L, Li X (2022) Oil Injection Cooling Design for the IPMSM Applied in Electric Vehicles. IEEE Trans. Transp. Electrific. 8 (3): 3427–3440.
Webb B W, Ma C-F (1995) Single-Phase Liquid Jet Impingement Heat Transfer. In: Ayyaswamy P S (ed) Advances in heat transfer 26. s.n, S.l. S. 105–217.
Wereszczak A A, Emily Cousineau J, Bennion K, Wang H, Wiles R H, Burress T B, Wu T (2017) Anisotropic Thermal Response of Packed Copper Wire. Journal of Thermal Science and Engineering Applications 9 (4): 438.
Wikipedia (accessed May 2023a) Stator and rotor by Zureks. Wikipedia. https://fr.m.wikipedia.org/wiki/Fichier:Stator_and_rotor_by_Zureks.JPG.

Wikipedia (accessed May 2023b) Curie Temperature. Wikipedia. https://en.wikipedia.org/wiki/Curie_temperature.

Wikipedia (accessed May 2023c) Thermal Boundary Layer Thickness formed by heated fluid flow along a plate. Wikipedia. https://en.m.wikipedia.org/wiki/File:Thermal_Boundary_Layer_Thickness_formed_by_heated_fluid_flow_along_a_plate.jpg.

Wikipedia (accessed May 2023d) Jablonski diagram. https://en.wikipedia.org/wiki/Jablonski_diagram .

Wright L M, Seitz S (2019) Thermal Development of an Impinging Jet Using Planar Laser Induced Fluorescence (PLIF) In: Proceedings of the ASME Turbo Expo. Turbomachinery Technical Conference and Exposition--2019-- presented at The ASME Turbo Expo 2019 Turbiomachinery Technical Conference and Exposition, June 17-21, 2019, Phoenix, Arizona, USA. The American Society of Mechanical Engineers, New York N.Y.

Xu Z, La Rocca A, Arumugam P, Pickering S J, Gerada C, Bozhko S, Gerada D, Zhang H (2017) A semi-flooded cooling for a high speed machine. Concept, design and practice of an oil sleeve. In: Proceedings, IECON 2017-43rd Annual Conference of the IEEE Industrial Electronics Society. China National Convention Center, Beijing, China, 29, October - 01, November, 2017. IEEE, Piscataway, NJ. S. 8557–8562.

Yang Y, Bilgin B, Kasprzak M, Nalakath S, Sadek H, Preindl M, Cotton J, Schofield N, Emadi A (2017) Thermal management of electric machines. IET Electrical Systems in Transportation 7 (2): 104–116.

Ye L, Tao F, Xuhui W, Yong L (2013) Numerical research on hydraulic and thermal performance of the motor water jackets based on the orthogonal experiment. In: Electrical Machines and Systems (ICEMS), 2013 International Conference on. IEEE. S. 860–863.

Yildirim M, Polat M, Kurum H (2014) A survey on comparison of electric motor types and drives used for electric vehicles. In: 16th International Power Electronics and Motion Control Conference (PEMC), 2014. 21-24 Sept. 2014, Antalya, Turkey. IEEE, Piscataway, NJ. S. 218–223.

Zhao L, Cerro R L (1992) Experimental characterization of viscous film flows over complex surfaces. International Journal of Multiphase Flow 18 (4): 495–516.

Zhou P, Kalayjian, N. R., Cutler G D, Augenbergs P K (2009) U.S. Patent No. 7,489,057. Washington, DC: U.S. Patent and Trademark Office.

Zysset E (2001) U.S. Patent No. 6,191,511. Washington, DC: U.S. Patent and Trademark Office.

DOI: 10.17185/duepublico/81552
URN: urn:nbn:de:hbz:465-20240314-092935-0